A Search for Very High Energy Gamma-Ray Emission from Active Galactic Nuclei using Multivariate Analysis Techniques

Stephen Gammell

Submitted to University College Dublin
for the degree of Ph.D. in the Faculty of Science

October 2004

Department of Experimental Physics
Prof. Gerard O' Sullivan

Supervised by Dr. John Quinn

Abstract

This thesis describes a search for Very High Energy (VHE) gamma-ray emission from Active Galactic Nuclei (AGN), based on four years of observations using the Whipple 10m telescope.

Active Galactic Nuclei are galaxies with an unresolved central nucleus which outshines the rest of the host galaxy. The emission is believed to result from accretion of matter onto a super-massive black hole. VHE observations of AGN provide an insight into some of the most physically extreme environments in our Universe. Over the last decade, great progress has been made in our understanding of these objects, however a number of important details remain unknown. To answer these questions requires detection and study of a greater number of AGN in the TeV energy domain. In an attempt to expand the VHE source catalogue this work has concentrated on a search for extragalactic sources of VHE gamma radiation. As part of the search, a number of new analysis techniques have been developed, aimed at extending the energy range in which gamma rays may be identified. In addition, this work details selection and analysis of a number of the most promising gamma-ray sources. The results of these analyses are discussed in terms of predicted gamma-ray flux levels and the potential for detection of these objects using next-generation experiments.

Contents

List of Figures

List of Tables

Chapter 1

Gamma-ray Astronomy

1.1 Introduction

Since the discovery, by Victor Hess in 1912, that the Earth is continuously bombarded by a population of high-energy particles, much effort has been expended in an attempt to elucidate their origins. These cosmic-ray particles comprise electrons, protons and heavier elements, spanning an energy range from 10^5 eV to 10^{20} eV, and must originate in some of the most extreme environments of our universe, most probably supernova explosions, rapidly rotating neutron stars or super-massive black holes. Evidence for acceleration of cosmic rays at such sites remains elusive, primarily due to the fact that it is extremely difficult to directly observe point sources of cosmic rays. As charged particles traverse the universe from their acceleration sites they are deflected by the random magnetic fields pervading space (Figure 1.1), resulting in an isotropic distribution of arrival directions here on Earth. Location of cosmic accelerators must therefore be achieved using indirect methods, by identifying by-products of cosmic-ray production which are uncharged and arrive at the Earth retaining their original trajectory. Three such candidates exist: the neutron, the neutrino and the photon. Free neutrons are unstable, decaying via β-decay to form protons, with a rest-frame half life of 15 minutes, making their detection here on Earth unlikely. Neutrinos are extremely light and weakly interacting, requiring expensive and complex detectors. This leaves photons, believed to be produced at acceleration sites via proton-proton interactions or particle-antiparticle annihilation, whose infinite lifetime, zero charge, and relatively simple detection method provide an excellent means for identification of cosmic-ray sources. Thus in an attempt to solve the cosmic-ray mystery the field of gamma-ray astronomy was born, and while the origins of cosmic rays remain elusive, gamma-ray astrophysics

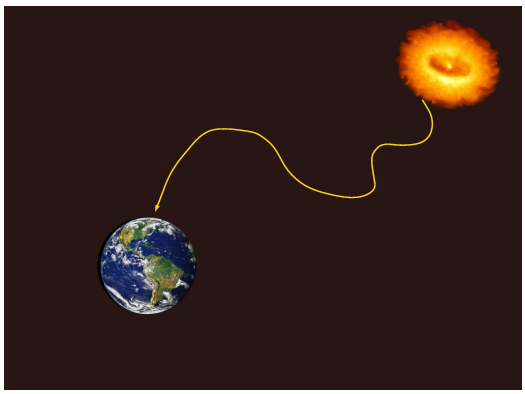

Figure 1.1: Point sources of cosmic-ray acceleration are extremely difficult to locate. As the charged cosmic rays traverse the galaxy they are deflected by random magnetic fields and thus arrive at the Earth having lost all details of their original trajectory.

has opened up numerous new areas of research. These include: the study of extreme regions of the universe; searches for dark matter, primordial black holes, relic particles from the big bang, cosmic strings and anti-matter; investigation of light produced by the first galaxies and tests of some theories of quantum gravity.

This chapter provides an introduction to the research field of gamma-ray astrophysics, giving a brief overview of its history, current status and future prospects. Discussion will be approached from the point of view of high energy (HE) and very high energy (VHE) gamma-ray astronomy, which are dominated by space-based and ground-based observing techniques respectively. Particular emphasis will be placed upon the current status of VHE astronomy utilising the Imaging Atmospheric Cherenkov Technique (IACT) as this thesis reports work carried out using the approach. Finally a broad outline of the thesis will be presented, detailing the topics covered by each of the subsequent chapters.

1.2 The gamma-ray domain

The term *gamma ray* is used to describe photons whose energy spans the range 100 keV (10^5 eV) to greater than 100 EeV (10^{20} eV), some 15 decades of energy and covering a region larger that the rest of the electromagnetic spectrum combined. Because of the extended nature of the gamma-ray regime it is customary to introduce some form of sub division. Using the schemes

of Weekes (2003b) and Hoffman et al. (1999), where division is based on the energy range spanned by different detection techniques, we have six regions within the gamma-ray domain. The energy region stretching from 0.1 MeV to 10 MeV is the low-energy (LE) domain. From 10 MeV up to 30 MeV lies the medium-energy (ME) region which is followed by the high-energy (HE) domain, covering energies from 30 MeV up to 100 GeV. The very-high-energy (VHE) domain comprises photons with energy between 100 GeV and 100 TeV, which leads onto the ultra-high-energy (UHE) domain spanning a region from 100 TeV to 100 PeV. The final gamma-ray domain consists of photons with energy greater than 100 PeV, and is known as the extremely-high-energy (EHE) domain. A summary of this division is given in Table 1.2. Currently the most active fields of gamma-ray astronomy are covered by the LE, HE and VHE ranges, which utilise space-based and ground-based detectors.

1.3 High-Energy Gamma-Ray Astronomy

The Earth's atmosphere is opaque to all radiation above 10 eV, meaning that to observe gamma rays directly requires placement of a detector above the Earth. Early experiments comprised spark-chamber detectors, mounted on-board balloons and carried to the top of the atmosphere. The first practical demonstration of the existence of cosmic gamma rays came from data recorded by the Explorer XI telescope in 1965 (Clark et al., 1968). The telescope, with its small collection area and poor angular resolution, observed a flux of gamma rays from space but could not pinpoint its location. A shift in gamma-ray astronomy, from using balloon-based detectors to satellite-based ones, was instigated by the launch of the NASA mission, SAS-2, in 1972 (Fichtel et al., 1975), followed three years later by the European mission COS-B (Scarsi et al., 1977). Although its period of orbit was cut short due to a power failure, SAS-2 provided the first evidence for pulsed gamma-ray emission from three sources, the Crab Nebula, Vela and an unidentified source, now known to be Geminga. COS-B, with its longer mission of seven years, also detected pulsed emission from the three sources seen by SAS-2 and, in addition, identified 25 discrete sources of gamma radiation (Swanenburg et al., 1981), including the first extragalactic source 3C 273. The success of both missions prompted efforts to commission a new experiment, with greater collection area and flux sensitivity.

Energy range	Designation	Detection technique
0.1 - 10 MeV	Low energy (LE)	Satellite-based Compton Telescope
10 - 30 MeV	Medium energy (ME)	Satellite-based Compton Telescope
30 MeV - 100 GeV	High energy (HE)	Satellite-based tracking detector
100 GeV - 100 TeV	Very high energy (VHE)	Ground-based atmospheric Cherenkov detector
100 TeV - 100 PeV	Ultra high energy (UHE)	Ground-based air-shower particle detector
$>$ 100 PeV	Extremely high energy (EHE)	Ground-based air fluorescence detector

Table 1.1: Summary of a scheme for dividing up, into more manageable pieces, the large area covered by the term *gamma ray*. The scheme is a combination of that proposed by Weekes (2003b) and Hoffman et al. (1999), whereby division is based on the energy range spanned by different detection techniques.

1.3.1 The Compton Gamma Ray Observatory

In spite of the widely acclaimed success of the SAS-2 and COS-B missions, astronomers had to wait a further decade for the launch of the next space-based gamma-ray experiment. The Compton Gamma Ray Observatory (CGRO), was eventually launched in April 1991, following a number of delays including the *Challenger* shuttle disaster. The satellite payload comprised four different experiments (Figure 1.2), which when combined provided energy coverage in the range 15 keV to 30 GeV. The CGRO instruments were:

- **BATSE:** The burst and transient source experiment, comprising eight wide-field, scintillation detectors, providing complete sky coverage, in search of gamma-ray bursts and transient gamma-ray events. The detectors were sensitive in the energy range 20 keV to 1.9 MeV and on detection of a burst of high-energy photons BATSE alerted the other detectors so that observations were carried out over a wider range. BATSE's major achievement was to show that the distribution of gamma-ray bursts (GRBs) was isotropic (Figure 1.3), which was unexpected and showed that at least some gamma-ray bursts must have extra-galactic origins (Paciesas et al., 1999).

- **OSSE:** The orientated scintillator spectrometer experiment, comprising four identical scintillators, aimed at making spectral observations between the energies of 0.1 and 10 MeV.

- **COMPTEL:** The imaging Compton telescope, which is sensitive in the historically difficult energy region spanning 1 to 30 MeV (Weekes, 2003b). COMPTEL was designed to search for evidence of nuclear reactions in events such as supernovae.

- **EGRET:** The energetic gamma-ray experiment telescope operated in the 20 MeV to $\sim$ 30 GeV energy range. EGRET was a pair-production telescope, similar in design to SAS-2 and COS-B, but with much improved sensitivity.

1.3.2 EGRET

EGRET is the CGRO experiment of most interest to the VHE gamma-ray community, since it operated at the high end of the energy spectrum covered by the instruments on-board. EGRET consisted of a spark chamber, divided into two parts. In the upper section electron-positron pairs are created by the incident gamma ray, the direction of which is reconstructed by recording

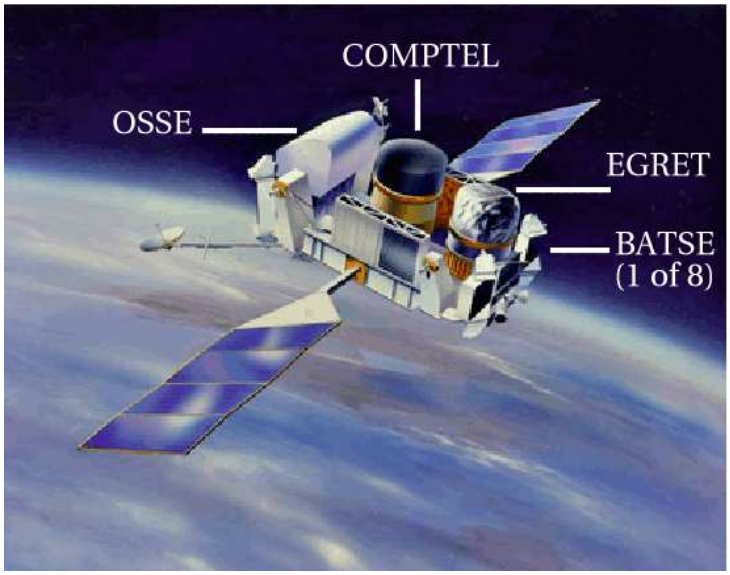

Figure 1.2: Artist's impression of the Compton Gamma Ray Observatory (CGRO). Carrying four different experiments, and staying in orbit for approximately a decade, the mission proved a great success, providing much information about the gamma-ray sky. Image is taken from http://cossc.gsfc.nasa.gov.

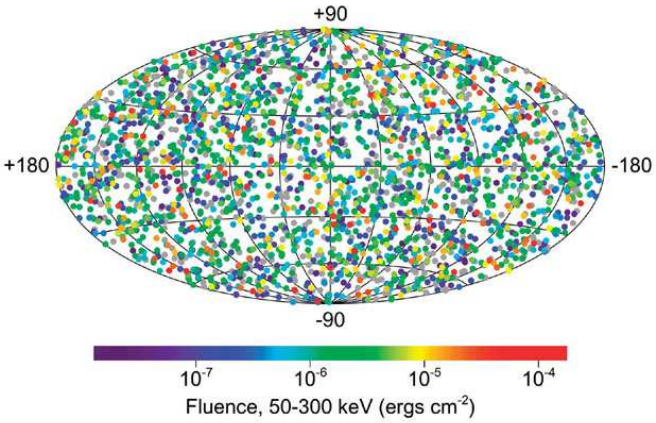

Figure 1.3: Map of the sky showing the distribution of gamma-ray bursts, based on observations by BATSE, on-board CGRO. Prior to first light of BATSE gamma-ray bursts (GRBs) were believed to be of galactic origin, and thus a GRB map was expected to show a higher population of events along the galactic plane. The isotropic distribution observed proved that a large percentage of GRBs originate outside our galaxy. Image is taken from http://cossc.gsfc.nasa.gov/batse.

the path taken by the pairs through the lower section of the chamber. The electron-positron pair deposit their energy in a sodium-iodide calorimeter, allowing the energy of the primary to be estimated. An anti-coincidence shield is used to eliminate cosmic-ray triggers. Although it operated at less than peak efficiency for much of its lifetime (due to a shortage of spark-chamber gas) EGRET was a huge success, performing the first all-sky survey in the 30 MeV to 10 GeV range (Thompson et al., 1995; Hartman et al., 1999) (Figure 1.4). Highlights of the mission include:

- Detection of diffuse gamma-ray emission from the galactic plane.
- Detection of diffuse galactic emission at higher galactic latitudes, most probably extragalactic in origin.
- Detection of six GRBs at HE.
- Detection of seven HE gamma-ray pulsars.
- Detection of HE emission from regions spatially coincident with supernova remnants.
- Detection of discrete sources of extra-galactic HE gamma-ray emission, with over 70 belonging to the object class known as blazars.
- Detection of approximately 170 HE sources with no identifiable counterparts at other wavelengths.

1.3.3 Next Generation Experiments

Following the de-orbit of the CGRO in June 2000, there were no gamma-ray satellites in operation until the launch of the International Gamma-Ray Astrophysics Laboratory (INTEGRAL) in October 2002. This is the first of a number of new space-based experiments due for launch within the next five years (Figure 1.5), a summary of which is presented in Table 1.2. The detectors most interesting to VHE gamma-ray astronomers are AGILE and GLAST, as for the first time direct detection of cosmic gamma rays will extend beyond the 30 GeV mark.

AGILE

The Astro-rivelatore Gamma a Immagini L'Eggero (Light Imaging Detector for Gamma-ray Astronomy), an Italian mission, is due to be launched in 2005

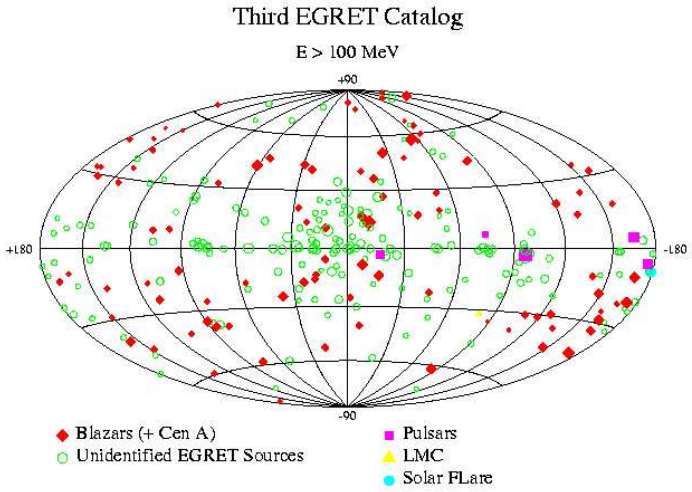

Figure 1.4: The third EGRET Catalog of HE gamma-ray sources (Hartman et al., 1999).

Mission	Country	Launch	Energy range
INTEGRAL[(a)]	ESA	2002	15 keV - 10 MeV
Swift[(b)]	NASA	2004	< 150 keV
AMS[(c)]	ISS	2005	> 10 GeV
AGILE[(d)]	Italy	2005	20 MeV - 50 GeV
GLAST[(e)]	NASA	2007	20 MeV - 300 GeV

Table 1.2: Summary of future gamma-ray satellites. Since the de-orbit of the CGRO there were no gamma-ray satellited operation until the launch of INTEGRAL in October 2002. The launch of GLAST should prove a milestone in gamma-ray astronomy, as when combined with the next-generation ground-based experiments, it will, for the first time, provide uninterrupted coverage from 20 MeV up to several TeV. (a) Teegarden and INTEGRAL Science Working Team (1999); (b) Chincarini et al. (2003); (c) Derome and The AMS Collaboration (2003); (d) Tavani (2003); (e) Ritz and GLAST Team (2003).

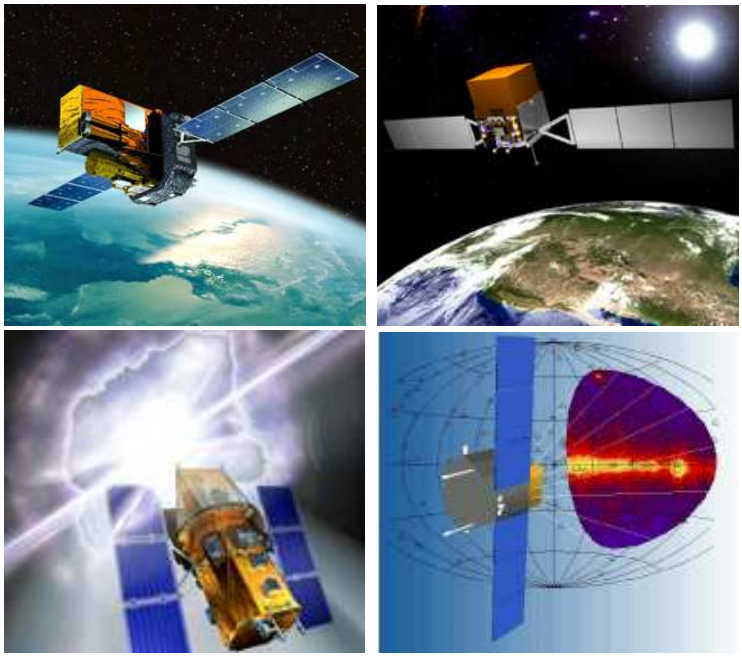

Figure 1.5: Artists' impressions of next-generation space-based gamma-ray observatories. Starting at top left and moving in a clockwise direction they are INTEGRAL (http:// www.esa.int/ SPECIALS/ Integral), GLAST (http:// glast.gsfc.nasa.gov), Swift (http:// swift.gsfc.nasa.gov/ docs/ swift) and AGILE (http:// agile.mi.iasf.cnr.it).

(Tavani, 2003). Comprising three detectors, it will detect photons in the 10 - 40 keV and 20 MeV - 50 GeV bands. The gamma-ray imaging detector (GRID), with its very large field of view and short dead-time, will be sensitive in the 30 MeV to 50 GeV range, while Super-AGILE will carry out x-ray observations of the same sources. The mini-calorimeter (MC) will operate independently, searching for transient events such as gamma-ray bursts in the 0.3 - 300 MeV range. AGILE will be the first HE gamma-ray telescope to depart from the spark-chamber detection method, instead utilising solid-state detectors, which will result in excellent angular resolution but limited energy resolution (due to the small thickness of its calorimeter). With overall sensitivity similar to EGRET, AGILE was conceived as a bridge between the EGRET and GLAST experiments.

GLAST

The Gamma-ray Large Area Telescope (Ritz and GLAST Team, 2003) is a next-generation telescope, the successor to EGRET. Although similar in design to EGRET, GLAST will utilise silicon-strip technology, resulting in a more compact and more efficient instrument with improved angular and energy resolutions. GLAST is due for launch in February 2007, and will consist of two telescopes; the Large Area Telescope (LAT) and the Gamma-ray Burst monitor (GRM). Although it will be only twice as heavy, GLAST will outperform EGRET in most areas by a factor of 10 - 40. The mission is conservatively estimated to last for five years, and will not experience many of the problems suffered by EGRET as operation does not depend on any replenishable materials. The most exciting feature of GLAST will be its overlap in energy with future ground-based observatories.

1.4 Very-High-Energy Gamma-Ray Astronomy

Due to falling photon flux and limited collection area, meaningful astronomy with space-based detectors is not possible above 100 GeV (until the launch of next-generation satellite experiments such as GLAST (Ritz and GLAST Team, 2003)). Although the Earth's atmosphere is opaque to gamma radiation, around this energy it becomes possible to detect cosmic radiation on the surface of the Earth, albeit using indirect methods. The opacity of the atmosphere, that is the interaction of gamma-ray photons or cosmic-ray particles with air molecules, results in a cascade of elementary particles and photons. Depending on the energy of the primary photon these cascades may survive

to ground level, making detection possible using arrays of particle detectors. Showers that die out high in the atmosphere are still observable via the short-pulsed Cherenkov emission of their relativistic constituents. Following detection of Cherenkov light from the night sky (Galbraith and Jelley, 1953), the possibility for ground-based gamma-ray observations was noted by Morrison (1958) and quickly followed by extremely optimistic flux predictions (Cocconi, 1959). This led to a sudden interest in the field of ground-based gamma-ray astronomy, however detection of sources proved much more difficult than first thought, due mainly to the high-level background of charged cosmic rays.

1.4.1 The Atmospheric Cherenkov Technique

Upon interaction with molecules in the atmosphere, a high-energy gamma ray initiates a predominantly electromagnetic cascade, which grows exponentially up to a certain atmospheric depth, after which it begins to attenuate and dies out before reaching ground level. The sub-atomic constituents of the cascade travel at a velocity exceeding the phase velocity of light, thereby emitting Cherenkov radiation in the forward direction. This radiation is easily detected, using a light collector and photomultiplier tube (PMT) assembly, however detection of gamma rays using this approach is limited by the almost overwhelming flux of cosmic-ray induced showers. Although similar, gamma-ray-initiated showers and cosmic-ray-initiated showers may be distinguished by differences in the angular distribution of their Cherenkov emission and shower arrival direction. To exploit these differences two main methods of discrimination are used, the imaging atmospheric Cherenkov technique (IACT) and the wavefront timing technique.

The Imaging Atmospheric Cherenkov Technique

The main components of an imaging telescope are a large optical reflector, a fast response camera and triggering system. The telescope records the development of a shower by imaging its Cherenkov emission onto a series of PMTs located in the focal plane of the reflector. Based on differences in the physics of the proton showers and gamma-ray showers it is possible to identify gamma rays and to estimate the energy of the primary photon. This has been the most successful ground-based approach to date, with a number of observatories operating worldwide (Table 1.3), and a current VHE catalogue comprising 18 sources of different variety (Horan and Weekes, 2004). The work presented in this thesis is based on observations utilising the IACT, and thus a more detailed discussion of the physics of extensive air showers

and the imaging approach to gamma-ray detection is reserved for Chapter 3 and Chapter 4. A summary of the current TeV source catalogue is presented in Section 1.4.3, while the next generation imaging detectors are discussed in Section 1.4.4.

The Wavefront Timing Technique

The energy threshold of existing second-generation ground-based telescopes is limited to energies around 200 GeV, primarily due to their mirror area. To lower the threshold by a factor of ten requires an increase in mirror area by two orders of magnitude. The use of solar power plants, with their massive mirror areas, for gamma-ray astronomy was first proposed by Danaher et al. (1982). A typical detector comprises a number of heliostats, whose light is focused onto individual phototubes via a secondary mirror. The complex focal plane instrumentation and often poor quality mirrors make this technique difficult, however at typical operational energies cosmic rays are much less efficient at producing Cherenkov light, thereby greatly reducing background. In addition, by utilising the lateral distribution of light as a discriminant, detection of a gamma-ray signal is possible, while estimation of the primary photon energy is ,in theory, more accurate due to multiple sampling of the Cherenkov light pool (Hoffman et al., 1999). A number of the more recent wavefront experiments are summarised in Table 1.4. Results from this branch of ground-based astronomy have been limited although STACEE, CELESTE and GRAAL have detected the Crab Nebula (Oser et al., 2001; de Naurois et al., 2002; Arqueros et al., 2002) while STACEE and CELESTE have also detected Markarian 421 (Boone et al., 2002; Holder and The Celeste Collaboration, 2001). The small field of view of these experiments make them unsuitable for observations of extended sources; however, their low energy threshold is ideal for detection of point sources with steep emission spectra.

1.4.2 Particle Wavefront Detection Techniques

Above approximately 10 TeV, a gamma-ray initiated EAS is sufficiently energetic to reach ground level, permitting estimation of the arrival direction and energy of the primary. Currently there are two different approaches to detection of such showers. The first utilises an array of scintillators, spread out over a vast area of $\sim 10^4$ - 10^5 m^2. By recording the arrival time of the shower front at different detectors it is possible to calculate the arrival direction. The energy threshold of such experiments depends on the altitude of the detectors, the spacing between the detector elements, and the number of detectors that must be triggered to accurately reconstruct the shower

Group	Site	Oper.	No. Telescopes	Aperture	Threshold (TeV)
CANG-II	Woomera Australia	n	2	10 m	0.50
CAT	French Pyrenees	n	1	3 m	0.25
Crimea	Crimea	y	2	2.4 m × 6	1.0
Durham	Narrabri, Australia	n	3	7 m	0.25
HEGRA	La Palma, Spain	n	5	3 m	0.5
7 TA	Utah, USA	n	7	2 m	0.5
SHALON	Tien Shen, Russia	n	1	4 m	1.0
TACTIC	Mt. Abu India	n	1	10 m	0.3
Whipple	Arizona, USA	y	1	10 m	0.25

Table 1.3: Some of the more recent ground-based IACT telescopes. Many of these second generation experiments are no longer operational, however next-generation arrays are already under construction (see Section 1.4.4).

Group	Site	Oper.	No. Reflectors	Threshold (GeV)
CELESTE	French Pyrenees	y	54	50
GRAAL	Almeria, Spain	n	63	250
Solar Two	California, USA	y	2000	–
STACEE	New Mexico, USA	y	48	140

Table 1.4: A summary of recent Cherenkov wavefront sampling experiments.

geometry. Discrimination between shower types is extremely difficult, and energy estimation is unreliable due to limited sampling of the shower front.

The second approach to characterizing the particle shower front uses a water-Cherenkov detector, comprising a large volume of water surrounded by a light-tight barrier. Particles entering the detector travel at a velocity exceeding the phase velocity of light in water and emit Cherenkov radiation. A series of PMTs, strategically placed around the water pool, provide a snapshot of the shower front based on Cherenkov emission of the particles. The arrival direction is reconstructed using the temporal characteristics of the front across the water pool. To distinguish between shower types a double-level array of PMTs is used; the top level detects emission by the shower front while the bottom level detects emission from a highly penetrating population of muons. Since cosmic-ray showers are muon-rich and gamma-ray showers are muon-deficient, discrimination is attainable.

Early scintillator experiments were plagued by many problems; however, more recent experiments (Table 1.4.2) with their higher density arrays, accompanying muon detectors, better timing, and lower energy thresholds, have proved more successful. The Tibet Air Shower Array (Amenomori and The Tibet As Γ Collaboration, 2001), with its high altitude location and low energy threshold, has reported detection of the Crab Nebula and Markarian 421 at TeV energies (Amenomori et al., 1999, 2003). At present there is only

Group	Site	Detector	Threshold (TeV)
Tibet	Tibet	Scintillator	3.0
MILAGRO	New Mexico, USA	Water Cherenkov	0.20

Table 1.5: Recent particle detector arrays used for ground-based gamma-ray astronomy.

one water-Cherenkov experiment in operation. Milagro (Sinnis, 2003), comprising a 50,000 m^3 volume of water observed by $\sim$ 700 PMTs has reported detection of the Crab Nebula (Atkins et al., 2003). Following a trend already seen with space-based observations, many of the early particle array results (e.g. Stamm and Samorski (1983)) have not been confirmed by later, more sensitive instruments.

1.4.3 VHE Observations

Establishment of ground-based gamma-ray astronomy as an observational discipline in its own right was slow to happen. This may be partly attributed to the fact that early results were reported based on weak signals and marginal detections. Indeed explanation of some observations (Lloyd-Evans et al., 1983; Samorski and Stamm, 1983) required the invention of new particle physics (Hoffman et al., 1999). Since the first unambiguous detection of the Crab Nebula at TeV energies using the IACT (Weekes et al., 1989) the field has enjoyed a period of rapid growth, and we now stand at a point where the catalogue of VHE sources has grown to a respectable 18 sources (Table 1.6, Figure 1.7). These sources belong to a variety of classes including blazars, supernova remnants, binaries, starburst galaxies, radio galaxies, and OB associations.

Supernova Remnants

At the end of its life-cycle a star may undergo a catastrophic explosion, whereby a huge amount of energy is released and matter expelled with high velocity into the surrounding space. Although the star is destroyed its remains may be detected as what is known as a supernova remnant (SNR).

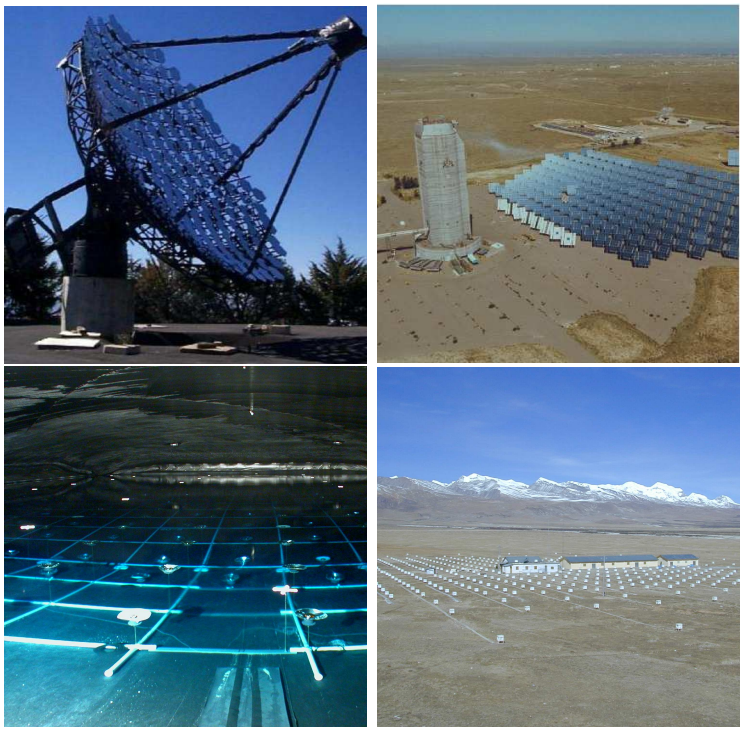

Figure 1.6: Different types of detectors used for ground-based gamma-ray astronomy. Starting at top left and moving clockwise are: (i) The Whipple 10m telescope, whose detection method is the IACT (http:// veritas.sao.arizona.edu); (ii) The STACEE experiment which detects the Cherenkov wavefront of EAS (http:// www.astro.ucla.edu/ stacee); (iii) The Tibet Air Shower Array which detects the particle shower-front using scintillators (http:// www.icrr.u-tokyo.ac.jp/ em); (iv) MILAGRO which detects the shower front particles as they pass through a massive water-Cherenkov detector (http://www.lanl.gov/ milagro).

TeV Catalogue	Name	Class	Discovery	EGRET	Grade	Reference
TeV 0047-2518	NGC 253	Starburst	CANG/2003	no	B	Itoh et al. (2003)
TeV 0219+4248	3C66A	Blazar	Crimea/1998	yes	C-	Neshpor et al. (1998)
TeV 0535+2200	Crab Nebula	SNR	Whipple/1989	yes	A	Weekes et al. (1989)
TeV 0834-4500	Vela	SNR	CANG/1997	no	C	Yoshikoshi et al. (1997)
TeV 1121-6037	Cen X-3	Binary	Durham/1999	yes	C	Chadwick et al. (2000a)
TeV 1104+3818	Mrk 421	Blazar	Whipple/1992	yes	A	Punch et al. (1992)
TeV 1231+1224	M87	Radio Gal.	HEGRA/2003	no	C	Protheroe et al. (2003)
TeV 1429+4240	H1426+428	Blazar	Whipple/2002	no	A	Horan et al. (2002)
TeV 1503-4157	SN1006	SNR	CANG/1997	no	B	Tanimori et al. (1998)
TeV 1654+3946	Mrk 501	Blazar	Whipple/1995	no	A	Quinn et al. (1996)
TeV 1710-4429	PSR 1706-44	SNR	CANG/1995	no	A	Kifune et al. (1995)
TeV 1712-3932	RXJ1713.7-39	SNR	CANG/1999	no	B+	Muraishi et al. (2000)
TeV 2000+6509	1ES1959+650	Blazar	7TA/1999	no	A	Nishiyama (1999)
TeV 2032+4131	CygOB2	OB assoc.	HEGRA/2002	yes	B	Aharonian et al. (2002b)
TeV 2159-3014	PKS2155-304	Blazar	Durham/1999	yes	A	Chadwick et al. (1999)
TeV 2203+4217	BL Lacertae	Blazar	Crimea/2001	yes	C	Neshpor et al. (2001)
TeV 2323+5849	Cas A	SNR	HEGRA/1999	no	B	Aharonian et al. (2001)
TeV 2347+5142	1ES2344+514	Blazar	Whipple/1997	no	A	Catanese et al. (1998)

Table 1.6: A summary of the different sources detected at VHE. Eighteen sources are listed, falling into six different types: blazars, supernova remnants, binaries, starburst galaxies, radio galaxies, and OB associations. One of the most striking aspects of the catalogue is that less than half of the sources have been detected by EGRET, clearly establishing VHE gamma-ray astronomy as a new observational field. The sources are graded, according to the quality of their detection, with an A grade given to those that have been independently verified at the $5\,\sigma$ level. It should be noted that using this criteria most EGRET detections would only warrant a grade B. Table is adapted from Horan and Weekes (2004).

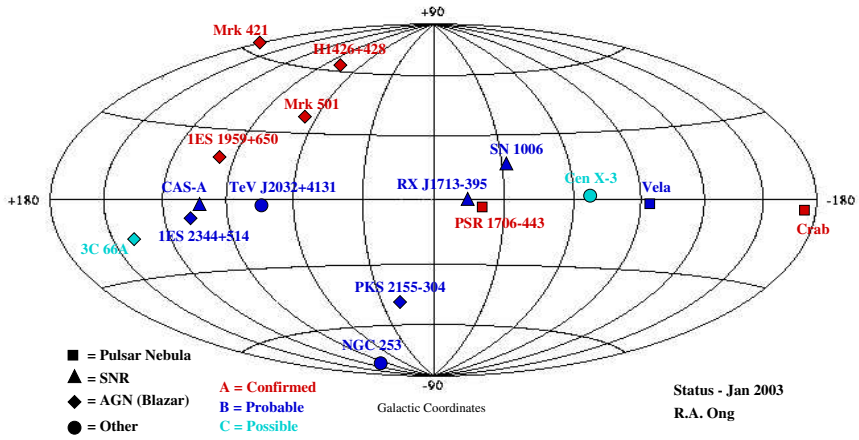

Figure 1.7: Map of the TeV gamma-ray sky. To date 18 sources have been detected with varying levels of significance. Figure is adapted from Ong (2003).

There are two main types of SNR; plerions in which relativistic electrons are constantly injected into the remnant by a central pulsar, and shell-type where the expanding shock sweeps up material as it propagates through the interstellar medium.

The Crab Nebula is an archetypal plerion, and was the first confirmed source of VHE gamma radiation, initially observed at the $9\,\sigma$ level following 60 hours of observations by the Whipple Observatory (Weekes et al., 1989). Subsequently detected by 8 experiments using different versions of the IACT, the Crab Nebula is now routinely detected by Whipple in an hour's observations. VHE emission from the Crab Nebula was predicted to be pulsed, however exhaustive analysis over the last decade (Kildea, 2003; Gillanders et al., 1997) has shown the Crab Nebula to be a steady source of gamma rays, to such an extent that it is now used as the standard candle for gamma-ray astronomy (in the northern hemisphere). The VHE spectrum of the Crab Nebula (Figure 1.8) has been derived (Hillas et al., 1998) and is consistent with an inverse Compton model for gamma-ray emission. In addition to the Crab Nebula, two other plerions have been observed at TeV energies, both in the southern hemisphere. PSR 1706-44 was reported at a $12\,\sigma$ level above 1 TeV by CANGAROO (Kifune et al., 1995), and later confirmed by the Durham Group (Chadwick et al., 1998). Like the Crab Nebula, PSR 1706-

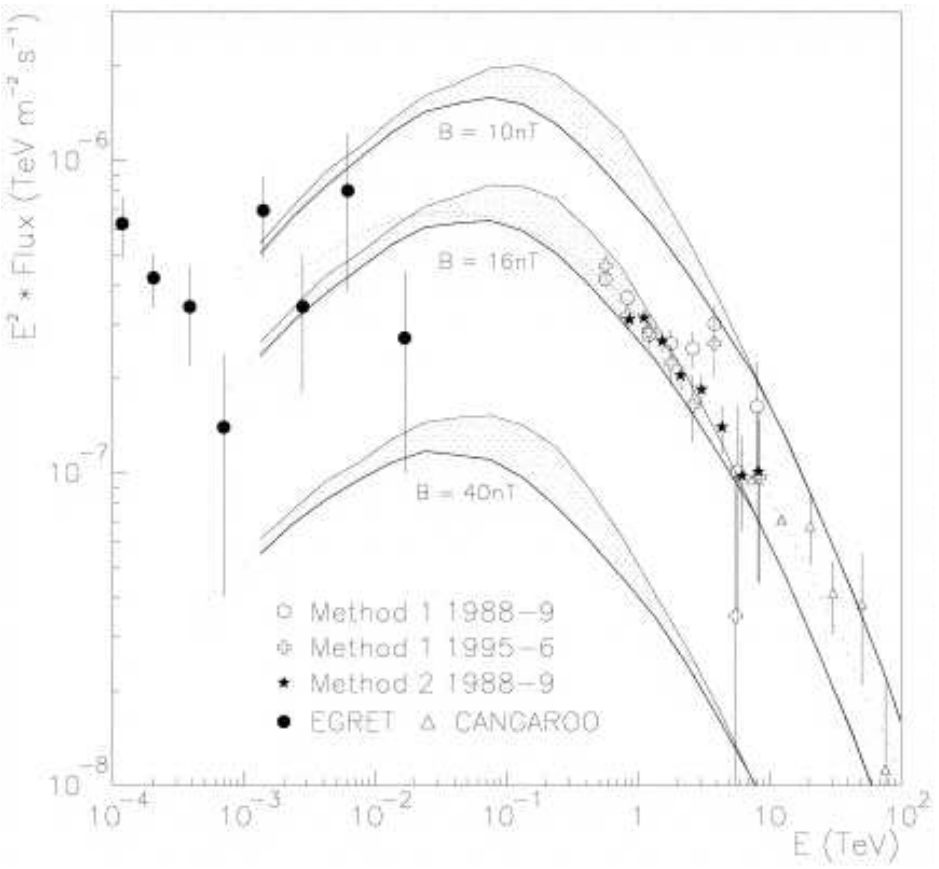

Figure 1.8: The Crab Nebula gamma-ray spectrum (Hillas et al., 1998), derived using data recorded with the Whipple telescope, and compared to EGRET and CANGAROO results. Also shown is the inverse-Compton spectrum, simulated for three different magnetic field strengths.

44 appears to be a steady source and has become the standard candle for observatories located in the southern hemisphere. VHE emission from the vicinity of the Vela pulsar has also been reported (Yoshikoshi et al., 1997), but awaits confirmation. Originally the CANGAROO Collaboration claimed that the emission was offset by 0.14° from the pulsar position; however, this is no longer claimed.

To date three shell-type SNRs have been detected. The first, SN1006, was detected by CANGAROO in 1997 (Tanimori et al., 1998), following observations of a strong x-ray flux. Emission was shown to originate in the northeast rim of the SNR shell, providing the first direct evidence for acceleration of particles to TeV energies at a shock front. Subsequent observations

using a more sensitive instrument allowed derivation of the energy spectrum (Tanimori et al., 2001), which is consistent with an inverse Compton model. RXJ1713.7-39 was first detected in 1999 by CANGAROO (Muraishi et al., 2000) and its energy spectrum was derived following deeper observations (Enomoto et al., 2002). The observations are not well fitted by an inverse Compton model, rather they are consistent with a hadronic model, thereby offering the first evidence for cosmic-ray acceleration in SNRs. The results are somewhat complicated by the presence of the EGRET unidentified 3EG J1714-38 in the field of view, whose HE spectrum is inconsistent with that of a proton model (Reimer and Pohl, 2002). Recent results also show that the spectrum may be fit using an inverse Compton model, assuming a large value for the magnetic field (Ong, 2003). The HEGRA Collaboration reported detection of a third shell-type SNR in 2001 (Aharonian et al., 2001). Cas A, the brightest source in the radio sky, was observed at a $5\,\sigma$ level following a deep exposure and is the weakest TeV source to date. In addition to the reported detections, upper limits on TeV emission from other shell-type SNRs are reported by Buckley et al. (1998), Chadwick et al. (2000b) and Lessard et al. (1999).

X-ray Binaries

X-ray binaries are among the most luminous galactic objects in the x-ray sky, and early VHE observations indicated that many were also TeV emitters (Chadwick et al., 1990). With the advent of more sensitive experiments many of these claims were not substantiated, however there may be one exception. The object Centaurus X-3, a high mass system containing an orbiting pulsar, has been observed at a $4.7\,\sigma$ level by the Durham group (Chadwick et al., 2000a). Again, confirmation of this detection is required.

Blazars

Active Galactic Nuclei (AGN) are galaxies whose emission is dominated by a bright central core, believed to be powered by a super-massive black hole. Approximately 15 % of AGN are radio loud, exhibiting a powerful outflow of relativistic particles along the poles of the galaxies (for a more detailed description of AGN see Chapter 2). One of the great successes of EGRET was the detection at HE of blazars, a subset of AGN whose jets are thought to be closely aligned with the line of sight. Motivated by the positive HE detections, ground-based gamma-ray observatories initiated a program aimed at monitoring the most promising extragalactic candidates. Based on this approach, eight blazars have been detected to date.

The first detection of an extragalactic TeV source was that of Markarian 421 (Mrk 421) by the Whipple Collaboration (Punch et al., 1992). Since this time, Mrk 421 has been the most intensively studied blazar at VHE, and its emission over the last decade may be characterised by a series of short-duration flares with a baseline below the sensitivity of the Whipple detector. During one outburst of activity, the flux level was observed to vary extremely quickly, with a doubling and decay time of less than 15 minutes (Gaidos et al., 1996). A period of sustained flaring activity throughout 2000 and 2001 allowed the energy spectrum of Mrk 421 to be accurately reconstructed (Figure 1.9). The spectrum is well described by a power law with an exponential cutoff (Krennrich et al., 2001), and is consistent with previous results by the Whipple Collaboration (Zweerink et al., 1997; Krennrich et al., 1999) and by the HEGRA collaboration (Horns et al., 2001). Recent results (Krennrich et al., 2002) have provided evidence for spectral variability, with a hardening of the spectrum observed with increasing flux.

Markarian 501 (Mrk 501) was the second extragalactic object detected at TeV (Quinn et al., 1996), and established VHE gamma-ray astronomy as a discipline in its own right, since at the time it had not been observed by EGRET. During the 1997 season Mrk 501 underwent a period of dramatic flaring, where it changed from being the weakest source in the gamma-ray sky to the brightest in a very short time (Bradbury et al., 1997). The spectrum of Mrk 501 has been measured by a number of groups, with an early result showing the spectrum to be well fitted by an expression with a curved term (Samuelson et al., 1998). Results since then have shown that the spectrum is best described by a power law with an exponential cutoff (Aharonian et al., 1999). Aharonian et al. (1999) have shown that the spectral index of Mrk 501 is stable over variations in flux by a factor of 30. Similarities in the cutoff energy of both Mrk 501 and Mrk 421 may indicate a common property of the acceleration mechanism, or provide evidence for TeV attenuation on the infrared background.

H1426+428 is the most distant source of TeV gamma rays that has been confirmed, following weak detections by three groups (Horan et al., 2002; Aharonian et al., 2002a; Djannati-Ataı and The CAT Collaboration, 2003). It is classified as an extreme source, since its synchrotron output peaks at an energy above 1 keV, and was not detected by EGRET. The energy spectrum has been derived (Aharonian et al., 2003a; Petry et al., 2002) and is well described by a power law. The steep spectral index is consistent with more distant sources where IR absorption effects become increasingly important (Stecker et al., 1992).

Detection of 1ES1959+650 was first reported by the Telescope Array Group in Utah (Nishiyama, 1999) and confirmation came following a series

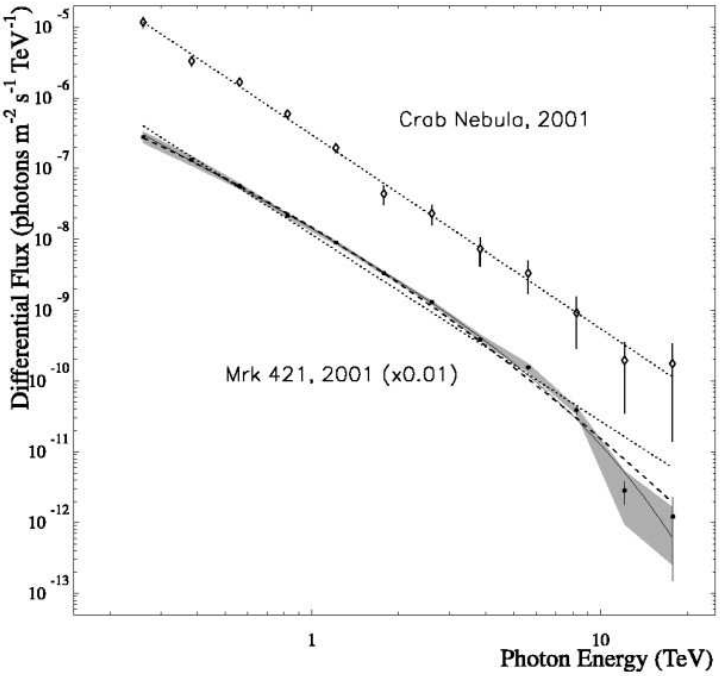

Figure 1.9: The VHE spectrum of Mrk 421 (Krennrich et al., 2001) and the Crab Nebula for comparison. The dotted lines correspond to power-law fits, the dashed line corresponds to a parabolic fit, and the solid line corresponds to a power-law fit with an exponential cut-off. While the Crab Nebula spectrum is well described by a pure power law, the Mrk 421 fit requires an exponential cut-off. Note that the spectrum of Mrk 421 has been offset by a factor of 0.01 for clearer presentation. Figure is taken from Krennrich et al. (2001).

of spectacular flares in 2002 (Holder et al., 2003; Aharonian et al., 2003b; Djannati-Ataı and The CAT Collaboration, 2003). The HEGRA Group also report detection of the source while in a quiescent state (Aharonian et al., 2003b). The energy spectrum of 1ES1959+650 is well described by a power law with exponential cutoff during a flaring state, and by a pure power law while in a low state (Aharonian et al., 2003b). Multiwavelength observations during 2002 (Krawczynski et al., 2004) have shown evidence for an *orphan* TeV flare, for which there is no counterpart at longer wavelengths.

PKS2155-304 is the first confirmed detection of a blazar in the southern hemisphere. Following reports of upper limits (Roberts et al., 1999), the first detection was claimed by the Durham Group (Chadwick et al., 1999) at a $6.8\,\sigma$ level. Confirmation of the source came following observations with the HESS telescope, which observed PKS2155-304 at a $10.2\,\sigma$ level in just over two hours of observations (for details see Horan and Weekes (2004)).

1ES2344+514 was first detected by the Whipple Collaboration (Catanese et al., 1998). Most of this detection was based on a single night's observations suggesting an extremely variable source. Confirmation of this source came following further observations by Whipple (Badran, 2001b) and HEGRA (Gotting et al., 2003). Two of the most recently detected blazars are 3C66A and BL Lac, both reported by the Crimean Astrophysical Observatory. 3C66A was observed at a $5.1\,\sigma$ level (Neshpor et al., 1998), although with its high redshift ($z\sim0.444$) and low-frequency synchrotron peak it is an unlikely candidate. Confirmation of this detection would pose many questions regarding the interaction of gamma rays with low-energy photons. BL Lac was observed at a $7.2\,\sigma$ level in 1998 (Neshpor et al., 2001) , while observations by other groups have only produced upper limits (Catanese et al., 1997). Its low-frequency synchrotron peak again makes it an unlikely source of TeV radiation.

OB Association

The source TeV 2032+4131, was discovered serendipitously by the HEGRA Collaboration following observations of Cygnus X-3 (Figure 1.10) and the EGRET source GeV J2035+4214 (Aharonian et al., 2002b). Initially reported at the $4.6\,\sigma$ level the source was confirmed following further observations (Gotting et al., 2003). The source is extended rather than point-like, and has a hard spectrum which indicates that the gamma-ray luminosity may peak in the TeV domain. TeV 2032+4131 is not identifiable with any known EGRET source or any x-ray source but may be associated with Cygnus OB2, a region populated by a large number of OB and O class stars. Analysis of Whipple archival data (Lang et al., 2004) has provided further evidence for

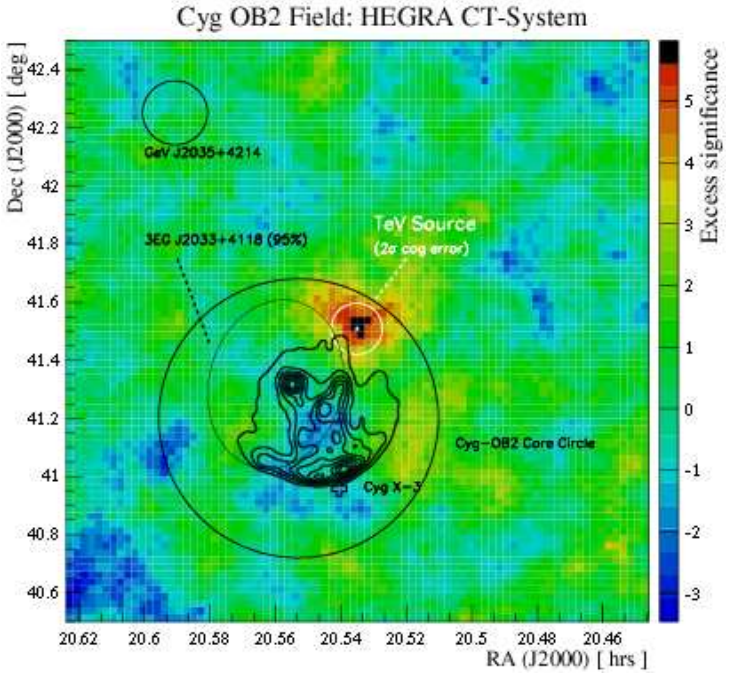

Figure 1.10: HEGRA skymap of the region around Cygnus-X3 (Aharonian et al., 2002b). The clearly identifiable excess of events has no counterpart at x-ray or GeV energies. The location of a number of EGRET sources is also shown, as is the Cygnus OB2 region. Recent analysis of Whipple archival data has provided further evidence for this source. Figure is taken from Ong (2003).

emission from this source.

Starburst Galaxies

Starburst galaxies are regions of extraordinary supernova activity and are predicted sources of cosmic rays and gamma rays (Völk et al., 1996). The CANGAROO Collaboration reported the detection of the starburst galaxy NGC 253 at a significance level of 11 σ (Itoh et al., 2003) and, at a distance of 2.5 Mpc, is the closest extragalactic source of gamma rays. The TeV emission is not well described by an inverse Compton approach, and the gamma rays may originate in the extended halo of the galaxy. Further observations of this object are required for confirmation.

Radio Galaxies

Detection of the radio galaxy M87 at TeV energies was unexpected, since with its jet mis-aligned by $\sim 30^{\circ}$ it is not a blazar-class object. The source was first detected by the HEGRA Group (Protheroe et al., 2003) and, although a rather weak ($4\,\sigma$) detection, it opens up the exciting possibility of observing other radio galaxies at VHE.

1.4.4 Next Generation IACT Experiments

The last decade has seen the *coming of age* of ground-based gamma-ray astronomy using the IACT. With 18 sources observed to date, the success of the approach is unquestionable; however, there is still much that we do not yet know. For example we still await conclusive evidence as to the origin of cosmic rays, the primary particle responsible for gamma-ray production is not yet known, and we still don't know the energy at which pulsed emission from plerions such as the Crab Nebula ceases. To answer these questions requires more sensitive observations, and with this in mind a number of next-generation experiments are currently under construction, three of which (CANGAROO-III, HESS and VERITAS) employ a stereoscopic approach, while the fourth (MAGIC) utilises a much larger light collector in conjunction with novel technologies. These next-generation detectors will have larger effective area (> 0.1 km^2), better flux sensitivity, energy thresholds below 100 GeV, improved energy resolution and angular resolution, and large fields of view. The improved performance levels will allow detection of objects with a flux level of 0.5 % of the Crab Nebula, in 50 hours of observations.

The use of stereoscopic imaging in relation to the IACT has already been shown to be successful by the HEGRA Group (HEGRA Collaboration et al., 1999). Stereoscopic imaging offers improved hadron discrimination from multiple image characterisation, elimination of the local muon background by using multiple-telescope trigger, and improved energy resolution and angular resolution from multiple views of the shower. A reduction in energy threshold may also be achieved by increasing the collection area (a larger mirror) and decreasing the signal integration time. At present four next-generation instruments are under construction (Figure 1.11), in the northern hemisphere VERITAS and MAGIC, and in the southern hemisphere HESS and CANGAROO-III.

Figure 1.11: Images of next generation ground-based gamma-ray observatories. Starting at top left and moving in a clockwise direction are (i) VERITAS (http://veritas.sao.arizona.edu), (ii) HESS (http://www.mpi-hd.mpg.de/hfm/HESS), (iii) CANGAROO-III (http://icrhp9.icrr.u-tokyo.ac.jp/c-iii)and (iv) MAGIC (http:// hegra1.mppmu.mpg.de/MAGICWeb). It should be noted that the VERITAS image is an artist's impression of the completed array.

VERITAS

VERITAS is an array of seven (initially four) imaging telescopes, currently under construction in southern Arizona by a group of academic institutions from the US, UK, Canada and Ireland. The array will be hexagonal in shape with a telescope at each of the six corners and one located in the centre. Based on the design of the Whipple Telescope, all detectors are identical and employ a Davies-Cotton reflector with a 499-pixel camera located in the focal plane. The array will incorporate a number of innovative technologies, most notably a 500 MHz flash analog-to-digital converter system to minimise dead-time. Although the first of the next-generation experiments to be proposed, VERITAS will probably be the last to come on-line with first light scheduled for 2005. Designed to be flexible, with operation possible as a single detector or a number of sub-arrays, VERITAS will offer a unique opportunity for in-depth studies of AGN, SNRs and gamma-ray bursts in the 100 GeV to 10 TeV range and with considerable sensitivity beyond. For a full review of the VERITAS project see Weekes (2003a).

MAGIC

The MAGIC group comprises research institutes from a number of European countries including; Germany, Spain and Italy. In contrast to the other next generation instruments MAGIC comprises a single large-area reflector. MAGIC is a so-called new technology telescope as it utilises many elements previously untried in ACT telescopes, including a lightweight space frame for mirror support, a fine pixellated camera using advanced hemi-spherical PMTs, and a 300 MHz flash analog-to-digital-converter system. The low energy threshold (< 50 GeV) will enable MAGIC to study AGN out to a redshift of 2 - 3, SNRs and diffuse emission from the galactic plane, while its rapid slew time makes it ideal for observing gamma-ray bursts. MAGIC is already operational and has observed the Crab Nebula at a $10\,\sigma$ level in less than one hour and Mrk 421 at $23\,\sigma$ in 100 minutes (Holder, 2004).

HESS

The HESS Collaboration is a joint German-French-British effort, comprising former members of the HEGRA and CAT collaborations. The HESS system is an array of four 12m telescopes arranged in a square configuration of side 120 m. Like VERITAS, the telescopes are Davies-Cotton design, with an f-number of 1.25, and a focal plane camera comprising 800 pixels. HESS Phase-I has already seen first light, and the four-element array located in Namibia, has been operational since September 2003. Already the

Crab Nebula has been observed at the $21\,\sigma$ level in 4.7 hours (Hinton, 2004), while a number of new sources of VHE gamma rays have been observed at a statistically significant level (Masterson, 2004). Rather interestingly, preliminary observations of SN1006 fail to show evidence of TeV emission, with upper limits imposed at 8 % of the flux reported by CANGAROO. Phase-II of HESS will involve construction of a single, large-diameter telescope at the centre of the current array (Punch, 2005).

CANGAROO-III

CANGAROO-III is a continuation of the successful Australian-Japanese CANGAROO group, and its array will comprise four telescopes arranged in a square, with inter-telescope spacing of 100 meters. In contrast to the VERITAS and HESS reflectors, CANGAROO-III utilises a parabolic mirror design, while the focal plane camera is made up of 427 pixels. All four telescopes are now in operation.

With their improved sensitivities and lower thresholds (Figure 1.12)., next-generation instruments will result in the detection of a number of new sources, and should help solve many of the current questions in high-energy gamma-ray astrophysics. More by accident than design, the location of the four experiments will provide almost complete coverage of the gamma-ray sky, and most crucially, observations will overlap in energy with the next-generation space-based observatories. While publishing of scientific results by these experiments are only just beginning, already work has begun designing future-generation detectors, which will have even larger collection areas and lower energy thresholds (Baixeras et al., 2004).

1.5 Guide to the Thesis

This thesis is a detailed account of a search for new extragalactic sources of TeV gamma rays. The search is carried out using a relatively new approach to gamma-ray discrimination, the *Kernel* method, and an empirical selection (*Minicuts*) developed by the author. Data recorded using the Whipple telescope over four observing seasons is used.

Chapter 2 deals with the classification and physics of AGN in detail. Current schemes for unification are discussed along with models of gamma-ray production. The selection of objects for study in this work is based on TeV flux predictions by a number by authors, and a description of the methods

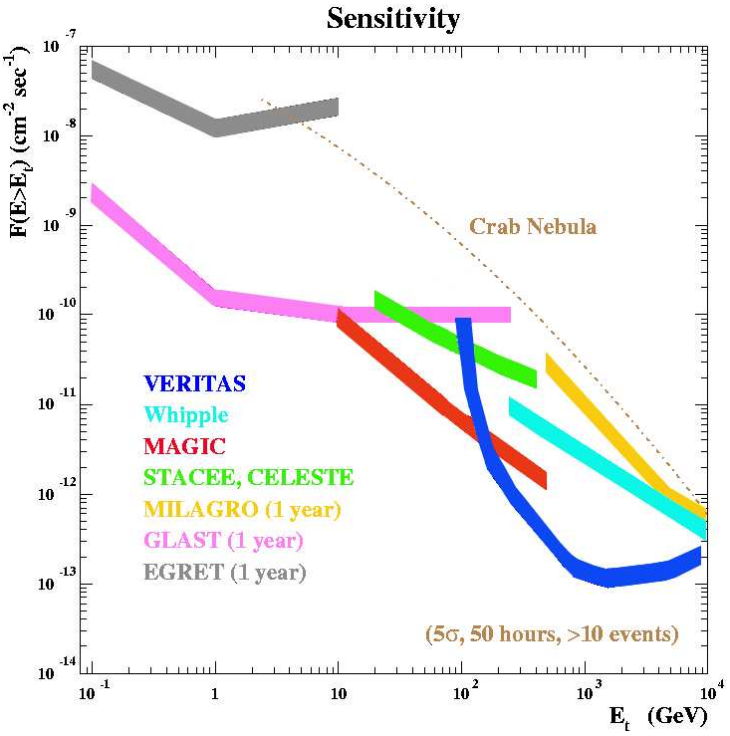

Figure 1.12: Comparison of sensitivity of next generation gamma-ray telescopes, to current and past experiments. Figure is adapted from Dunlea (2001).

used to identify the most promising candidates is provided. A list of the sources chosen for this work is presented. Chapter 3 provides an account of the physics of extensive air showers, including a description of the Imaging Atmospheric Cherenkov Technique. Chapter 4 details the design and operation of the Whipple 10m telescope, including a summary of the standard approach to data reduction, image cleaning, parameterisation and signal estimation. Chapter 5 discusses, in detail, the development of a new gamma-ray selection, known as *Minicuts*, and an alternative approach to gamma-ray discrimination known as *Kernel* analysis. As part of the development process each method was tested for possible sources of bias and compared in terms of efficiency. The chapter concludes with an in-depth study of the methods utilised for estimating background levels, including the introduction of an alternative approach known as matched analysis. Chapter 6 summarises the results of the application of all analyses to the data , including discussion of results in relation to different models of gamma-ray production and implications for future experiments. Finally, Chapter 7 provides a concise overview of the work presented in this thesis.

Chapter 2

Active Galactic Nuclei

2.1 Introduction

Although the energy output of most galaxies is dominated by thermal radiation produced in stars, there exists a small percentage of galaxies which display a bright central core that outshines the rest of the galaxy. The power output of these Active Galactic Nuclei (AGN) is such that it is difficult to explain via the process of nuclear fusion. The ultimate source of AGN luminosity is widely believed to be gravitational potential energy of a super-massive black hole at the centre of the host galaxy. AGN are characterised by non-stellar continuum emission stretching across the electromagnetic spectrum, from radio waves to gamma rays, and exhibit variability at all wavelengths. In this chapter an outline of the different classes of AGN is given, including discussion of recent efforts to unify the many different types into a single class. This thesis is concerned with the detection and study of a specific subclass of AGN, the blazars. Accordingly a more in-depth discussion of the properties of blazars is presented, concentrating on the characteristics of their spectral energy distributions and the processes by which gamma rays are believed to be produced. The chapter concludes with a detailed description of the methods by which the most promising gamma-ray candidates were selected for analysis later in this work (Chapter 6).

2.2 AGN Classification

Over the past 30 years AGN observations at a variety of wavelengths have led to the discovery of a multitude of galaxies with different properties. In an attempt to understand the different AGN species that exist a complex classification scheme has evolved, based on various observational properties

Figure 2.1: High Resolution Hubble Space Telescope image of an active galaxy, showing the core of the galaxy outshining the rest of the host. The high luminosities and spectra observed from these objects indicate that non-thermal processes are at work. The ultimate source of AGN luminosity is believed to be a super-massive black hole located at the galaxy centre. Image is taken from http://hubble.nasa.gov.

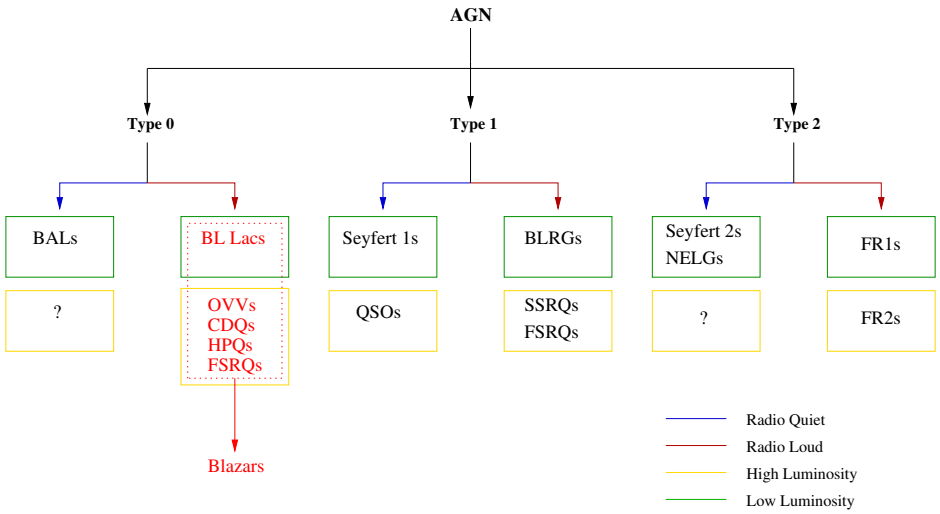

Figure 2.2: AGN classification scheme of Urry and Padovani (1995), based on the ultra violet and optical properties of AGN spectra. A detailed description of the division is provided in the text.

including; the existence of powerful radio emission in the form of jets, the presence of certain optical lines, and the degree of polarisation. Recently, Urry and Padovani (1995) have devised a scheme whereby AGN are divided into three broad classes, based on the characteristics of their optical and ultraviolet spectra, and with further subdivision within each class (Figure 2.2).

Type 1

Type 1 AGN are characterised by bright continua and broad emission lines, presumably produced by high-velocity gas moving in the vicinity of the black hole. In the radio-quiet group we have low-luminosity *Seyfert 1s*, which are bright at ultra-violet and x-rays and are among the first AGN to be discovered. Due to their low luminosity they are only seen nearby, making the host galaxy distinguishable from the bright core. Their high-luminosity counterparts are known as *quasi-stellar objects* (QSOs), which comprise a central core so bright that the host galaxies cannot be distinguished. By their very definition, that is the unresolved host galaxy, QSOs tend to be detected at high redshift only. In the radio-loud group there are low-luminosity *broad-line radio galaxies* (BLRGs), and the high-luminosity *radio-loud quasars*. *Radio-loud quasars* may be further divided into *flat-spectrum radio quasars* (FSRQs), or *steep-spectrum radio quasars* (SSRQs), with the cut-off being drawn at $\alpha_r = 0.5$ (where α_r is the spectral index in the 100 MHz - 30

GHz range). Here FSRQs include *optically violent variable quasars* (OVV), *highly polarised quasars* (HPQ) and *core dominated quasars* (CDQ), as there is mounting evidence to suggest that they are all basically the same type of object.

Type 2

Type 2 AGN are characterised by weak continua and narrow emission lines. This means that either they contain no high-velocity gas or more likely that the broad-line emission region is hidden from the observer by the dusty torus (Figure 2.3). In the radio-quiet group there are low-luminosity *Seyfert 2s* and the *narrow emission line x-ray galaxies* (NELG), while currently there are no clearly-defined high-luminosity counterparts. The radio-loud group, often known as the *narrow line radio galaxies* (NLRGs), contain two distinct types. The low-luminosity *Fanaroff-Riley* type 1 exhibit radio emission whose intensity falls off with distance from the nucleus while the higher-luminosity *Fanaroff-Riley* type 2 display more collimated radio-jets which terminate as well defined radio-lobes.

Type 0

To account for those AGN which exhibit unusual spectral characteristics a third type is defined. AGN falling into this category are believed to have their jets aligned at an acute angle to the line of sight. Type 0 AGN include BL Lacertaes (BL Lacs), objects which are characterised by an almost featureless optical continuum, and lack strong emission and absorption features. BL Lacs exhibit strong optical polarisation and rapid optical variability. A subset of Type 1 AGN, the FSRQs, exhibit similar continuum emission to that of BL Lacs, suggesting that they too are observed at a shallow angle. Consequently, and in spite of the fact that they have strong emission lines, they are included in the Type 0 category. Collectively, BL Lacs and FSRQs are often referred to as blazars. BL Lacs may be further classified as either x-ray selected or radio selected, based on the ratio of their luminosities at radio and x-ray wavelengths. An alternative and more physical classification has been devised (Padovani and Giommi, 1995), based on the frequency at which synchrotron emission from the source is maximum, resulting in BL Lacs being classified as low-peaked (LBL) or high-peaked (HBL).

2.3 AGN Unification

The complex AGN classification scheme described above somewhat belies the general consensus that AGN share a number of fundamental properties (though certainly with intrinsic variations in black hole mass, density, luminosity, size etc.). The basic AGN model (Figure 2.3) may be described as follows:

- At the centre of AGN lies a super-massive black hole (10^6 - 10^8 $M_\odot$), whose gravitational potential is the ultimate source of AGN luminosity.
- Outside the black hole there is an accretion disk. As matter spirals toward the event horizon it loses angular momentum through collisions with material in the disk. Thus the disk is heated and brightly glows from optical through to soft x-ray energies.
- Hard x-ray emission is also observed, and is most likely produced in a corona of hot electrons which pervades the region above the accretion disk.
- Clouds of gas move at high velocity in the gravity well of the black hole and emit radiation in the form of broad optical lines. This is the so-called broad line region.
- Partially enclosing the broad-line region is a warped disk of gas and dust, often referred to as the torus, although there is no definitive evidence as to its shape.
- Slower moving clouds of gas exist beyond the torus, emitting narrow-line radiation.
- Approximately 15 - 20 % of AGN exhibit powerful radio emission. This is produced by a relativistic outflow of particles in the form of collimated jets along the poles of the galaxy. These jets originate within approximately 100 Schwarzschild radii of the black hole and extend outward for tens of kpc and in some cases as far as a Mpc. The remaining, radio-quiet AGN are believed to be lacking in these jets.

Based on this axis-symmetric picture of AGN it is relatively easy to understand how such a variety of source types exist. The model described demonstrates how emission from AGN is anisotropic, arising from obscuration of the central core regions, and in the case of radio-loud galaxies relativistic beaming effects.

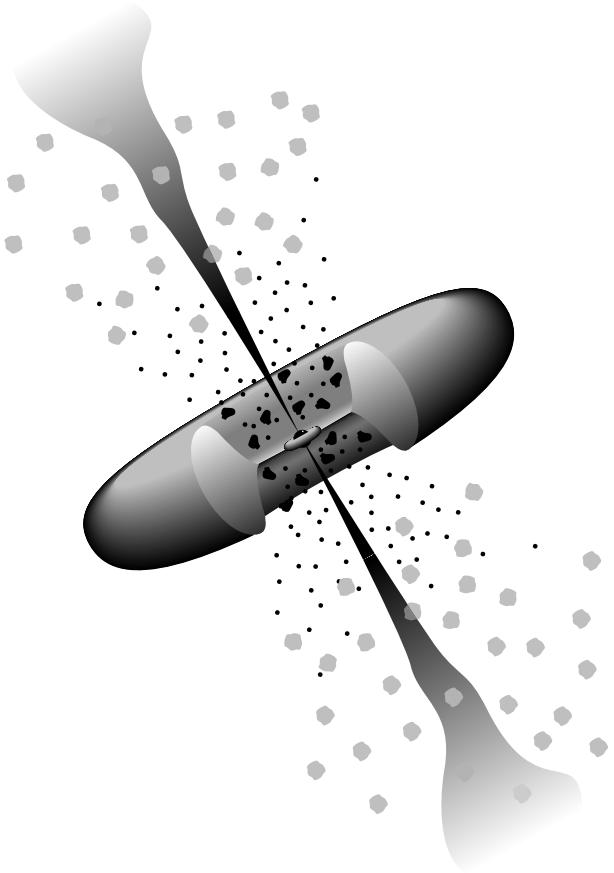

Figure 2.3: Model of a radio-loud AGN (Urry and Padovani, 1995). A supermassive black hole lies at the centre of the galaxy. Matter accreting onto the black hole glows at optical to soft x-ray wavelengths. Beyond the accretion disk fast moving clouds of gas produce broad emission lines which may be hidden from view by a warped disk of dust and gas (the torus). At larger distances slower moving clouds produce narrow emission lines, while relativistic jets of plasma are emitted along the poles.

2.3.1 Obscuration

For different aspect angles, the broad-line region of the active galactic core may or may not be hidden from view by the dusty torus (Figure 2.3). Thus classification of AGN as *type 1* or *type 2* depends on the angle of orientation between the active galaxy and the line of sight. Direct evidence of obscuration has been observed, in the form of polarimetric observations (Antonucci and Miller, 1985), infrared and x-ray observations (Ueno et al., 1994), and observations of narrow emission line gas (Wilson et al., 1993).

2.3.2 Relativistic Beaming

The anisotropic view of radio-loud AGN also results from the fact that their powerful jets emit radiation which is beamed in the forward direction. This beaming is a direct consequence of the Lorentz transformations of special relativity and the classical Doppler effect (Figure 2.4). Consider a source of radiation, which emits an initial pulse of light at time $t=0$, followed by a second pulse some time later. If the source is stationary then a distant observer will observe the intrinsic period of the source. However, if the source is moving, with velocity $v=\beta c$ and at an angle θ toward the observer, then by the time the second pulse of light is emitted the source will have moved forward a distance $\beta ct\cos\theta$. Thus the period of the source, as recorded by the observer will be modified according to:

$$T_{obs} = T_{src} - \beta\cos\theta\, T_{src} = T_{src}(1 - \beta\cos\theta) \tag{2.1}$$

The factor by which the period of the source is modified is known as the Doppler factor:

$$\delta = \frac{1}{1 - \beta\cos\theta} \tag{2.2}$$

For a source moving at relativistic velocities, the effect of time contraction is accounted for by introducing the Lorentz factor, $\gamma = (1-\beta^2)^{-\frac{1}{2}}$, resulting in a relativistic Doppler factor:

$$\delta = \frac{1}{\gamma(1 - \beta cos\theta)} \tag{2.3}$$

The Doppler factor relates the intrinsic and observed flux for a source moving with respect to an observer. Its dependence on the angle between the motion of the source and the observer shows that the observed properties of AGN are dependent on the angle of view. The observed flux increases with decreasing angle, culminating in maximum flux for an observer located

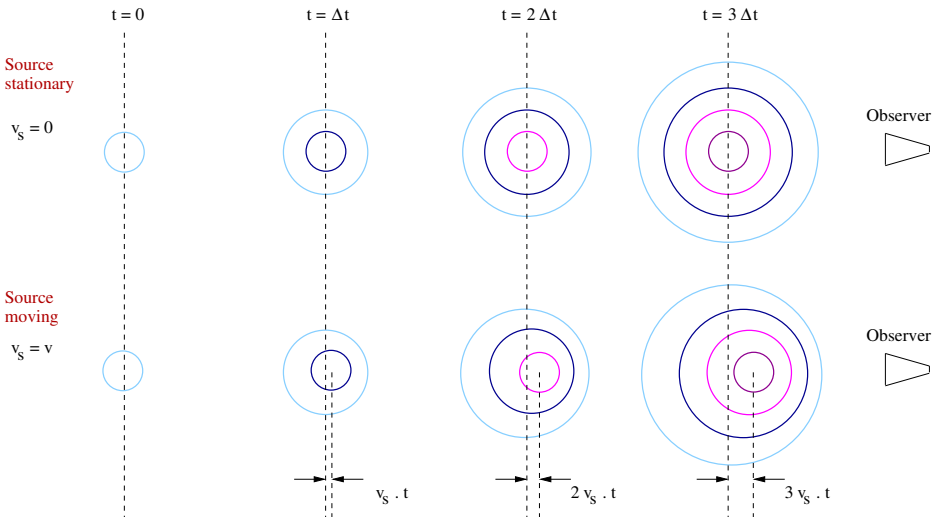

Figure 2.4: Effect of a moving source on the frequency recorded by a distant observer. If the source is stationary, the observer records the intrinsic frequency (or period) of the radiation being emitted. However if the source is moving, the waves in front of the source become compressed together, resulting in a shorter period or higher frequency as recorded by the observer. In the case of a source moving at relativistic velocities there is an additional effect caused by time contraction. These two effects combine to boost the observed flux from a source.

directly in the path of the source (in the case of AGN this happens when the observer is looking at the jet end on). There is plenty of evidence for relativistic beaming being present in AGN, including gamma-ray observations (Section 2.4.2), observed superluminal motion in radio jets (Vermeulen and Cohen, 1994), observed asymmetries in radio jets (Garrington and Conway, 1991), and brightness temperature calculations (Ghisellini et al., 1993).

2.4 Blazars

The majority of extragalactic sources of gamma radiation observed to date fall under the subclass heading of blazars. This makes blazars unique in the extragalactic sky by virtue of the fact that they are observable over the known electromagnetic spectrum, some nineteen decades of energy. Blazars are characterised by extremely high luminosity non-thermal emission, short and long time-scale variability, and with energy output in the gamma-ray domain often dominating the bolometric power. Currently over 70 AGN have been detected at high energy (HE) by EGRET (Hartman et al., 1999),

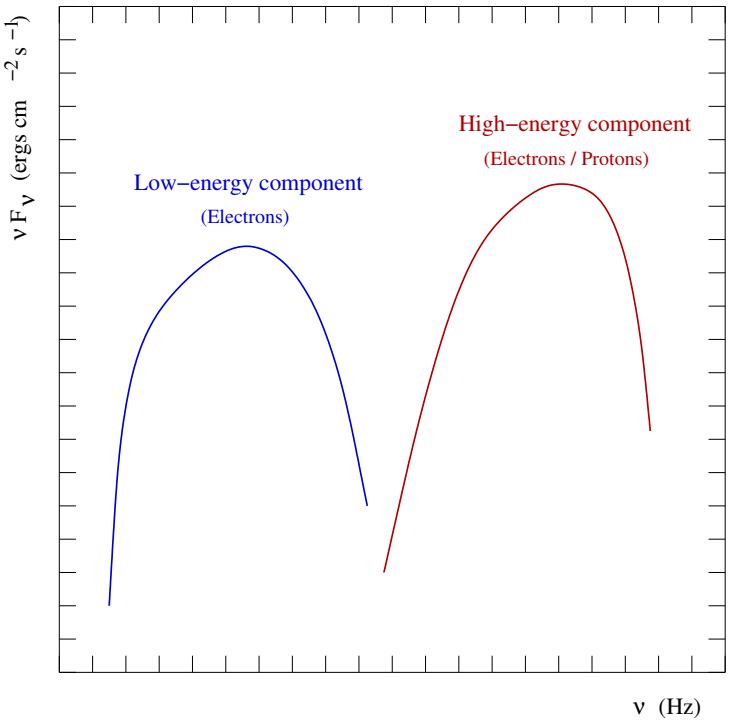

Figure 2.5: General shape of the SED of gamma-ray blazars. The SED is characterised by two broad peaks, both roughly parabolic in shape. The origins of the first peak is widely agreed to be due to synchrotron radiation of high-energy electrons, while the origins of the second peak is still open to debate.

with eight AGN detected at very high energy (VHE) by various ground-based experiments (for a summary see Horan and Weekes (2004)). The majority of sources detected at HE and VHE are blazars, with FSRQs making up the major component of HE detections, and BL Lacs dominating the VHE sample. The spectral energy distribution (SED) of blazars is characterised by two broad peaks in a $\nu F(\nu)$ plot (Figure 2.5). The origin of the lower peak, which is seen to stretch from radio through to ultra violet wavelengths (and in some cases as high up as x-rays), is widely attributed to incoherent synchrotron emission from high-energy electrons within the jet. The source of the second, more energetic peak, which stretches from x-rays to the very-highest-energy gamma rays, has not yet been determined. A number of the more widely-accepted theoretical models, aimed at explaining the higher-energy peak, are discussed later (Section 2.4.2).

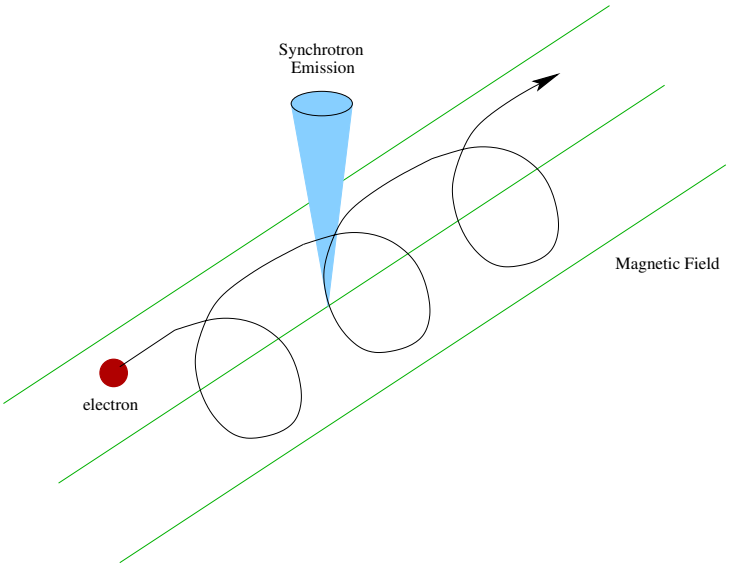

Figure 2.6: Synchrotron emission resulting from acceleration of a relativistic electron in the presence of a magnetic field. The emitted radiation is beamed in the instantaneous forward direction.

2.4.1 The Low-Energy Peak

When an electron moves in the presence of a magnetic field it experiences a force, constraining it to a helical path along the magnetic field lines. The resultant acceleration causes the electron to radiate. For a low-energy electron the emission is dipolar and monochromatic, while if the electron is relativistic with a Lorentz factor γ, the emission is beamed forward in a narrow cone of width $\frac{1}{\gamma}$ (Figure 2.6), producing a continuous power-law spectrum of polarised synchrotron radiation. Emission at longer wavelengths has been shown to be consistent with the synchrotron mechanism, and since the lower peak is continuous it is likely that all emission under it is of similar origin.

2.4.2 The High-Energy Peak

While the origin of the low-energy peak of gamma-ray blazars is widely agreed upon, there is no consensus as to the source of the high energy component. Initially two broad classes of theoretical models were employed to explain the existence of the higher peak, namely those which associate production of gamma rays directly with accretion onto the central black hole, or those which assume gamma rays are produced in relativistic jets. Mounting evidence for relativistic beaming of radiation emitted by blazars lead to development of

models based on the latter premise. These models may be further subdivided into two groups; (1) leptonic models, and (2) hadronic models.

Relativistic Beaming of Gamma Rays

Evidence for gamma-ray beaming is based on two factors, the short time-scale variability of blazars and their extremely high luminosities. Large amplitude flux variations over short time scales have been observed from a number of gamma-ray blazars. For example, EGRET observed the HE intensity of 3C 279 decline by a factor of five in approximately three days (Kniffen et al., 1993). Even more dramatically the Whipple telescope observed doubling of the VHE flux from Markarian 421 (Figure 2.7) over a period of fifteen minutes (Gaidos et al., 1996). A limit on the size of the emission region (R) may then be imposed using the causality relationship:

$$R = dt_{obs}\, c \tag{2.4}$$

where dt_{obs} is the shortest time scale over which variability is observed. The small emission region implied, makes it virtually impossible for gamma rays to escape, due to pair production on the dense low-energy photon field. This problem may be overcome if beaming of the gamma rays is assumed. Under such conditions the observed variability time scale is a factor δ smaller than the intrinsic variability resulting in an increase in the size of the emission region given by:

$$R = \delta\, dt_{obs}\, c \tag{2.5}$$

This increase in dimension is sufficient to decrease the opacity of the region so that gamma rays can escape.

The flux levels of gamma-ray blazars are very impressive, too impressive in fact, corresponding to isotropic luminosities exceeding $L_\gamma \sim 10^{49}\,\mathrm{erg\,s^{-1}}$. Such powerful emission is difficult to explain in terms of current particle acceleration models. In addition, if all radio-loud quasars emitted isotropically in this way the sky would glow in GeV gamma rays at levels ~ 10 - 100 above the measured values (Coppi, 1999). Assuming gamma-ray emission from blazars is ultimately tied to accretion onto black holes, the observed luminosities infer black hole masses much higher than that predicted following observations at longer wavelengths. Again these problems may be overcome by introducing the concept of beaming. This leads to a reduction in frequency (and thus energy) by a factor of $\frac{1}{\delta}$ according to:

$$\nu_{obs} = \delta \nu_{src} \tag{2.6}$$

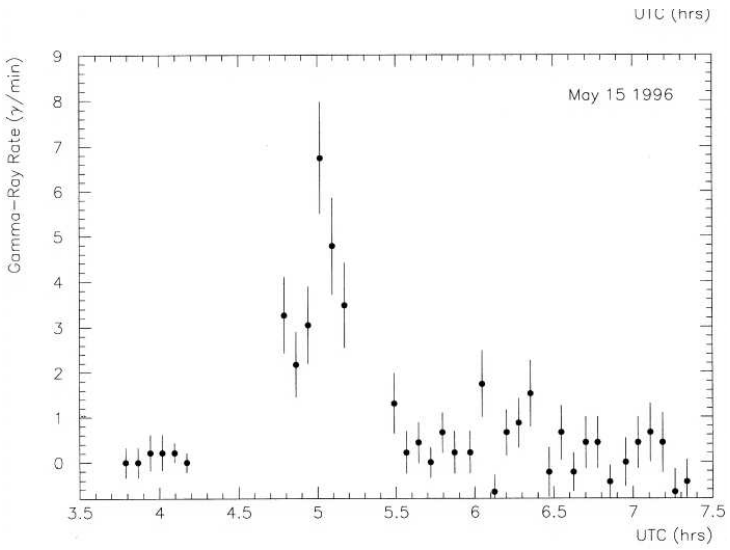

Figure 2.7: Light curve of a VHE flare from Markarian 421 in May 1996. The extremely short doubling-time indicates a very compact emission region. The size of the region is such that gamma rays should not be observed due to absorption by soft photons. This problem is overcome by assuming relativistic beaming. Figure is taken from Gaidos et al. (1996).

The intrinsic luminosity of the source is also reduced by a factor of δ^4 (Urry and Padovani, 1995), bringing it within the limits of current acceleration mechanisms.

Leptonic Models

Similarities between the general shape of the SED of TeV blazars and that of the Crab Nebula immediately provide a clue to a process which is capable of producing VHE gamma rays in blazars. Electrons produced in the vicinity of the black hole are accelerated as they travel down the jet, most likely by shocks resulting from collisions of volumes of variable density moving at different speeds downstream. The electrons, in the presence of a magnetic field, radiate via the synchrotron process producing the first peak of the SED. The same electrons may then interact with soft photons present in the jet, up-scattering them, via the inverse Compton process, to higher energies. Compton scattering occurs when a photon interacts with a free electron, while the inverse Compton process is physically the same process and may be explained as follows: to an observer within the rest frame of the electron the stationary electron appears to scatter an energetic photon, with the photon

acquiring considerable energy during the interaction. The scattering may be described using basic principles of conservation of energy and momentum (Figure 2.8):

$$E = m_e\, c^2(1 - \frac{v^2}{c^2})^{-\frac{1}{2}} = \gamma\, m_e\, c^2 \tag{2.7}$$

where E is the energy of the scattered electron, v is the velocity, and m_e is the mass of the electron. Defining:

$$\alpha = \frac{h\nu}{m_e c^2} \tag{2.8}$$

we have via conservation of energy:

$$m_e c^2 + h\nu = E + h\nu' \tag{2.9}$$

and via conservation of momentum:

$$\frac{h\nu}{c} = \frac{h\nu'}{c} cos\theta + \gamma m_e v cos\phi \tag{2.10}$$

$$0 = \frac{h\nu'}{c} sin\theta - \gamma m_e v sin\phi \tag{2.11}$$

Solving these equations we get an expression for the frequency (energy) of the scattered photon:

$$h\nu' = \frac{m_e c^2}{1 - cos\theta + \frac{1}{\alpha}} \tag{2.12}$$

The expression for the scattered photon energy shows that low-energy photons are only up-scattered in energy by a small amount, while higher-energy photons experience a greater degree of energy boosting. The cross section for this process is also dependent on energy and may be obtained by complex quantum mechanical calculations. Approximately, for small values of α Compton scattering operates under the Thompson regime, resulting in scattered photon energies $\sim \gamma_e^2 h\nu$, while for higher values of α the process operates under the Klein-Nishina regime where up-scattered photons have energy $\sim \gamma_e h\nu$ (where γ_e is the electron Lorentz factor and $h\nu$ is the soft photon energy).

The source of the soft-photons is currently unclear, with synchrotron self Compton models (SSC) (Marscher and Gear, 1985; Bloom and Marscher, 1996; Maraschi et al., 1992) preferring a target population comprising photons produced via synchrotron cooling, while external radiation Compton models (ERC) opt for an externally produced soft-photon field. A number of

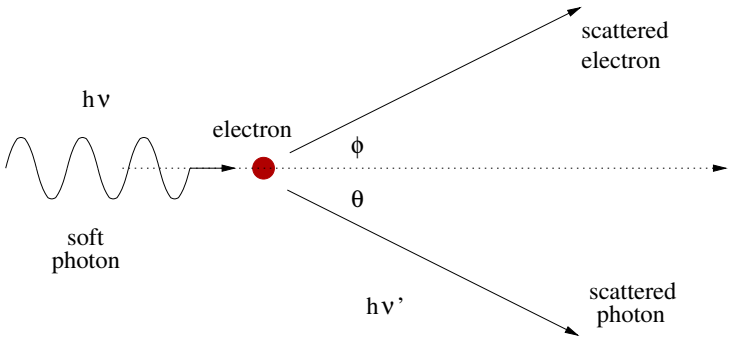

Figure 2.8: Inverse Compton scattering. A low-energy photon interacts with a high-energy electron resulting in the photon acquiring some of the electron's energy, up-shifting it to higher energies. According to leptonic models of gamma-ray emission, this process is responsible for the high-energy component of the SED of blazars.

external photon sources are postulated including UV to soft x-ray emission direct from the accretion disk (Dermer et al., 1992; Dermer and Schlickeiser, 1993), photons from the disk which are first reprocessed in the broad-line region (Sikora et al., 1994; Blandford and Levinson, 1995; Dermer et al., 1997), or jet synchrotron radiation initially lost to the jet but then reflected back in by the broad-line clouds (Ghisellini and Madau, 1996; Bednarek, 1998; Bottcher and Dermer, 1998). It should be noted that some models include photon fields produced both internal and external to the jet (Ghisellini et al., 1998).

Hadronic Models

Hadronic models detailing emission of gamma rays from AGN were not only motivated by attempts to explain this relativistic phenomenon, but also by a desire to solve the age-old problem of the source of cosmic rays up to energies of 10^{20} eV. Early models concentrated on interactions of protons with material making up the accretion disk, however, with the realisation that gamma rays were produced in relativistic jets of plasma where the matter density is too low for such processes to be important, efforts turned to emission via proton cooling on dense populations of low-energy photons. There is a number of variants of the proton blazar model, but most begin with the basic assumption that a population of co-spatial electrons and protons gain energy via some form of shock acceleration within the jet. The energetic protons suffer energy loss via adiabatic expansion, direct synchrotron cooling, or proton-photon interactions such as:

$$p + h\nu \rightarrow p + \pi^0$$

$$p + h\nu \rightarrow n + \pi^+$$

Before decaying, the mesons may experience synchrotron loss, while the muons, produced by their decay, are cooled in a similar way before decay. The target photon field for the above interaction is undecided, with photons produced in the accretion disk thought to be most important if acceleration takes place close to the black hole (< 1 parsec). Alternatively, synchrotron photons produced by the aforementioned electrons are believed to be dominant when acceleration occurs at distances further out (i.e. the synchrotron photons which make up the first peak of the blazar SED, somewhat similar to the SSC process for leptons) (Mannheim, 1996). Interaction of a proton with the soft energy target population initiates a pair-synchrotron cascade, comprising π^0 cascades, $\pi^{\pm}$ cascades, proton-synchrotron cascades, $\mu^{\pm}-$synchrotron cascades and Bethe-Heitler cascades. These cascades have the effect of redistributing the photon power to lower energies and, most critically, below the threshold for pair production, making it possible for gamma rays to escape the acceleration region. The proton-synchrotron cascades and the $\mu^{\pm}-$synchrotron cascades are responsible for the high-energy peak of the SED, while synchrotron emission by the directly-accelerated electrons and those produced during the cascade process are responsible for the low-energy peak. There are also some proton-based models where the high-energy peak results from inverse-Compton scattering of high energy electrons which are produced following decay of high-energy protons (Kazanas and Mastichiadis, 1999).

Application of Models to Observations

At present there are no definite conclusions as to the primary particle type and mechanism responsible for gamma-ray emission from blazars. Observations of sources in the EGRET energy range favour application of ERC models to explain the SED, with successful fits applied to a number of FSRQs (Dermer et al., 1997; Sambruna et al., 1997; Hartman and Boettcher, 1999). While SSC models prove inadequate at GeV energies, they fit the TeV spectra of blazars very well (Pian et al., 1998; Mastichiadis and Kirk, 1997). It is most likely that, if lepton-based models prove correct, gamma-ray emission is based on interactions between electrons and soft photons produced inside and outside the jet, with each target population proving dominant for different source types. For example, for HBLs where there is little evidence

for the existence of external soft-photon fields the SSC process is most relevant, while for higher luminosity LBLs, where broad line regions are evident, the ERC mechanism dominates. Using this argument it is easy to explain observations to date. The majority of EGRET detections comprise FSRQs, objects that are known to posses a copious amount of soft photons outside the jet. For such objects one would expect gamma-ray production via the ERC mechanism to be prevalent and EGRET-measured spectra provide strong evidence for this. In contrast, almost all detections at VHE pertain to BL Lacs, objects partially defined by their lack of low-energy photon fields. Under such circumstances one would expect gamma-ray production to originate via the SSC mechanism, a fact supported by VHE spectral measurements.

Early proton models were unable to account for a number of SED features, most notably the double-peak shape and the short variability time scales observed for a number of blazars. Weekes (2003b) notes that for some models, in which gamma-ray production occurs close to the base of the jet, high density photon fields make it difficult for the gamma rays to escape. Furthermore these models predict an energy dependence on the radius at which the optical depth for pair production drops below unity, that is the higher the energy of the gamma ray the further away from the base of the jet it must be in order to escape. Accordingly VHE gamma-ray emission should vary either later or more slowly compared to emission in the HE domain, a trend absent from all multiwavelength observations to date. While a strong temporal correlation between x-ray and VHE flares has been observed, thereby favouring SSC models, the recent detection of an orphan gamma-ray flare (Krawczynski et al., 2004) suggests an alternative, perhaps proton-based, emission mechanism. More recent proton models are capable of reproducing the double-peaked nature of blazar SEDs, with acceptable fits applied to a number of sources (Dar and Laor, 1997; Mücke et al., 2003). One possible means of identifying the progenitor particle is via neutrino astronomy. Proton models predict a flux of neutrinos from blazars, produced during the proton initiated cascade. Observations with next generation neutrino telescopes may provide the answer, while more detailed multiwavelength observations of established sources and detection of new sources will help to further our understanding of gamma-ray production in AGN.

2.5 A Search for Blazars

The current catalogue of blazars comprises over 70 sources at GeV energies and a rather meagre eight at TeV energies. Although detection of VHE emission from blazars has resulted in significant progress regarding the under-

standing of these objects, there is still much that we do not know, including the dominant emission mechanism. To provide answers to these questions requires more detailed studies of the SED of blazars and an increase in the number of detected sources. To reveal the true form of blazar emission spectra it is also necessary to quantify the effect of absorption of gamma rays as they traverse intergalactic space.

2.5.1 Propagation of Gamma Rays Through Space

As gamma rays travel the vast distances between galaxies they remain undeflected by pervading magnetic fields but may still interact with low-energy photons that populate the region. These photons are remnants of an earlier epoch, and may have been produced by such mechanisms as reprocessing of starlight by dust and normal galaxy formation or by more exotic processes such as pre-galactic star formation or decay of relic particles from the big bang (Bond et al., 1986). Accurate measurements of this extragalactic background light (EBL) are very important with regard to current theories of cosmological evolution. Gamma rays interact with the soft photons via pair-production

$$\gamma + \gamma \rightarrow e^+ + e^-$$

for which the cross-section is maximum when

$$\epsilon = 0.5 \frac{1TeV}{E} eV \tag{2.13}$$

where E is the energy of the gamma ray, and ϵ is the energy of the soft photon. For a gamma ray of typical energy 1 TeV the cross-section is maximum for a soft-photon field in the infra-red region of the spectrum ($\lambda \sim 2\mu m$), thus the extragalactic background light is often called infra-red background radiation (IRB). The effect of this interaction is to modify our view of extragalactic sources, resulting in an observed spectrum which is a convolution of the intrinsic source spectrum and effects due to the IRB. To fully understand the acceleration mechanisms at work in blazars we need some method by which effects due to the EBL may be determined. This may be achieved via detection of a greater number of VHE blazars at different redshifts. Since redshift is a measure of the distance traversed by a gamma ray through the IRB, different levels of TeV flux attenuation should be observable for different redshifts, thereby providing a method for deconvolving the spectra. While the interaction of gamma rays with the IRB complicates our understanding of AGN, it also provides a somewhat unique opportunity to peer back in time to

a younger universe. The density of the IRB contains a wealth of information regarding formation of the earliest galaxies, allowing constraints to be placed on current theories of cosmological evolution. Experiments that measure the IRB directly are plagued by foreground sources of infra-red radiation and already calculations using TeV gamma-ray spectra have placed upper limits on the density of the IRB that are an order of magnitude lower than direct measurements (Biller et al., 1998). Preliminary evidence for attenuation due to IRB absorption is presented by Krennrich et al. (2001).

2.5.2 Candidate TeV blazars

This thesis is partly based on attempts to expand the TeV source catalogue by observing emission, at TeV energies, from previously undetected AGN. The search for new sources of gamma radiation is based on predictions made by a number of authors - Costamante and Ghisellini (2002) and Stecker et al. (1996), from here on denoted as *CG2* and *S96* respectively. Two methods for identifying the most promising candidates and three additional methods for estimating the TeV flux are used.

Identification of Targets

The methods used for source selection are relatively similar, with some minor differences. For a number of reasons both approaches concentrate on samples of BL Lac objects detected at lower energies. To date all definitive observations of TeV emission have come from nearby BL Lac objects. This may be due to the fact that FSRQs tend to lie at higher redshifts than BL Lacs, making attenuation of TeV radiation on the IRB likely. Calculations based on one of the closest known FSRQs ($z = 0.361$) predict that more than 99 % of VHE gamma rays are absorbed (Stecker and de Jager, 1997). Combined with the fact that they exhibit steep spectra which may not extend to the VHE range, FSRQs are unlikely sources of TeV radiation. *S96* argues that HBLs are more likely candidates, since most VHE BL Lacs detected to date fall into this category and the high-energy synchrotron peak of HBLs suggests that the more energetic component stretches into the TeV domain.

The *CG2* approach is based on the SSC model, requiring sufficient numbers of high-energy electrons and seed photons for VHE emission to be detectable. For a synchrotron component peaking at a relatively high frequency (≈ 1 keV), inverse-Compton scattering between synchrotron photons at the peak and the electrons producing the peak operates under the Thompson regime. Under such circumstances the bulk of the synchrotron photons at the peak are up-scattered. For a higher-frequency synchrotron peak (> 500

keV) there are, in principle, more energetic electrons present, capable of producing even higher-energy inverse-Compton photons. However, due to Klein-Nishina effects, the shift in peak energies results in a significant decrease in the scattering cross-section between electrons and photons at the synchrotron peak. This has the overall effect that, in spite of higher electron energies being present, fewer photons are up-scattered resulting in a decrease in the inverse-Compton luminosity. Thus there is a trade-off, with TeV emission requiring a synchrotron peak frequency large enough to ensure the existence of enough high-energy electrons but low enough so that there are sufficient seed-photons to be scattered. This balance is clearly seen in Figure 2.9.

Although the seed photons most effective for inverse-Compton scattering are in the IR-optical band, *CG2* uses the radio flux as opposed to the optical flux as a measure of the soft-photon target population. The optical flux was not used due to the potential for contamination from a number of sources, but most severely the host galaxy itself. As a measure of the high-energy electron population the x-ray flux is used, due to the fact that x-ray emission results from synchrotron cooling of electrons. This approach agrees with observations of BL Lacs detected at VHE, all of whom exhibit high luminosity at radio and x-ray frequencies. The approach applied to source selection by *S96* is based on the SSC model also, but uses a high x-ray flux only as an indicator of likely TeV emission. Thus *CG2* bases identification of potential TeV emitters on the existence of a high radio and high x-ray flux (Figure 2.10) while *S96* bases selection on the existence of a high x-ray flux only. From a database of 246 BL Lacs observed at radio, optical and x-ray wavelengths *CG2* identified 33 most likely sources, while when applying their criteria to the *Einstein* slew survey sample (Perlman et al., 1996), *S96* identified 23 promising sources.

TeV Flux Predictions

Identification of the most likely sources is helpful, especially for low-duty-cycle, narrow-field-of-view Cherenkov telescopes, which have a limited amount of observation time. However, so that estimates on the time required to observe these sources at a statistically significant level may be made, a TeV flux prediction is desired. Both *S96* and *CG2* attempt to estimate the VHE flux from selected candidates using different approaches.

CG2 utilises two different methods for estimating the gamma-ray flux of BL Lacs. The first method applies a SSC fit to the low-energy peak of the SED, and from this the shape and luminosity of the inverse-Compton peak is extrapolated. Due to a lack of observations on a number of sources, resulting

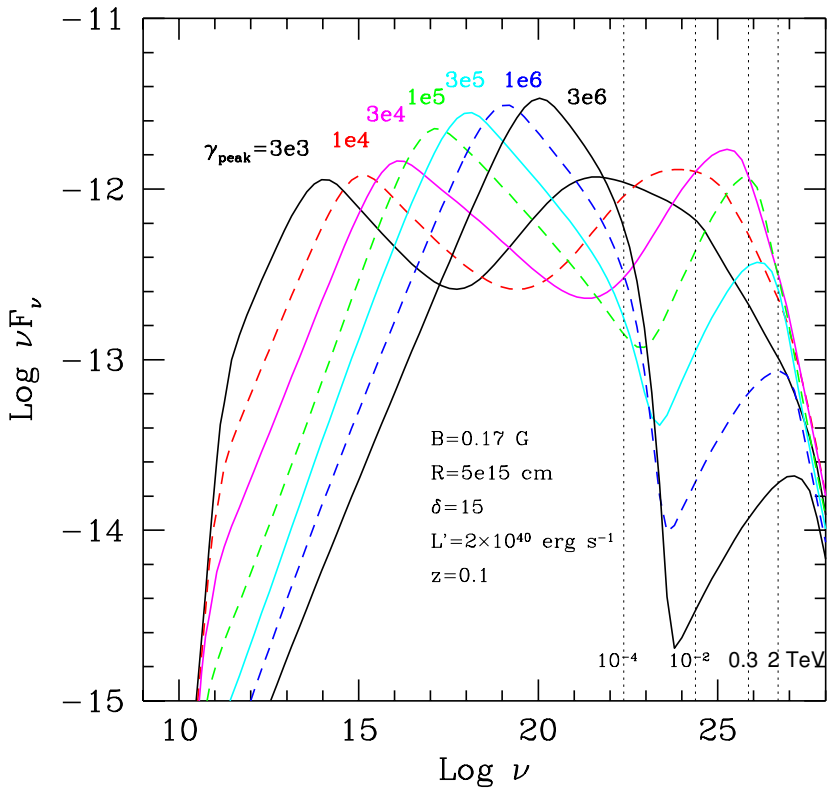

Figure 2.9: Effect of varying the position of the synchrotron peak on the luminosity of the high energy component of the SED, based on the SSC model of gamma-ray emission. Although it was previously assumed that the higher the synchrotron peak frequency the higher the probability of TeV emission, this is not necessarily true. A sufficiently high peak frequency is required, indicative of a population of high-energy electrons, however if the peak is too high there are insufficient numbers of target photons for efficient scattering to occur. Figure is courtesy of Costamante and Ghisellini (2002).

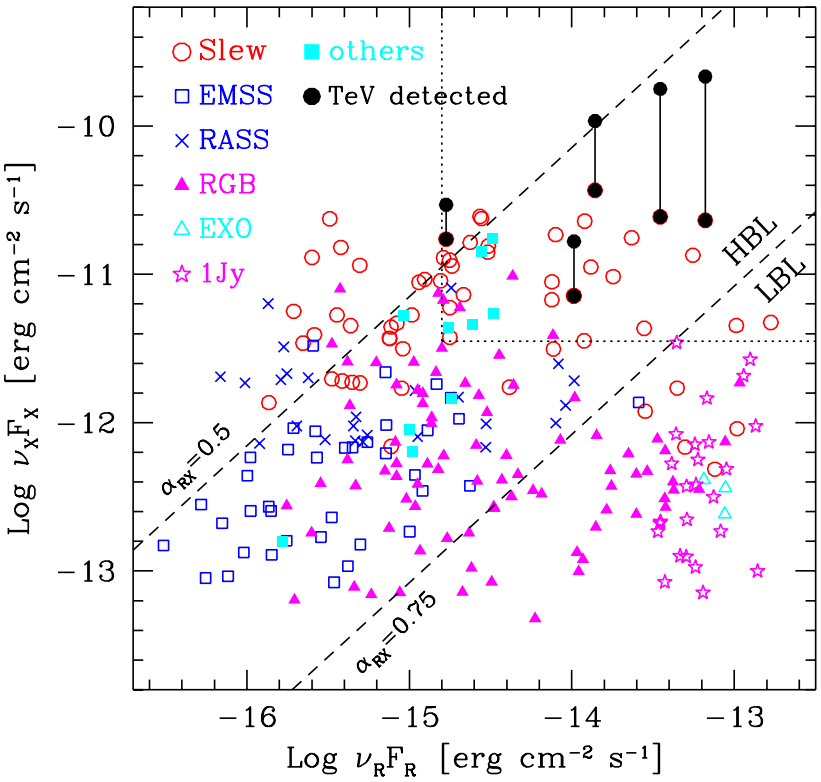

Figure 2.10: Plot of radio flux versus x-ray flux for 246 BL Lacs (Costamante and Ghisellini, 2002). Objects identified as the most promising TeV candidates have both high radio and x-ray flux, indicative of the presence of a population of high-energy electrons and soft photon seeds, and fall within the dashed rectangle. Radio flux was preferred to optical flux as an indicator of target photon levels due to the possibility of contamination of the optical flux observations. However, in a distribution of optical flux versus x-ray flux, the same sources appear at the high end.

in poorly-defined synchrotron peaks, flux estimates were not possible for all candidates. Motivated by this, a second approach was applied based on a modified version of the phenomenological description of blazars by Fossati et al. (1998). Under this scheme radio luminosity is assumed to be the dominant parameter in determining the position of the synchrotron peak. Using a fitting technique based on this parameterisation the position and intensity of the inverse-Compton peak was determined.

The approach of *S96* is also based on the SSC model of gamma-ray production but utilises a simple scaling argument to calculate fluxes. According to the SSC model the inverse-Compton spectrum is similar to the synchrotron one (Macomb et al., 1995; Fossati et al., 1998) but shifted to higher energy by $\sim \gamma_{peak}^2$ where γ_{peak} is the Lorentz factor of electrons emitting at the peak. Based on observations of Markarian 421 an up-shifting factor $\sim 10^9$ and a ratio of peak luminosities $L_c/L_{syn} \sim 1$ were calculated. Assuming that all HBLs have similar properties to Markarian 421 the following scaling law may be derived:

$$\frac{\nu_o F_o}{L_{syn}} \sim \frac{\nu_{GeV} F_{GeV}}{L_c} \quad \text{and} \quad \frac{\nu_{\rm x} {\rm F_x}}{\rm L_{syn}} \sim \frac{\nu_{\rm TeV} {\rm F_{TeV}}}{\rm L_c} \tag{2.14}$$

or

$$\nu_{GeV} F_{GeV} \sim \nu_o F_o \quad \text{and} \quad \nu_{\rm TeV} {\rm F_{TeV}} \sim \nu_{\rm x} {\rm F_x} \tag{2.15}$$

Using the average spectral index between 0.1 and 10 GeV and the spectral index of Markarian 421 above 0.3 TeV it is possible to estimate the integral TeV flux for any object. Both *S96* and *CG2* predict integral flux levels above 40 GeV, 300 GeV and 1 TeV. This work is most interested in predictions around 300 GeV since it is in this energy range that the Whipple telescope is most sensitive. One final difference between the flux predictions should be noted, *S96* predictions take the effect of IRB attenuation into account while *CG2* predictions do not.

2.5.3 Selection of Most Suitable Candidates

In total, between the *S96* (33 candidates) and *CG2* (23 candidates) samples there were 46 identified targets, allowing for overlap. Of these, ten were not observed by the Whipple telescope for a variety of reasons, while two sources have been detected since these lists were first published (1ES 1959+650, 1ES 2344+514) and are not subjected to further analysis. This leaves 24 objects in total as potential targets for this work. Before proceeding with detailed analysis, the observation time required for detection of each source at a statistically significant level was determined. To do this the predicted

flux is first expressed in terms of the gamma-ray flux from the Crab Nebula and then, using the sensitivity of the Whipple telescope to Crab Nebula observations, the required time is calculated. First the gamma-ray flux of the Crab Nebula (usually quoted in terms of an integral flux above 1 TeV) is converted to an integral flux above 300 GeV using the following method:

$$F(> 1\,\mathrm{TeV}) = \mathrm{A}.\int_{1\mathrm{TeV}}^{\infty} \mathrm{E}^{-2.49}\mathrm{dE} \tag{2.16}$$

where A is a normalisation constant. Using the flux level quoted by Hillas et al. (1998):

$$F(> 1\,\mathrm{TeV}) = (2.1 \pm 0.2_{\mathrm{stat}} \pm 0.3_{\mathrm{sys}}) \times 10^{-11}\mathrm{cm}^{-2}\mathrm{s}^{-1}$$

a value for A is easily obtained as:

$$A = 3.1129 \times 10^{-11}\mathrm{cm}^{-2}\mathrm{s}^{-1}$$

Applying this, the integral flux above 300 GeV may be calculated using:

$$F(> 0.3\,\mathrm{TeV}) = \mathrm{A}.\int_{0.3\mathrm{TeV}}^{\infty} \mathrm{E}^{-2.49}\mathrm{dE} \tag{2.17}$$

giving an value of:

$$F(> 0.3\,\mathrm{TeV}) = 12.6272 \times 10^{-11}\mathrm{cm}^{-2}\mathrm{s}^{-1}$$

which may be used to calculate source flux levels in units of the Crab Nebula gamma-ray flux (Table 2.1).

When the source flux in terms of the Crab Nebula is known it is possible to calculate the time required to observe a source at a certain statistical significance using the detector sensitivity, which may be estimated as follows: The statistical significance of a detection (σ) may be expressed in terms of the number of events selected from the source region (N_{on}), compared to the number of events selected from the control (N_{off}):

$$\sigma = \frac{N_{on} - N_{off}}{\sqrt{N_{on} + N_{off}}} \tag{2.18}$$

This assumes that the *ON*-source observation time and the control observations are of similar duration. Accounting for the fact that this may not always be the case we have:

$$\sigma = \frac{N_{on} - R_t N_{off}}{\sqrt{N_{on} + R_t^2 N_{off}}} \tag{2.19}$$

Source	$F_{>0.3TeV}$ ($\times 10^{-11} cm^{-2} s^{-1}$)			$F_{>0.3TeV}$ (crab units)		
	Fos	Cos	Steck	Fos	Cos	Steck
1ES 0033+595	2.040	0.250	—	0.162	0.020	—
1ES 0120+340	0.280	0.300	—	0.022	0.024	—
RGBJ0214+517	5.930	0.070	—	0.471	0.006	—
1ES 0229+200	0.960	0.310	0.200	0.076	0.025	0.016
1ES 0323+022	0.840	0.010	0.400	0.067	0.001	0.032
1ES 0806+524	1.360	—	—	0.108	—	—
1ES 0851+202	0.420	—	—	0.033	—	—
1ES 1028+511	0.430	—	—	0.034	—	—
1ES 1011+496	0.120	0.140	—	0.010	0.011	—
RXJ 1136+673	0.920	0.100	—	0.073	0.008	—
1ES 1417+257	0.380	0.210	—	0.030	0.017	—
1ES 1440+122	0.780	0.090	0.100	0.062	0.007	0.008
1ES 1544+820	0.540	0.220	—	0.043	0.017	—
1ES 1553+113	0.200	0.420	—	0.016	0.033	—
1ES 1727+502	5.190	0.070	0.500	0.412	0.006	0.040
1ES 1741+196	3.590	0.290	0.400	0.285	0.023	0.032
1ES 0145+138	0.550	—	—	0.044	—	—
1ES 0927+500	0.120	—	—	0.010	—	—
1ES 1118+424	0.380	—	—	0.030	—	—
1ES 1212+078	0.070	—	—	0.006	—	—
1ES 1239+069	1.200	—	—	0.095	—	—
1ES 1255+244	0.880	—	—	0.070	—	—
1ES 2155+304	1.700	—	—	0.135	—	—
1ES 2321+419	0.130	—	—	0.010	—	—

Table 2.1: Summary of the predicted integral flux levels above 300 GeV, in standard flux units and also converted to units of the Crab Nebula flux. Results for the three methods of flux estimation are presented. *Fos* corresponds to the Fossati phenomenological approach to blazar characterisation, as adapted by Costamante and Ghisellini (2002) to calculate flux levels. *Cos* corresponds to the SED modeling approach predictions by Costamante and Ghisellini (2002) and *Steck* corresponds to the predictions of Stecker et al. (1996) using a simple scaling approach. Conversion to units of Crab Nebula flux is described in the text.

where $R_t = t_{on}/t_{off}$ is the ratio of *ON*-source observation time to *OFF*-source observation time. The number of events in the *ON* dataset may be expressed in terms of the gamma-ray rate (G) as follows:

$$N_{on} = G \times t \tag{2.20}$$

or alternatively in terms of the excess number of events (N_{excess}) in the *ON* dataset compared to the number in the *OFF* dataset:

$$N_{on} = (N_{excess} + B) \times t \tag{2.21}$$

where B is the rate (min^{-1}) of events in the background dataset. Using these relationships the expression for significance may be re-arranged:

$$\sigma = \frac{t}{\sqrt{t}} \times \frac{N_{excess} + B(1 - R_t)}{\sqrt{N_{excess} + B(1 + R_t^2)}} \tag{2.22}$$

Assuming that similar amounts of time are spent *ON* and *OFF* source (i.e. $R_t = 1$) we find:

$$\sigma = \sqrt{t} \times \frac{N_{excess}}{\sqrt{N_{excess} + 2B}} \tag{2.23}$$

where

$$S = \frac{N_{excess}}{\sqrt{N_{excess} + 2B}} \tag{2.24}$$

is the sensitivity of the telescope (Figure 2.11). The time required for detection of a source in terms of *ON*-source and *OFF*-source event rates, at a σ level of significance, is easily obtained as:

$$t = \frac{\sigma^2(N_{excess} + 2B)}{N_{excess}^2} \tag{2.25}$$

Assuming that the source in question has a spectrum similar to the Crab Nebula and that the rate of events in the respective control regions are similar the time required, in terms of the intrinsic source flux, may be calculated using:

$$t = \frac{\sigma^2(\phi_{source} R_{crab} + 2B)}{(\phi_{source} R_{crab})^2} \tag{2.26}$$

where ϕ_{source} is the source flux in units of the Crab Nebula, and R_{crab} is the gamma-ray rate ($\gamma\, min^{-1}$) of the Crab Nebula. Using this method the time required to observe each source at a $5\,\sigma$ level of significance was calculated

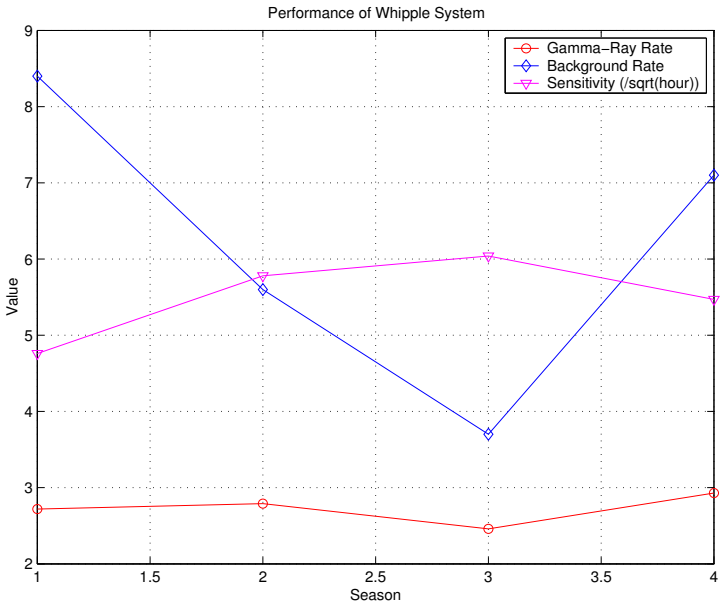

Figure 2.11: Performance of the Whipple telescope and standard analysis method for the last four observing seasons. In spite of the telescope sensitivity being relatively stable, there has been a noticeable change in the detector. The fact that the sensitivity is unaffected is due to a decrease in background rate compensating for a similar decrease in gamma-ray rate. The decrease in rate is probably due to degradation of the PMTs, a fact confirmed in October 2003 following hardware tests. Since this time the high-voltage supply to the PMTs has been increased, explaining the increase in rates for last season. The sensitivity for the 2003/2004 season was used when estimating the time required to detect a source at a significant level.

based on the three different flux predictions, and are summarised in Table 2.2, along with the time spent observing each source with the Whipple telescope.

The results presented in Table 2.2 show that even for the most promising candidates the required observation time, in most cases, is beyond the scope of the current telescope due to the short duty cycle ($\sim 10\,\%$) of the instrument. Combined with the fact that all candidates were observed for less than 40 hours makes detection of VHE emission highly unlikely, if the source is in a quiescent state. However, it should be remembered that detection of most AGN at TeV energies has occurred when these objects were in a high state of emission (Punch et al., 1992; Quinn et al., 1996), and since the work of Stecker et al. (1996) and Costamante and Ghisellini (2002) was published, two of the predicted sources have been detected during periods of flaring (Catanese et al., 1998; Holder et al., 2003). Thus it is worthwhile analysing

Source	Required Time (Hours)			Observations (Hours)
	Fos	Cos	Steck	
1ES 0033+595	27	1773	—	27.4
1ES 0120+340	1413	1232	—	36.4
RGBJ0214+517	3.5	22545	—	23.0
1ES 0229+200	121	1154	1413	30.1
1ES 0323+022	159	1×10^6	695	8.6
1ES 0806+524	61	—	—	36.5
1ES 0851+202	630	—	—	2.5
1ES 1028+511	601	—	—	1.0
1ES 1011+496	7678	5642	—	5.8
RXJ 1136+673	132	11052	—	9.7
1ES 1417+257	769	2511	—	0.6
1ES 1440+122	184	13643	7678	0.3
1ES 1544+820	382	2288	—	0.3
1ES 1553+113	2768	630	—	9.7
1ES 1727+502	4.4	22545	428	6.9
1ES 1741+196	9.1	1318	601	6.2
1ES 0145+138	368	—	—	7.9
1ES 0927+500	7678	—	—	3.8
1ES 1118+424	769	—	—	5.0
1ES 1212+078	23000	—	—	3.9
1ES 1239+069	78	—	—	3.8
1ES 1255+244	144	—	—	3.6
1ES 2155+304	39	—	—	0.5
1ES 2321+419	6543	—	—	10.4
3C 66A	5642	–	–	24.2
BL Lac	12	4205	–	6.3

Table 2.2: The required observation times for detection of sources at the 5σ significance level, based on the TeV flux predictions of Costamante and Ghisellini (2002) and Stecker et al. (1996). *Fos* corresponds to the predictions of Costamante and Ghisellini (2002) using a modified version of Fossati's (Fossati et al., 1998) phenomenological approach to blazar characterisation. *Cos* also corresponds to predictions by Costamante and Ghisellini (2002), this time using a SSC fitting approach. *Steck* corresponds to the predictions of Stecker et al. (1996) using a simple scaling methodology. The observation times were calculated using the method described in the text, which is based on the sensitivity ($= 5.47/\sqrt{(h)}$) of the Whipple detector during the 2003/2004 season (Figure 2.11).

these sources in search of evidence for TeV emission. Before proceeding with this analysis a further cut was applied to the source sample, based on the quality of observations made by the Whipple telescope. A number of objects were eliminated due to their data comprising observations carried out during adverse weather only.

It should be noted that two blazars, included in the predictions of Stecker et al. (1996) and Costamante and Ghisellini (2002), have been detected by the Crimean astrophysical observatory but await confirmation. The first source, 3C66A was observed at a statistically significant level of $5.1\,\sigma$ (Neshpor et al., 1998) and, at such a large redshift ($z \sim 0.444$), would be the most distant BL Lac detected at TeV energies to date. It is difficult to explain the detection of this source given its high redshift and current theories of gamma-ray absorption; however, this concern is somewhat tempered by the fact that the quoted redshift is not well established (Kildea, 2004). The second source, BL Lac, after which the class is named, has a reported detection at the $7.2\,\sigma$ level (Neshpor et al., 2001). The final sample of TeV candidates, totaling 16 objects, as analysed in this work, is presented in Table 2.3.

2.6 Summary

This chapter has presented a detailed discussion of the physics of Active Galactic Nuclei. An overview of recent efforts to unify the numerous classification schemes into a single paradigm has been provided which included details of the most widely accepted AGN model. An explanation of the shape of the spectral energy distribution of blazars has been presented, whereby the lower peak of the distribution is attributed to synchrotron emission by high energy electrons. The origin of the higher peak remains open to debate and with this in mind the two most popular models, namely the inverse-Compton and proton models, have been discussed in terms of their success in explaining observations to date. The last part of the chapter described the selection of the most promising candidates for gamma-ray emission which are analysed later in this work, in the search for new sources of VHE radiation. This search is based on detection of gamma-rays via their interaction with the Earth's atmosphere. Subtle characteristics of the resultant particle cascade and accompanying Cherenkov emission allow gamma-rays to be identified amongst the large background of cosmic-ray showers. To understand the mechanism by which gamma rays may be identified, an in-depth knowledge of particle cascades in the atmosphere is necessary. To this end a detailed discussion of the physics of extensive air showers is presented in the next chapter.

Source	Type	R. A. ($h\|m\|s$)	DEC ($d\|m\|s$)	z	Flux$_{>0.3TeV}$ ($\times 10^{-11} cm^{-2} s^{-1}$)			Observations (h)
					Fossati [(i)]	*Costamante* [(ii)]	*Stecker* [(iii)]	
1ES 0033+595	HBL	00 35 53	+59 50 05	0.086	2.04	0.25	–	27.4
1ES 0120+340	HBL	01 23 09	+34 20 50	0.272	0.28	0.300	–	36.4
RGBJ0214+517	HBL	02 14 18	+51 44 52	0.049	5.93	0.07	–	23.0
1ES 0229+200	HBL	02 32 48	+20 17 16	0.139	0.96	0.31	0.20	30.1
1ES 0323+022	HBL	03 26 14	+02 25 15	0.147	0.84	0.01	0.40	8.6
1ES 0806+524	HBL	08 09 49	+52 18 59	0.138	1.36	–	–	36.5
1ES 1011+496	HBL	10 15 04	+49 26 00	0.200	0.12	0.14	–	5.8
RXJ 1136+673	HBL	11 36 30	+67 37 04	0.135	0.92	0.10	–	9.7
1ES 1553+113	HBL	15 55 43	+11 11 24	0.360	0.20	0.42	–	9.7
1ES 1727+502	HBL	17 28 19	+50 13 11	0.055	5.19	0.07	0.50	6.9
1ES 1741+196	HBL	17 43 58	+19 35 09	0.084	3.59	0.29	0.40	6.2
1ES 0145+138	HBL	01 48 29	+14 02 18	0.125	0.55	–	–	7.9
1ES 1118+424	HBL	11 20 47	+42 12 24	0.124	0.38	–	–	5.0
1ES 2321+419	HBL	23 23 52	+42 11 00	0.059	0.13	–	–	10.4
3C 66A	LBL	02 19 30	+42 48 30	0.444	0.14	–	–	24.2
BL Lac	LBL	22 02 43	+42 16 40	0.069	3.32	0.17	–	6.3

Table 2.3: The list of sources selected for analysing during this work. Selection was based on a sample of the most promising candidates compiled by Costamante and Ghisellini (2002) and Stecker et al. (1996). The table shows the source name, BL Lac type, right ascension, declination, redshift, flux predictions (3) and the hours spent *ON*-source by the Whipple telescope. The Flux predictions are *(i)* those calculated by Costamante and Ghisellini (2002) using a modified version of the Fossati (Fossati et al., 1998) method for characterising the SEDs of blazars, *(ii)* those calculated by Costamante and Ghisellini (2002) using a SSC fit to the blazar SEDs, and *(iii)* those calculated by Stecker et al. (1996) using a simple SSC scaling argument to calculate the TeV flux. The sources 3C 66A and BL Lac are part of the original list of candidates but detection of both sources has already been claimed (but not yet confirmed) by the Crimean astrophysical observatory. The flux quoted for is $3.0 \pm 1.0 \times 10^{-11}$ cm^{-2} s^{-1} above 0.9 TeV for 3C 66A (Neshpor et al., 1998) and $2.1 \pm 0.4 \times 10^{-11}$ cm^{-2} s^{-1} above 1 TeV for BL Lac (Neshpor et al., 2001).

Chapter 3

The Physics of Extensive Air Showers

3.1 Introduction

Up until approximately 30 years ago our main understanding of the universe was garnered from radio, optical and infra-red observations, the higher energy regions of the electromagnetic spectrum remaining largely unexploited. This was in no small part due to the opacity of the Earth's atmosphere to high energy radiation. Accordingly, development of x-ray and gamma-ray astronomy only became possible with the ability to place detectors above the protective shield of the atmosphere, either in the form of high-altitude balloon experiments or expensive satellites. A number of such experiments have been deployed over the last 30 years, proving a great success (for details see Chapter 1). The most successful gamma-ray mission to date has been EGRET which facilitated detection of gamma rays up to an energy of 10 GeV (Hartman et al., 1999). Above this energy, the negligible expected flux (1 photon m^{-2} $year^{-1}$), allied to the small collection area of such instruments makes meaningful science practically impossible.

Fortunately it is about this energy that detection of gamma rays on the Earth's surface becomes possible, albeit via an indirect mechanism. Primary gamma rays above 100 GeV interact with the atmosphere, producing a cascade of subatomic particles which descend toward the surface of the Earth. For ultra-high-energy photons (> 50 TeV) the resultant showers penetrate deep enough to be detected at mountain altitudes using arrays of particle detectors (Figure 3.1). For lower-energy primaries, the resultant cascade attenuates before reaching ground level, however detection is still possible thanks to the accompanying Cherenkov emission (Figure 3.1). This radia-

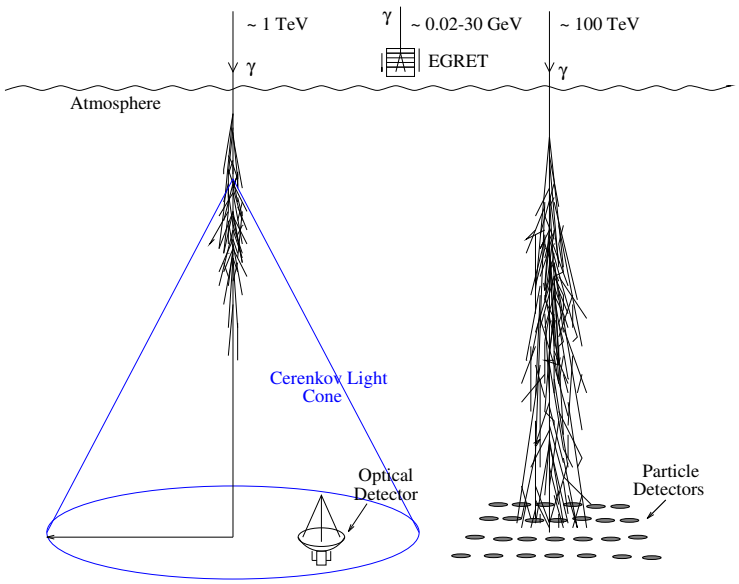

Figure 3.1: Detection of gamma rays at different energies.

tion is a direct result of the sub-atomic shower components traveling at speeds greater than the phase velocity of light in air. Unfortunately, detection of gamma rays using this approach is greatly complicated by the presence of a large experimental background. In the case of ground-based gamma-ray astronomy the main source of background is provided by cosmic-ray induced cascades, which have similar properties to gamma-ray-induced showers, but are vastly superior in number. The essence of the Atmospheric Cherenkov Technique (ACT) is discrimination between the two populations of events.

This chapter summarises the development of the ACT, including the process by which Cherenkov radiation is produced and how it may be detected above the night-sky background. The general characteristics of Cherenkov radiation in the atmosphere are outlined. The physics of extensive air showers is discussed and the main differences between gamma-ray-induced and hadron-induced showers presented. Finally the methods by which shower discrimination may be achieved are introduced and one approach, the Imaging Atmospheric Cherenkov Technique, is detailed.

3.2 Cherenkov Radiation

Cherenkov radiation arises from the coherent response of a dielectric medium to a relativistic particle passing through it, at a speed exceeding the local

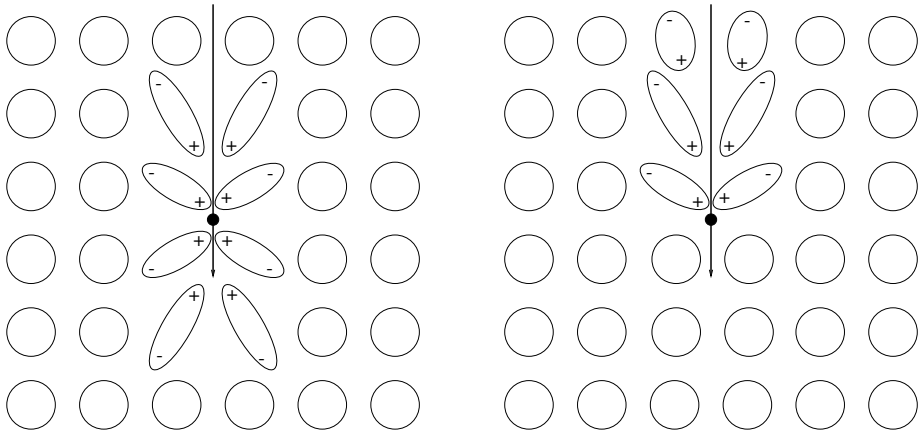

(a) Slower than local phase velocity of light

(b) Faster than local phase velocity of light

Figure 3.2: Ionisation due to the movement of a charged particle through a dielectric medium.

phase velocity of light. The effect was first observed as far back as 1910 by Marie Curie; however, subsequent experiments in the 1920's by Mallet (1926) failed to provide an explanation of the phenomenon. A series of elegant experiments performed by the Russian physicist Pavel Cherenkov, in the late 1930's, yielded results in agreement with the theoretical predictions of Frank and Tamm (1937).

The production of Cherenkov radiation may be explained as follows: as a charged particle travels through a dielectric medium, ionisation of surrounding atoms results. When each atom relaxes back to its ground state it emits a small burst of light. If the particle is moving with velocity less than that of light in the medium, ionisation is symmetric and the radiation emitted by each atom is incoherent (Figure 3.2(a)). If, on the other hand, the particle travels faster than the local phase velocity of light, the resulting ionisation is asymmetric (Figure 3.2(b)). This asymmetry is due to the electromagnetic field of the particle traveling slower than the particle itself and results in the emission of wavefronts that are in phase with each other. Accordingly the wavefronts interfere constructively to produce a coherent pulse of radiation, emitted at a specific angle with respect to the particle's trajectory. This Cherenkov angle, θ_c, is easily defined using a simple geometrical construction (Figure 3.3):

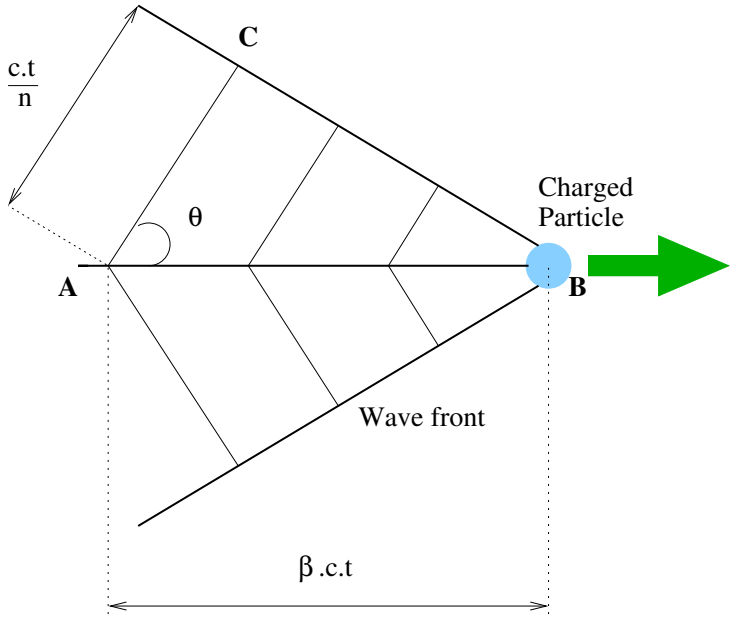

Figure 3.3: Geometrical explanation of Cherenkov emission.

$$\cos\theta = \frac{\frac{c}{n}.\Delta t}{\beta.c.\Delta t} = \frac{1}{\beta.n} \tag{3.1}$$

where β.c is the velocity of the particle, n is the refractive index of the medium and Δt is the time taken for the particle to traverse a distance AB. Using Equation 3.1 some of the fundamental properties of Cherenkov emission may be established:

1. For a given refractive index n, there exists a threshold velocity: $\beta_t = 1/\mathrm{n}$, below which no Cherenkov emission occurs. The corresponding threshold energy is: $E_t{=}m_0c^2/\sqrt{1-\beta_t^2}$, where m_0 is the rest mass of the particle.

2. The maximum emission angle for an ultra-relativistic particle occurs for: $\theta_{max}{=}cos^{-1}(1/n)$.

3. Due to the frequency dependence of the refractive index n, the condition $\beta_t = 1/\mathrm{n}$ can only be satisfied for air in the UV to near IR region of the spectrum. Consequently, there is no Cherenkov emission at x-ray or gamma-ray energies.

3.2.1 Cherenkov Emission in the Atmosphere

The form of the Cherenkov emission spectrum is highly dependent on the properties of the dielectric medium in which emission takes place. In the case of ground-based gamma-ray astronomy, the Earth's atmosphere provides the medium and accordingly it is important to understand its effect with regard to Cherenkov production. The refractive index of the atmosphere is not constant, rather it scales with height as the density of the atmosphere varies. This effect may be accounted for by writing the refractive index in the form:

$$n = 1 + \eta \tag{3.2}$$

where η ($<< 1$) is roughly proportional to the density of the atmosphere. Using this approach Jelley (1967) showed that the maximum emission angle in the atmosphere is:

$$\theta_{max} = \sqrt{2\eta} \tag{3.3}$$

and that the threshold energy for Cherenkov production is:

$$E_{min} = m_0 c^2 \left(\sqrt{2\eta} - 1\right) \tag{3.4}$$

Thus the Cherenkov angle decreases with altitude while the threshold energy increases. At sea level the Cherenkov angle is 1.3° and the equivalent energy threshold is 21 MeV for electrons, 4.4 GeV for muons, and 39 GeV for protons. Based on these figures it is clear that the majority of Cherenkov light is produced by relativistic electrons, with other particles producing a negligible effect. For the specific case of an electron moving along a track length l in air, the number of photons emitted is:

$$N = 2\pi\alpha l \left(\frac{1}{\lambda_2} - \frac{1}{\lambda_1}\right)\left(1 - \frac{1}{\beta^2 n^2}\right) \tag{3.5}$$

where z is the charge, α is the fine structure constant, and λ_1 and λ_2 define the wavelength range over which emission occurs. The linear dependence of the number of photons on wavelength implies a continuously decreasing spectrum with respect to wavelength. Atmospheric processes, comprising Rayleigh scattering, Mie scattering and ozone absorption intervene to produce a spectrum peaking in the UV region, around 330 nm (Figure 3.4).

3.2.2 Detection of Cherenkov Radiation

The possibility of Cherenkov radiation, produced by cosmic rays striking the atmosphere, contributing to night-sky background light was first mooted by

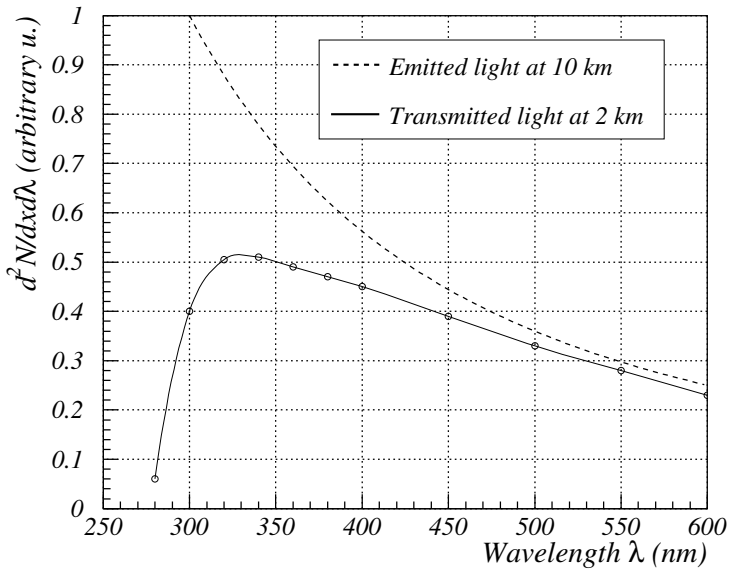

Figure 3.4: The intrinsic Cherenkov emission spectrum, compared to the spectrum after interacting with the atmosphere. Figure taken from de la Calle Perez (2003).

Blackett (1948) and later proved by Jelley (1958). Although the Cherenkov photon flux is small compared to the overall night-sky-light flux, the short duration of Cherenkov flashes ($\sim$ 5 ns) makes their detection possible. A typical Cherenkov pulse, produced by a 1 TeV gamma-ray primary yields approximately 50 photons m^{-2} within 100 m of the shower axis. The night-sky light flux is of the order of 10^{12} photons m^{-2} s^{-1} sr^{-1} in the 330 to 450 nm range. It is possible to greatly reduce the night-sky light flux, to as little as 1 - 2 photons m^{-2}, by matching the field of view of the detector to the angular extent of the Cherenkov flash and by limiting the integration time. Accordingly Cherenkov light may be readily detected above the background night sky, using a relatively simple set-up comprising a light collector, photo-multiplier tube (PMT) and fast trigger. The energy threshold of this type of system is highly dependent on the night-sky background and may be defined in terms of the detector's signal to noise ratio. The signal to noise ratio, defined as the ratio of the Cherenkov light intensity to that of the background night-sky, is given by:

$$\frac{S}{N} = \frac{\int_{\lambda_1}^{\lambda_2} C(\lambda)\epsilon(\lambda)\Omega A d\lambda}{\sqrt{\int_{\lambda_1}^{\lambda_2} B(\lambda)\epsilon(\lambda)\Omega t A d\lambda}} = \int_{\lambda_1}^{\lambda_2} C(\lambda)\sqrt{\frac{\epsilon(\lambda)\Omega A}{B(\lambda)t}d\lambda} \tag{3.6}$$

where

- C(λ) is the Cherenkov photon flux
- B(λ) is the background light flux
- $\epsilon(\lambda)$ is the quantum efficiency of the PMT
- Ω is the solid angle of the detector
- t is the integration time
- d is the mirror area
- λ_1 and λ_2 define the wavelength range over which the detector is sensitive

The smallest detectable Cherenkov light pulse, which is inversely proportional to the signal to noise ratio, is a measure of the threshold energy of the detector. Thus the energy threshold may be quantified as:

$$E_t \propto \frac{1}{C(\lambda)} \sqrt{\frac{B(\lambda)t}{\epsilon(\lambda)\Omega d}} \tag{3.7}$$

From this expression it is clear that the minimum energy threshold, corresponding to maximum signal to noise ratio, is achieved by matching the integration time of the detector to the duration of the Cherenkov pulse.

3.2.3 Detector Flux Sensitivity

Although it has been proved that, based on their interaction with the atmosphere, detection of cosmic gamma rays is possible, an additional factor must be taken into account when considering detection of a gamma-ray source. For a signal to be considered genuine it must be sufficiently strong to rule out the possibility of it being due to a statistical fluctuation in the background. Accordingly in the case of ACT experiments, where detector flux sensitivity is dominated by the cosmic-ray background, the signal is normally expressed in terms of the expected level of background fluctuation, which is given by:

$$N = \sqrt{k_b E_b^{-1.7} A_b(E_b) \Omega t} \tag{3.8}$$

For a gamma-ray flux defined as:

$$S = k_g E_g^{-G} A_g(E_g) t \tag{3.9}$$

the relative signal strength, or simply the signal to noise ratio, is given by:

$$N_{sig} = \frac{k_g E_g^{-G} A_g(E_g) T^{\frac{1}{2}}}{\sqrt{k_b E_b^{-1.7} A_b(E_b) \Omega}} \tag{3.10}$$

where

- E_g is the gamma-ray energy
- E_b is the background cosmic-ray energy
- G is the integral power law exponent of the gamma-ray source
- $A_g(E_g)$ is the gamma-ray collection area
- $A_b(E_b)$ is the cosmic-ray collection area
- Ω is the detector solid angle
- t is the observation time
- k_g and k_b are constants characterising the flux levels of the source and background.

Assuming $E_g \propto E_b$ and that A_g and A_b may be expressed in some energy-independent way this may be simplified as follows:

$$N_{sig} \propto \frac{A_g T^{\frac{1}{2}} E^{0.85-G}}{\sqrt{A_b \Omega}} \tag{3.11}$$

From Equation 3.11 it is obvious that measures may be taken to obtain the best signal to noise ratio (and flux sensitivity). Practically speaking this may be achieved by:

1. Increasing the gamma-ray collection area.
2. Minimising the background collection area.
3. Maximising observation time (of limited value for variable sources).
4. Operating at energies which give maximum N_{sig}.

The first two points are particularly important as by employing a suitable analysis it may be possible to greatly reduce the number of background events selected, while still retaining a large number of gamma rays. The employment of gamma-ray selection techniques is the main difference between first and second generation Atmospheric Cherenkov detectors, and is based on the fact that cascades produced by different progenitors vary in some respect to one and other. To achieve efficient discrimination between gamma rays and cosmic rays, an in-depth knowledge of the physical aspects of air showers is required.

3.3 Extensive Air Showers

An extensive air shower (EAS) is a cascade of particles produced by the interaction of a high-energy cosmic ray or gamma ray with the Earth's atmosphere. The cascade experiences an initial phase of exponential growth up to a maximum point, beyond which the shower quickly abates. Typically such showers spread out to cover an area of the order of 10^5 m^2, hence the term "extensive". EAS were first suggested as a means to explain correlations between cosmic-ray fluxes recorded by Geiger counters, separated by large distances. Methods used in the detection of such showers are dependent on the energy of the incident particle. For primaries with energy in the region of 50 TeV or greater, the resultant particle cascade is sufficiently penetrating to allow direct detection at mountain altitudes using arrays of particle detectors. Incident particles with energy of the order of a TeV produce showers which die out high in the atmosphere. Detection of such showers is achieved through collection of the Cherenkov light emitted by their relativistic constituents.

The interactions which occur during creation and development of EAS may be divided into two categories; *charged-particle - matter* interactions and *radiation - matter* interactions. In the first instance three processes are dominant (Figure 3.5):

- Bremsstrahlung - the emission of a high energy photon when a charged particle is accelerated in the field of a non-relativistic nucleus.
- Coulomb scattering - the change in direction of a charged particle in the field of a nucleus involving insignificant transfer of energy.
- Ionisation - the transfer of energy from a charged particle to an atom following inelastic collision of the particle with the atomic electrons.

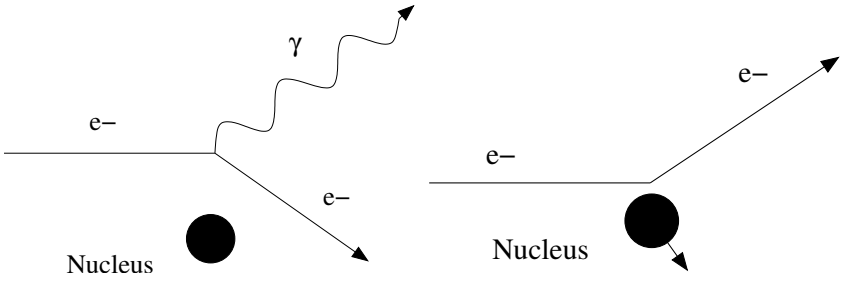

(a) Bremsstrahlung **(b)** Coulomb scattering

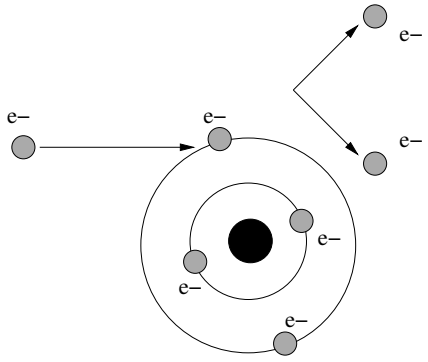

(c) Ionisation

Figure 3.5: Important *charged-particle - matter* processes.

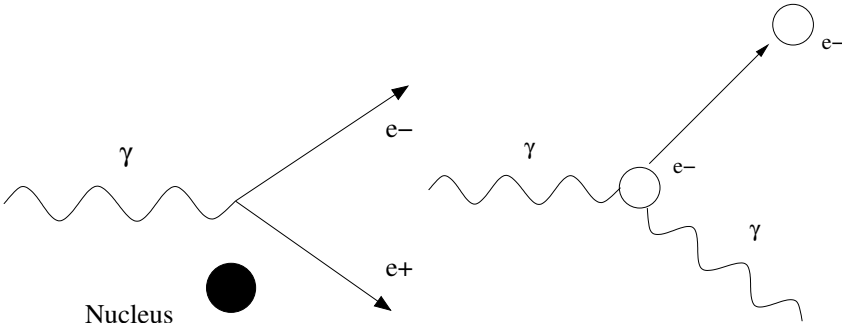

(a) Pair production **(b)** Compton scattering

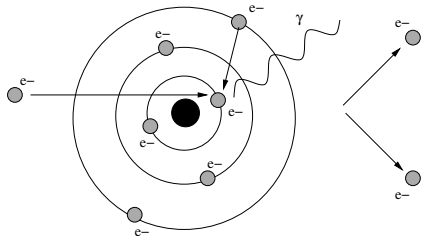

(c) Photoelectric effect

Figure 3.6: Important *radiation* - *matter* processes.

In the case of *radiation* - *matter* interactions the three dominant effects are (Figure 3.6):

- Pair production - the production of an electron-positron pair following the interaction of a high-energy photon in the field of an atomic nucleus.
- Compton scattering - the interaction of a photon with a quasi-free electron resulting in the transfer of some of the photon's energy to the electron.
- Photoelectric effect - the complete transfer of a photon's energy to a bound electron.

The cross section for these three processes are dependent on the energy of the incident photon (Figure 3.7). Pair production becomes important at energies of 1 MeV and is dominant above 25 MeV. Compton scattering is important at energies of a few tens of MeV while the photoelectric effect is

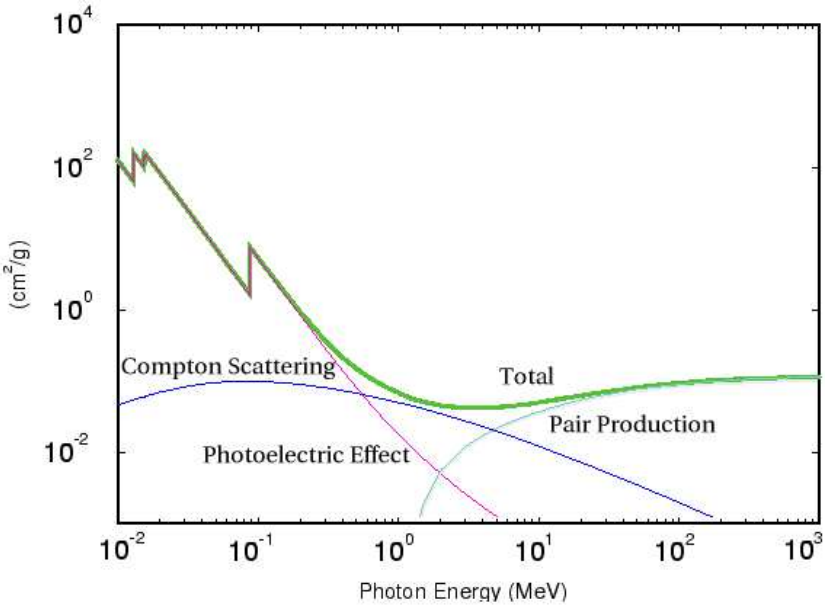

Figure 3.7: The mass attenuation coefficients (equivalent to the cross sections) for the different processes by which gamma rays interact with lead. Although the actual values change for different materials, the functional form of the graph remains the same.

most important at low energies. Accordingly pair production is the dominant *radiation - matter* interaction when considering extensive air showers.

As alluded to earlier, EAS may be categorized by the primary particle responsible for their production. Thus we have two types; *gamma-ray-induced* and *cosmic-ray-induced* showers. Because showers initiated by cosmic rays are much more numerous that their gamma-ray counterpart, in order to detect a gamma-ray source one must be able to differentiate between the two shower types. To do so requires detailed knowledge of the characteristics of EAS.

3.3.1 Gamma-Ray-Initiated Showers

When a high-energy gamma ray enters the atmosphere it undergoes pair production in the field of an atomic nucleus (the nucleus is required for conservation of momentum):

$$\gamma \rightarrow e^+ + e^-$$

In the case of ultra-relativistic air showers the cross-section for pair produc-

tion is independent of energy. Given a radiation length for pair production equal to 37.7 g cm^{-2} and a typical atmospheric depth of 1038 g cm^{-2}, the initial interaction must occur near the top of the atmosphere (at an altitude of $\sim$ 20 km). The resultant electron-positron pair is sufficiently energetic to interact via Bremsstrahlung, creating two additional high-energy photons.

This double process (pair production followed by Bremsstrahlung) is repeated numerous times, generating a shower which is predominantly electromagnetic in nature (Figure 3.8). The shower experiences a period of exponential growth up to the point where the average energy of the particles reaches a value known as the critical energy. The shower has now reached maximum development. Below the critical energy, dissipation processes begin to dominate over creation processes and the shower quickly attenuates. The critical energy for electrons is defined as the energy below which losses due to ionisation outweigh those due to Bremsstrahlung. In air this occurs at an energy of 83 MeV. The critical energy for photons is the energy below which Compton scattering becomes dominant over pair production (in air $\sim$ 84.2 MeV). The agreement of the critical-energy values is reflective of the similarity of the two processes. Using a simplified model of an electromagnetic cascade, proposed by Heitler (1954), Greisen (1956) showed that the number of particles at the shower maximum is given by:

$$N_{max} = \frac{E_0}{10E_c} \tag{3.12}$$

where E_0 is the energy of the primary gamma ray and E_c is the critical energy. Thus, for a 1 TeV gamma ray, the shower comprises $\sim$ 1200 particles and the shower maximum occurs at an altitude of $\sim$ 8 km.

Although gamma-ray showers are predominantly electromagnetic in nature there is a possibility that some muons may be produced in photo-nuclear interactions. The cross-section for such interactions is tiny in comparison to that for pair production and Bremsstrahlung (a factor of 10^{-4} smaller), so gamma-ray-induced showers are expected to have negligible muon content.

3.3.2 Hadron-Initiated Showers

Hadron-initiated showers result from the interaction of a cosmic-ray proton or nucleus with the atmosphere. These showers are comprised of three components; the nuclear-active component, the muonic component, and the electromagnetic component. The mean free path for a proton in air is 80 g cm^{-2} so the initial interaction takes place at an altitude of approximately 16 km. This interaction is generally a proton-proton one, of the form:

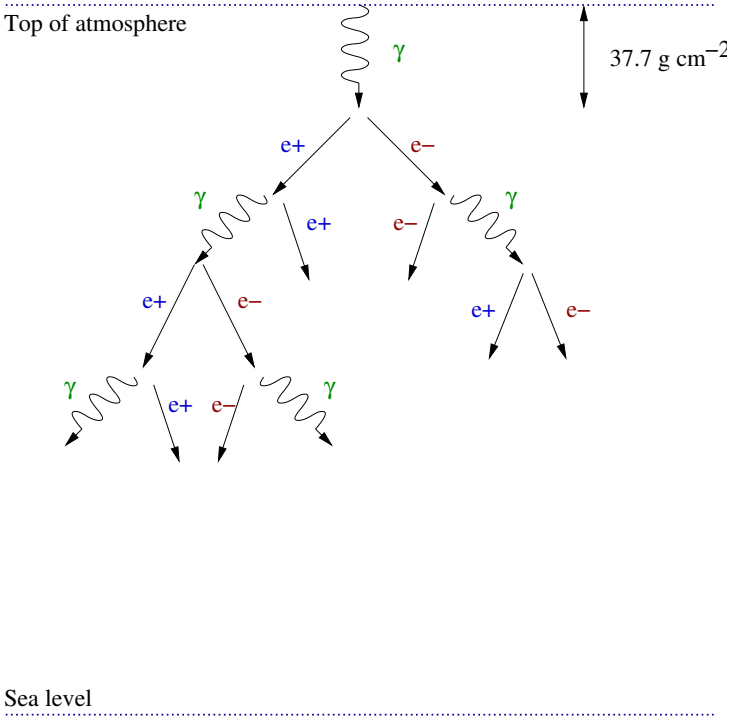

Figure 3.8: Structure of an electromagnetic shower produced by the interaction of a high-energy gamma ray with the Earth's atmosphere.

$$p^+ + p^+ \rightarrow \pi^0 + \pi^+ + \pi^- + \textit{nucleonic debris} + \gamma$$

The secondary particles are strongly beamed in the forward direction due to the high energies involved. If the primary proton is of sufficient energy the daughter nucleons which are produced may themselves undergo similar transitions, leading to the development of the shower's nucleonic component. This portion of the shower will continue to grow, up to the point where the resultant nuclei fall below the threshold energy required for multiple pion production (approximately 1 GeV). When this occurs the nuclear core of the shower quickly attenuates.

The pion triplets produced during each stage of the nucleonic cascade decay according to the following regime:

$$\begin{aligned} \pi^0 &\rightarrow \gamma + \gamma \\ \pi^- &\rightarrow \mu^- + \bar{\nu}_\mu \\ \pi^+ &\rightarrow \mu^+ + \nu_\mu \end{aligned}$$

Due to its short lifetime ($\sim 1.7 \times 10^{-16}$ s) the neutral pion decays soon after its production, generating a pair of gamma rays. The gamma rays in turn undergo pair production, initiating an electromagnetic cascade similar to that described in the previous section (Section 3.3.1). The muons produced via decay of the charged pions (*lifetime* $\sim 2.5 \times 10^{-8}$ s) play no further role in shower development. Low energy muons either decay to produce neutrinos and electrons, or are brought to rest through ionisation. In contrast, their higher-energy counterparts may penetrate to ground level by virtue of Lorentz contraction. A proton shower may therefore be thought of as a shower with a nucleonic core continually initiating small electromagnetic cascades. A picture of a typical hadronic shower is presented in Figure 3.9.

During a nucleonic interaction approximately one third of the total energy available at that point is given to the electromagnetic shower. This means that overall, the electromagnetic component of the shower contains most of the energy of the primary hadron. As seen in Figure 3.9 hadronic showers tend to have significant lateral spread, due to the large opening angle of the pion interaction process.

3.3.3 Shower Differentiation

The subtle differences which exist between gamma-ray-induced showers and hadron-induced showers offer the possibility of picking out a gamma-ray signal amongst the large population of background events. Although the general

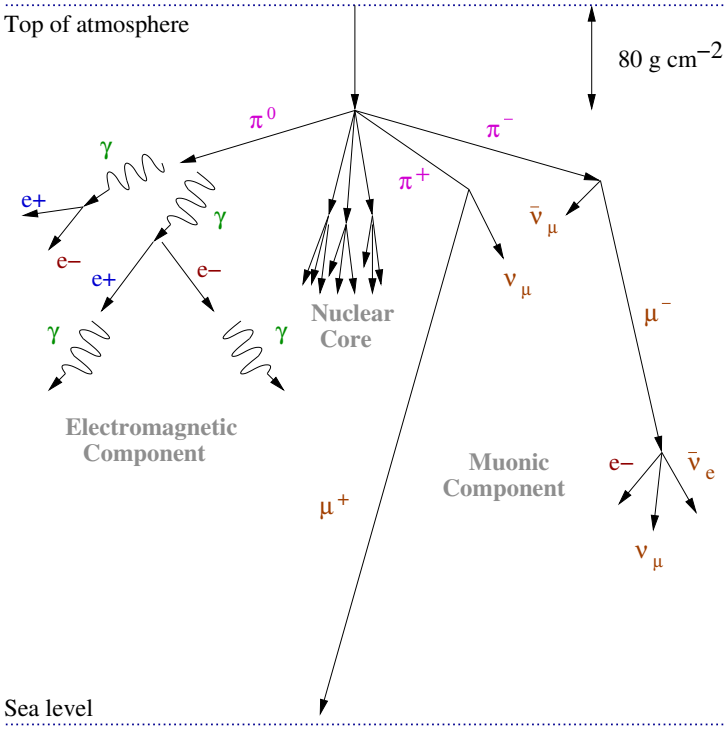

Figure 3.9: Structure of an air shower produced by the interaction of a high-energy cosmic ray with the Earth's atmosphere.

differences between shower types have already been outlined, if the differences are to be fully exploited a more analytical description of shower development is required,. To characterise the development of EAS, Monte-Carlo simulations are used.

The first air shower simulations were produced by Rieke and Weekes (1969). Since then the level of complexity has increased to incorporate amongst others, atmospheric effects and effects due to the Earth's magnetic field. Within the VERITAS collaboration there are a number of simulation codes currently in operation; however, throughout this work a single package, developed at Iowa State University (in conjunction with Grinnell College), has been used (for further details see Section 5.3.1). Much of the early efforts in establishing a reliable means of distinguishing between gamma-ray and cosmic-ray showers was carried out by Hillas (for a detailed overview see Hillas (1996)). Hillas's work was based on his own air-shower-simulations package, which characterised showers based on their lateral and longitudinal development profiles. The lateral distribution is highly dependent on the longitudinal development of the shower, due to the fact that higher energy showers develop deeper into the atmosphere and last longer, resulting in greater scattering of their constituents. The differences in these distributions for gamma-ray and hadronic showers give rise to differences between their resultant Cherenkov light distributions. The general shape of a typical gamma-ray and hadronic shower is shown in Figure 3.10.

The mean free path of a high-energy gamma ray in the atmosphere is considerably less than that of a proton with similar energy. Accordingly proton showers are initiated at lower altitudes and survive to greater depth, even without considering their highly penetrating muon component. This longitudinal difference is shown in Figure 3.11, with the light due to muons omitted to show that even the core electron-photon cascade differs between the two types of shower. Hadronic showers exhibit larger shower-to-shower fluctuations in their longitudinal profiles than gamma-ray showers. Showers due to heavier nuclei are even more well distinguished from gamma-ray showers; however, differences in longitudinal profiles are not enough to reliably differentiate between hadronic and gamma-ray showers. Luckily, differences also exist between the respective lateral distributions.

The greater lateral spread of hadronic showers, compared to gamma-ray showers, is due to the different physical processes responsible for shower development. Broadening of gamma-ray showers is due to the opening angles of scattering, Bremsstrahlung, pair production and Coulomb scattering, with Coulomb scattering dominant. The lateral spread of hadronic showers is down to the large transverse momentum imparted to the charged pions during their production. Since the opening angle for multiple pion production is

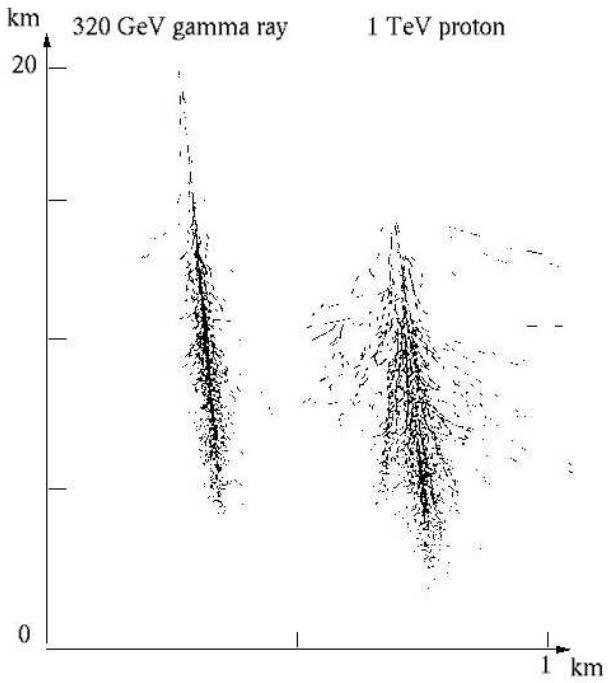

Figure 3.10: A typical gamma-ray and hadronic shower. It is clear that differences between the shower types exist. Figure taken from Hillas (1996).

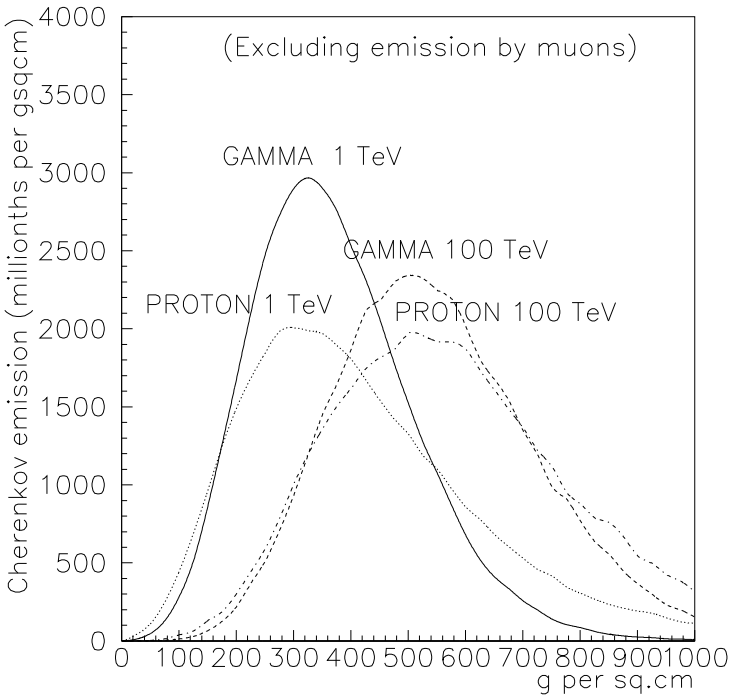

Figure 3.11: Longitudinal profiles of Cherenkov light from gamma-ray and proton showers. Figure adapted from Hillas (1996).

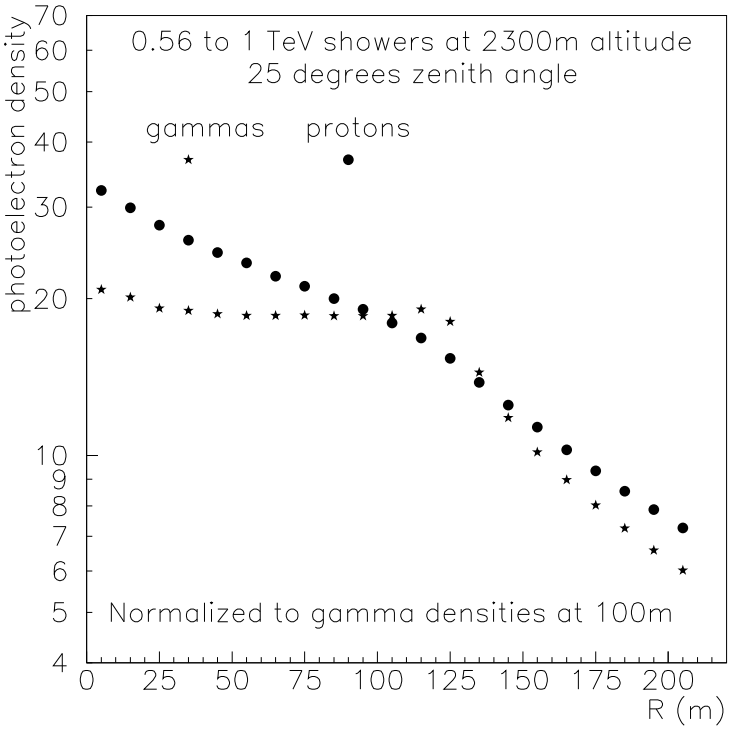

Figure 3.12: Lateral distribution of Cherenkov light from gamma-ray and proton showers. Figure taken from Hillas (1996).

greater than that for Coulomb scattering, hadronic showers tend to be less compact than gamma-ray showers. For example, for a 1 TeV gamma ray the majority of Cherenkov emitting particles lie within 21 m of the shower axis. For a cosmic ray of similar energy the same fraction of emitting particles fall in a region reaching out to 70 m from the shower core. This difference results in two distinctly different Cherenkov light distributions on the ground (Figure 3.12), and may be explained in terms of the development of the showers and the characteristics of Cherenkov emission.

For the gamma-ray lateral Cherenkov distribution alone (Figure 3.12) there are a number of features which warrant discussion. The first is the bump in the distribution, occurring between $\sim$ 100 - 130 m from the shower axis. This is produced by the large population of particles which exist within 21 m of the shower core at the point of maximum development. The presence of the peak may be attributed to the change in Cherenkov emission angle with atmospheric depth, which varies from 1.5° at the top of the atmosphere to 0.8° at sea level. Cherenkov light emitted by relativistic particles at different depths is projected onto the ground at different radial distances from

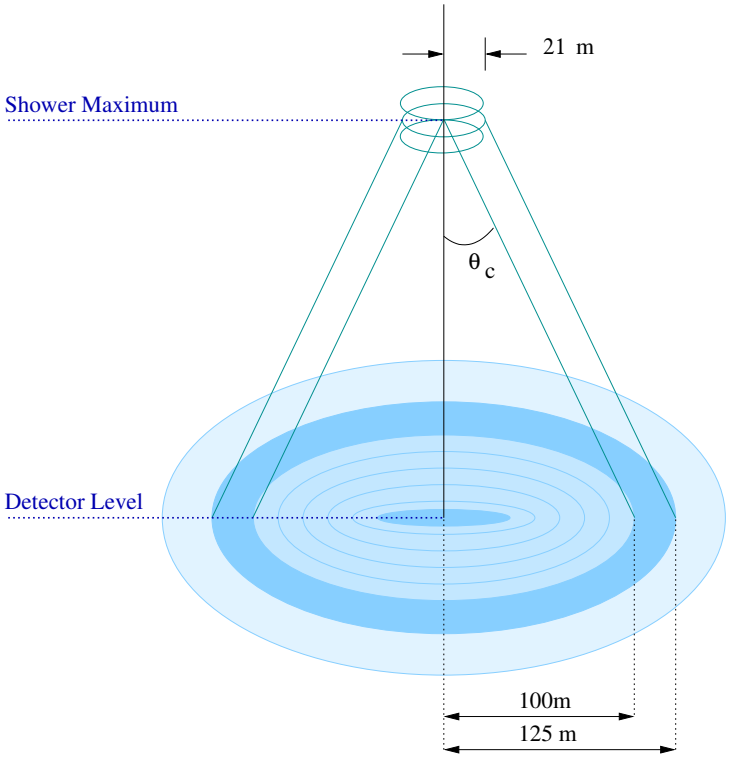

Figure 3.13: Mapping of Cherenkov light from a gamma-ray shower onto the ground.

the shower impact point. If shower particles experienced no lateral displacement the Cherenkov distribution on the ground would take the form of a narrow annulus. For a 1 Tev gamma-ray primary whose maximum occurs approximately 8 km above sea level, the Cherenkov light would fall within a ring of 110 - 145 m from the shower impact point. As stated previously, Coulomb scattering dominates over the Cherenkov emission angle, resulting in the broadening of this ring into a small bump in the distribution. The Cherenkov ring is most prominent for low energy primaries, when the shower dies out high above the observer. Because photons in this region are produced close to shower maximum, they provide a reliable estimation of the primary's energy, making them most useful for spectral work (Mohanty et al., 1998). A graphical description of how Cherenkov radiation, from gamma-ray showers, is mapped onto the ground is shown in Figure 3.13.

The second notable feature in the lateral Cherenkov light distribution is the inner peak, which occurs close to the shower axis. This is made up of light emitted by local, penetrating particles. Although the Cherenkov

emission angle is larger at lower altitudes, the light still falls close to the shower impact point because of the short distances it has to travel and since it is produced by particles in the shower tail is most liable to fluctuations. Finally there is the outer region of the Cherenkov light distribution, where the number of photons falls off rapidly as one moves further from the shower axis.

The lateral distribution of Cherenkov radiation produced by cosmic-ray showers is quite different to the gamma-ray distribution. The cosmic-ray Cherenkov distribution may be characterised by falling intensity as one moves away from the shower impact point. Because of the longer interaction lengths of particles in proton showers, more particles will penetrate deeper into the atmosphere. When this is combined with the light from the highly penetrating muonic component, the intensity of light from a hadronic shower is highest close to the shower impact point. There is no Cherenkov ring associated with proton showers because of the larger transverse momentum of its particles. Since the lateral development of showers is dependent on the longitudinal development, and the longitudinal profile of proton showers fluctuates, there are also significant fluctuations in the lateral distribution of Cherenkov light from hadronic showers.

The spectral composition of Cherenkov radiation due to gamma rays and cosmic rays also differs. Shower maximum occurs at higher altitudes for gamma-ray showers than for hadronic showers. As a result their Cherenkov photons travel a greater distance through the atmosphere before reaching detector level. The atmosphere is a UV absorber, meaning that gamma-ray induced showers will have poor UV content compared to proton-induced showers.

To exploit the various differences between gamma-ray and cosmic-ray showers, a number of experiments, in the form of a suitably configured detector and discrimination technique, have been carried out. These experiments are based on, amongst others, wavefront sampling, duration of the shower front, and spectral content techniques. The relative merits of each approach are discussed in Fegan (1992); however, the most successful method to date has been the Imaging Atmospheric Cherenkov Technique.

3.4 The Imaging Atmospheric Cherenkov Technique

The Imaging Atmospheric Cherenkov Technique (IACT) has its origins in early work by Hill and Porter (1961), Weekes and Turver (1977), Weekes

(1981), and Cawley et al. (1983). Over the past 20 years it has proved to be the most successful ground-based technique for detection of gamma rays in the 100 GeV to 30 TeV energy range, and has a number of desirable attributes. The collection area of an IACT telescope is not limited to the physical dimensions of the detector, rather it depends on the lateral extent of the showers. The resulting collection area, of the order of 50,000 m^2, although huge compared to satellite-based detectors, is necessary due to falling gamma-ray flux. Typical detectors also have high angular resolution ($\sim 0.1^\circ$), and reasonable energy resolution ($\sim 30 - 40\%$), while on the negative side IACT telescopes have small fields of view ($< 5^\circ$), and low duty cycles (~ 10 %).

Discrimination between shower types using the IACT is based on differences in shower development which transmit to differently-shaped images as recorded by a typical IACT telescope. As part of his pioneering simulations, Hillas modeled the response of the 37 tube camera, on the Whipple 10m reflector, to showers generated by protons and gamma rays. The simulations predicted that a focusing mirror on the ground at 60 to 130 m from the shower axis would see the shower at its maximum development as if it were a glowing column of air. For a 1 Tev gamma-ray shower, whose maximum development occurs at a height of 8 km, viewed from an altitude of 2 km (the altitude of the Whipple Observatory), the projection of the resulting "glowing air column" onto the camera forms an image 0.2° in radius. For a proton shower of similar energy, due to its different lateral and longitudinal distributions, the image formed has a radius of 0.75°. This difference suggests that the shape of a Cherenkov image may be used as a method of discrimination. Another possible means of discrimination is the orientation of the image. Since gamma rays are uncharged they travel through space in a straight line from their point of origin. Cosmic rays on the other hand carry charge, resulting in numerous changes in direction as they journey through intergalactic space. Combining this with the fact that air showers retain a high degree of their primary's directionality, one would expect gamma-ray images to be aligned in the direction of the source, in contrast to cosmic-ray images which should have no preferential orientation. Using a selection method based on the shape and orientation of Cherenkov images, the Crab Nebula was detected as the first cosmic source of VHE gamma rays (Weekes et al., 1989).

3.5 Summary

During this chapter a number of important aspects pertaining to ground-based gamma-ray astronomy have been discussed. The process by which Cherenkov light is created has been reviewed, including the unique properties which allow its detection above the night-sky background. The physics of extensive air showers has been examined, concentrating on the differences between gamma-ray-induced and cosmic-ray-induced cascades. It has been shown that subtle differences exist between shower types, which opens up the possibility for detecting gamma-ray events amidst the numerically superior population of cosmic rays. Finally, the imaging technique has been introduced as a viable means for exploiting these differences. This thesis is based on data recorded by an imaging detector, the Whipple 10m telescope. Accordingly, the next chapter provides a detailed overview of the Whipple telescope, including its design, operation and subsequent analysis of data.

Chapter 4

The IACT at the Whipple Observatory

4.1 Introduction

The aim of the Imaging Atmospheric Cherenkov Technique (IACT) is detection and study of cosmic sources of VHE gamma radiation. Detection of a source involves identifying an excess of candidate gamma-ray events coming from the source direction, compared to a control region of sky. The indirect nature of the IACT, that is the detection of gamma rays via their interaction with the atmosphere, introduces an almost overwhelming background due to cosmic rays, single local muons and extraneous background light. As outlined in the preceding chapter, a flux of gamma rays may still be identified amidst this background using a suitably configured detector and complementary selection algorithm.

This chapter provides an overview of the implementation of the IACT at the Whipple Observatory in southern Arizona. A detailed outline of the operation of the Whipple 10m telescope, including optical design, data acquisition and diagnostic sub-systems is presented. An intricate part of the IACT is its use of off-line analysis to reject a large percentage of the cosmic-ray background and so the standard Whipple analysis is discussed in depth. This includes calibration of the detector, image cleaning, noise padding, gamma-ray selection and signal estimation.

4.2 The Whipple 10m Telescope

The VERITAS Collaboration (formerly the Whipple Collaboration) is an international research group consisting of scientists from a number of academic

institutions in Ireland, Britain, the United States and Canada (for a full list of members see Appendix C). The group operates an Imaging Atmospheric Cherenkov Technique (IACT) reflecting telescope located at Mount Hopkins in southern Arizona (longitude: 110° 53.1' W, latitude: 31° 41.3'N, altitude: 2320 m a.s.l). The Arizona climate is ideal for observations using this technique as its monsoonal nature results in approximately nine months of clear, dry nights, a prerequisite of the IACT. The Whipple 10m Reflector was built in 1968 (Weekes et al., 1972) and has been in continual operation since 1982, when its first imaging system was installed. Although the detector as a whole is a combination of several parts, it may be sub-divided into its two major components; the optical system (reflector) and the imaging system (camera and electronics).

4.2.1 Optical Design

The Ten Meter Reflector is based on the Davies and Cotton design (Davies and Cotton, 1957) and while originally intended for use in solar observations, was first used for astronomical purposes in 1966 (Hanbury-Brown, 1966). A Davies-Cotton reflector comprises a large spherical dish, onto which a number of identical mirrors is attached. The radius of curvature of each mirror facet is exactly twice that of the overall dish. The Davies-Cotton design has a number of advantages:

1. The use of a large number of small mirrors, as opposed to one large reflecting surface, means that the reflector is relatively cheap to construct and maintain.

2. Alignment of the reflector is simple. This is achieved by manually adjusting each mirror facet such that their central axes pass through a point which is at a distance of twice the curvature of the dish from its centre along the frame axis (Figure 4.2).

3. The overall structure of the reflector is compact and rigid.

4. Both on-axis and off-axis aberrations are small compared to parabolic reflectors (Lewis, 1990).

The main disadvantage of this design is its an-isochronous nature, caused by the varying time required for light from different portions of the reflector to reach the focal plane. In general, light striking the outer regions of the reflector arrives in the focal plane before light striking the central region, which results in a measurable (6 ns) broadening of the optical signal. The

resulting reduction in the signal to noise ratio of the system is negligible in comparison to that introduced, later in the system, by the electronics.

The Whipple Ten Meter Reflector (Figure 4.1) consists of a spherical dish, of radius 7.3 m, with an opening diameter of 10 m. This gives a $f/0.73$ focal ratio system, with a plate scale of 12.8 cm/deg (Figure 4.2). The reflecting surface is provided by 248 hexagonally shaped glass facets, attached to the frame in nine concentric rings. The facets are front-alluminized to increase reflectivity of UV light (glass is an efficient absorber of UV light, which is the main component of a Cherenkov signal). Although the Arizona climate is generally favourable for astronomical observations, the wide temperature range, combined with occasional high winds and precipitation, result in degradation of the reflecting surfaces. To compensate for this, the mirrors are re-coated at regular intervals or when such degradation is observed. The results of the last coating (Figure 4.3), carried out in 2000, clearly show the benefit of this procedure.

With a lateral extent of 61 cm, the mirrors combine to provide an overall reflecting area of 75 m^2. The facets have a radius of curvature of 14.6 cm (as required by the Davies-Cotton design) and to facilitate alignment are mounted on adjustable tripods. Alignment of the reflector has been observed to degrade over time. This degradation contributes to the deterioration of the point spread function (PSF) of the reflector, which in turn diminishes the ability to discriminate between gamma-ray and background images. Accordingly, the PSF of the system is also measured at regular intervals and the system re-aligned if required. To facilitate easy and rapid alignment a number of innovative methods have been devised (Kildea, 2002). The alignment of the reflector is also observed to change with elevation, increasing as the telescope is moved toward the zenith and is most likely due to flexure of the optical support structure (OSS) under the influence of gravity. To maximize the ability to identify gamma rays it is important to minimize the PSF of the reflector at small zenith angle, where the majority of observations are made. To achieve this a bias-alignment is performed, whereby the reflector is intentionally mis-aligned at low-elevation, so that when it is moved toward the zenith, it falls into alignment (as the OSS flexes). The benefit of the bias-alignment procedure is evident from PSF measurements taken in 2001/2002 (Figure 4.4). For a detailed description of alignment procedures see Kildea (2002) and references within.

4.2.2 The Camera

The Whipple camera is located in the focal plane of the reflector and is held in position by quadropod arms. The camera is composed of a closely

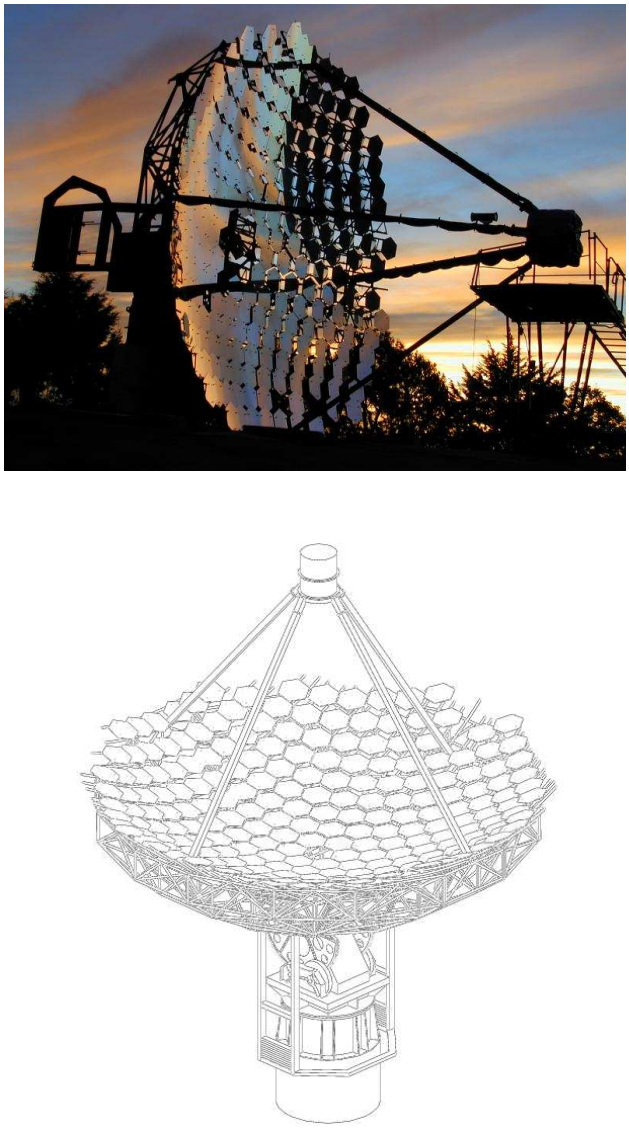

Figure 4.1: The Whipple Ten Meter Telescope.

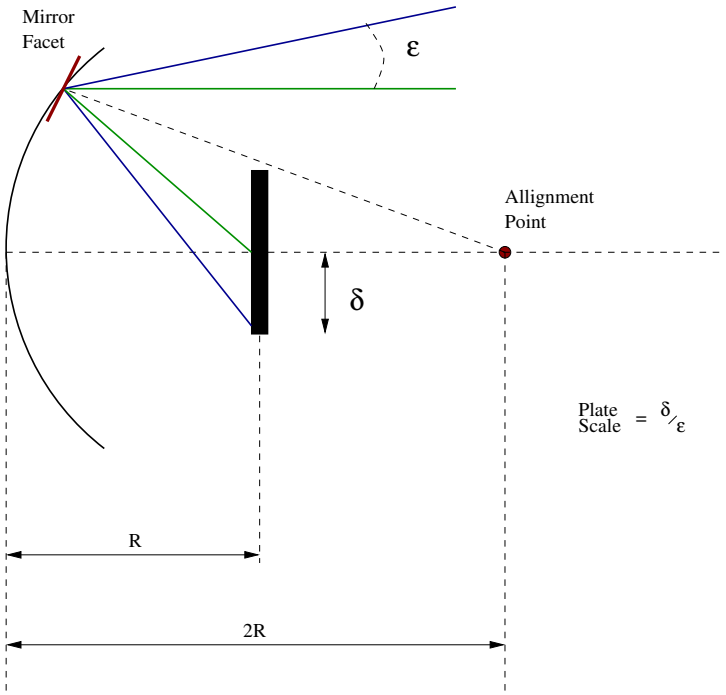

Figure 4.2: Optical Configuration of Davies-Cotton Design.

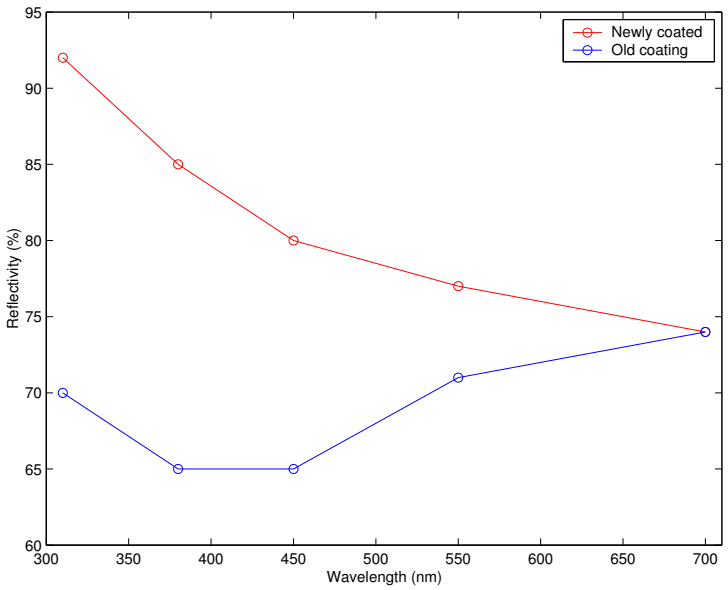

Figure 4.3: Average reflectivity of a sample of 66 mirrors, prior to and after being re-coated. The difference in reflectivity is pronounced, and clearly shows the effect that exposure of the reflector to the southern Arizona climate has on telescope performance.

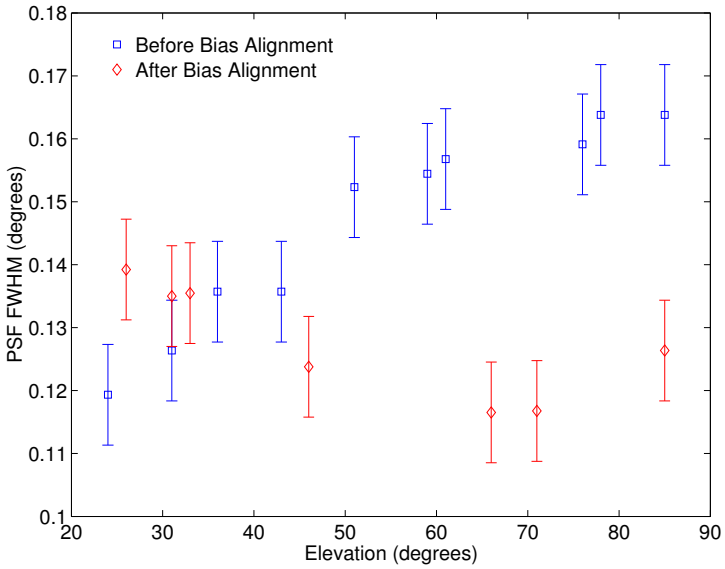

Figure 4.4: PSF measurements for the Whipple 10m Reflector, taken before and after bias-alignment was carried out. The resulting decrease in PSF at high elevation, and therefore improved alignment, is clear. Correct alignment of the system at zenith angles close to 20° is important, since this is where the majority of observations are made. Figure courtesy of Kildea (2002).

packed array of photomultiplier tubes (PMTs), which convert the optical signals arriving in the focal plane to measurable electrical current. The PMT array is housed in a cylindrical box, with a removable cover to provide some protection from the desert climate. The PMTs used are chosen specifically to detect Cherenkov light and accordingly are: (1) fast response, of the order of ns, similar to the duration of Cherenkov pulses, (2) high gain, 10^5 - 10^6, to avoid the use of pre-amplifiers and (3) high quantum efficiency ($\sim 20\,\%$) in the blue to UV region of the spectrum (where the Cherenkov spectrum peaks). A significant amount of light falling on the camera may be lost due to dead space between PMTs. The source of this dead space is obvious when one considers the make-up of a PMT which consists of a photocathode surrounded by μ-metal shielding, encased in a plastic cover. As a result the photocathode accounts for as little as 36% of the total area of each PMT. To limit the amount of light lost in this way light guides are fitted to deflect photons falling on the dead space onto the photocathode. These are specifically designed so that only light coming from the direction of the reflector is retained. This helps to reduce noise caused by extraneous background light.

Over the last 15 years the camera has been subject to a number of upgrades, with the aim of increasing sensitivity while simultaneously reducing the energy threshold. The original camera (Cawley et al., 1990) comprised an array of 109 one-inch PMTs, with a combined field of view of 3°. In 1996 an additional 42 PMTs were added. Over the period spanning 1997 - 1999 a major development program, known as the GRANITE III upgrade, was undertaken (Finley et al., 2000). The first stage of this involved the commissioning of a large-pixelated camera. Comprising 331 PMTs the camera had an overall field of view of 5°, making it ideal for the study of extended sources. The second stage of the upgrade was the addition of a hardware pattern recognition trigger (Section 4.2.3). The third and final stage of the upgrade was the installation of a 490 fine-pixelated camera, which was carried out in the summer of 1999 and is still in use today. The 490 pixel, high-resolution camera comprises an inner array of 379 half-inch Hamamatsu H3165 PMTs, surrounded by an annular array of 111 one-inch Hamamatsu R1398 PMTs, giving an overall field of view of 4°. The PMTs are powered by three LeCroy High Voltage (HV) modules, mounted in crates on the telescope counterweights and controlled remotely via ethernet and monitored using a graphical user interface. The fine pixelation of the inner camera is optimal for determining the shape and orientation of Cherenkov images, resulting in a very sensitive detector. The actual field of view of the camera is reduced to 2.6° due to the fact that signals from the outer tubes are not used in standard image analysis. Attempts have been made to analyze data

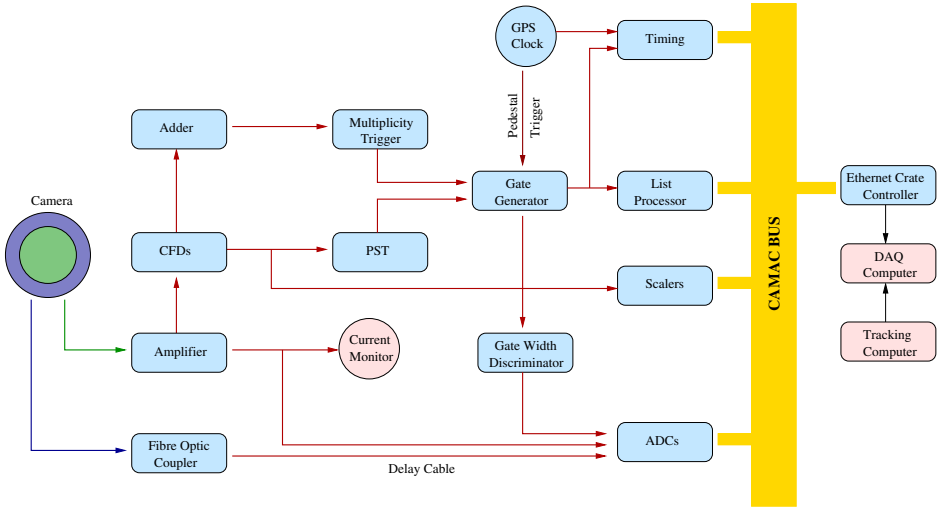

Figure 4.5: The Whipple Data Acquisition System. The diagram shows the path taken by a signal, on its way from the camera to the DAQ computer.

from the camera as a whole but have met with limited success (Fegan, 2002). Due to difficulties in using signals from the larger PMTs and to facilitate development of the VERITAS prototype the outer three rings of PMTs were removed in January 2003.

4.2.3 Data Acquisition System

The signal output from the PMTs is passed onto the data acquisition (DAQ) system, which performs a multitude of important tasks, including triggering, timing, recording and diagnostics. Data acquisition for the Whipple telescope is based on the CAMAC system of crates and modules (Rose et al., 1995). The readout of these modules is achieved using Hytec 1342 list processors, which form the basis of the DAQ system. The list processors interface with the DAQ computer, via a Hytec 1365 Ethernet CAMAC Crate Controller, and are programmed to carry out data acquisition commands. Once their programs are initialised the list processors operate independently of any intervention or requirement of resources of the DAQ computer, resulting in a maximum achievable data-rate readout. The path taken by a signal, as it is passed from the camera to the DAQ computer, is shown in Figure 4.5.

Electronics

The signal output from the camera may be divided up into two parts. The first, signals from the outer 111 tubes, are transferred via fibre-optic cable to a coupling device, which converts the light back into an electric current. Signals from the inner 379 tubes are transferred from the camera to the amplifiers, via RG58 coaxial cable. The amplifiers are high quality LeCroy 612A models, each with a gain factor of 10. The output from the amplifiers is three-fold. The first output is a DC-coupled signal from each of the 379 inner PMTs which is sent to the current monitor. The second output is also from the inner 379 tubes, AC-coupled to remove the average night-sky background light and passed via 45 m of RG58 co-axial cable to the ADCs (Analogue to digital converters). The third and final output is from the inner 331 pixels only and is passed onto the constant fraction discriminators (CFDs).

The CFDs, LeCroy 3420 in design, represent the first stage of the trigger electronics and decide if a PMT has fired or not. The discriminators take the amplified PMT signal as their input and output a pulse of predetermined amplitude and duration when the signal amplitude exceeds a preset threshold. The timing of the leading edge of the output pulse is determined using a constant fraction of the input signal, giving a more accurate synchronisation of signal and trigger pulse than that of a standard arbitrary-value discriminator. The output from the CFDs is again three-fold. The first is to the single rate scalers, which record the number of times each individual PMT fires. The single rate scalers are recorded only for *pedestal* events (Section 4.2.3) and may be used to identify problematic PMTs. The second output is to an Adder which sums the signals from the CFDs, outputting a pulse proportional to the number of PMTs which fired, which is immediately passed onto the multiplicity trigger. The third and final output from the CFDs is to the pattern selection trigger (Section 4.2.3).

Multiplicity Trigger

The multiplicity trigger is used to determine if a requisite number of tubes have fired (known as the multiplicity of the system, and denoted N) for data recording to be initiated. In general the Whipple telescope is operated in conjunction with a three-fold trigger. Its use helps to reduce the raw trigger rate due to accidental triggers caused by background-light fluctuations and provides a low time-jitter signal which is used to initiate signal integration by the ADCs.

Pattern Selection Trigger

As stated earlier, as part of the GRANITE III upgrade program a new trigger system was added to the Whipple telescope to further reduce the level of background events. This Pattern Selection Trigger (PST) uses the location of signals output from the CFDs to decide if the trigger is background related. While the multiplicity trigger will initiate recording if N tubes pass the CFD threshold, the PST requires that for these three tubes must be adjacent. The inclusion of the PST further reduces the number of accidental triggers, thus reducing the raw trigger rate and as a result the system may be operated at a lower CFD threshold. The Whipple telescope is operated using both triggers; the PST decides if an event should be recorded, while the multiplicity trigger decides when the recording should begin. A third type of trigger exists, known as the *pedestal* trigger, whereby the system is artificially triggered once every second, under the instruction of a GPS clock. These *pedestal* events are used for calibration and diagnostic purposes (Section 4.3.1).

Digitisation and Read-out

The outputs from the PST and multiplicity trigger are fed into the gate generator which is instructed to output a negative square pulse if the PST requirements are met. This pulse is transmitted to the ADCs via a discriminator which sets the width of the pulse to be approximately 25 ns. Although Cherenkov pulses are typically 5 ns in duration, their path through the electronics introduces some dispersion so that the pulse arriving at the ADCs is closer to 25 ns in duration, hence the rather large gate width. The signals from the amplifier (and the fibre-optic coupler) are synchronised, using delay cables, to arrive at the ADCs at the same time as the gate pulse, facilitating digitisation of the signals. The ADCs are 10-bit LeCroy 2249 modules, which integrate the signals over the duration of the gate (Figure 4.6).

When the integration of the signals by the ADCs is complete, data is transferred to the List Processor. The List Processor performs an important task by providing a buffer between the CAMAC crates and the DAQ computer. The List processor stores the output from the ADCs, as well as timing and singles rates information, until the DAQ computer is ready to begin read-out. The DAQ computer, a DEC VAX 4000-90, operating under VMS, receives this data from the List Processor, as well as tracking information (Section 4.2.4) from the tracking computer (via ethernet). All this data is archived for subsequent off-line analysis.

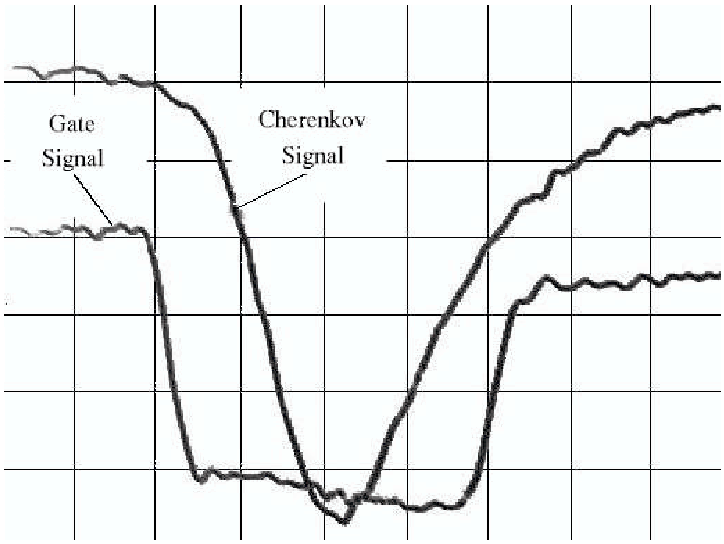

Figure 4.6: Digitisation of analogue signal. The amplified pulse from the PMTs is delayed so that it arrives in synch with the negative gate pulse. The pulse is integrated over the duration of the gate. Figure courtesy of Kildea (2002).

Timing

Timing is a critical feature of any observatory, whether it be for periodic analysis of sources, tracking sources across the sky, or collaborative observing campaigns. The Whipple telescope uses two independent GPS (Global Positioning Satellite) clocks to provide timing to an accuracy of 250 μs. The accuracy of the timing is further increased to 0.1 μs using a 10 MHz oscillator. On receipt of a signal from the trigger electronics, timing information is passed to the list processor. The output from the oscillator is also fed into two scalers. The first is activated at the beginning of each run and measures the elapsed time. The second is active only when the trigger gate is open and provides a measure of the live time of the system.

4.2.4 Tracking

Movement of the Whipple telescope is facilitated by an Alt-Azimuth mount, where each axis is controlled by an independent drive motor, of resolution 0.01°. The elevation of the telescope may be varied from 0° to 90° while the azimuthal range runs from 0° to 270° in both directions. The positioning of the telescope is independent of the DAQ system, rather it is controlled by a computer interface which sends instructions to the telescope drive controls via

fibre optic link. This link is also used by the telescope to send back diagnostic information, such as the altitude and azimuth of the telescope, to the tracking computer. The telescope control software consists of a number of complex tracking algorithms which, based on the local sidereal time (obtained from a remote Network Time Server) and the equatorial co-ordinates of a source, instruct the telescope to continually adjust its position so that it follows a source across the sky.

To limit the possibility of damaging the telescope and electronics, a system of safeguards is implemented to prevent the telescope from moving beyond its limitations. The system has two levels, the first of which is composed of a series of software limit switches. If the telescope is instructed to move beyond its limits, a program will intervene and instruct the drive controllers to stop moving. In the event of a software failure the second level system is implemented. This comprises a series of hardware switches, attached directly to the telescope drive, which prevent the telescope from moving beyond its range. In the event of a complete system failure, the telescope may be moved to the stow position manually.

Although tracking diagnostic information is provided, an independent check of the pointing accuracy of the telescope is carried out each night. These *pointing checks* involve pointing the telescope at a bright star and recording the anode currents of the central seven tubes. A perfectly pointing telescope will show a central tube recording the highest anode current, with some leakage into the surrounding six tubes. Any deviation in pointing will show up as a non-centralised anode-current distribution.

4.2.5 Calibration

To analyse data from any experiment it is necessary to have some measure of the performance of the instrument. The Whipple 10m telescope is a complex instrument, comprising numerous optical and electronic devices. To ensure a uniform response across the camera, and to monitor changes in the instrument over time, calibration data is vital. This data consists of two main types, *pedestals* and *gains*.

Pedestals provide a measure of the output of the ADCs corresponding to zero input. The ADC *pedestals* are typically set to 20 digital counts (d.c.), so that negative fluctuations in the night-sky background may be recorded. *Pedestal* events are initiated once every second, when the GPS clock artificially triggers the gate generator, and are tagged to distinguish them from real events. The mean of the *pedestal* distribution over the course of an observing run provides a measure of the *pedestal* value of the ADC, while the variance of the distribution is an accurate measure of noise due to

the night-sky background. The mean *pedestal* and *pedestal* variance form an important part of off-line analysis (Section 4.3.1).

Gains provide a means of measuring the response of the camera on a pixel-by-pixel basis. Although each PMT is set to a similar gain, small differences remain and must be accounted for during analysis of the data. The gains of the PMTs are measured at least once every night in what is known as a *nitrogen* run. This run lasts for approximately one minute, during which time a blue nitrogen arc lamp, located in the centre of the reflector, uniformly illuminates the camera. The high frequency lamp triggers the system a large number of times during the run and the data is subsequently used to calculate the gain of each PMT, relative to the mean gain of the camera as a whole. These gain values are applied during subsequent analysis of the data, in a process known as *flat fielding* whereby the output of each PMT is scaled by the appropriate gain value.

4.2.6 Monitoring

There are a number of other quantities which are regularly measured at the Whipple Observatory, including atmospheric conditions and anode currents. Due to the nature if the IACT, that is its use of the atmosphere as its detection medium, it is important to maintain a record of the conditions under which observations are made. Each night the atmospheric conditions are manually noted by the observer, with the quality of the atmosphere graded as A, B or C, corresponding to good, mediocre or bad weather. To provide a less subjective measure of the observing conditions a weather station and far-infrared (FIR) pyrometer were installed on-site in 2001. The weather station measures information such as wind speed, temperature and humidity, while the FIR pyrometer provides details on sky clarity by measuring the temperature of the night-sky (in the case of cloud cover the FIR pyrometer registers a rise in temperature). An optical CCD camera, mounted near the telescope focus box, is used for a number of tasks; it shows the presence of bright stars in the field of view, it provides a crude measure of atmospheric clarity and it may be used as an independent check of telescope pointing. Details of the FIR pyrometer and CCD camera are given in Dowdall (2003).

Aside from observing records, telescope monitoring has an important role to play in operational safety. For example, observing should not be carried out during high winds due to the size of the telescope structure nor should it take place when humidity is high, due to the high voltages involved. In addition, the presence of bright stars in the field of view are capable of damaging the camera. The CCD camera, with its wide field of view, provides the observer with an early warning of potential problems caused by bright

stars. As a further safety feature a graphical interface, providing information on the anode current of each PMT, is used to alert the observer to PMTs which are running high. In such cases the PMTs are switched off.

4.3 Standard Image Analysis Methods

The analysis methods applied to data recorded using the Whipple 10m telescope are numerous and varied, and subject to constant redevelopment (Badran, 2001a; Quinn and Moriarty, 2003) in an ongoing effort to increase selection efficiency and to account for changes in the instrument. Although these methods vary in some respect they are all based on four principle steps (Figure 4.7):

1. Image preparation
2. Image parameterisation
3. Gamma-ray selection
4. Signal calculation (including background estimation)

4.3.1 Image Preparation

Prior to parameterisation, an image must first be subjected to a number of calibration and cleaning processes. These preparatory procedures are employed to ensure a uniform response across the camera and to identify PMTs which contain genuine Cherenkov signals, whilst rejecting those containing light due to fluctuations of the night sky only. There are a number of stages involved in the preparation of an image:

Pedestal Subtraction

The ADCs (Section 4.2.3) are designed to handle positive signals only. Since the night sky background fluctuates both positively and negatively about some mean value, if one wishes to record negative fluctuations a small offset must be applied to the ADCs. This offset is known as the *pedestal* and is a measure of the ADC output corresponding to zero input stimulus. Before determining the true amount of light recorded by a PMT the *pedestal* must be calculated and then subtracted. *Pedestal* values are measured by artificially triggering the camera, approximately once per second, during the course of a normal observation run. The mean of the resulting pulse height distribution

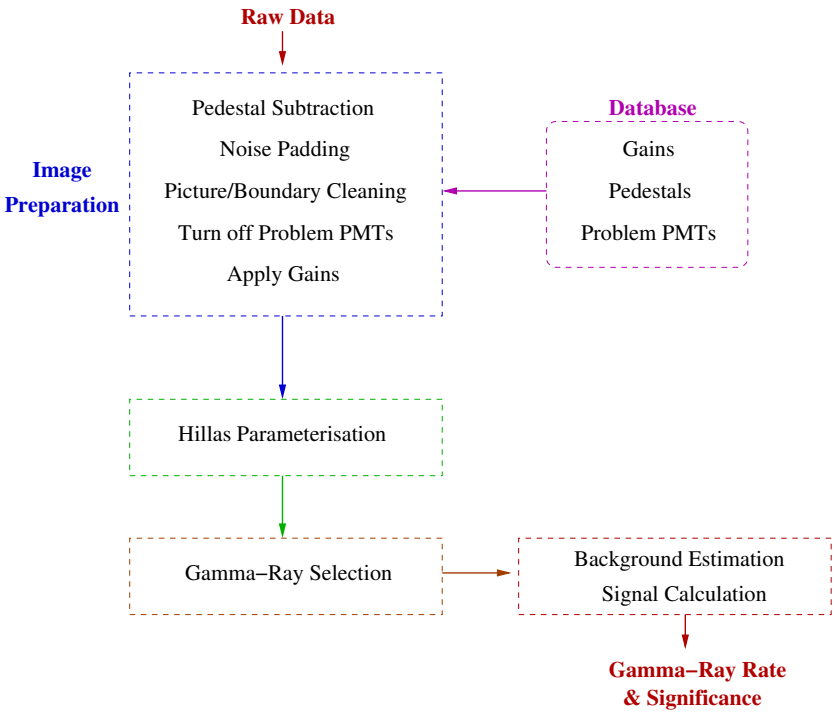

Figure 4.7: Flow diagram showing steps involved during analysis of Whipple IACT data. Although a number of variants on the standard analysis procedures exist they are all based on the above steps. In most cases the analyses differ only by the way in which one of the steps are applied. For example, in many cases, it is the gamma-ray selection techniques only that differ.

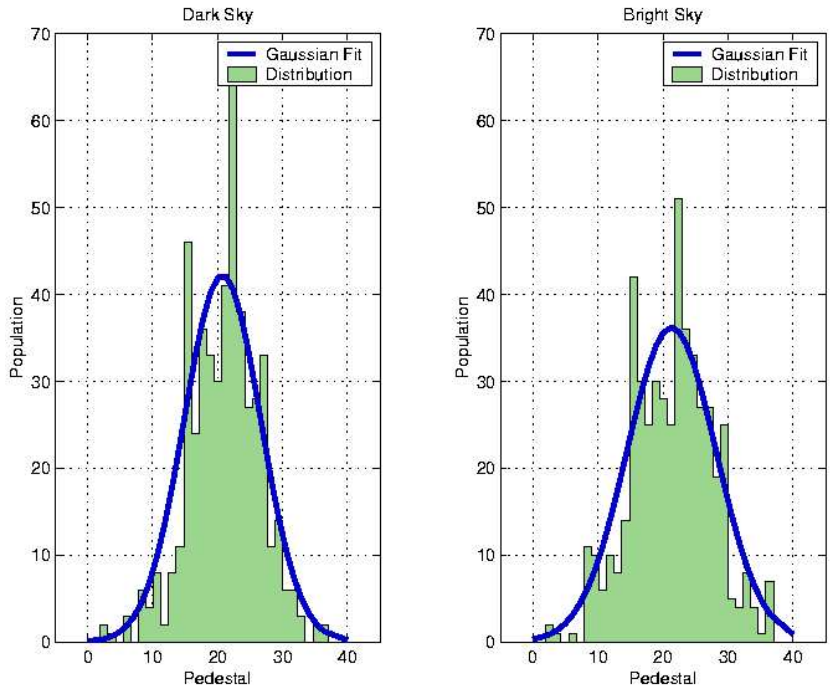

Figure 4.8: *Pedestal* distribution for a PMT pointed at a dark region of sky, compared to the distribution when pointed at a bright region of sky. The mean of the distribution is used as a measure of the ADC *pedestal* value, while the variance of the distribution is used as a measure of sky-brightness. The *pedestal variance* values are 5.2 and 6.6 for the dark and bright sky regions respectively, showing that the pedestal distribution is considerably wider in the case of the brighter sky. The *pedestal variance* is used at a later stage of the analysis to eliminate bias introduced by sky-brightness differences.

(Figure 4.8) is taken as the *pedestal* of the ADC, while the variance provides an accurate measure of the sky noise. Both the *pedestal* and *pedestal variance* may also be used for diagnostic purposes, with large values of either quantity indicating hardware problems or the presence of a bright star in the field of view. In such cases the signals in these PMTs are zeroed and play no part in subsequent analysis. An alternative approach to *pedestal* calculation, using genuine Cherenkov-triggered events may also be used (Fegan et al., 1994).

Image Cleaning

Each event recorded by the Whipple camera is made up of a number of pixels, some containing a mixture of background and genuine Cherenkov signals,

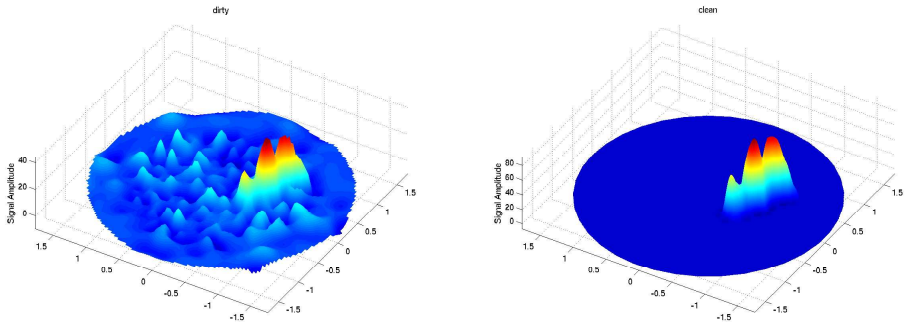

(a) Not cleaned **(b)** Cleaned

Figure 4.9: A typical event recorded by the Whipple telescope. The image on the left is before *picture/boundary* cleaning is applied and to the right is the image after cleaning. Cleaning is required to eliminate pixels whose signal results from sky noise only.

others constituting background light only. To eliminate these noise-induced signals from the overall image, a filtering process known as *picture/boundary* cleaning (Punch, 1991) is employed. For the signal in a PMT to be deemed as arising from a genuine Cherenkov pulse it must pass one of two criteria. The first requires that the signal amplitude is above some multiple of the *pedestal variance* for that tube and is known as the *picture* threshold. The second requires that the signal is greater than some lower-value multiple of the *pedestal variance* (the *boundary* threshold) and is adjacent to a PMT passing the first criterion. The signal in any PMT which fails the *picture/boundary* selection process is set to zero. Figure 4.9 shows a sample image, before and after cleaning has been applied, clearly indicating its success in removing unwanted noise. The standard, optimised *picture/boundary* values for the current camera configuration, in units of standard deviations, are 4.25/2.25.

Gain Application

The current camera configuration utilised by the Whipple 10m Telescope comprises 379 PMTs with individually adjustable gains. Although the high voltage supply to each PMT is manually set to provide a uniform response across the camera, small differences remain. To account for these differences the response of the camera is measured at the start of each night's observations, by means of a calibration or *nitrogen* run. A typical *nitrogen* run lasts for one minute, during which time the face of the camera is uniformly

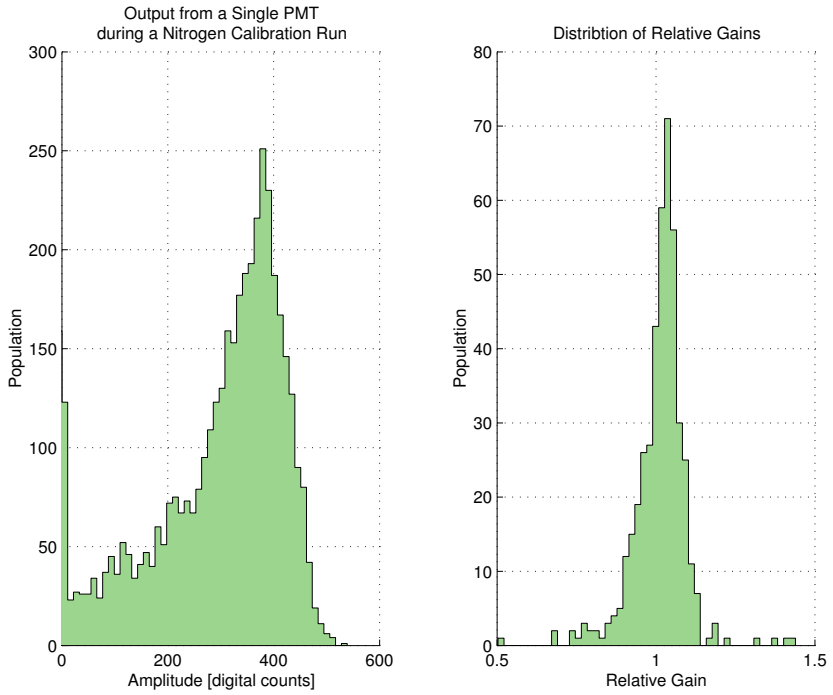

Figure 4.10: An example of data recorded during a calibration or *nitrogen* run at the beginning of a night's observations. The picture to the left shows the output from a single ADC. The mean of this distribution is calculated, taking care to eliminate signals that are too small or too large, and then compared to that of the camera as a whole, thereby calculating a relative gain value. The distribution of relative gains is shown in the plot on the right. Although the distribution is centred on one and ranges from 0.5 to 1.5 there are tubes with values outside this range (these are not shown here). Such tubes are deemed to be malfunctioning, and play no further part in image analysis.

illuminated by a fast Optitron arc lamp, which emits pulses of light similar to Cherenkov radiation. Data collected during this run are used to calculate a gain for each tube, relative to the mean gain of the camera as a whole (Figure 4.10). By adjusting the signal content of each PMT by these relative gain values a more accurate picture of the Cherenkov light incident on the camera is achieved. The gains may also be used for diagnostic purposes, whereby damaged PMTs show up as having wildly fluctuating values and are omitted from subsequent analysis. A second method by which the gains may be determined, using Cherenkov-triggered events, has been proposed by Fegan et al. (1994). The processes of *pedestal* subtraction and gain application are collectively known as flat fielding.

4.3.2 Image Parameterisation

Over 99 % of events recorded by IACT telescopes originate from non-gamma-ray events and are mainly due to hadrons, local muons and sky noise (Figure 4.11). Subtle differences in the Cherenkov images formed by gamma-ray-induced EAS, compared to those formed by the interaction of cosmic rays with the atmosphere or single local muons, make it possible to identify gamma-ray events amongst such a dominant background (Chapter 3). Where images of gamma-ray-induced cascades tend to be compact and aligned in the direction of the source, cosmic-ray-induced images are more diffuse and show no preferential arrival direction. To exploit these differences Hillas (1985) devised a moment fitting procedure, by which he defined a set of six parameters to describe the shape and orientation of an image. The original set of Hillas parameters are defined in Table 4.1 and shown in Figure 4.12. A full mathematical definition of each parameter is given in Appendix B.

4.3.3 Gamma-Ray Selection

By choosing an appropriate range of values for each Hillas parameter, it is possible to define a region in multi-dimensional parameter space where the majority of events are gamma-ray in origin (Figure 4.13). Using this approach Hillas defined specific ranges for each of the six parameters (or parameter cuts), where most gamma rays reside. By requiring that an event must fall into four of these domains to be deemed a gamma ray, Hillas predicted it would be possible to identify $\approx 60\,\%$ of gamma rays while rejecting over 98 % of background. Using a similar selection policy the discovery of the first TeV gamma-ray emitter was announced with the detection of the Crab Nebula in 1989 (Weekes et al., 1989). In attempts to increase efficiency and adapt to an evolving instrument, the original Hillas criteria have grown to include a number of new parameters and complementary selection cuts. These additional parameters are also given in Table 4.1. The most successful selection mechanism to date is *Supercuts* (Punch, 1991), a variant of the original Hillas procedure, and optimised using observations of the Crab Nebula. *Supercuts* has been used by the VERITAS Collaboration in the discovery of a number of new sources (Punch et al., 1992; Quinn et al., 1996; Horan et al., 2002; Holder et al., 2003) and has itself been subject to changes over the years to accommodate upgrades to the telescope. The *Supercuts* selection, as used throughout this work is outlined in Table 4.2.

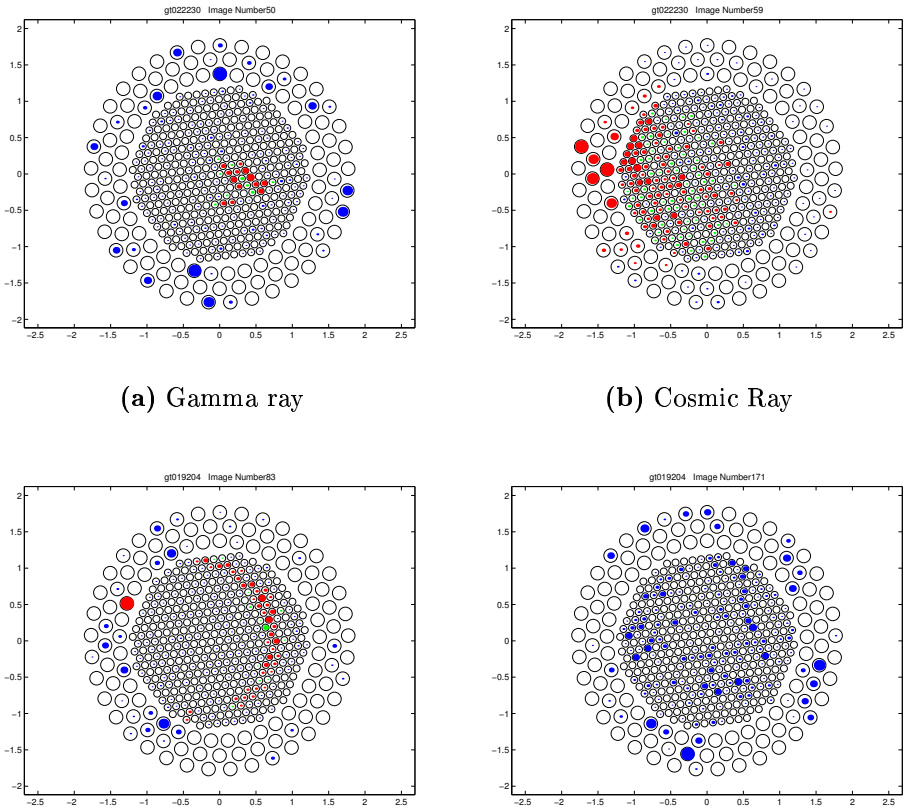

(a) Gamma ray

(b) Cosmic Ray

(c) Local Muon

(d) Sky noise

Figure 4.11: The four main types of images seen by an IACT telescope. To detect a gamma-ray signal, images formed by cosmic rays, local muons, and sky noise must be eliminated using off-line analysis.

Size	Total number of digital counts in all pixels which form part of the image; a rough measure of the energy of the progenitor gamma ray.
Frac 3 †	Fraction of total light in image contained in the three highest tubes; used to eliminate events caused by sky noise or by particles physically passing through the camera.
Length †	RMS spread of light along major axis of image; a measure of the shape of the image.
Width †	RMS spread of light along minor axis of image; a measure of the shape of the image.
Azwidth †	RMS spread of light perpendicular to the line connecting the image centroid with the centre of the field of view; a measure of the shape and orientation of the image.
Miss†	Perpendicular distance between the major axis of the image and the centre of the field of view; a measure of the orientation of the image.
Distance†	Distance between the image centroid and the centre of the field of view; a measure of the impact parameter of the particle cascade.
Alpha	Angle between the major axis of the ellipse and a line joining the centroid of the ellipse to the centre of the field of view; a measure of the orientation of the image.
Asymmetry	Measure of how asymmetric an image is. Gamma-ray images should be shaped like a tear drop, with their light distributions skewed toward their source position.
Max1, Max2, Max3	The signal amplitude in the highest three tubes. By requiring that these three tubes are above some preset threshold images due to sky-noise are eliminated.
Length/Size	Measure of the compactness of the image in relation to its total light content; used to eliminate background due to local muons.

Table 4.1: Original six Hillas Parameters (denoted †) plus additional parameters introduced to increase gamma-ray selection efficiency. Note that in original Hillas selection *frac3* was replaced by *frac2*, the fraction of total light in the image contained in the two highest tubes.

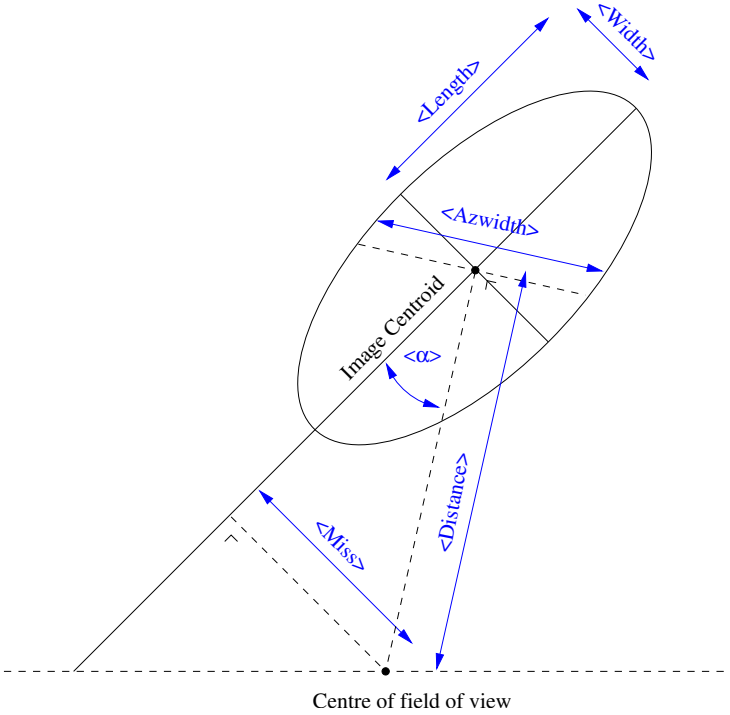

Figure 4.12: Geometrical definition of Hillas parameters. Figure courtesy of Dunlea (2001).

Parameter	Lower Bound	Upper Bound
Frac 3	-	0.98
Length	0.13°	0.25°
Width	0.05°	0.12°
Distance	0.4°	1.0°
Alpha	0°	15°
Max1	30 d.c.	-
Max2	30 d.c.	-
Max3	0 d.c.	-
Length/Size	-	4×10^{-4} °/d.c.

Table 4.2: *Supercuts* selection criteria. To be deemed as having a gamma-ray progenitor an image must pass all of the above selection cuts. These values are the standard *Supercuts* selection, as used throughout this work.

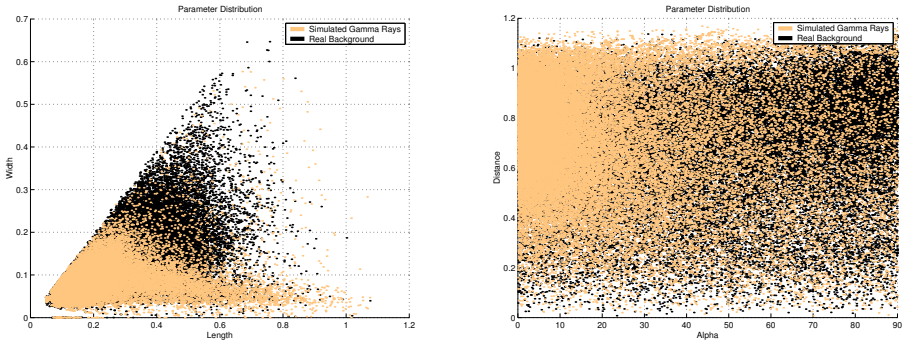

(a) *Length* / *Width* Space **(b)** *Alpha* / *Distance* Space

Figure 4.13: Distribution of image parameters for a simulated set of gamma-ray events and real background. It is clear that there are regions where the majority of events are gamma rays. By selecting events within a number of discrete parameter ranges it is possible to reject a majority of background and still retain a large percentage of real gamma rays.

4.3.4 Signal Estimation

The complex and indirect nature of the IACT means that it is never possible to identify gamma-ray events with 100 % certainty, one can only ever do so with a high level of confidence. The subtle nature of the differences between images formed by gamma-ray induced showers and those due to background mean that, in a large dataset, a number of events will be mistakenly classified as gamma rays. This fact needs to be accounted for when calculating the excess number of gamma rays in a dataset and requires accurate estimation of the number of misclassified events (this is the background). Accordingly, two observing strategies and complimentary analyses are traditionally employed: *ON/OFF* and *TRACKING*.

ON/OFF Mode

When operating in *ON/OFF* mode the telescope tracks the source of interest for approximately 28 minutes (this is the *ON* run). Allowing two minutes slew time, the telescope commences another 28-minute scan of a region of sky assumed to be gamma-ray dark, with azimuth and elevation identical to *ON* run, but offset by 30 minutes right ascension. This is the *OFF* run or experiment control. Using the *OFF* data the expected number of background events misclassified as gamma rays in the *ON* run may be estimated. A

gamma-ray signal is usually quoted in terms of the significance of the event excess above that expected due to statistical fluctuations in the background. Assuming a Poisson background distribution the gamma-ray significance is given by:

$$\sigma_{on/off} = \frac{N_{on} - N_{off}}{\sqrt{N_{on} + N_{off}}} \tag{4.1}$$

where N_{on} is the number of events passing selection cuts in the *ON* dataset and N_{off} is the number of events passing selection cuts in the *OFF* dataset. The associated gamma-ray rate and error, usually expressed in events per minute, is given by:

$$R_{on/off} = \frac{N_{on} - N_{off}}{t} \pm \frac{\sqrt{N_{on} + N_{off}}}{t} \tag{4.2}$$

where t is the time spent *ON*-source. When calculating the excess number of gamma-ray events in a dataset it is useful to examine the distribution of *alpha* for events passing all other selection cuts (except *alpha*). Because gamma rays are uncharged they should be aligned in the source direction and therefore have small values of *alpha*. For a real gamma-ray source the resulting *alpha* distribution should exhibit a clear excess of events at small *alpha*, while at larger values no excess should be evident. An example of an *alpha* distribution produced using observations of Markarian 421, while in a state of high emission, is shown in Figure 4.14. As expected there is a clearly visible excess of counts in the *ON* dataset at small *alpha* values. The agreement of the *ON* and *OFF* distributions at large *alpha* angles is also expected and lends confidence to the assumption that the number of background events in the *OFF* data is an accurate representation of the background level in the *ON*. In some cases this assumption may not be true. Although the *ON* and control data are recorded under identical atmospheric and instrumental conditions, the region of sky observed in each case is different. Because of this, bias may be introduced into the number of events identified as gamma rays in the *ON* and *OFF* datasets, meaning that the control may not provide an accurate measure of the level of background in the *ON* observations. To account for this possible source of error, when carrying out *ON/OFF* observations, an additional preprocessing step is applied.

Noise Padding

Noise padding is a process applied to data recorded in *ON/OFF* mode, in an attempt to compensate for possible bias in the selection of candidate gamma-ray events, caused by sky-brightness differences between the *ON*-source sky

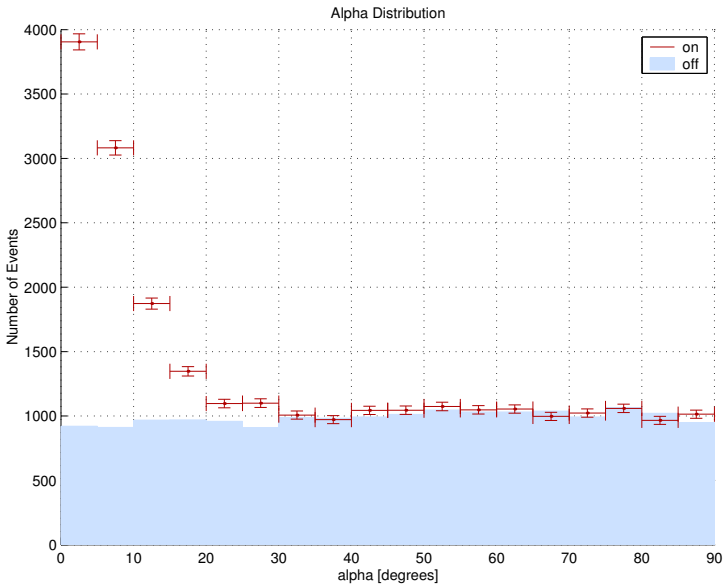

Figure 4.14: An *alpha* distribution, produced following observations of the BL Lac object Markarian 421 while in a period of high flux. A large signal excess is evident at small *alpha* values as expected, since gamma ray images point back toward the source. The closely matched *alpha* distributions of the *ON* and *OFF* data, beyond 20°, indicates that using the counts in the control run to estimate the background level in the *ON* run is a reliable approach.

region and control. Such differences may arise due to the presence of stars or diffuse photon fields in or around either field of view. This bias may be explained by considering what happens to *boundary* pixels when image cleaning is applied (Section 4.3.1). The pulse height spectra of *boundary* tubes (Figure 4.15) is asymmetrical, a combination of a Poisson noise distribution and Cherenkov component. For a tube with a low level of sky noise, the Cherenkov light dominates and, in most cases, this tube will pass *picture/boundary* cleaning. An increase in the noise level of a PMT increases the *boundary* threshold and makes it more likely that the Cherenkov component will be canceled out by a negative noise fluctuation. On average, compared to less-noisy PMTs, a greater number of these noisier PMTs fail the image cleaning process. Because this alters the shape of the image, a bias may be introduced into the number of events passing selection in the *ON* and *OFF* datasets. Problems of sky-brightness differences were recognised during the pioneering days of the first Cherenkov telescopes (Jelley, 1958; Fruin and Jelley, 1968), indeed attempts were made to negate the effect using padding lamps. Such cumbersome devices have long since fallen out of favour, however a new method based on similar principles has been developed. This approach, known as noise padding (Cawley, 1993), works by injecting noise in software to the data on a tube by tube basis, so that channels in the *ON* and *OFF* runs have similar noise levels. Using the *pedestal variance* as a measure of the noise level in a tube (Section 4.3.1), and assuming that the distribution of sky noise is perfectly Gaussian, the signal (S) recorded by a PMT may be described by:

$$S = P + \sigma G_{0:1} + C + \sqrt{C}\, G_{0:1} \tag{4.3}$$

where P is the mean ADC *pedestal*, σ is the *pedestal* deviation, C is the Cherenkov component of the signal and $G_{0:1}$ is a random number drawn from a Gaussian distribution of zero mean and unit variance. The element of the signal due to noise for *ON* and *OFF*-source observations are:

$$\eta_{on} = \sigma_{on}\, G_{0:1} \tag{4.4}$$

and

$$\eta_{off} = \sigma_{off}\, G_{0:1} \tag{4.5}$$

Considering the case of a single PMT which observes a region of sky that is brighter during the *ON*-source observations than during the *OFF*-source observations (and therefore η_{on} is greater than η_{off}) the amount of additional noise (η_+) injected into the PMT signal is given by:

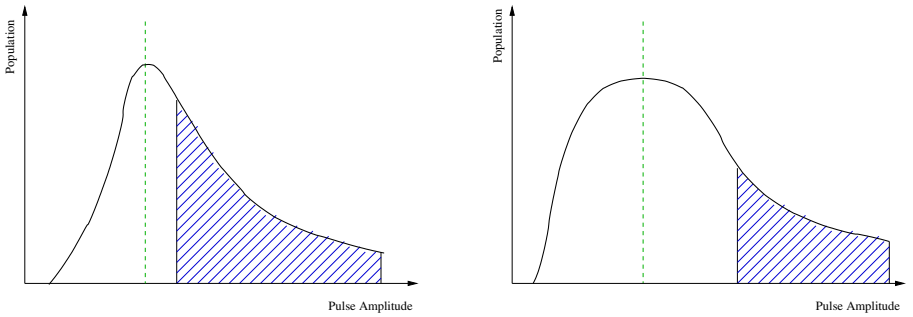

(a) Low noise level **(b)** High noise level

Figure 4.15: Pulse Height Spectra of noise-dominated pixels, showing the effect of noise on tubes passing *picture/boundary* cleaning. As the level of noise in a tube increases so does the cleaning threshold. As a result, a *boundary* tube observing a bright region of sky will fail the cleaning process more often than the same tube observing a dark region of sky. This is shown by the shaded area, which is greater for low noise than high noise. Noise padding is applied to counteract this effect, which has consequences when estimating background. Figure is adapted from Cawley (1993) and distribution shapes are exaggerated for clarity.

$$\eta_{+} = \sqrt{\eta_{on}^2 - \eta_{off}^2} \tag{4.6}$$

so that

$$\eta_{on^2} = \sqrt{\eta_{off}^2 + \eta_{+}^2} \tag{4.7}$$

This gives an *OFF* signal of the form:

$$S_{off} = P_{off} + \sigma_{off}\, G_{0:1} + \eta_{+}\, C_{off}\, G_{0:1} + \sqrt{C_{off}}\, G_{0:1} \tag{4.8}$$

To demonstrate the effectiveness of noise padding, a test was performed using 18 control runs. The data was divided into two subsets, namely the *ON* and *OFF* datasets, and analysed in *ON/OFF* mode. The pairs were chosen so that the conditions under which they were recorded were as similar as possible (similar in elevation, atmospheric conditions, and recorded on the same night). In addition the *ON* dataset was chosen to have, on average, 20 % more sky-noise than the *OFF* dataset. The resulting *alpha* distributions (Figure 4.16), without and with noise padding applied, show the importance of the procedure. When noise padding is not used, the number of events

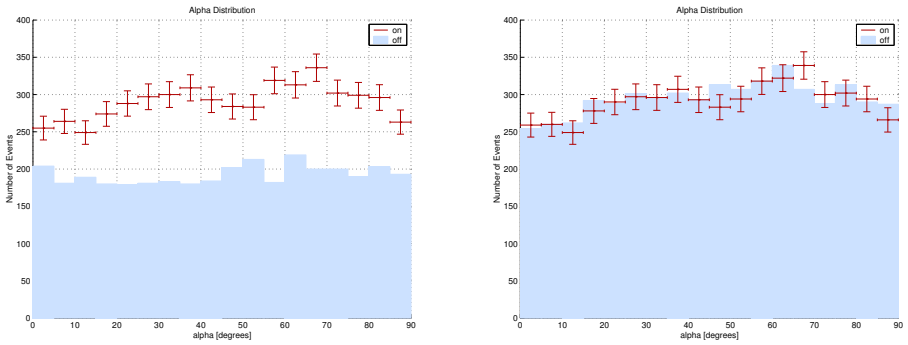

(a) Noise Padding not applied **(b)** Noise Padding applied

Figure 4.16: Effect of noise padding on data taken from two regions of sky with gross brightness differences. The data was specifically chosen so that the *ON* dataset comprised runs taken from a region of sky with 20 % more noise than the *OFF* dataset. The mean pedestal variance was used to characterise the brightness. All data used here is *OFF* data, with each pair taken from the same night.

passing selection in the *ON* and *OFF* datasets differs greatly. If the gamma-ray excess was calculated for this dataset a strong signal would result. This is clearly incorrect, since all data used was recorded on gamma-ray-dark sky regions. Following application of noise padding the number of events in both distributions is very similar and, as expected, there is no excess of events at low values of *alpha*. An alternative approach to noise padding, using noise drawn from a Poisson distribution is currently under investigation (O'Neill, 2004; Power-Mooney, 2004).

TRACKING Mode

Although *ON/OFF* analysis has proved to be extremely reliable, and has been used in the detection and study of a number of sources, it is not without its disadvantages. The requirement of independent control data for each *ON* observation means that time spent observing sources is reduced by 50 %. This is far from ideal, especially considering the low duty-cycle ($\approx 10\,\%$) of Imaging Atmospheric Cherenkov telescopes. In addition, to study the temporal characteristics of VHE sources, continuous observations are required but are not possible when using the *ON/OFF* approach.

In an attempt to increase time spent *ON*-source an alternative mode of operation is used. This *TRACKING* mode (Horan, 2001) involves observing

a source for as long as desired (in 28 minute scans), without recourse to *OFF* observations. The subsequent analysis does not require an *OFF* run for background estimation, rather the background is estimated using the *ON* data itself in conjunction with control data recorded for other sources. This is possible due to the fact that the distribution of the parameter *alpha* is independent of gamma-ray source beyond approximately 20°. In other words an *alpha* distribution of events recorded while pointing at a gamma-ray source and an *alpha* distribution of events from a similar region of sky that is gamma-ray dark are comparable beyond 20° (Figure 4.14). If the ratio of the number of events in the 20° to 65° region to the number of events in the 0° to 15° region, the *tracking ratio*, is known in the absence of a gamma-ray signal, the expected number of background events in the 0° to 15° region of the *ON* run may be calculated using the number of events in the 20° to 65° region of the same run. This approach is predicated on the shape of the *alpha* distribution being stable for different sky-brightness fields and over the course of an observing season (in the absence of a gamma-ray source). Although independent control data is not required for each *ON*-source observation *OFF* data is still necessary. Using a large number of *OFF*-source observations the shape of the *alpha* distribution is characterised by calculating the aforementioned *tracking ratio*. The *tracking ratio* (ρ) and its associated statistical error is given by:

$$\rho \pm \Delta\rho = \frac{N_{0-15}}{N_{20-65}} \pm \sqrt{\frac{N_{0-15}}{N_{20-65}^2} + \frac{N_{0-15}^2}{N_{20-65}^3}} \tag{4.9}$$

where N_{0-15} is the number of events in the *OFF* data set with *alpha* values between 0° and 15° and N_{20-65} is the number of events in the 20° - 65° region. Using this approach to background estimation, the signal excess (in terms of standard deviations above background) and gamma-ray rate are:

$$\sigma_{track} = \frac{N_{0-15} - \rho N_{20-65}}{\sqrt{N_{0-15} + \rho^2 N_{20-65} + (\Delta\rho)^2 N_{20-65}^2}} \tag{4.10}$$

and

$$R_{track} = \frac{N_{0-15} - \rho\, N_{20-65}}{t} \pm \frac{\sqrt{N_{0-15} + \rho^2 N_{20-65} (\Delta\rho)^2 N_{20-65}^2}}{t} \tag{4.11}$$

In recent years, the stability of the *tracking ratio* for different sky regions and over the course of a season has been called into question. Early results (Quinn et al., 2001; de la Calle Perez and Holder, 2001) indicate that the

shape of the *alpha* distribution in the absence of a gamma-ray source may not be consistent. This issue is discussed in detail in Section 5.6.

4.4 Upper Limits

In the case of an analysis producing a non-detection it is possible to impose upper limits on the number of gamma rays coming from a particular source. In this work counts upper limits are calculated using the method of Helene (1983), then converted to an upper limit in terms of the Crab Nebula flux, using the method of Aharonian, and finally converted to a flux upper limit by assuming a Crab Nebula like spectrum. The Helene method calculates the probability density function of the number of source events based on the number of events in the *ON* and *OFF* data. Using the probability density function it it possible to determine the maximum number of events coming from the source with a given confidence level, assuming statistical fluctuations only (Figure 4.17). In practice the counts upper limit is calculated by numerically solving the equation:

$$\alpha = \frac{I\left(\frac{N_{ul}-N}{\sigma}\right)}{I\left(\frac{-N}{\sigma}\right)} \tag{4.12}$$

where α is the desired confidence level, N_{ul} is the counts upper limit, N is the excess number of events, σ is the background number of counts and I(z) is the error function:

$$I(z) = \frac{1}{2\pi}\int_z^\infty e^{\frac{-x^2}{2}}\,dx \tag{4.13}$$

To convert the counts upper limit to a flux upper limit an intermediate step is applied whereby the counts upper limit is converted to an upper limit in terms of the Crab Nebula flux. Using the method of Aharonian et al. (2000) a lower limit on the number of events coming from the Crab Nebula (MIN_c) is calculated using contemporaneous Crab Nebula observations. The source upper limit in counts (MAX_s) is converted to an upper limit in terms of the Crab Nebula using:

$$UL_s = \frac{MAX_s}{MIN_c}\cdot\frac{t_c}{t_s} \tag{4.14}$$

where t_c and t_s are the number of hours spent observing the Crab Nebula and the source respectively. Finally this upper limit is converted into an absolute flux above the energy threshold of the telescope by assuming a Crab Nebula like spectrum:

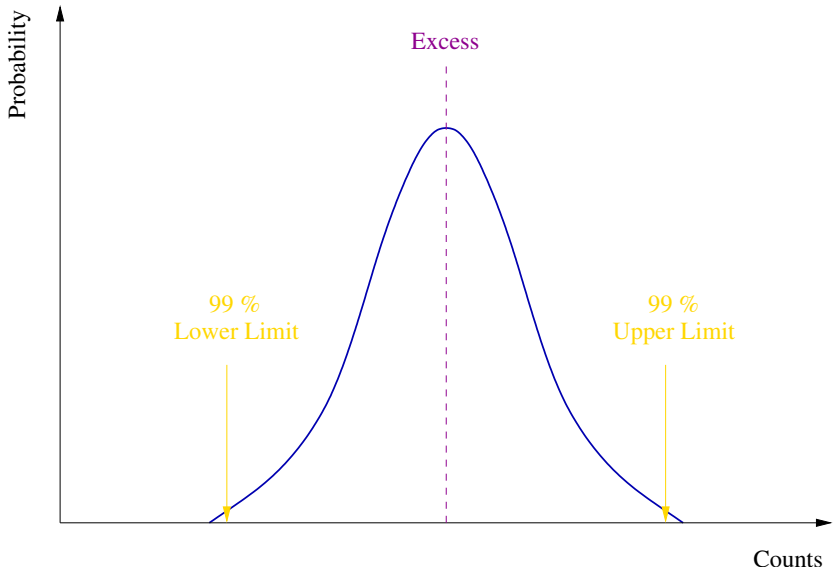

Figure 4.17: Explanation of upper limit calculations using the method of Helene (1983). By estimating the probability density distribution of an excess of counts it is possible to calculate the maximum (or minimum) number of counts that is statistically equivalent to the excess, at a desired confidence level. Here the 99 % upper limit and 99 % lower limit are shown for a sample excess. The 99 % lower limit is equal to the 1 % upper limit.

$$UL_{abs} \;=\; UL_s \,.\, F_c\,(>\, E_{th}) \tag{4.15}$$

where $\mathrm{F}_c\,(>\, E_{th})$ is the Crab Nebula integral flux above the energy threshold of the telescope (E_{th}). A detailed discussion of the Whipple telescope energy threshold is reserved for Section 5.4. The Crab Nebula flux is calculated using:

$$F_c\,(>\, E_{th}) \;=\; \alpha \,.\, \int_{E_{th}}^{\infty} E^{-\gamma}\, dE \tag{4.16}$$

where α is the flux constant and γ the spectral index of the Crab Nebula as quoted by Hillas et al. (1998).

There are alternative methods for calculating flux upper limits based on the effective collection area of the detector (Lessard, 1996), however these methods rely on detector simulations. The disadvantage of such an approach is that observations carried out under different conditions require their own simulations. By using appropriate Crab Nebula observations, to convert the counts upper limit to a flux upper limit, changes to the instrument, variable weather and elevation effects are accounted for.

4.5 Summary

During this chapter an overview of the Whipple approach to recording and analysing IACT data has been presented. As part of the description, the design and characteristics of the detector have been discussed including the optical reflector, camera, data acquisition system, telescope control and diagnostic subsystems. The standard approach to data analysis as used by the VERITAS Collaboration has been presented, divided into its logical steps which include image preparation, image parameterisation, gamma-ray selection and signal calculation. Although the analysis detailed has proved a great success there are a number of disadvantages associated with it, including bias against low and high energy events and possible bias in background estimation. In an attempt to address these issues a number of new techniques have been developed aimed at selecting lower-energy gamma rays and providing an alternative to background estimation. The development of these techniques are discussed in the next chapter.

Chapter 5

Alternative Data-Analysis Methods

5.1 Introduction

The standard analysis methods, as used by the VERITAS Collaboration, have proved a great success, with detection of a number of cosmic point sources of gamma rays (Weekes et al., 1989; Punch et al., 1992; Quinn et al., 1996; Horan et al., 2002; Holder et al., 2003). This is not to say that the methods are perfect; on the contrary there are a number of undesirable features. One of the major disadvantages of the analysis is the limits imposed by the gamma-ray selection, *Supercuts*. Although *Supercuts* was specifically designed with source detection in mind it may not be ideal when searching for certain types of sources, due to its bias against events of low and high energy. It is conceivable that a number of sources may have steeply falling emission spectra or low-energy cut-offs, in which case the majority of their output would occur in an energy domain below the threshold of *Supercuts*. Additionally, this work is concerned with a search for extragalactic sources of gamma rays, whose gamma-ray emission is expected to be attenuated by intergalactic photon fields. Since the level of absorption is predicted to increase with energy, a decrease in the analysis energy-threshold could prove beneficial in terms of source detection. The second major issue with the current analyses is the method by which background is estimated. As stated earlier (Section 4.3.4) there are two commonly used approaches, corresponding to observations taken in *ON/OFF* or *TRACKING* mode. The relative merits of each method have been discussed but more recently the stability of the *TRACKING* approach has been called into question (Quinn et al., 2001; de la Calle Perez and Holder, 2001; de la Calle Perez, 2003)).

This chapter details the development of new gamma-ray selection and background estimation techniques. In an attempt to lower the energy threshold of the detector-analysis system, two new selection methods have been developed and tested rigorously. The first, known as *Minicuts*, has been designed to be sensitive to gamma-ray images in a *size* domain below that in which *Supercuts* is most efficient. The second technique, known as *Kernel* multivariate analysis, has already been shown to outperform traditional box selection methods at low and high energy. Further development of this method, aimed specifically at increasing sensitivity to lower-energy gamma rays, is detailed. In an attempt to address the issue of instability in *TRACKING* analysis a number of tests are performed to determine the constancy of the *tracking ratio*. In addition a third and alternative method for background estimation is presented and tested for evidence of instability.

5.2 *Minicuts*

One of the most important additions to the *Supercuts* selection was the so called *length/size* cut. Introduction of this cut to data recorded with the earlier vintage, 109 pixel camera was shown to enhance selection efficiency (Catanese et al., 1995). *Length/Size* is designed to reject background images caused, primarily, by single local muons. The images formed by muons tend not to be very intense because their light comes from a single particle, and so muon images have low light content per unit pixel (Figure 5.1). Although low-energy gamma rays and short muon arcs are virtually indistinguishable, it is possible to greatly reduce the muonic component of background by rejecting images with large values of *length/size*. Application of the *length/size* cut is not without disadvantage, namely elimination of a large number of low-energy gamma rays and the introduction of an energy threshold which is difficult to interpret (Figure 5.2). With this in mind, attempts were made to design a new set of parameter cuts, aimed specifically at identifying low-energy events which *Supercuts* traditionally discards. This selection is known as *Minicuts*.

5.2.1 Data Selection

It was decided that *Minicuts* would be an empirical selection, based on a database where there was a definite low-energy gamma-ray signal present. The presence of a low-energy signal was assumed on the basis of a measured signal at higher energies. The dataset used comprised observations taken over three contiguous nights, in 2001, during a strong Markarian 421

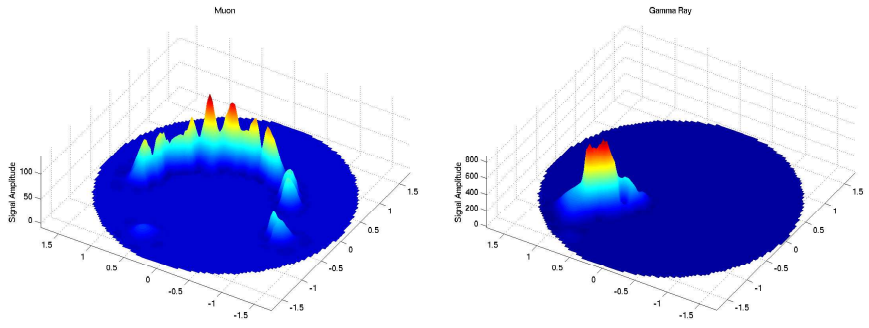

(a) Muon **(b)** Gamma Ray

Figure 5.1: The image formed by a local muon has low light content per unit pixel, compared to that of a gamma ray. By applying an appropriate *length/size* cut it is possible to reject a large percentage of muon events. The downside to this process is that a large number of low-energy gamma-ray candidates are also rejected. Note different scales on axes.

flare. Observations were made in *TRACKING* mode, but rather than use the standard approach to analysing this data, *matched analysis* was used (Section 5.7). Each chosen file exhibited at least a $10\,\sigma$ excess following *Supercuts* selection. The list of data files used are given in Table 5.1.

5.2.2 Development of Cuts

The dataset was first subjected to standard calibration and cleaning procedures, and then parameterised. At this point the data was divided into two subsets corresponding to: (a) those events with *size* less than 450 d.c. and (b) those events with *size* greater than 450 d.c.. The 450 d.c. boundary was chosen to minimise overlap between events chosen by the new selection and standard *Supercuts*. Only events below this boundary were used to develop the new cuts. To determine if a gamma-ray excess was present in the *ON* data, parameter distributions for both the *ON* and *OFF* datasets were constructed and compared. These distributions, shown in Figure 5.3, illustrate that an excess number of events exists in the *ON* dataset and that this excess is confined to specific ranges. In the case of the *length* parameter the majority of the excess occurs in a range between $0.1\,^\circ$ and $0.3\,^\circ$, while for *width* the excess falls between $0.6\,^\circ$ and $0.14\,^\circ$. The *alpha* distribution exhibits a clear excess at low values which is encouraging as real gamma rays should be aligned in the source direction. For *distance* an excess is evident, however

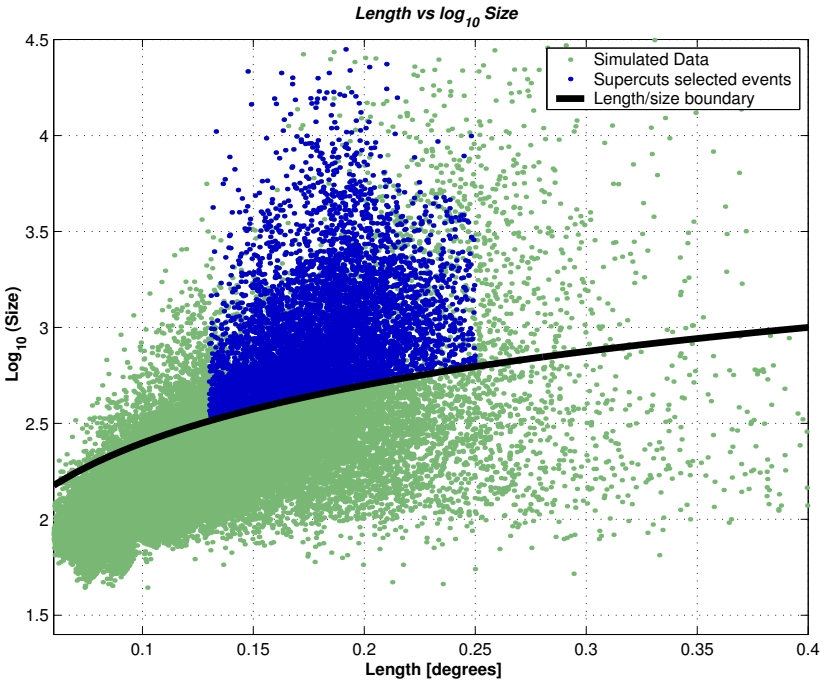

Figure 5.2: Effect of application of *length/size* cut on *Supercuts* selection of simulated gamma-ray data (Section 5.3.1). *length/size* creates a threshold, below which no gamma rays are selected. Although this increases efficiency at higher energies, it has a possible detrimental effect when searching for emission from sources with steeply falling spectra.

Date	*On Run*	*Off Run*	*Nitrogen Run*	Excess	Rate (min^{-1})
010325	17551	17556	17547	$13.53\,\sigma$	10.97 ± 0.81
010325	17552	17557	17547	$12.69\,\sigma$	10.38 ± 0.82
010325	17553	17558	17547	$11.21\,\sigma$	9.51 ± 0.85
010325	17554	17559	17547	$15.75\,\sigma$	14.63 ± 0.93
010326	17574	17577	17565	$10.07\,\sigma$	8.23 ± 0.82
010326	17575	17579	17565	$10.62\,\sigma$	9.42 ± 0.89
010327	17593	17560	17585	$14.20\,\sigma$	12.9 ± 0.91
010327	17594	17561	17585	$15.74\,\sigma$	14.84 ± 0.94

Table 5.1: List of files used during development of *Minicuts*. *OFF* data used is taken from other sources and matched to the *ON* data. *OFF* data includes *ON* data from other sources, where there was no signal present.

Parameter	Lower Bound	Upper Bound
Length	0.10	0.25
Width	0.07	0.13
Distance	0	1.1
Size	0	450
Alpha	0	50
Frac3	-	0.98
Max1	0	-
Max2	0	-
Max3	0	-
Length/Size	-	-

Table 5.2: Initial set of crude parameter cuts, used to determine if it was possible to extract a significant excess of gamma-ray events from a set of data, in the lower-*size* range. Using these cuts an excess of 6.2 ± 1.1 min^{-1}, corresponding to a significance of $5.4\,\sigma$, was obtained showing the potential of the new selection. The associated *alpha* distribution is shown in Figure 5.4.

it does not appear to be confined within a specific range. Based on these regions of excess a crude set of parameter cuts was chosen (Table 5.2) and re-applied to the data, yielding a statistically significant excess of $5.4\,\sigma$ and suggesting that a search for a gamma-ray signal in this lower-energy region is worthwhile.

There still remained a possibility that the observed excess may be due to events which *Supercuts* normally picks up. To test this, *Supercuts* was applied to the original dataset (i.e. before it was sub-divided) and to the subset containing events with *size* greater than 450 d.c.. The results, presented in Table 5.3, show that addition of a lower-*size* cut to *Supercuts* reduces the number of events passing selection, as indicated by a decrease in rate. This proves that *Supercuts* is capable of selecting a number of events below the 450 d.c. boundary. However, the fact that there is no decrease in significance when the lower-*size* cut is applied (in fact there is a small increase) implies that *Supercuts* is not particularly sensitive to gamma-ray events of small *size*. The implication is that by applying *Minicuts*, it is possible to extract a gamma-ray excess in addition to that of *Supercuts*.

5.2.3 Optimisation

Confident that *Minicuts* was capable of distinguishing gamma-ray events of small *size*, the next step was to maximise efficiency of selection by perform-

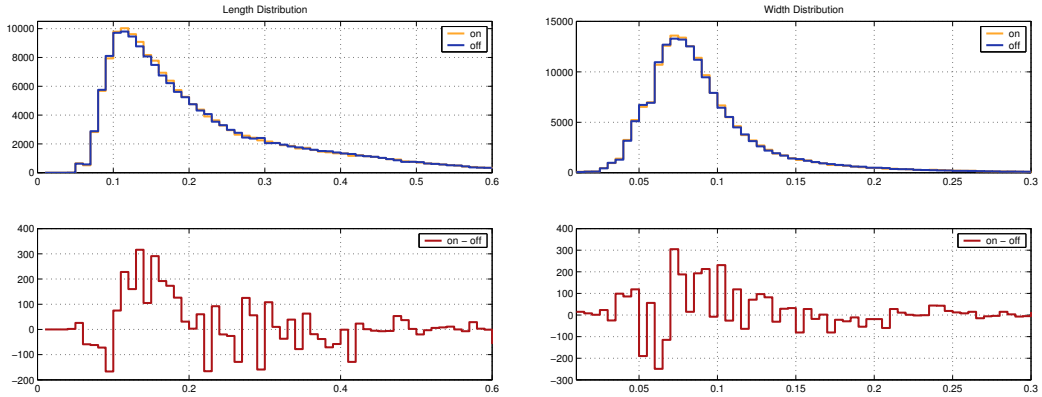

(a) Length

(b) Width

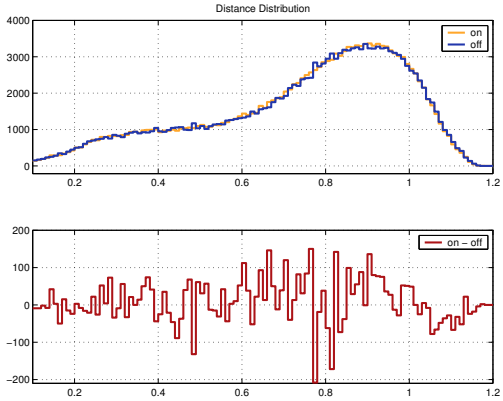

(c) Distance

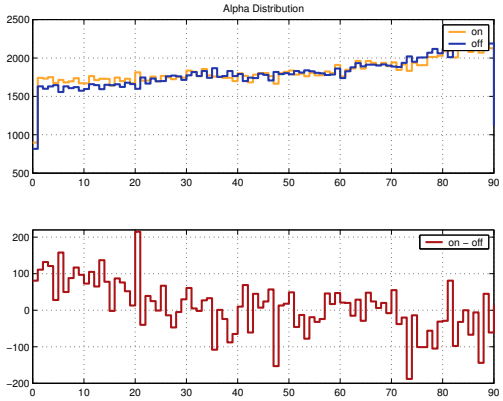

(d) Alpha

Figure 5.3: Parameter Distributions of events passing *picture/boundary* cleaning. The plots show the *ON* and *OFF* distributions and the *ON*-*OFF* distribution for four Hillas parameters. The distributions were used to: (1) determine if there was an excess of gamma-ray events in this small-*size* dataset and (2) determine the approximate regions of parameter space in which the excess occurs. It is clear that there is an excess of gamma-ray candidates in the *ON* data and that this excess lies in a specific region. The implication is that by selecting events within this region, it should be possible to extract a statistically significant gamma-ray signal.

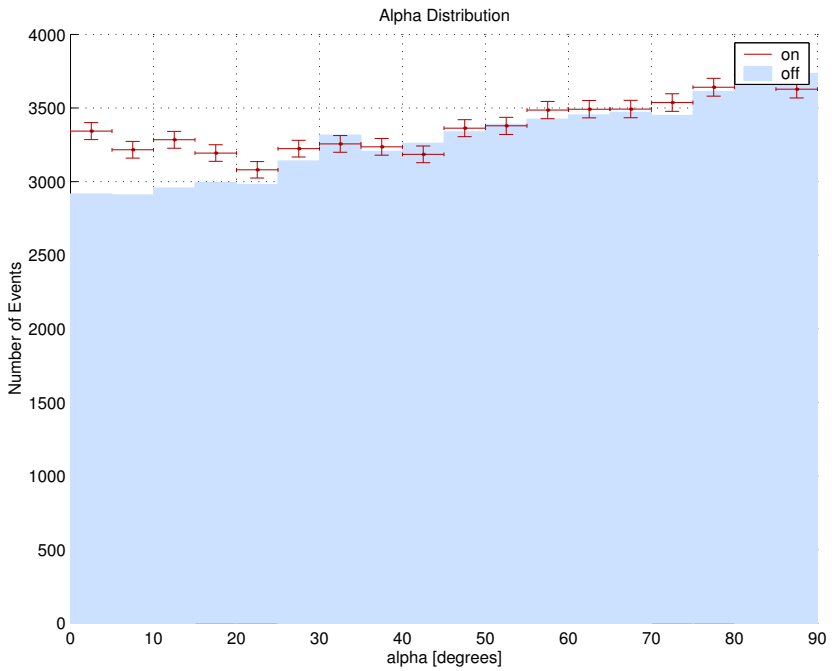

Figure 5.4: Early indication of potential of *Minicuts*. Using a crudely devised set of parameter cuts it is evident that an excess of gamma rays may be identified in the data.

Dataset	N_{on}	N_{off}	Excess	Rate (min^{-1})
All	3538	1052	$36.69\,\sigma$	11.29 ± 0.31
Subset†	2987	703	$37.60\,\sigma$	10.37 ± 0.28

Table 5.3: Results of applying *Supercuts* to the entire dataset and to those events with *size* $\geq$ 450 d.c.. The fact that there is no decrease in excess indicates that *Supercuts* has limited sensitivity below 450 d.c. and implies the *Minicuts* selection is sensitive to gamma-ray events in a region where *Supercuts* is not († Subset contains only those event with *size* $\geq$ 450 d.c.).

ing an optimisation. The optimisation comprised three iterations; in the first pass four parameters, *length*, *width*, *distance* and *alpha*, were optimised. During this process the bounds on each parameter were varied over a wide range (Table 5.4) while all other cuts were held constant at some predetermined set of values (Table 5.4). By plotting the gamma-ray significance and rate as a function of parameter bound, the most efficient cuts were identified.

Results of the first-pass optimisation are shown in Figure 5.5. In general the optimal values were chosen as those yielding a high gamma-ray significance and rate. In the case of *length*, significance increases as the lower bound is relaxed, reaching a maximum around 0.11° before dropping off. The gamma-ray rate is also close to its maximum value at this point, thus a lower bound of 0.11° was chosen. For the *length* upper bound the optimal value was chosen as 0.22°, corresponding to a stable peak in significance. Although an increased rate and similarly high significance is achievable by relaxing the upper bound further, the significance is not as stable in this region. As a result an upper bound of 0.22° was deemed most appropriate. When varying the *width* lower bound the significance rises to a maximum, levels off and then decreases slightly. The optimal value was chosen as 0.06°, the midpoint of the maximum plateau, which also yields a high rate. The *width* upper bound was chosen as 0.11°, corresponding to the point of maximum significance and maximum rate. In the case of the *distance* lower bound, significance and rate are maximum in a region centred on 0.5°, thus this was chosen as the optimal value. For the *distance* upper bound the excess increases sharply up to 1.0°, after which it levels off. Although loosening the upper bound further has no adverse effect on significance there is nothing to be gained in terms of increased rate, and images close to the edge of the camera tend to suffer from truncation. For these reasons the upper *distance* bound was set to 1.0°. In the case of *alpha* the most suitable choice of upper bound is not clear because of fluctuations in significance. The peak of the distribution occurs somewhere between 15° and 25°, so any value from within this range is appropriate. To obtain a high rate the *alpha* upper bound was set equal to 22°. A summary of the first-pass optimisation is given in Table 5.4.

Following completion of the initial optimisation a second pass was performed to optimise the remaining parameters; *size*, *max1*, *max2*, *max3* and *length/size*. Using an approach similar to that of the first-pass process, each parameter bound was varied individually while all others were held fixed at some predetermined set of values. In the case of *length*, *width*, *distance* and *size* these were held constant at their optimal values as determined during the first optimisation. The *"loose bounds"* applied to the other parameters are detailed in Table 5.5. The results of the optimisation are shown in Fig-

Parameter	Loose Bounds		Optimisation Range		Optimum Values	
	lower bound	upper bound	lower bound	upper bound	lower bound	upper bound
Length	0.08	0.25	0.05 - 0.15	0.15 - 0.30	0.11	0.21
Width	0.05	0.15	0.03 - 0.10	0.08 - 0.16	0.06	0.11
Distance	0.3	1.2	0.3 - 0.7	0.6 - 1.2	0.5	1.0
Alpha	0	40	–	10 - 50	–	22
Size	0	450	–	–	–	–
Max1	0	–	–	–	–	–
Max2	0	–	–	–	–	–
Max3	0	–	–	–	–	–
Length/Size	–	–	–	–	–	–

Table 5.4: Summary of first-pass optimisation procedure. The *"loose bounds"* column corresponds to the values at which all other parameters were set during the optimisation of each individual bound. The *"optimisation range"* column gives the range over which each bound was varied during optimisation. The *"optimum values"* column correspond to the bounds chosen to a obtain high gamma-ray significance and rate. The choice of these values is discussed in detail in the text. Parameters optimised during this first-pass process are highlighted in red.

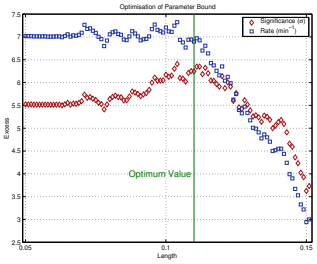

(a) *length* - lower bound

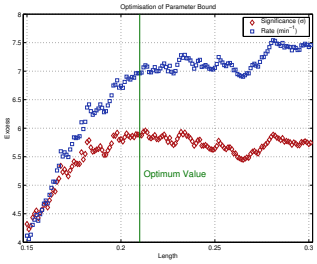

(b) *length* - upper bound

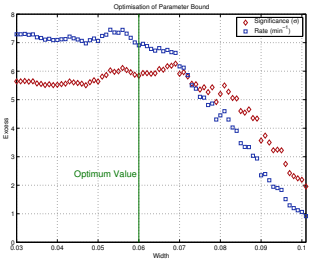

(c) *width* - lower bound

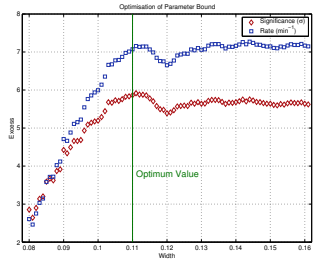

(d) *width* - upper bound

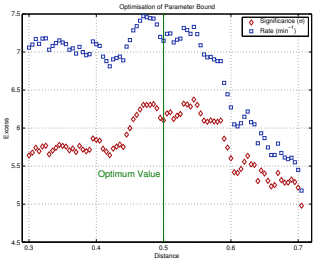

(e) *distance* - lower bound

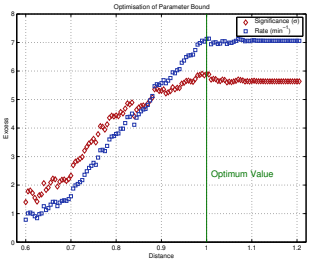

(f) *distance* - upper bound

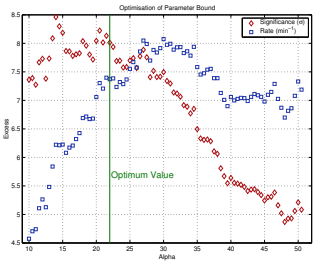

(g) *alpha* - upper bound

Figure 5.5: Plots used during first-pass optimisation of *Minicuts*. In general optimal values were chosen as those yielding maximum significance and rate. For a detailed discussion of the values chosen see text.

ure 5.6 where, as in the case of the first-pass process, the optimal bounds were chosen as those yielding maximum significance and rate. For the *size* parameter, significance changes very little as the lower bound is relaxed. Above 150 d.c. there seems to be a trend toward marginally higher significance; however, this is counter-balanced by a falling rate. As a compromise between maximum significance and high rate a lower *size* bound of 205 d.c. was chosen. Somewhat expectedly, as the upper *size* bound is raised both significance and rate increase sharply, reaching a maximum at 450 d.c.. This implies that *Minicuts* is sensitive to events with *size* greater than 450 d.c.; however, because this would result in overlap with *Supercuts*-selected events the upper bound was left unchanged at 450 d.c.. In the case of *max1*, as the lower bound is decreased the significance grows, peaking between 30 and 40 d.c., before settling down to a steady value. To obtain a high rate the optimal bound was set to 33 d.c.. The inclusion of a cut based on *max2* and *max3* seems to be of no benefit, thus both were set to zero. For *length/size* significance increases sharply, reaching maximum between 6×10^{-4} and 8×10^{-4}, before decreasing by a small amount. The optimal value was chosen as 7.5×10^{-4} which results in maximum significance and near maximum rate. A summary of the second-pass optimisation process is provided in Table 5.5.

A third and final pass was made through the data. Setting each parameter to their optimum values, as determined during the first and second pass processes, all upper and lower bounds were varied to determine if any improvement in significance was achievable. The results of this process are shown in Figure 5.7 and 5.8. The *length* lower bound was decreased from 0.11° to 0.105°, yielding a marginally improved significance and rate. The *width* lower bound was also decreased, to 0.055°, again producing a small increase in excess. The *length* and *width* upper bounds, and the *distance* lower and upper bounds were left unchanged. By lowering the *alpha* upper bound to 20°, an improved significance was obtained, however at the expense of a small decrease in rate. The *size* lower bound was raised to 255 d.c. while the *length/size* bound was decreased to 6.5×10^{-4}; both yielding small increases in significance. The *max1*, *max2* and *max3* cuts produce no improvement in excess and thus it was decided that no trigger cut should be applied. The final set of optimised cuts, as used throughout the rest of this work, are presented in Table 5.6.

The importance of the optimisation process is highlighted by re-applying the new cuts to the Markarian 421 dataset. The resulting excess is $10.3\,\sigma$, almost double that obtained by applying the initial crude set of cuts. The contribution of each parameter cut to the overall significance may be demonstrated by applying each individual cut to the dataset while all others are set to zero. Table 5.7 summarises the results of this process. It is clear that

Parameter	Loose Bounds		Optimisation Range		Optimum Values	
	lower bound	upper bound	lower bound	upper bound	lower bound	upper bound
Length	0.11	0.21	–	–	–	–
Width	0.06	0.11	–	–	–	–
Distance	0.5	1.0	–	–	–	–
Alpha	0	22	–	–	–	–
Size	0	450	0 - 330	300 - 450	205	450
Max1	0	–	0 - 50	–	33	–
Max2	0	–	0 - 50	–	0	–
Max3	0	–	0 - 50	–	0	–
Length/Size	–	–	–	1×10^{-4} - 1×10^{-3}	–	7.5×10^{-4}

Table 5.5: Summary of second-pass optimisation procedure. The *"loose bounds"* column corresponds to the values at which all other parameters were set during the optimisation of each individual bound. The *"optimisation range"* column corresponds to the range over which each bound was varied during optimisation. The *"optimum values"* column correspond to the bounds chosen to obtain a high gamma-ray significance and rate. The choice of these values is discussed in detail in the text. Parameters optimised during this second-pass process are highlighted in red.

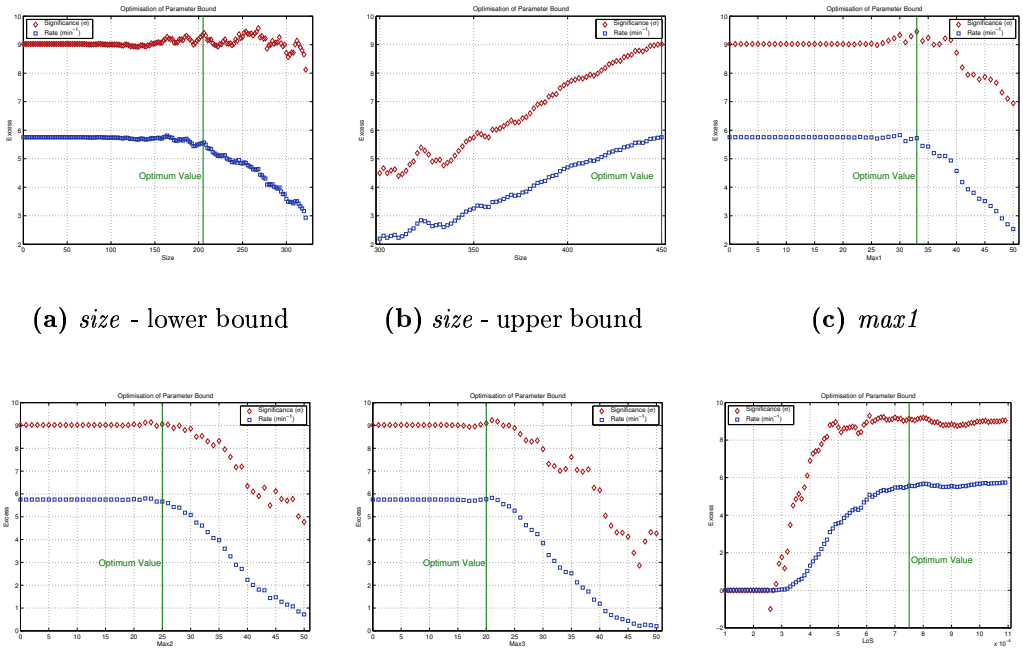

(a) *size* - lower bound **(b)** *size* - upper bound **(c)** *max1*

(d) *max2* **(e)** *max3* **(f)** *length/size*

Figure 5.6: Plots used during second-pass optimisation of *Minicuts*. In general optimal values were chosen as those yielding maximum significance and rate. For a detailed discussion of the values chosen see text.

Parameter	Lower Bound	Upper Bound
Length	0.105	0.22
Width	0.055	0.11
Distance	0.5	1.0
Size	255	450
Alpha	0	20
Max1	0	-
Max2	0	-
Max3	0	-
length/size	-	6.5×10^{-4}

Table 5.6: Optimum values of *Minicuts* selection.

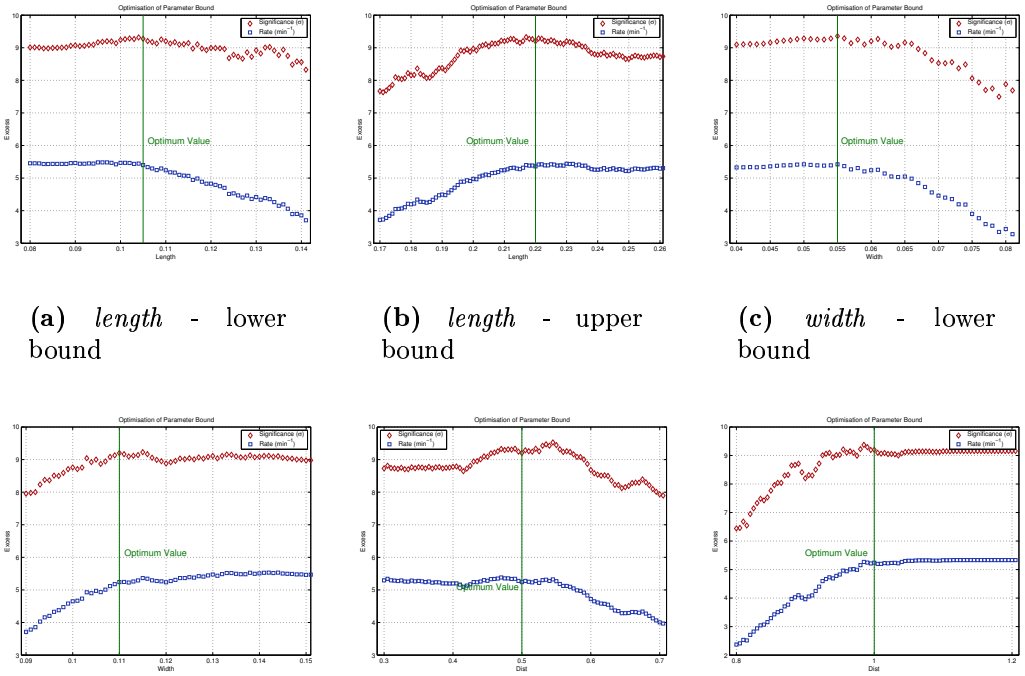

(a) *length* - lower bound

(b) *length* - upper bound

(c) *width* - lower bound

(d) *width* - upper bound

(e) *distance* - lower bound

(f) *distance* - upper bound

Figure 5.7: Plots used during final-pass optimisation of *Minicuts*. For a detailed discussion of the values chosen see text.

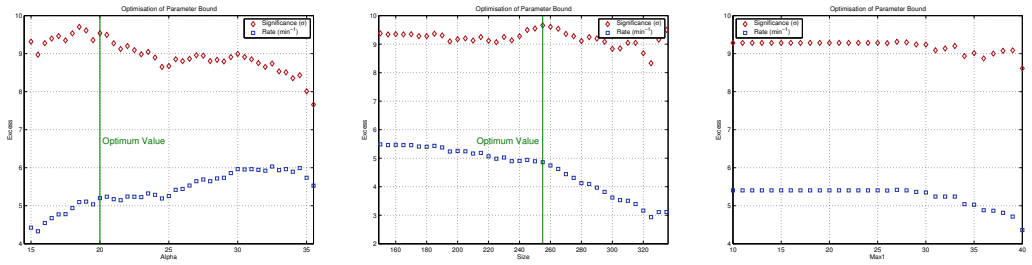

(a) *alpha* - upper bound

(b) *size* - lower bound

(c) *max1*

(d) *max2*

(e) *max3*

(f) *length/size*

Figure 5.8: Plots used during final-pass optimisation of *Minicuts*. For a detailed discussion of the values chosen see text.

Applied Cut	Significance (σ)	Rate (min^{-1})
None	2.79	7.33 ± 2.62
Length	4.17	7.56 ± 1.81
Width	3.19	5.94 ± 1.87
Distance	3.37	7.41 ± 2.20
Size	3.19	5.94 ± 1.87
Alpha	7.62	9.02 ± 1.19
length/size	4.40	8.11 ± 1.84
All	10.25	5.11 ± 0.49

Table 5.7: Contribution of each parameter cut to the overall significance. When applying no selection a significance of $2.8\,\sigma$ is obtained, while application of optimised *Minicuts* yields a $10.3\,\sigma$ excess. It is clear that the cuts which contribute most to this increase are, in descending order: *alpha*, *length/size* and *length*. The other cuts produce a marginal increase compared to that achieved by applying no cuts. *Max1*, *max2* and *max3* values are not shown as the final *Minicuts* selection does not incorporate any software trigger cut.

the *alpha* parameter is most effective for discriminating between gamma rays and background. By its application alone, significance increases to $7.6\,\sigma$ compared to $2.8\,\sigma$ when no selection cuts are applied. The *length* and *length/size* cuts are also important, yielding an additional excess of approximately $1.5\,\sigma$ each. The remaining parameters are not as effective; however, they still produce a marginal increase in signal.

5.2.4 Testing *Minicuts*

It has been shown that *Minicuts* is capable of extracting a significant excess from the Markarian 421 dataset; however, this is hardly conclusive evidence of its worth considering that this is the dataset on which the selection was optimised. To determine if *Minicuts* was suitable for applying to other data, a number of datasets, comprising Crab Nebula observations, were compiled. The results of application of *Minicuts*, *Supercuts* and *Supercuts* with the 450 d.c. lower boundary included, are presented in Table 5.8. In all cases *Minicuts* extracts at least a $3\,\sigma$ excess, proving is applicability to other datasets. The reduction in rate, following application of the 450 d.c. *size* cut to *Supercuts*-selected events, proves that *Supercuts* selects events in the *Minicuts* range. However the fact that there is no decrease in significance indicates that *Supercuts* has limited efficiency for small-*size* events. These results prove that it is more efficient to employ the twin selection of *Minicuts* and *Supercuts*

Season	Selection	N_{on}	N_{off}	Excess	Rate (min^{-1})
2000/'01	*Supercuts*	5006	3742	$13.51\,\sigma$	2.94 ± 0.22
	Minicuts	14714	14201	$3.02\,\sigma$	1.19 ± 0.39
	Modified Supercuts	3577	2470	$14.24\,\sigma$	2.57 ± 0.18
2001/'02	*Supercuts*	3909	2702	$14.85\,\sigma$	2.81 ± 0.19
	Minicuts	13080	12266	$5.11\,\sigma$	1.89 ± 0.37
	Modified Supercuts	3033	1931	$15.64\,\sigma$	$2.56 \pm .016$
2002/'03	*Supercuts*	2855	1773	$15.91\,\sigma$	2.51 ± 0.16
	Minicuts	6453	5753	$6.34\,\sigma$	1.62 ± 0.26
	Modified Supercuts	2470	1475	$15.84\,\sigma$	2.30 ± 0.15
2003/'04	*Supercuts*	3190	2270	$12.45\,\sigma$	2.67 ± 0.21
	Minicuts	5783	5388	$3.74\,\sigma$	1.15 ± 0.31
	Modified Supercuts	2595	1756	$12.72\,\sigma$	2.43 ± 0.19

Table 5.8: Results of applying *Supercuts*, *Supercuts* with an additional lower *size* cut, and *Minicuts* to Crab Nebula observations, recorded over four seasons. It is clear that application of *Minicuts* produces an excess in addition to that of *Supercuts*. From this point onward *Supercuts*, with the additional lower-size cut included, will be denoted *Modified Supercuts*. A full list of the four datasets used is given in Appendix A.

with the additional lower-*size* cut, than standard *Supercuts* alone. This approach ensures that events selected by both processes are mutually exclusive while offering greater efficiency over a wider energy range. When searching for new sources of gamma rays, especially those with steeply falling spectra or low-energy cut-offs, application of this dual analysis is particularly beneficial. From this point onward application of *Supercuts*, with the additional lower-*size* cut included, will be denoted *Modified Supercuts*.

When developing any new analysis it is prudent to test for evidence of instability. Some selection methods may produce inconsistent results because of oversensitivity to small changes within the data. Because *Minicuts* operates in a lower-energy domain it is more likely to be susceptible to variations in sky brightness or telescope performance. To determine the reliability of *Minicuts* a test was devised based on the fact that, over an extended period of time, VHE emission from the Crab Nebula has proved constant. By applying *Minicuts* to a set of Crab Nebula observations its stability may be calculated using a χ^2 test for constant rate:

$$\chi^2 = \sum_{i=1}^{N} \frac{(r_i - \bar{r})^2}{\Delta r_i^2} \tag{5.1}$$

where N is the number of observations, r_i are the individual rates, Δr_i the associated errors and $\bar{r}$ the weighted mean rate defined by:

$$\bar{r} = \frac{\sum_{i=1}^{N} \frac{r_i}{\Delta r_i^2}}{\sum_{i=1}^{N} \frac{1}{\Delta r_i^2}} \tag{5.2}$$

The χ^2 value is used to determine the probability (P_{χ^2}) of the rate being constant and the number of trials is accounted for by estimating the probability of P_{χ^2} occurring in N trials:

$$P_{trials} = 1 - (1 - P_{\chi^2})^{Ntrials} \tag{5.3}$$

The test was applied to the four Crab Nebula datasets previously used to illustrate the effectiveness of *Minicuts*. For comparison both *Supercuts* and *Modified Supercuts* were also tested. The results of this process are illustrated in Figure 5.9 and summarised in Table 5.9. It appears that in general *Minicuts* is stable over the course of a season as evidenced by the high probability of constant emission. The same conclusion may be drawn for *Supercuts* and *Modified Supercuts*. There is tentative evidence to suggest that the rate may no be constant when applying *Minicuts* to data from the 2001/2002 season, with a probability of constant emission, after trials, equal to 4.5×10^{-3}. A review of the observing records throughout this period shows that a number of modifications were made to the telescope configuration, including two bias alignments (December 17^{th} 2001 and February 2^{nd} 2002) and repositioning of the camera in the focal plane (January 15^{th}). There is no such instability evident when *Supercuts* and *Modified Supercuts* are applied to the 2001/2002 dataset indicating that, as suggested earlier, *Minicuts* is more sensitive to changes in the instrument. Overall it was concluded that *Minicuts* is stable over the course of a given season, however when analysing 2001/2002 data the possibility of unstable rates should be taken into account.

5.3 *Kernel* Analysis

Supercuts and *Minicuts* may be thought of as box selection techniques, where events are identified as gamma rays (or background) based on their presence within (or absence from) an n-dimensional box. The boundaries of this region are sharply defined in terms of a number of parameters and optimised using

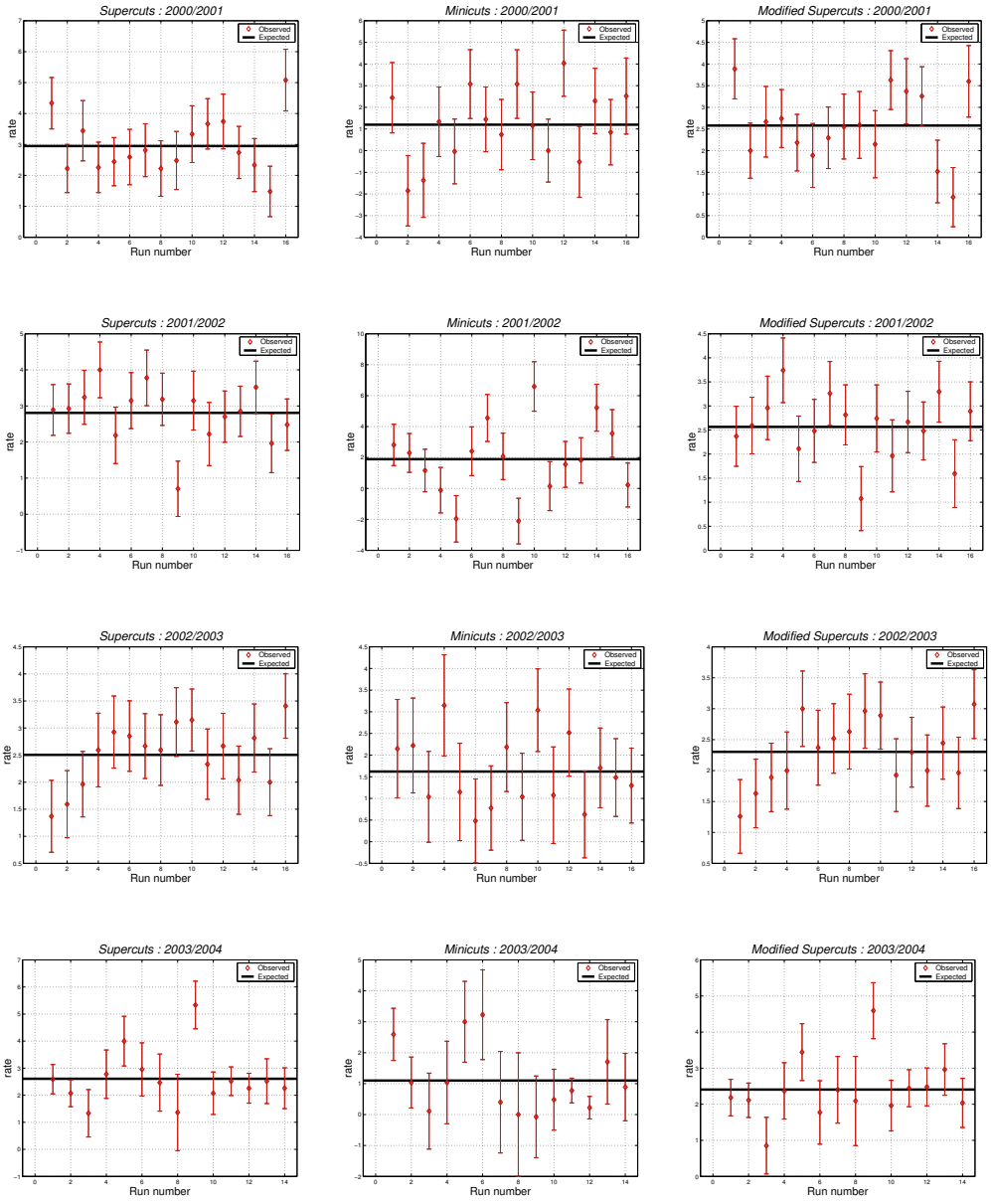

Figure 5.9: Stability of three different selections, tested using Crab Nebula data. VHE emission from the Crab Nebula is constant thus the stability of an analysis may be determined by testing for constant rate. The first column shows the results of applying *Supercuts* to four seasons' data, the second column give the *Minicuts* results and the third gives the *Modified Supercuts* results. Probabilities for constant rate are given in Table 5.9.

Season	Selection	$\bar{r}$	χ^2/df	P_{χ^2}	P_{trials}
2000/'01	*Supercuts*	2.89	16.18 / 15	0.37	0.84
	Minicuts	1.22	16.34 / 15	0.39	0.83
	Modified Supercuts	2.56	20.18 / 15	0.17	0.51
2001/'02	*Supercuts*	2.82	15.87 / 15	0.39	0.86
	Minicuts	1.84	37.06 / 15	1.2×10^{-3}	5×10^{-3}
	Modified Supercuts	2.59	14.5 / 15	0.49	0.93
2002/'03	*Supercuts*	2.52	12.75 / 15	0.62	0.98
	Minicuts	1.59	9.86 / 15	0.83	0.99
	Modified Supercuts	2.30	12.50 / 15	0.64	0.98
2003/'04	*Supercuts*	2.53	17.07 / 13	0.20	0.58
	Minicuts	0.79	14.32 / 13	0.35	0.82
	Modified Supercuts	2.38	16.05 / 13	0.25	0.68

Table 5.9: Results of testing different selections for evidence of instability over the course of an observing season. Tests were applied to four seasons' data, thus the number of trials was set equal to four.

real data to maximise efficiency. This domain may be viewed as a somewhat crude approximation to the peak of the gamma-ray probability density distribution, where the likelihood of an event being gamma-ray in origin is highest. An alternative approach to gamma-ray selection is to define an equal probability surface, whereby events on one side have high probability of being a gamma ray, and events on the opposite side are most likely background. Such a surface may be calculated in terms of a log-likelihood function:

$$\log\left(R\left(p\right)\right) = \log\left(\frac{f_\gamma\left(p\right)}{f_b\left(p\right)}\right) \tag{5.4}$$

where $f_\gamma\left(p\right)$ is the gamma-ray probability distribution for a point p in n-dimensional parameter space, and $f_b\left(p\right)$ is the background probability distribution. The essence of the *Kernel* technique (Dunlea, 2001; Dunlea et al., 2001; Kildea, 2002) is careful characterisation of this surface based on precise calculation of gamma-ray and background probability densities.

Due to the complex way in which gamma-ray events (and background) populate parameter space (Figure 4.13) it is not possible to describe their distribution in terms of a simple function. The most elementary probability density estimator is a histogram; however, this is far from ideal for a num-

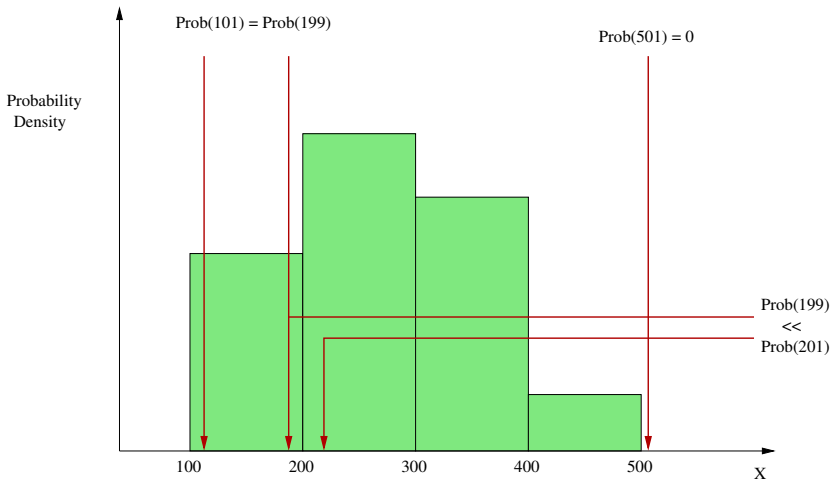

Figure 5.10: Illustration of problems associated with using a histogram as a probability density estimator. Due to finite cell width, and the position of cell boundaries, points which are far apart may have equal probability, while points close together can have very different probabilities. In addition, a point which occurs just beyond the end cell of the histogram has zero probability.

ber of reasons, including fixed cell width, limited range, and cell boundary discontinuities (Hand, 1982). These problems may be understood by considering two values, a and b, separated by a distance δ. Choosing δ to be quite large, and depending on the choice of histogram cell width, both a and b may populate the same cell, thus having equal probability. Conversely if a and b are close together they may still fall into different cells, again depending on the choice of boundary position (Figure 5.10).

The *Kernel* estimator attempts to remove these problems, by convolving each data point with a point spread function and summing the results to produce a smooth, continuous approximation to the probability distribution (Figure 5.11). The basic *Kernel* estimator is given by:

$$f_\gamma = \frac{1}{N_\gamma h_\gamma} \sum_{i=1}^{N_\gamma} K\left(\frac{p - p\gamma_i}{h_\gamma}\right), \tag{5.5}$$

where p is a point in parameter space, $p\gamma_1, \ldots, p\gamma_{N_\gamma}$ are vectors of parameters of an N_γ simulated sample of gamma rays, and h_γ is a scale factor (a measure of the width of the point spread function). As discussed by Hand (1982) and Scott (1992) the *Kernel* function, K, may be any scalar function in n-dimensional space. For IACT data the following function has been shown to be an appropriate *Kernel* (Samuelson, 1999; Moriarty and Samuelson, 2000):

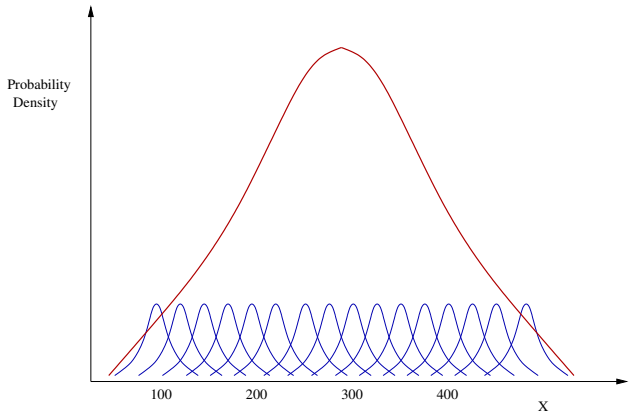

Figure 5.11: Illustration of how the *Kernel* probability density estimator works. Each data point is convolved with a point spread function then summed, producing a smooth approximation to the probability density distribution. Using this approach a more accurate picture of the true distribution is achieved, where points close together have similar probabilities and points far apart do not.

$$K = \frac{1}{\sqrt{(2\pi)^n \left|\xi_\gamma\right|}} \exp\left(-\frac{1}{2}\left(\frac{p - p\gamma}{h_\gamma}\right)^{\mathsf{T}} \xi_\gamma^{-1} \left(\frac{p - p\gamma}{h_\gamma}\right)\right) \tag{5.6}$$

where n is the number of parameters and ξ_γ is the covariance matrix of the gamma-ray dataset (a measure of the extent to which each parameter is correlated with every other parameter). For a *Kernel* that is the product of Gaussians, with one Gaussian in each dimension, the scale factor that minimises the mean integrated squared error between a *Kernel* estimator and an actual distribution is (Hand, 1982) :

$$h_\gamma = \left(\frac{4}{N_\gamma\,(n+2)}\right)^{\frac{1}{n+4}} \tag{5.7}$$

For this work a multivariate Gaussian rather than the product of univariate Gaussians is used and the gamma-ray probability density distribution is defined as:

$$f_\gamma = \frac{1}{N_\gamma h_\gamma \sqrt{(2\pi)^n \left|\xi_\gamma\right|}} \sum_{i=1}^{N_\gamma} \exp\left(-\frac{1}{2h_\gamma^2}\left(p - p\gamma_i\right)^{\mathsf{T}} \xi_\gamma^{-1} \left(p - p\gamma_i\right)\right) \tag{5.8}$$

The background probability density distribution may be similarly defined.

5.3.1 Gamma-Ray Simulations

In practice the *Kernel* technique calculates the probability of an event being gamma-ray or background by comparing its properties to that of a database of simulated gamma rays and real background events. For use throughout this work, the GrISU (Grinnell - Iowa State University) Monte-Carlo simulations package was used to generate a large dataset of gamma-ray events. In addition to being applied during *Kernel* analysis, these simulations were also used to illustrate the differences between images formed by gamma rays and background (Figure 4.13), to calculate collection areas (Section 5.4), and to estimate the energy threshold of the detector (Section 5.4). The GrISU simulations package may be divided into three distinct parts:

- simulation of extensive air showers
- simulation of Cherenkov emission
- simulation of the detector

Generation of extensive air showers (EAS) is based on a modified version of *Kascade*, an EAS simulation program originally developed in 1989 (Kertzman and Sembrowski, 1989). *Kascade* creates a detailed 3-D map of the EAS, following each constituent particle as it descends through a model atmosphere until it reaches ground level, interacts or decays. The next stage of the process, *Cherenkf* (Carter-Lewis, 1992), uses the 3-D maps to simulate the Cherenkov emission from each of the particles and in a similar way to *Kascade* tracks each photon until it arrives at detector level. The response of the Whipple 10m telescope is modeled during the final part of the simulation process, by the *GrISUDet* program. *GrISUDet* traces each photon as it reflects from the mirrors and illuminates the camera, subsequently modeling charge pulses produced by the PMTs and electronics. At this stage artificial noise, in terms of photoelectrons per nanosecond per square metre per steradian, is injected into the data to reflect the level of background light falling on the telescope. Observations of the Crab Nebula from 2003/2004 were used to determine the most appropriate background noise level. By varying the amount of noise in the simulations, and comparing the resulting *pedestal variance* distribution to that of the real data, the most suitable value was identified. This process is illustrated in Figure 5.12 and shows that a background level of ≈ 650 photoelectrons ns^{-1} m^{-2} str^{-1} is most appropriate. In addition to varying noise levels, the simulations package contains a number of input parameters which may be adjusted to reflect different sources, atmospheric conditions and detector configurations. A summary of the most

Parameter	Value
Particle Type	Gamma Ray
Minimum Energy	100 GeV
Maximum Energy	15 TeV
Source Spectral Index	-2.49
No. showers	140,000
Elevation	70 °
Maximum Impact Parameter	250 m
Detector Configuration	2000/2001
Diffuse Noise Level	650 pe ns^{-1} m^{-2} str^{-1}

Table 5.10: Outline of simulations' input parameters used to generate gamma ray database for this work.

important input parameters, used in generating the simulations database for this work, is presented in Table 5.10.

5.3.2 Optimisation

In an ideal world, where gamma-ray and background events are distinctly different the log(R) boundary separating both populations would occur at zero, making discrimination easy. Unfortunately this is not the case and with both distributions overlapping to some extent, optimisation is required to determine the most efficient log(R) cut. *Kernel* optimisation is a much simpler process than the equivalent for box selection because, although selection is based on five parameters (*length*, *width*, *distance*, *size* and *alpha*), only one optimisation is required since these are combined into a single log(R) score. To calculate the probability of an event being a gamma ray, the *Kernel* requires a reference database of simulations and real background (Figure 5.13). During this work a single control run was used as the background reference, and a similar number of simulations were used as the gamma-ray reference. Details of these datasets are provided in Table 5.11. Optimisation was carried out using Crab Nebula observations, recorded in *ON/OFF* mode throughout the 2003/2004 season. Ideally the same dataset as used during development of *Minicuts* would have been used here, however because the *Kernel* is expected to be sensitive to differences in the datasets it was decided to use a pure *ON/OFF* sample instead. A full list of the Crab Nebula data used is provided in Appendix A.

It has already been shown, during development of *Minicuts*, that an additional excess of events may be extracted using selection criteria optimised

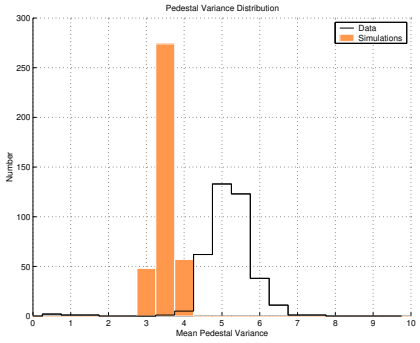

(a) Noise Level : 300

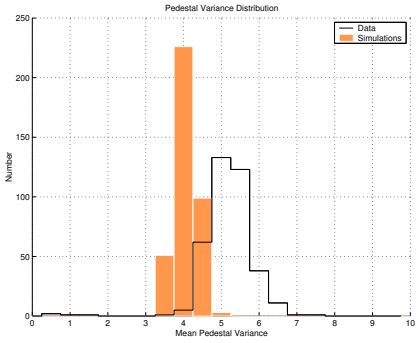

(b) Noise Level : 400

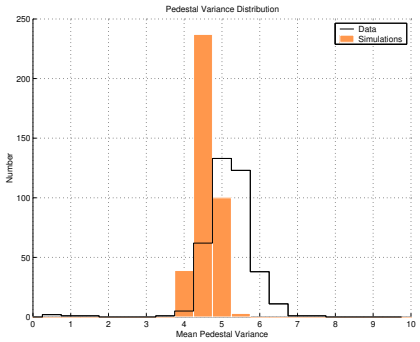

(c) Noise Level : 500

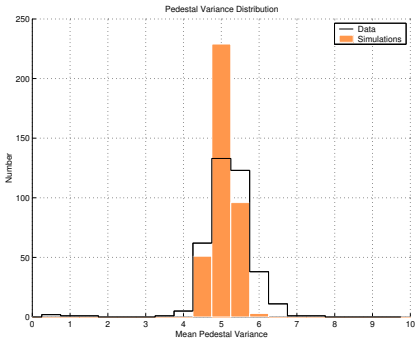

(d) Noise Level : 600

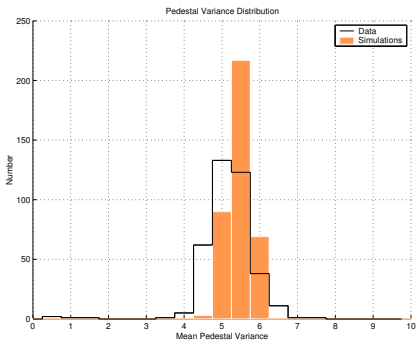

(e) Noise Level : 700

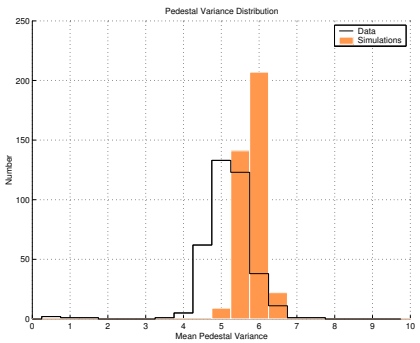

(f) Noise Level : 800

Figure 5.12: Estimation of background noise level, for application to gamma-ray simulations. By adjusting the level of noise injected into simulated data, and comparing the resultant *pedestal variance* distribution to that of real data, the most suitable value was identified.

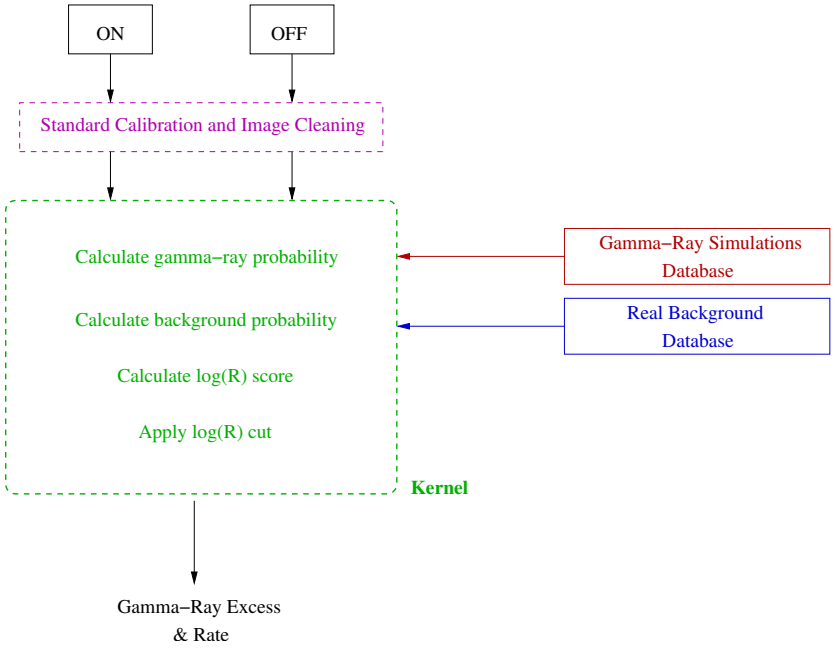

Figure 5.13: Outline of *Kernel* Analysis procedure. Data is first subjected to standard calibration and image cleaning. After parameterisation a list of event parameters is passed to the *Kernel* which works out the probability of each event being either gamma-ray or background, by comparison with simulations and real background. Using an optimised boundary in log(R) space gamma-ray events are selected and the excess number of events in the *ON* data calculated.

	Background	Gamma-Ray
Run I.D.	025871	111111
No. Events	44,002	46,655
Elevation	75 °	70 °

Table 5.11: Details of reference datasets used by *Kernel* selection. The *Kernel* works by comparing events with a reference set of simulations and background. Real control data was used as the background reference and chosen to have a similar elevation to the dataset. A subset of the gamma-ray simulations database, comprising 46,655 events, was used as the gamma-ray reference.

Size Range	log(R)	N_{on}	N_{off}	Excess	Rate (min^{-1})
No Limit	3.60	2965	1427	$23.11\,\sigma$	2.39 ± 0.10
$\leq$ 450 d.c.	1.15	68441	65341	$8.48\,\sigma$	4.82 ± 0.57
$>$ 450 d.c.	3.60	2704	1161	$24.82\,\sigma$	2.40 ± 0.10

Table 5.12: Optimisation of log(R) boundary for three *size* ranges. Although *Kernel* is more efficient than box selection over a wide range of energies (or *size*), by optimising in different *size* bands it should be possible to obtain a greater efficiency. The results presented here show that this is indeed the case; by optimising above and below the 450 d.c. boundary an additional excess is obtained.

in specific *size* ranges. Although one of the major advantages of the *Kernel* technique is its greater efficiency over a wider energy range, it may be possible to further increase efficiency by using different log(R) cuts for events of different *size*. For consistency with the approach used in developing *Minicuts*, the *Kernel* was optimised in three different bands corresponding to those events; (1) with *size* greater than 450 d.c., (2) with *size* less than 450 d.c. and (3) of all *sizes*. The optimum log(R) value for each *size* band was chosen as that yielding maximum significance (Figure 5.14). In the case of events of all *sizes* and those with *size* above 450 d.c. the optimal log(R) boundary occurs at 3.60. For events with *size* less than 450 d.c. the boundary is much lower, with a value of 1.15. This difference in optimum cut values implies that selection is more efficient in discrete *size* bands, a view that is confirmed after re-applying the optimum cuts to the data. The results (Table 5.12) show that by limiting the *Kernel* to events with *size* greater than 450 d.c. a significance is obtained which is equal to that achieved when applying the *Kernel* over an unlimited *size* range. By applying a log(R) cut optimised below the 450 d.c. boundary an additional 8σ excess is obtained. The standard *Kernel* is capable of discriminating between event types below 450 d.c. as evidenced by a decrease in rate when the 450 d.c. cut is applied; however, the fact that there is no corresponding decrease in significance proves that this *Kernel* has limited sensitivity to events of small *size*. It may be concluded that, in a similar way to box selection, the application of a dual approach to *Kernel* analysis is more beneficial than a single selection cut.

5.3.3 Testing the *Kernel*

The potential of *Kernel* selection has already been shown following its application to the dataset on which it was optimised. To determine the robustness of the *Kernel*, that is its ability to discriminate between gamma rays

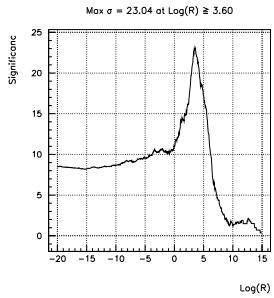

(a) Size Range: No Limit

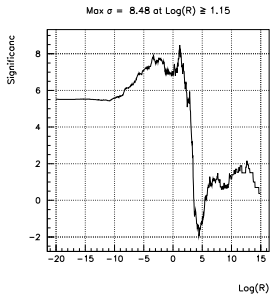

(b) Size Range: ≤ 450 d.c.

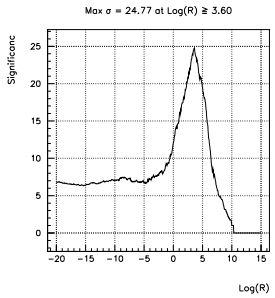

(c) Size Range: > 450 d.c.

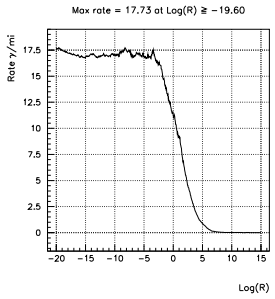

(d) Size Range: No Limit

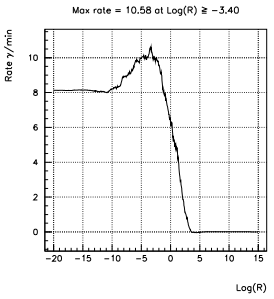

(e) Size Range: ≤ 450 d.c.

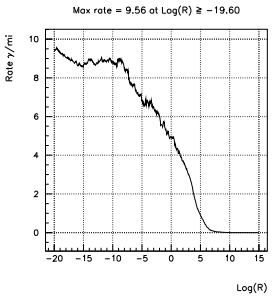

(f) Size Range: > 450 d.c.

Figure 5.14: Optimisation of *Kernel* selection in three different *size* bands. Plots (a), (b) and (c) show the gamma-ray significance as a function of log(R) while plots (d), (e) and (f) show the gamma-ray rate. The optimum values were chosen as those yielding maximum significance, and are detailed in Table 5.12.

Season	*Size* Range	N_{on}	N_{off}	Excess	Rate (min^{-1})
2000/'01	No Limit	1413	580	$18.66\,\sigma$	1.87 ± 0.10
	$\leq$ 450 d.c.	55265	54485	$2.35\,\sigma$	1.75 ± 0.74
	$>$ 450 d.c.	1316	503	$19.06\,\sigma$	1.83 ± 0.10
2001/'02	No Limit	1391	483	$20.98\,\sigma$	2.04 ± 0.10
	$\leq$ 450 d.c.	65420	63249	$6.05\,\sigma$	4.89 ± 0.81
	$>$ 450 d.c.	1341	439	$21.38\,\sigma$	2.03 ± 0.09
2002/'03	No Limit	1369	509	$19.85\,\sigma$	1.92 ± 0.10
	$\leq$ 450 d.c.	34852	32788	$7.94\,\sigma$	4.62 ± 0.58
	$>$ 450 d.c.	1301	463	$19.95\,\sigma$	1.88 ± 0.09
2003/'04	No Limit	1296	627	$15.26\,\sigma$	1.88 ± 0.12
	$\leq$ 450 d.c	26029	25114	$4.05\,\sigma$	2.57 ± 0.63
	$>$ 450 d.c.	1256	586	$15.61\,\sigma$	1.88 ± 0.12

Table 5.13: Results of applying *Kernel* to Crab Nebula data recorded over the course of four seasons. By applying *size* dependent log(R) cuts it is possible to extract, from the data, an excess that is in addition to that obtained by using a single cut over all *sizes*. A full list of the datasets used is given in Appendix A.

and background when applied to different observations, a number of datasets were analysed. This data is the same as that used to test *Minicuts*, comprising Crab Nebula observations from the last four years. The results of the application of the *Kernel* to this data are shown in Table 5.13, and prove its ability to extract an excess of events from different datasets. Applying the *Kernel* to events with *size* greater than 450 d.c. produces a significance equal to that obtained by applying the *Kernel* to events of all *sizes*. By applying the lower-energy *Kernel* to events below the 450 d.c. boundary an additional, statistically significant excess is achieved. This proves that the dual selection approach is more efficient than a single log(R) cut and is in keeping with the results of the *Kernel* optimisation.

To determine the stability of the *Kernel* technique, a test for constant emission was applied to the four Crab Nebula datasets. This test was identical to that used earlier in the case of *Minicuts*. Each of the three *Kernel* selections was tested and the results of this process are illustrated in Figure 5.15 and summarised in Table 5.14. In general it appears that the *Kernel* is stable over the course of an observing season, as evidenced by the high probabilities for constant rate. For *Kernel* selection in the smaller-*size* band

Season	*Size* Range	$\bar{r}$	χ^2/df	P_{χ^2}	P_{trials}
2000/'01	No Limit	1.86	16.88 / 15	0.33	0.79
	$\leq$ 450 d.c.	1.72	17.97 / 15	0.26	0.71
	$>$ 450 d.c.	1.80	16.24 / 15	0.37	0.84
2001/'02	No Limit	2.01	19.91 / 15	0.18	0.54
	$\leq$ 450 d.c.	4.56	40.20 / 15	4.2×10^{-4}	1.7×10^{-3}
	$>$ 450 d.c.	1.99	19.82 / 15	0.18	0.55
2002/'03	No Limit	1.91	10.68 / 15	0.775	0.997
	$\leq$ 450 d.c.	4.57	12.85 / 15	0.61	0.98
	$>$ 450 d.c.	1.87	14.82 / 15	0.47	0.92
2003/'04	No Limit	1.85	12.83 / 13	0.46	0.92
	$\leq$ 450 d.c.	1.76	17.81 / 13	0.17	0.51
	$>$ 450 d.c.	1.87	14.58 / 13	0.35	0.80

Table 5.14: Results of testing different *Kernel* selections for evidence of instability over the course of an observing season. Tests were applied to four seasons' data, thus the number of trials was set equal to four.

there is tentative evidence for variable rate in the 2001/2002 dataset. This is consistent with results produced following application of *Minicuts* to the same dataset and as stated earlier there were a number of changes made to the telescope throughout 2001/2002. Because the smaller-*size Kernel* selects events in a region closer to the telescope threshold, it should be more susceptible to changes in the atmosphere and instrument. This view is supported by the fact that the larger-*size Kernel* shows no evidence of variability, even in the case of the 2001/2002 dataset.

It is concluded that *Kernel* analysis is stable over the course of a given season. However, when dealing with data from the 2001/2002 season, the possibility of variability should be taken into account. It should be noted that the results presented in Table 5.14 suggest that the rate of gamma rays detected by the lower-energy *Kernel* is not constant from season to season and further strengthens the assertion that the *Kernel* in this energy range is particularly sensitive to experimental conditions. A variable rate has consequences when combining results from different years and is discussed in more detail in Section 5.5.

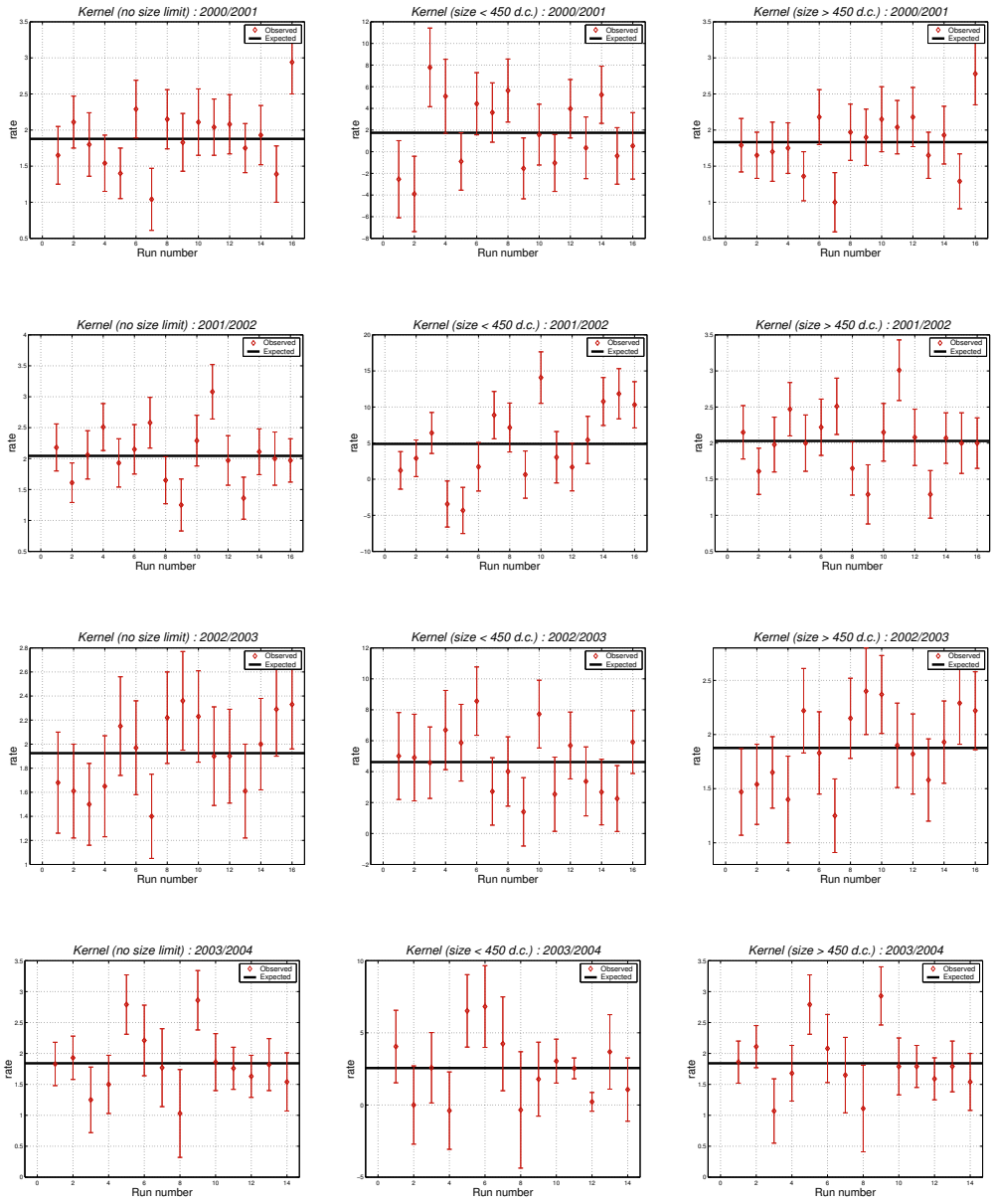

Figure 5.15: Stability of three different *Kernel* selections, tested using Crab Nebula data. VHE emission from the Crab Nebula is constant, thus the stability of an analysis may be determined by testing for constant rate. The first column shows the results of applying the *Kernel* to events of all *size*, the second column gives the *Kernel* results for events with *size* less than 450 d.c and the third gives the results of *Kernel* selection above 450 d.c.. The corresponding probabilities of constant rate are given in Table 5.14.

5.4 Energy Thresholds

In the previous two sections it has been shown that by using selections optimised above and below 450 d.c. it is possible to extract an additional excess of gamma-ray events. This additional excess originates in a region of smaller *size*. In the case of ground-based gamma-ray astronomy the *size* of the image is closely related to the energy of the primary gamma ray; however, it has not yet been determined the specific energy range in which the new selections are sensitive. For a Cherenkov telescope, efficiency depends on both the detector configuration and the method of discrimination used, and is usually defined in terms of collection area or energy threshold. Collection area provides a measure of performance of the *detector-analysis* system at a given energy. It is calculated by simulating a large number of gamma-ray induced EAS falling randomly over an area A_0 and then recording the number of events that trigger a detector located at the centre of this area, and pass subsequent analysis. This is defined as:

$$A\,(E) \;=\; A_0\,.\,\left(\frac{Number\ of\ \gamma - rays\ selected\ at\ energy\ E}{Number\ of\ \gamma - rays\ simulated\ at\ energy\ E}\right) \qquad (5.9)$$

Although the collection area is useful for determining the sensitivity of the telescope to gamma rays of different energies it provides little information regarding the response of the detector to a given source. To incorporate the effect of a given source, the collection area is convolved with the source spectrum to produce a differential response curve:

$$\frac{dr}{dE} = A(E)\ .\ \alpha\ .\ E^{-\gamma} \qquad (5.10)$$

where r is the gamma-ray rate, α is the flux constant and γ is the differential spectral index. The peak of the differential response curve, or peak response energy, is taken as the energy threshold of the *detector-analysis* system. Using a subset of the simulations database detailed in Section 5.3.1, collection-area and energy-threshold values were calculated for both box and *Kernel* selections in all three *size* bands. The energy thresholds were calculated assuming a Crab Nebula like spectrum.

The collection areas are illustrated in Figure 5.16 and reveal a wealth of information about each selection process. Comparing *Supercuts* to the *Kernel* optimised over an unlimited *size* range, it is clear the *Kernel* has greatly improved collection area at low and high energies. Unlike *Supercuts*, where the collection area begins to drop off above a certain energy, the *Kernel* exhibits no such decrease. In the case of *Modified Supercuts* and the *Kernel*

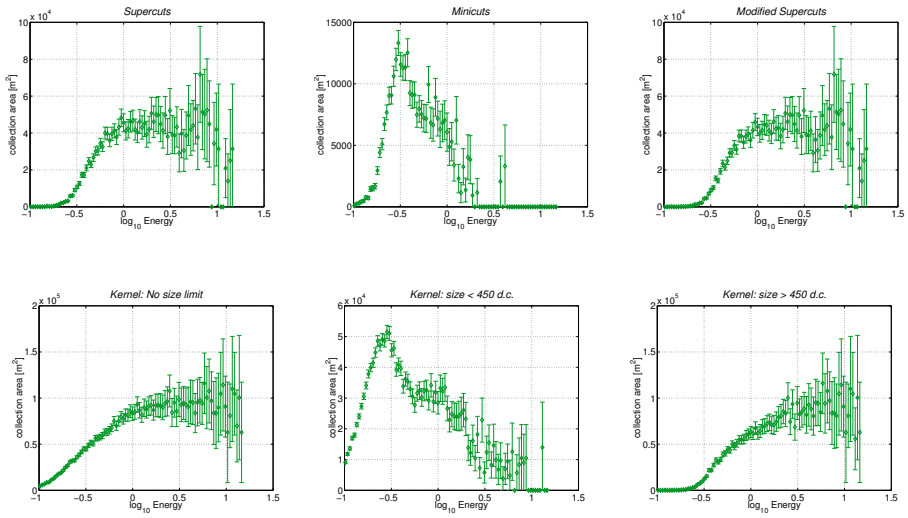

Figure 5.16: Collection areas for box and *Kernel* selections. The top row shows the collection area for box selections in the three different *size* bands. The bottom row shows the collection area for *Kernel* selections in the same three *size* bands.

optimised in the same *size* band a similar trend is evident and is in agreement with previous results from a number of authors (Dunlea, 2001; Dunlea et al., 2001; Kildea, 2002). Comparing *Minicuts* to the smaller-*size Kernel* selection it is again obvious that the *Kernel* has greater sensitivity at lower energies. The sharp fall in collection area for both approaches, as the energy increases beyond a certain value, is a direct consequence of applying the 450 d.c. upper-*size* cut and indicates that above a certain energy both selections have greatly reduced efficiency. Consequently it is no longer appropriate to talk about *Minicuts* (and its *Kernel* equivalent) as selecting events above a certain energy threshold, rather it is more precise to talk in terms of selection between lower and upper energy bounds. The lower energy bound is simply the peak response energy, whose calculation is outlined above. The upper bound was approximated using a similar process; however, instead of applying an upper *size* cut of 450 d.c., a lower *size* cut of identical value was applied. The resulting peak in the differential response curve was taken as the upper energy bound of the *Minicuts* selection. The upper bound on the smaller-*size Kernel* was calculated in the same way.

The differential response curve for each selection is shown in Figure 5.17. The energy thresholds, chosen as the peak of these curves, are listed in Table 5.15 and further highlight the benefit of applying *size* specific selections.

	Peak Response Energy (GeV) *Size* Range		
Selection	No Limit	$\leq$ 450 d.c.	$>$ 450 d.c.
Box	378 ± 76	236 ± 38	403 ± 79
Kernel	147 ± 39	131 ± 35	393 ± 76

Table 5.15: Peak response energies for different selection methods.

In the case of box selection the energy threshold for *Supercuts* is approximately 380 GeV, indicating that below this energy it has limited efficiency. Development of *Minicuts* was motivated by an attempt to increase selection efficiency at lower energy, with the aim of detecting sources with steeply falling spectra or low-energy cut-offs. With an energy threshold of $\sim$ 240 GeV *Minicuts* clearly accesses a region of the gamma-ray spectrum below that of *Supercuts*. The similarity of the energy thresholds of *Modified Supercuts* and *Supercuts* shows that *Supercuts* is not very sensitive to events with *size* less than 450 d.c.. In general the *Kernel* selections have lower energy thresholds than their box-selection counterparts. For the single log(R) cut, optimised over all *sizes*, the energy threshold is extremely low, with a value of $\sim$ 150 GeV. A small decrease in energy threshold is achieved by utilising the *Kernel* optimised in the smaller *size* band, but it is not possible to conclude if this is a true decrease due to the magnitude of the error on both quantities. The upper energy bound on *Minicuts* is in close agreement with the lower bound on *Modified Supercuts* indicating that the method by which the upper bound was calculated is accurate. Comparing *Minicuts* to its *Kernel* equivalent it is obvious that application of the *Kernel* is most suitable when searching for evidence of low-energy emission, due to its significantly lower threshold.

5.5 Detector Stability Over the Course of Four Years

It has already been shown that both box selection and *Kernel* selection are stable over the course of a given observing season. In this work data recorded on a number of BL-Lac objects, over the course of four observing seasons, is analysed in a search for VHE gamma-ray emission. It is only possible to combine data from different years if the energy threshold of the *detector-analysis* system is constant throughout that time period. The energy threshold for each season may be calculated using the approach outlined in Sec-

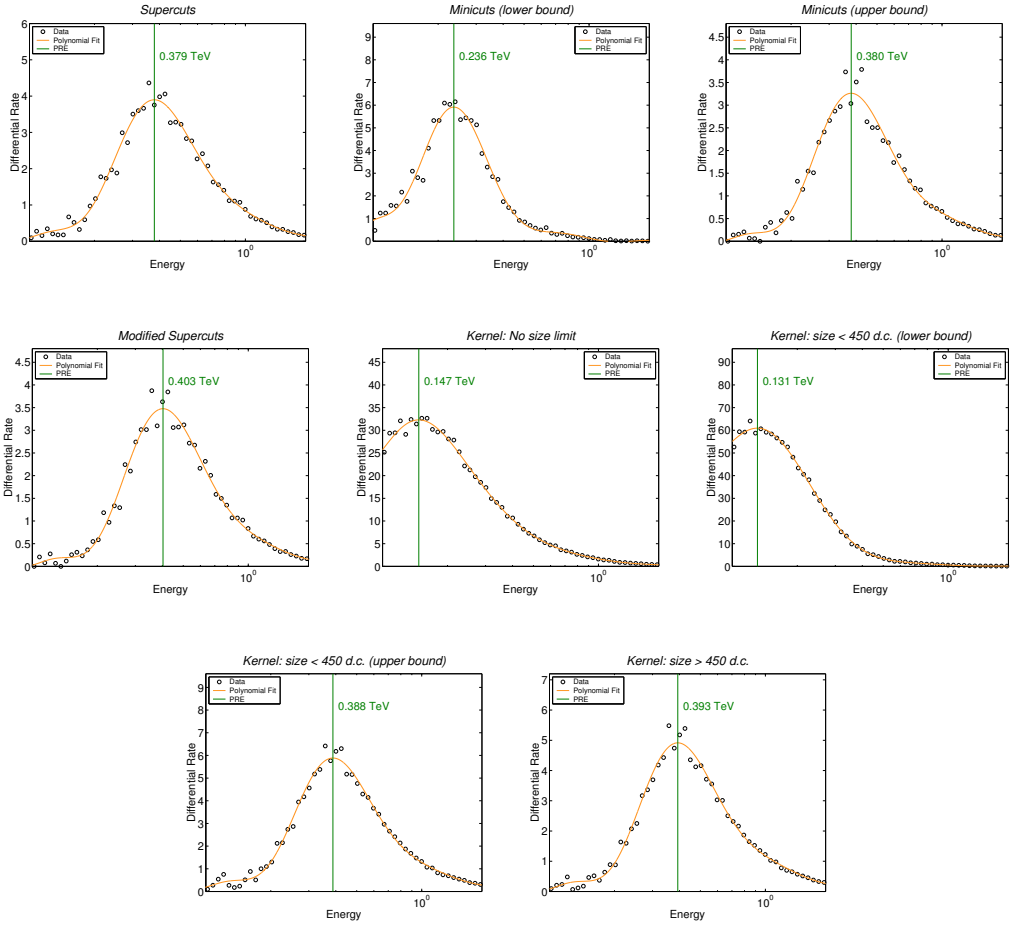

Figure 5.17: Differential response curves for box and *Kernel* selections. The peak of these curves are taken as the energy threshold of the detector-analysis system.

tion 5.4. However to do so, changes in detector performance must be taken into account, requiring season-specific simulations. To accurately model the response of the telescope at a given time, a vast amount of information is necessary including details of mirror reflectivity and PMT gains. This is a complex task and, as yet, generation of accurate simulations for the last three seasons is not possible. Fortunately there is a second, albeit indirect, method for estimating the energy thresholds for different seasons.

The energy threshold for each selection method has already been calculated for the 2000/2001 observing season. Knowing the energy threshold it is possible to calculate the flux of photons coming from the Crab Nebula using:

$$F(>E_{th}) = \int_{E_{th}}^{\infty} \alpha \, . \, E^{-\gamma} \, dE \tag{5.11}$$

where α is the flux constant, γ is the spectral index and E_{th} is the threshold of the *detector-analysis* system. The Crab Nebula is known to be a steady source of gamma rays over an extended period of time, so any changes in flux must result from a change in energy threshold. The gamma ray flux for each of the subsequent years (i.e. 2001/2002, 2002/2003 and 2003/2004) can be estimated by scaling the 2000/2001 flux by the ratio of the average Crab-Nebula rate for a given season to that of 2000/2001. By extrapolating backward, using equation 5.11, the energy threshold for each season may be estimated.

The results of this process are summarised in Table 5.16 for box selections and Table 5.17 for the *Kernel*. For all box selections the energy threshold is consistent from season to season, within errors. This means that all data recorded during this period may be combined and analysed using any of the box selection techniques. In the case of the *Kernel*, the energy threshold is constant when the *Kernel*, optimised over an unlimited *size* range, is applied. This is also true for the *Kernel* optimised above the 450 d.c. boundary. When the lower-energy *Kernel* is applied, large fluctuations in the average Crab Nebula rate from season to season are evident and translate to a variable energy threshold. This makes it inappropriate to combine data from different seasons when selecting events with the low-energy *Kernel*.

The variable Crab Nebula rates and energy thresholds, observed when applying *Kernel* selection, are probably due to small changes in the detector. These changes should be most prominent at low energies, close to the telescope hardware threshold, a view which is supported by the fact that only the low-energy *Kernel* shows evidence of variable rate. The source of these instrumental changes is unclear; however, there is evidence in Table 5.17 to suggest that PMT degradation may be responsible. It has been shown that since the 2000/2001 observing season there has been a decrease in PMT

gains across the camera. This decrease was compensated for near the start of the 2003/2004 season by raising the high voltage supply to each PMT. For seasons 2001/2002 and 2002/2003 the mean gamma-ray rates, as determined using the low-energy *Kernel*, are consistent within errors. This is also true for the 2000/2001 and 2003/2004 rates, suggesting that the change in rates is due to variable PMT performance.

By applying a lower *size* cut of 250 d.c. to events selected by the low-energy *Kernel* it is possible to obtain consistent rates and consistent energy thresholds over the four seasons. This comes at the expense of an increase in energy threshold to 229 $\pm$ 38 GeV. Because a low energy threshold is desirable when searching for new sources it was decided that each source would be analysed over the course of a given season using the original low-energy *Kernel*, but when combining data from different seasons the lower *size* cut should be included.

5.6 Stability of *TRACKING* Analysis

Tracking Analysis assumes that in the absence of a gamma-ray source, the shape of the *alpha* distribution is constant over the course of an observing season and over all dark-field regions. Recently this assumption has been called into question (Quinn et al., 2001; de la Calle Perez and Holder, 2001; de la Calle Perez, 2003). The implication of an inconsistent *alpha* distribution is that the use of a single value *tracking ratio* to characterise the shape, may produce a false signal excess (or deficit). While not critical when dealing with data where there is a strong gamma-ray signal, this effect could pose major problems when dealing with weak signals, for example in the case of a marginal ($3\,\sigma$) detection.

As part of the development of *Minicuts* (Section 5.2), specifically its extension to incorporate data recorded in *TRACKING* mode, it was decided that this topic warranted further investigation. This was based on the concern that non-statistical effects would be most evident in the lower energy region in which *Minicuts* operates. Since the *tracking ratio* is a measure of the shape of the *alpha* distribution, the task of testing the consistency of the shape may be reduced to simply testing the constancy of the *tracking ratio*. Two tests were carried out on dark-field data taken from observing seasons 2000/2001, 2001/2002, 2002/2003 and 2003/2004. The tests were applied to events selected with the standard *Supercuts* selection, the newly developed *Minicuts* and *Modified Supercuts*. The *Kernel* selections were not included in these tests as the *TRACKING* method of background estimation is not applicable to *Kernel* analysis.

Size Range : No Limit
Crab Rate (2000/2001 season) : 2.94 ± 0.22 min^{-1}
E_{th} (2000/2001 season) : 378 ± 76 GeV
Flux (2000/2001 season) : 9.15 ± 0.9 × 10^{-11} ph cm^{-2} s^{-1}

Season	Rate (min^{-1})	Rate (00/'01 rate)	Flux (ph cm^{-2} s^{-1})	E_{th} (GeV)
2001/2002	2.81 ± 0.19	0.96 ± 0.10	8.75 ± 1.20 × 10^{-11}	389
2002/2003	2.51 ± 0.16	0.85 ± 0.08	7.81 ± 1.10 × 10^{-11}	420
2003/2004	2.67 ± 0.19	0.91 ± 0.09	8.31 ± 1.19 × 10^{-11}	303

Size Range : ≤ 450 d.c.
Crab Rate (2000/2001 season) : 1.19 ± 0.39 min^{-1}
E_{th} (2000/2001 season) : 236 ± 39 - 379 ± 71 GeV
Flux (2000/2001 season) : 9.35 ± 1.65 × 10^{-11} ph cm^{-2} s^{-1}

Season	Rate (min^{-1})	Rate (00/'01 rate)	Flux (ph cm^{-2} s^{-1})	E_{th} (GeV)
2001/2002	1.89 ± 0.37	1.59 ± 0.61	14.85 ± 6.24 × 10^{-11}	198
2002/2003	1.62 ± 0.26	1.36 ± 0.50	12.73 ± 5.16 × 10^{-11}	211
2003/2004	1.15 ± 0.31	0.97 ± 0.41	9.03 ± 4.15 × 10^{-11}	239

Size Range : > 450 d.c.
Crab Rate (2000/2001 season) : 2.57 ± 0.18 min^{-1}
E_{th} (2000/2001 season) : 403 ± 79 GeV
Flux (2000/2001 season) : 8.32 ± 0.83 × 10^{-11} ph cm^{-2} s^{-1}

Season	Rate (min^{-1})	Rate (00/'01 rate)	Flux (ph cm^{-2} s^{-1})	E_{th} (GeV)
2001/2002	2.56 ± 0.18	0.99 ± 0.10	8.29 ± 1.17 × 10^{-11}	404
2002/2003	2.30 ± 0.15	0.90 ± 0.09	7.45 ± 1.03 × 10^{-11}	434
2003/2004	2.43 ± 0.19	0.95 ± 0.10	7.87 ± 1.14 × 10^{-11}	418

Table 5.16: Summary of tests for constant energy threshold as applied to box selected data. The average Crab Nebula rate for each season was calculated, compared to the 2000/2001 average rate, and then converted into a flux and energy threshold.

Size Range : No Limit
Crab Rate (2000/2001 season) : 1.87 ± 0.10 min^{-1}
E_{th} (2000/2001 season) : 147 ± 39 GeV
Flux (2000/2001 season) : 37.38 ± 5.28 × 10^{-11} ph cm^{-2} s^{-1}

Season	Rate (min^{-1})	Rate (00/'01 rate)	Flux (ph cm^{-2} s^{-1})	E_{th} (GeV)
2001/2002	2.04 ± 0.10	1.09 ± 0.08	40.78 ± 6.47 × 10^{-11}	139
2002/2003	1.92 ± 0.10	1.03 ± 0.08	38.38 ± 6.13 × 10^{-11}	144
2003/2004	1.88 ± 0.09	1.01 ± 0.07	37.58 ± 5.95 × 10^{-11}	147

Size Range : ≤ 450 d.c.
Crab Rate (2000/2001 season) : 1.75 ± 0.74 min^{-1}
E_{th} (2000/2001 season) : 131 ± 35 - 388 ± 76 GeV
Flux (2000/2001 season) : 35.58 ± 6.98 × 10^{-11} ph cm^{-2} s^{-1}

Season	Rate (min^{-1})	Rate (00/'01 rate)	Flux (ph cm^{-2} s^{-1})	E_{th} (GeV)
2001/2002	4.89 ± 0.81	2.79 ± 1.27	99.40 ± 49.18 × 10^{-11}	72
2002/2003	4.62 ± 0.58	2.64 ± 1.17	99.90 ± 45.35 × 10^{-11}	75
2003/2004	2.57 ± 0.63	2.47 ± 0.72	53.30 ± 27.52 × 10^{-11}	106

Size Range : > 450 d.c.
Crab Rate (2000/2001 season) : 1.83 ± 0.10 min^{-1}
E_{th} (2000/2001 season) : 393 ± 76 GeV
Flux (2000/2001 season) : 8.64 ± 0.86 × 10^{-11} ph cm^{-2} s^{-1}

Season	Rate (min^{-1})	Rate (00/'01 rate)	Flux (ph cm^{-2} s^{-1})	E_{th} (GeV)
2001/2002	2.03 ± 0.09	1.14 ± 0.08	9.58 ± 1.16 × 10^{-11}	404
2002/2003	1.88 ± 0.09	1.03 ± 0.08	8.87 ± 1.09 × 10^{-11}	434
2003/2004	1.88 ± 0.12	1.03 ± 0.09	8.87 ± 1.15 × 10^{-11}	418

Table 5.17: Summary of tests for constant energy threshold as applied to *Kernel* selected data. The average Crab Nebula rate for each season was calculated, compared to the 2000/2001 average rate, and then converted into a flux and energy threshold.

Season	*Tracking Ratio*		
	Supercuts	*Minicuts*	*Modified Supercuts*
2000/'01	0.3225 ± 0.0017	0.3327 ± 0.0010	0.2999 ± 0.0020
2001/'02	0.3181 ± 0.0019	0.3501 ± 0.0011	0.2977 ± 0.0022
2002/'03	0.3030 ± 0.0027	0.3617 ± 0.0019	0.2957 ± 0.0029
2003/'04	0.3254 ± 0.0021	0.3522 ± 0.0015	0.3063 ± 0.0022

Table 5.18: Seasonal values of *tracking ratio* calculated for *Supercuts*, *Minicuts* and *Modified Supercuts*.

The first test was used to determine if the *tracking ratio* was constant over all dark-field regions. This involved splitting up the *OFF* data by dark-field, calculating a *tracking ratio* for each field, and comparing these with the mean *tracking ratio* calculated over the season as a whole (Table 5.18). A second test was applied to determine if there was some systematic change in the shape of the *alpha* distribution over the course of an observing season, from September to June. Again the dark-field data was split up, this time on a month-by-month basis, and a *tracking ratio* calculated for each month. These monthly ratios were then compared to the mean value. In both tests the comparison mechanism used was the χ^2 statistic:

$$\chi^2 = \sum_{i=1}^{n} \frac{(\rho_i - \overline{\rho})^2}{\Delta\rho_i^2} \tag{5.12}$$

where ρ_i are the individual *tracking ratios*, $\Delta\rho_i$ the associated errors, and $\overline{\rho}$ the weighted mean *tracking ratio*. Plots of the *tracking ratios* calculated for each season, compared to the mean value, are shown in Figure 5.18, Figure 5.19 and Figure 5.20. Using the χ^2 value the probability of the *tracking ratio* being constant for each season was calculated, with the number of trials taken into account using Equation 5.3.

The results of the χ^2 test for constancy, on a month-by-month basis, are presented in Table 5.19. Throughout the 2000/2001 season there is no evidence for varying *tracking ratio*. This is not true for the subsequent season, with low probability after trials for constant *tracking ratio* in the case of all three selection methods. As discussed previously (Section 5.2.4) a number of changes were made to the detector during this time and these are most likely responsible for the variations. For season 2002/2003 the *tracking ratio* is stable for two of the three selections, with tentative evidence for a non-constant ratio in the case of *Minicuts*. During the last season, 2003/2004, *tracking ratios* calculated with all three methods are stable. The results of the dark-field tests are shown in Table 5.20. For seasons 2000/2001 and

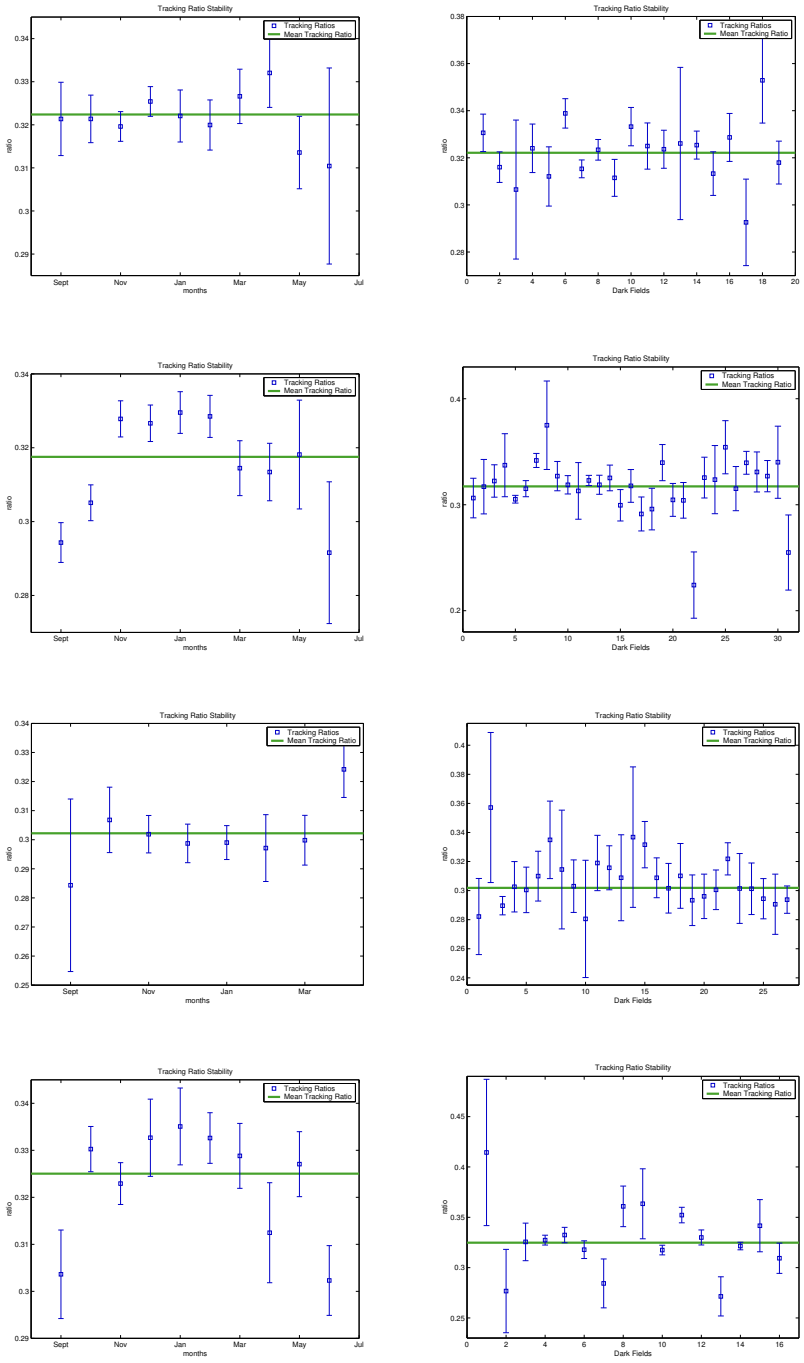

Figure 5.18: *Tracking Ratio* stability for *Supercuts* selection . Left: *Tracking ratios* calculated on a month-by-month basis, compared to the seasonal value. Right: *Tracking ratios* calculated by dark-field, compared to the seasonal value.

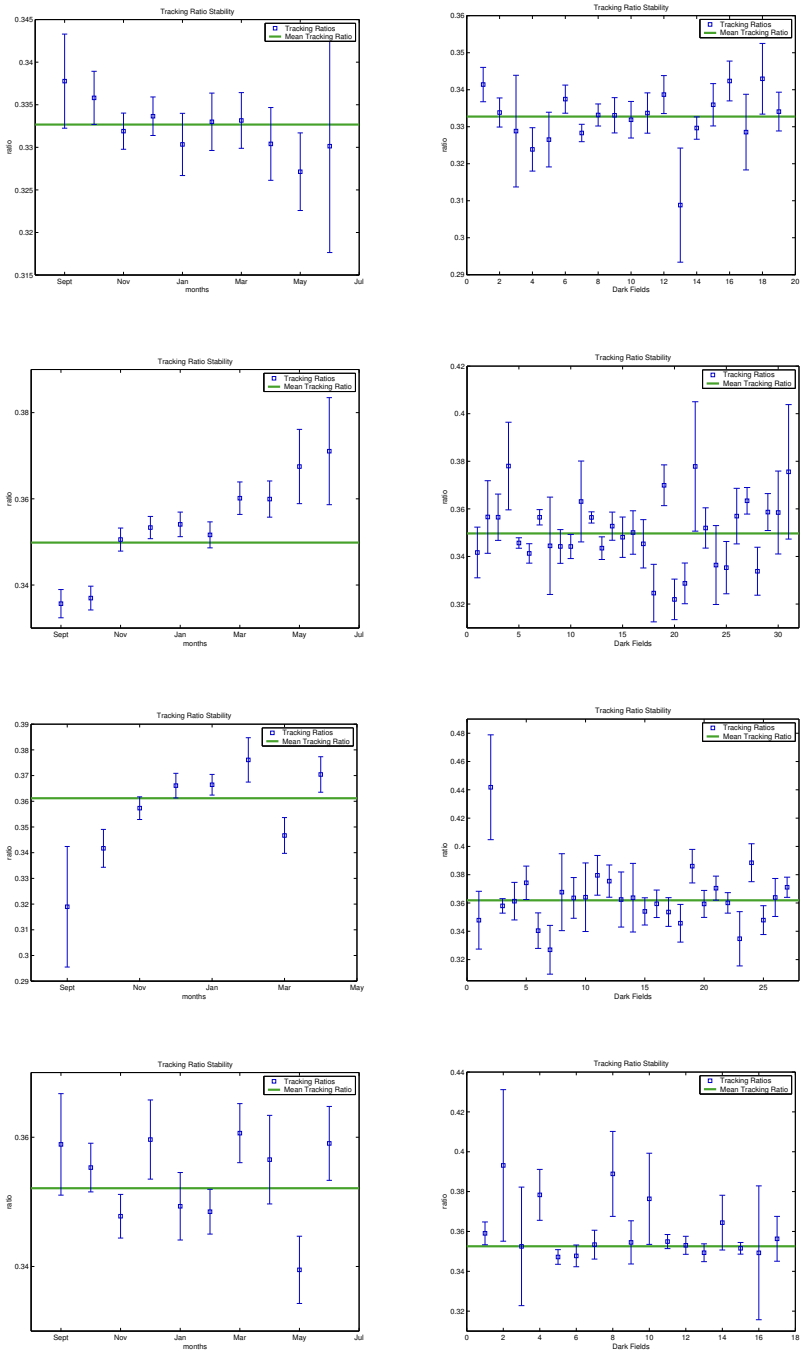

Figure 5.19: *Tracking Ratio* stability for *Minicuts* selection. Left: *Tracking ratios* calculated on a month-by-month basis, compared to the seasonal value. Right: *Tracking ratios* calculated by dark-field, compared to the seasonal value.

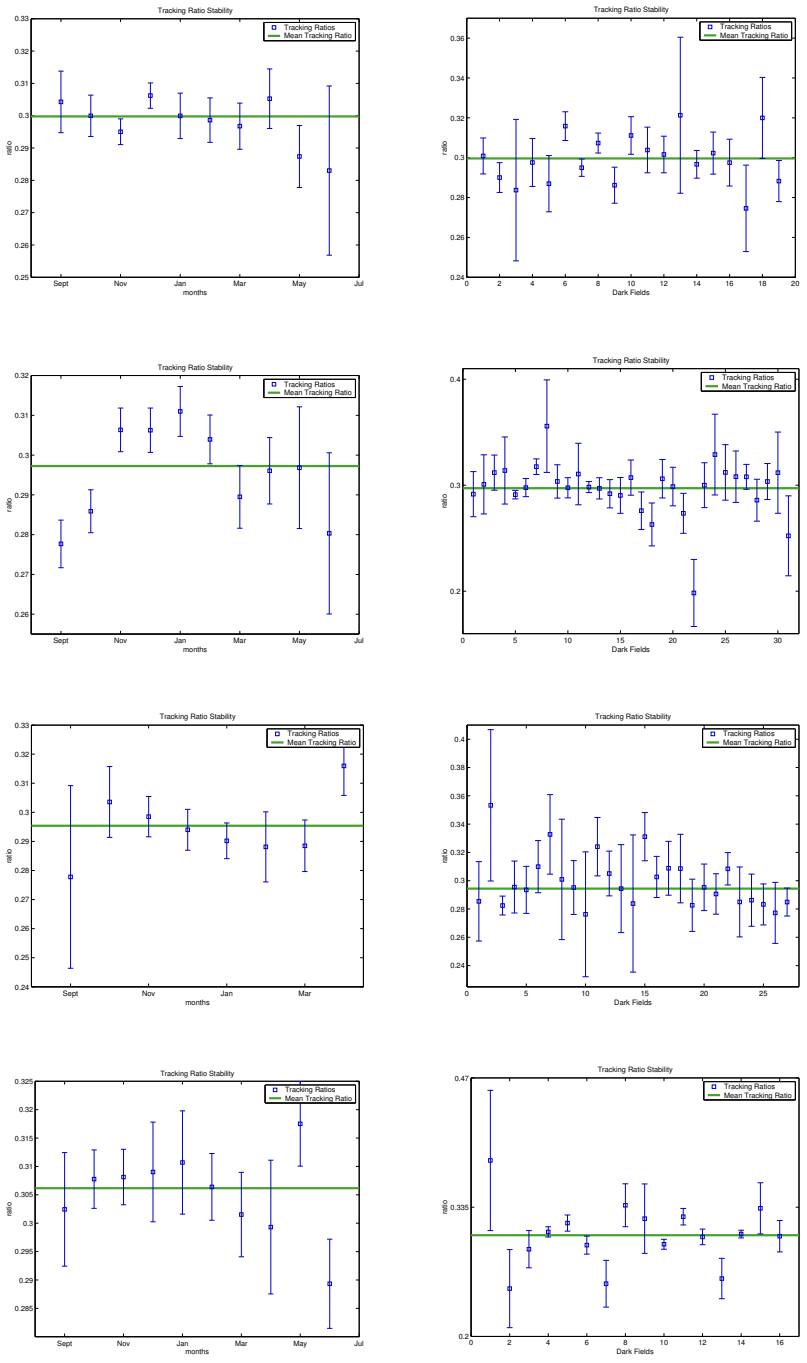

Figure 5.20: *Tracking Ratio* stability for *Modified Supercuts* selection. Left: *Tracking ratios* calculated on a month-by-month basis, compared to the seasonal value. Right: *Tracking ratios* calculated by dark-field, compared to the seasonal value.

Year	Selection	$\bar{\rho}$	χ^2/df	P_{χ^2}	P_{trials}
2000/'01	*Supercuts*	0.3239	4.93/9	0.84	0.99
	Minicuts	0.3327	4.42/9	0.88	0.99
	Modified Supercuts	0.2998	6.98/9	0.64	0.98
2001/'02	*Supercuts*	0.3175	43.42/9	1×10^{-6}	7×10^{-6}
	Minicuts	0.3498	65.29/9	1×10^{-10}	0
	Modified Supercuts	0.2972	28.17/9	8.9×10^{-4}	3×10^{-3}
2002/'03	*Supercuts*	0.3022	6.56/7	0.48	0.93
	Minicuts	0.3612	22.88/7	1.8×10^{-3}	7×10^{-3}
	Modified Supercuts	0.2954	6.82/7	0.49	0.91
2003/'04	*Supercuts*	0.3250	22.09/9	8×10^{-3}	0.03
	Minicuts	0.3521	17.27/9	0.05	0.17
	Modified Supercuts	0.3062	8.38/9	0.50	0.94

Table 5.19: Probability of the *tracking ratio* being constant on a month-by-month basis over the course of a season.

2002/2003 the *tracking ratio* is constant, as shown by the high probabilities obtained. For the 2001/2002 season, the *tracking ratio* is variable for *Supercuts* and *Minicuts* selected events yet stable in the case of *Modified Supercuts*. The instability of the two selections is probably due to the changes made to the instrument. The fact that this instability is not apparent in the case of *Modified Supercuts* is most likely due to the increased energy threshold, which makes the selection less sensitive to small changes in conditions. For 2003/2004 the *tracking ratio* is constant for *Minicuts* and *Modified Supercuts* with tentative evidence of variability for *Supercuts*.

Although clear that the *tracking ratio* is relatively stable (at least for three out of four seasons), it is unclear how small differences in the ratio affects background estimation. Minute differences, although not important in the case of small datasets, may produce a measurable effect as the amount of data analysed increases. In an attempt to quantify this effect, a test was applied to *OFF* data recorded during 2002/2003. The test involved splitting the *OFF* data into a number of subsets, with an increasing amount of data in each one. For all subsets the signal excess (expressed in standard deviations above background) was calculated for a range of *tracking ratio* values. Since the test is applied strictly to *OFF* data, where there is no true gamma-ray

Year	Selection	$\bar{\rho}$	χ^2/df	P_{χ^2}	P_{trials}
2000/'01	*Supercuts*	0.3221	24.61/18	0.14	0.44
	Minicuts	0.3328	21.51/18	0.25	0.69
	Modified Supercuts	0.2996	19.27/18	0.38	0.85
2001/'02	*Supercuts*	0.3173	58.49/30	1×10^{-3}	6×10^{-3}
	Minicuts	0.3497	69.74/30	5×10^{-5}	2×10^{-4}
	Modified Supercuts	0.2972	33.98/30	0.28	0.73
2002/'03	*Supercuts*	0.3019	18.69/26	0.85	0.99
	Minicuts	0.3619	34/26	0.12	0.39
	Modified Supercuts	0.2944	20.21/26	0.78	0.99
2003/'04	*Supercuts*	0.3248	37.19/15	1×10^{-3}	5×10^{-3}
	Minicuts	0.3256	15.44/16	0.49	0.93
	Modified Supercuts	0.3058	28.14/15	0.02	0.08

Table 5.20: Probability of *tracking ratio* being consistent over all dark-field regions for a given season.

excess, any excess introduced is due to a shift in *tracking ratio* away from its true value. The *tracking ratio* was varied by $\sim 5\,\%$ either side of the mean *tracking ratio* value for the season. When applying these different *tracking ratios* to the data the error on the mean *tracking ratio* value was applied. The results of this process are illustrated in Figure 5.21, showing the change in significance as a function of *tracking ratio* for a number of differently-sized datasets. From this plot is is obvious that as the data size increases a small change in *tracking ratio* produces a larger false excess, proving that effects due to variations in *tracking ratio* are more pronounced for larger datasets.

To quantify the change in significance as a function of change in *tracking ratio*, a fit was applied to the results for each differently sized dataset. For a dataset of given size the change in significance was found to vary linearly with changing *tracking ratio*. Thus the change in *tracking ratio* required to produce a nominal σ effect may be calculated by:

$$\Delta\,\rho = \frac{\Delta\,\sigma}{R_{\,\sigma}} \tag{5.13}$$

where $\Delta\,\rho$ is the change in *tracking ratio*, $\Delta\,\sigma$ is the change in significance, and $R_{\,\sigma}$ is the rate at which the significance changes (or the slope of the afore-

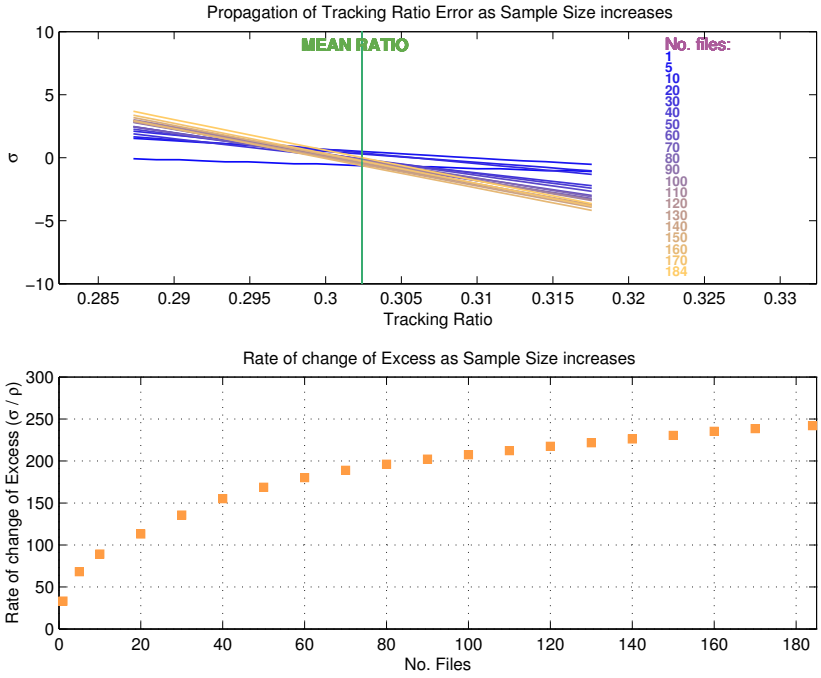

Figure 5.21: Effect of changing *tracking ratio* on signal excess as the amount of data analysed is increased. For a number of differently sized datasets, the signal excess was calculated using different *tracking ratio* values. The top plot shows the change in σ for differently sized datasets and different values of *tracking ratio*. The bottom plot shows the rate at which the excess changes (per change in *tracking ratio* for differently sized datasets, effectively a plot of the slopes of the lines shown in the top figure).

mentioned fit). Using this approach it is possible to calculate the percentage change in *tracking ratio* required to introduce a 3σ effect into a dataset of given size. The results of such a calculation, shown in Figure 5.22, are very interesting. For analysis of data using the *Supercuts* selection, a small change in *tracking ratio* ($\sim 5\,\%$) may introduce a false 3σ excess when the dataset includes approximately 80 files (each of duration 28 minutes). This is in agreement with previous results regarding changes in *tracking ratio* (de la Calle Perez and Holder, 2001; de la Calle Perez, 2003), and calls into question the use of *TRACKING* analysis when attempting to detect a weak gamma-ray signal from deep-exposure observations. The effect is slightly less pronounced when selecting events using *Modified Supercuts*, most likely due to a small decrease in rate caused by the addition of the lower *size* cut. Most worryingly, but somewhat expected, when applying *Minicuts* the same 3σ effect is manifest for a much smaller dataset. This may be attributed to the increased rate in the energy region in which *Minicuts* operates. As a result of these tests it was concluded that *TRACKING* analysis should not be used when applying *Minicuts* and that an alternative method should be investigated.

5.7 Matched Analysis

Since it was decided that the *TRACKING* approach to background estimation was unsafe for use with *Minicuts*-selected events some alternative method is required. The *ON/OFF* approach would be ideal, were it not for the fact that a large amount of data is recorded in *TRACKING* mode. A third approach to estimating background levels was first proposed by Quinn et al. (2001). This approach, known as matched analysis, attempts to accurately estimate the background level using *OFF* data recorded for different sources. The *OFF* data is chosen so that it "best matches" the *ON*; basically the control data is chosen so that the conditions (both atmospheric and telescopic) under which *ON* and *OFF* runs are recorded are most similar. A more formal approach to the matching process was devised by de la Calle Perez (2003), where the *ON* and *OFF* run are compared using five parameters:

1. Modified Julian Date
2. Relative Throughput
3. Elevation
4. Mean Night-Sky Background

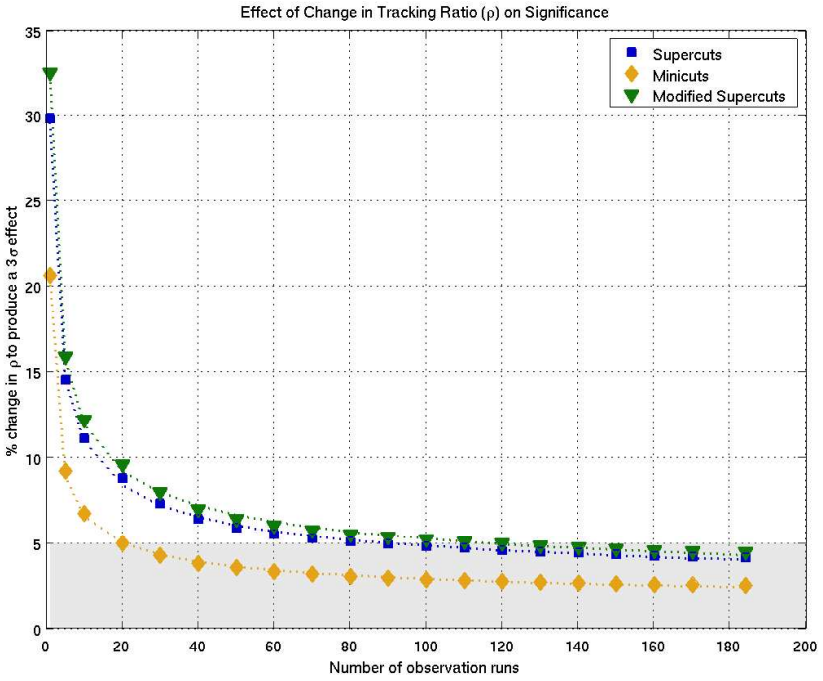

Figure 5.22: Effect of changing *tracking ratio* on gamma-ray excess as the amount of data analysed is increased. It is clear that a small change in *tracking ratio* is capable of producing a noticeable effect. While important only in the case of deep exposures when applying *Supercuts*, the effect becomes noticeable for any modestly-sized datasets when applying *Minicuts*.

5. Number of pixels turned on

The first two parameters, Modified Julian Date, and Relative Throughput are chosen to ensure that both weather and telescope conditions are as similar as possible.

Relative Throughput is defined as the ratio of the Cherenkov luminosity produced by the same extensive air shower, under different conditions (Lebohec and Holder, 2003). Assuming that the spectrum of cosmic rays is constant at TeV energies, differences between the luminosity distribution of two observations must arise from differences between the conditions under which both observations were made. Thus, relative throughput provides a measure of changes in the atmosphere and telescope over time. For data recorded with the Whipple telescope, luminosity is defined as the total light content of an image (or the parameter *size*), after cleaning has been applied. To calculate throughput, first a reference run is chosen to which all subsequent data is compared. The luminosity distribution of the reference run and that of a given dataset are constructed, and for the example shown in Figure 5.23 the two distributions are offset. The event luminosities of the data are scaled, by a range of factors, until the luminosity distribution matches that of the reference dataset. The scale factor that minimises the difference between the two distributions (as determined using a χ^2 test) is defined as the relative throughput.

The three remaining parameters; elevation, mean night-sky background and number of pixels are included in the matching procedure to ensure comparable raw rates. Using all five parameters a matching score is calculated as follows:

$$Match = \frac{\Delta_{mjd}}{\omega_{mjd}} + \frac{\Delta_{tru}}{\omega_{tru}} + \frac{\Delta_{ele}}{\omega_{ele}} + \frac{\Delta_{nsb}}{\omega_{nsb}} + \frac{\Delta_{npix}}{\omega_{npix}} \tag{5.14}$$

where the Δ terms represent the differences between matching parameters for the *ON* and *OFF* files being compared, and the ω terms are the weighting factors used by de la Calle Perez (2003). Although matching scores close to unity are considered best (the weighting terms were chosen to produce such a result), analysis in the next section questions the importance of the absolute value of the score (Section 5.7.1). When applying matched analysis to a set of *ON*-source observations (of size N), a database of *OFF* runs (of size M) is first constructed, then every *ON* run is compared to every *OFF* run to produce an N $\times$ M matrix of matching scores. The best matched pairs are identified as those with the lowest scores, taking care to ensure that each *OFF* run is used only once. The best-matched pairs are then subject to standard analysis procedures (including calibration, image cleaning, noise padding,

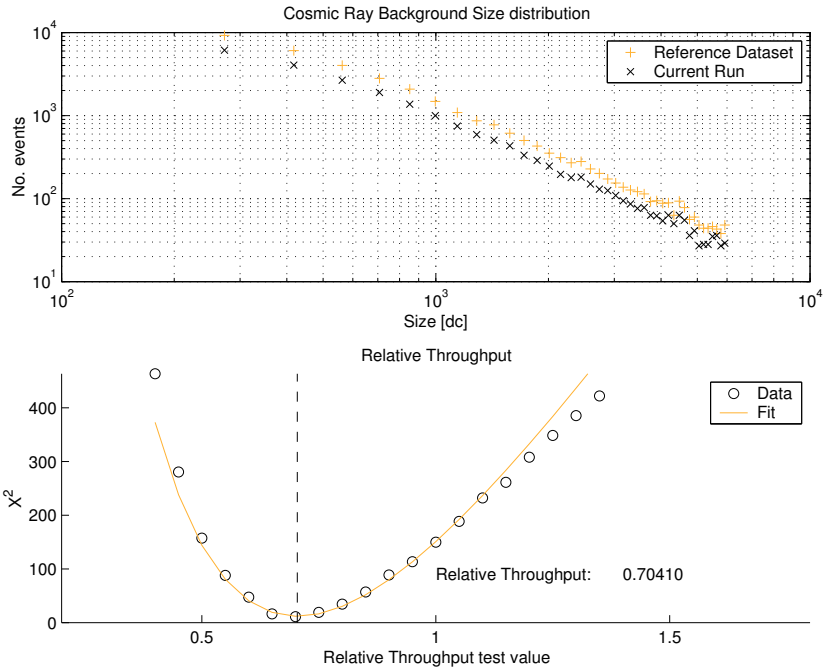

Figure 5.23: Calculation of relative throughput factor. In the top figure the luminosity (or *size*) distributions for a given dataset and reference dataset are shown. The given distribution is adjusted by a range of scaling factors, and a χ^2 test applied to compare the scaled distribution to the reference distribution. The scale factor which produces the best fit, identified as that with the minimum χ^2 value, is the relative throughput (shown in the bottom plot).

parameterisation and gamma-ray selection), after which the background level may be calculated by one of two methods:

1. The *OFF* run may be used to calculate a run-specific *tracking ratio*. By applying this to the *ON* data the number of background events may be estimated.

2. With the addition of a scaling factor the background level may be estimated using the traditional *ON/OFF* approach.

Throughout this work the second approach to background estimation is used. As stated, this method requires addition of a scaling factor, to account for differences between the number of events passing selection in the *ON* and *OFF* datasets. The scaling factor is defined as:

$$\alpha_{\,match} = \frac{C_{\,ON}}{C_{\,OFF}} \tag{5.15}$$

where C_{ON} and C_{OFF} are the number of counts in the *ON* and *OFF alpha* distributions from 20° to 65°, and is applied to the *OFF* dataset. In the case of *Kernel* analysis the scaling factor is calculated as the ratio of events in the *ON* and *OFF* datasets that fail the log(R) selection cut. The gamma-ray rate for matched analysis is given by:

$$R_{match} = \frac{N_{on} - \alpha_{match}\, N_{off}}{t} \;\pm\; \sqrt{\frac{N_{on} + \alpha^2_{match}\, N_{off} + (\Delta\, \alpha_{match})^2\, N^2_{off}}{t^2}} \tag{5.16}$$

and the corresponding significance is:

$$\sigma_{match} = \frac{N_{off} - \alpha_{match} N_{off}}{\sqrt{N_{on} + \alpha^2_{match}\, N_{off} + (\Delta\, \alpha_{match})^2\, N^2_{off}}} \tag{5.17}$$

5.7.1 Stability of Matched Analysis

It has already been shown that small changes in *tracking ratio* can adversely affect the estimation of background, which in turn has a profound influence on the signal strength. This effect is due to sky-brightness differences between the different dark-fields used to estimate background and changes in telescope response over time. Since the matching technique is reliant on *OFF* data from dark-field regions that are associated with other sources, a similar effect may occur, resulting in a false excess (or deficit). To determine if such effects were manifest *OFF* data from four seasons, 2000/2001, 2001/2002,

2002/2003 and 2003/2004, was used to test the stability of the matched approach. Each year's data was randomly divided into two groups, A and B. The files in group A were matched to those in group B and although a number of pairs were poorly matched (with a high score) all data was used. Two tests were applied to the data, the first was a test of overall significance which is expected to be zero since both dataset comprise observations of gamma-ray dark sky regions. The second test was a test of the distribution of rate, again because observations comprise *OFF* data only the rate distribution should be consistent with zero. The following χ^2 statistic was used to test this hypothesis:

$$\chi^2 = \sum_{i=1}^{n} \frac{(R_i - 0)^2}{\Delta R_i^2} \tag{5.18}$$

where R_i are the individual rates and ΔR_i the associated statistical errors. The tests were applied to data analysed using box selection and *Kernel* selection, over the three *size* ranges previously defined. The results of this process (Table 5.21) provide no evidence to suggest that box selection of matched data introduces a false excess. In all cases the overall excess is not statistically significant and the probability of the rate distribution being consistent with zero is above the rejection level of one percent after trials. The results for *Kernel*-selected events are very different, with extremely low probabilities ($\ll 1\,\%$) of zero rate in all cases. This indicates that the application of *Kernel* selection in conjunction with matched data may not be sufficiently robust. With its extremely low energy threshold, the *Kernel* is sensitive to events near to the telescope's threshold where small differences between datasets (such as sky brightness) are more pronounced. Results for both selection methods are illustrated in Figure 5.24. In the case of box-selected events, the rate distribution appears to be consistent with zero, within statistics. This cannot be said for kernel-selected events, where there are a number of data points inconsistent with zero, a fact further illustrated by comparing the distribution of significance for both approaches. In the case of box-selected events the distribution is well contained by a Gaussian of zero mean and unit variance; however, for *Kernel*-selected data there are a number of points which fall outside the expected distribution.

Although a matching score close to unity is considered ideal, there is no consensus as to what value is unacceptable. It is important to select the best matched pairs, however results presented (Table 5.21) show that the magnitude of the matching score is not critical when using box selection. The low probability of zero excess following application of *Kernel* analysis, suggests that the magnitude of the matching score may be important when dealing

Size Range	Box Selection				*Kernel* Selection			
/ Year	Excess	χ^2/df	P_{χ^2}	P_{trial}	Excess	χ^2/df	P_{χ^2}	P_{trial}
2000/2001								
No Limit	-0.552 σ	146/143	0.41	0.88	-0.582 σ	363/142	0	0
$\leq$ 450 d.c.	0.580 σ	166/142	0.08	0.29	0.177 σ	654/142	0	0
$>$ 450 d.c.	-0.598 σ	138/143	0.61	0.98	-0.264 σ	330/142	0	0
2001/2002								
No Limit	-0.289 σ	214/189	0.10	0.35	0.670 σ	323/189	10^{-9}	0
$\leq$ 450 d.c.	0.519 σ	209/188	0.14	0.454	-0.619 σ	539/189	0	0
$>$ 450 d.c.	-0.047 σ	181/189	0.66	0.99	0.842 σ	292/189	10^{-6}	10^{-6}
2002/2003								
No Limit	0.626 σ	201/162	0.02	0.08	-2.78 σ	308/162	0	0
$\leq$ 450 d.c.	-0.490 σ	177/161	0.19	0.56	-2.368 σ	764/162	0	0
$>$ 450 d.c.	0.596 σ	204/162	0.02	0.06	-3.97 σ	375/162	0	0
2003/2004								
No Limit	1.370 σ	132/117	0.17	0.51	-3.020 σ	280/117	0	0
$\leq$ 450 d.c.	-1.197 σ	115/117	0.53	0.95	0.49 σ	515/117	0	0
$>$ 450 d.c.	1.276 σ	131/117	0.18	0.54	-2.320 σ	279/117	0	0

Table 5.21: Results of testing the matched analysis process for evidence of an excess. Two test were applied, the first to determine if the overall significance was zero, the second to determine if the distribution of rate was consistent with zero. Rejection of the null hypothesis was at a probability level of one percent. The table shows that there is no evidence of a false excess when box selection methods are used, as indicated by low excess and high probability values. The results following application of *Kernel* analysis are very different, with higher overall excess and low probabilities indicating a non-zero rate. Note that probability values less than 10^{-10} were set to zero.

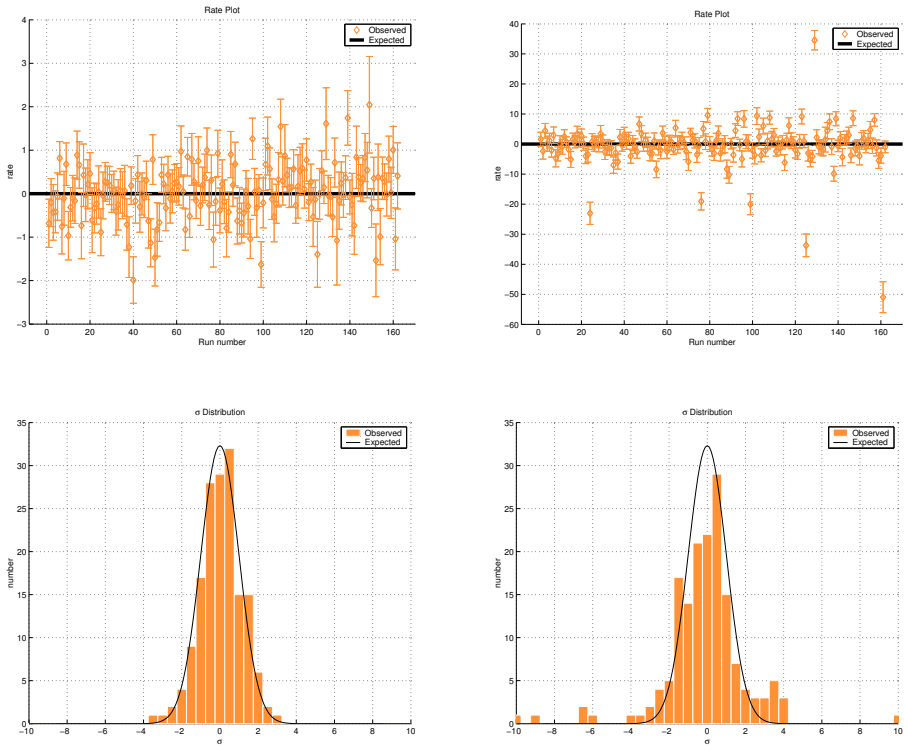

Figure 5.24: Illustration of results of matched analysis stability test applied to box-selected events and *Kernel*-selected events. Data selected using traditional box methods are shown on the left while *Kernel* data are shown on the right. The rate distribution is consistent with zero for box data, but not so for *Kernel* data. This is further illustrated by the significance distributions. Whereas the box distribution is well described by a Gaussian of zero mean and unit variance, the *Kernel* distribution is much more diffuse, with a number of outliers clearly inconsistent with zero. These plots were made using events selected over the entire *size* range, for data recorded during the 2002/2003 season.

with the more sensitive *Kernel* approach. The implication is that by limiting the dataset to pairs with sufficiently low matching scores, *Kernel* analysis may be applied. To determine if the instability of the *Kernel* approach was a result of poorly-matched data, the A/B datasets were further divided into subsets comprising pairs with matching scores: (a) between zero and three, (b) between three and five, and (c) greater than five and subjected to the same stability tests outlined above. For completeness the tests were applied to events selected using *Kernel* analysis and box analysis.

The results of these tests for box-selected events (Table 5.22) are in agreement with those already obtained. The probability of the rate distribution being consistent with zero is high for all datasets, irrespective of the level of matching. This further illustrates the point that although matching is important as a means to identify the most suitable background data, the magnitude of the matching score does not appear critical. Results of tests applied to *Kernel*-selected events are not as straightforward. In most cases the probability of zero rate is low (Table 5.23), indicating that the *Kernel* is unstable even when analysis is restricted to well-matched pairs. There are exceptions to this overall trend; in the case of 2001/2002 data the rate is consistent with zero for matching scores less than three and between three and five. This implies that the matching score may be important, however the fact that the probability for zero rate is higher in the *3-5* dataset than in the *0-3* data suggests otherwise. Overall it is concluded that *Kernel* analysis is too sensitive to small differences between datasets for application to matched data.

5.8 Summary

Development and testing of a number of methods for gamma-ray selection have been presented. It has been shown that the newly-developed *Minicuts* provides access to a region of the gamma-ray spectrum previously unexplored by *Supercuts*. The selection technique is stable over the course of a season and the energy threshold is constant throughout the last four years. By applying *Minicuts* in conjunction with *Modified Supercuts* a more efficient selection is achieved, compared to that obtained by application of traditional *Supercuts*. The *Kernel* approach to event selection has also been discussed, with a dual *Kernel* approach also proving more efficient than a single selection. The *Kernel* offers an extremely low energy threshold; however, because of this it is very sensitive to changes in detector or observing conditions. Although the *Kernel* selection is stable for a given season its energy threshold varies from year to year, thus it is not possible to combine observations from different

Year / Subset	No Limit				$\leq$ 450 d.c				$>$ 450 d.c.			
	Excess	χ^2/df	P_{χ^2}	P_{trial}	Excess	χ^2/df	P_{χ^2}	P_{trial}	Excess	χ^2/df	P_{χ^2}	P_{trial}
2000/2001												
0 - 3	-1.37	97/90	0.28	0.74	-1.29	86/89	0.56	0.97	-1.21	86/90	0.61	0.97
3 - 5	0.96	28/27	0.40	0.88	2.02	44/27	0.02	0.08	0.59	28/27	0.40	0.88
≥ 5	0.25	12/26	0.77	0.99	1.80	35/26	0.11	0.38	0.22	24/26	0.59	0.97
2001/2002												
0 - 3	-0.76	158/153	0.19	0.85	0.83	160/142	0.14	0.46	-0.19	131/143	0.75	0.99
3 - 5	0.49	16/23	0.86	0.99	-1.35	32/23	0.10	0.34	1.07	22/23	0.53	0.95
≥ 5	0.52	40/23	0.01	0.06	0.74	17/23	0.78	0.99	-0.69	28/23	0.23	0.62
2002/2003												
0 - 3	-0.61	145/112	0.02	0.08	-0.36	129/111	0.12	0.39	-0.46	138/112	0.05	0.18
3 - 5	1.34	29/28	0.38	0.88	-0.30	30/28	0.36	0.84	1.28	35/28	0.18	0.53
≥ 5	1.45	27/22	0.22	0.61	-0.15	18/22	0.70	0.99	1.13	31/22	0.09	0.33
2003/2004												
0 - 3	1.12	95/98	0.21	0.62	-1.47	70/85	0.88	0.99	1.14	95/85	0.22	0.62
3 - 5	0.42	25/23	0.33	0.82	0.53	27/23	0.28	0.69	0.22	26/23	0.28	0.76
≥ 5	0.86	11/9	0.28	0.73	-0.64	19/9	0.03	0.13	0.76	10/9	0.39	0.82

Table 5.22: Results of tests applied to *OFF* data to determine if the level of matching is important for box selection methods. The *OFF* dataset was divided up based on matching score and tested for non-zero rate. The consistently high probabilities presented prove that matched data may be used in conjunction with box selection methods and further illustrate the point that the magnitude of the matching score is not important.

Year / Subset	No Limit				$\leq$ 450 d.c				$>$ 450 d.c.			
	Excess	χ^2/df	P_{χ^2}	P_{trial}	Excess	χ^2/df	P_{χ^2}	P_{trial}	Excess	χ^2/df	P_{χ^2}	P_{trial}
2000/2001												
0 - 3	-0.73	156/89	10^{-5}	10^{-5}	-1.14	226/89	0	0	-1.70	139/89	10^{-4}	10^{-3}
3 - 5	-2.41	60/27	10^{-4}	10^{-3}	3.81	108/27	10^{-11}	0	-0.04	57/27	10^{-4}	10^{-3}
$\geq$ 5	2.68	147/26	0	0	-1.29	320/26	0	0	2.63	134/26	0	0
2001/2002												
0 - 3	0.15	236/142	10^{-6}	10^{-6}	-0.14	327/142	0	0	0.96	186/142	10^{-3}	0.03
3 - 5	2.12	30/23	0.16	0.48	-1.17	139/23	0	0	0.43	38/23	0.02	0.09
$\geq$ 5	-0.66	57/23	10^{-4}	10^{-4}	-0.31	74/24	10^{-7}	10^{-6}	-0.13	67/24	10^{-6}	10^{-5}
2002/2003												
0 - 3	-1.35	171/112	10^{-4}	10^{-3}	-2.09	342/112	0	0	-2.60	183/112	10^{-5}	10^{-4}
3 - 5	-2.61	71/28	10^{-5}	10^{-5}	0.20	277/28	0	0	-1.50	66/28	10^{-5}	10^{-4}
$\geq$ 5	-2.30	66/22	10^{-6}	10^{-5}	-2.08	146/22	0	0	-3.95	126/22	0	0
2003/2004												
0 - 3	-1.72	159/85	10^{-6}	10^{-6}	0.81	404/85	0	0	-1.37	155/85	10^{-6}	10^{-5}
3 - 5	-1.15	59/23	10^{-5}	10^{-4}	1.02	64/23	10^{-5}	10^{-5}	-0.66	60/23	10^{-5}	10^{-4}
$\geq$ 5	-3.39	61/9	0	0	-2.44	48/9	10^{-5}	10^{-5}	-3.44	64/9	0	0

Table 5.23: Results of tests applied to *OFF* data to determine if the level of matching is important for *Kernel* analysis. The *OFF* dataset was divided up based on matching score and tested for non-zero rate. The low probabilities presented prove that, irrespective of the level of matching, *Kernel* selection is not sufficiently robust to use with matched data.

seasons into a single dataset. This problem may be overcome by applying a lower *size* cut of 250 d.c., which equalises the thresholds for all four seasons, but this comes at the expense of a higher energy threshold. It was decided that the low-energy *Kernel* would be applied to observations from within any given season and that data recorded over the course of several seasons would be analysed by including the lower *size* cut. In general it was shown that the *Kernel* outperforms traditional box selection techniques yielding higher significances, improved collection areas and lower energy thresholds.

The *TRACKING* approach to background estimation has been shown to be relatively stable over the course of a season, however it has also been shown that small differences in the shape of the *alpha* distribution can introduce a false excess. As a result it was concluded that *TRACKING* analysis should not be used when applying *Supercuts* to a large dataset in the search for new gamma-ray sources. It was also proved that *TRACKING* analysis should never be used in conjunction with *Minicuts* as a false excess is likely even for medium-sized datasets.

The matching approach to background estimation has been introduced and discussed with a number of tests carried out to determine the stability of the approach. It was concluded that box selection methods may be applied to data analysed in matched mode, however the *Kernel* technique is too sensitive to differences in the data to be applied.

The analyses described throughout this chapter will now be applied to data recorded on a number of BL-Lac objects over the last four years, in the search for new sources of VHE radiation. The results of this analysis are presented in the next chapter.

Chapter 6

A Search for VHE Gamma-ray Emission from Blazars

6.1 Introduction

This thesis is concerned with detection of new sources of VHE gamma radiation. Although ground-based gamma-ray astronomy has made considerable progress over the last decade there are many details of AGN physics which remain unknown. One of the major obstacles to studying extragalactic sources of gamma rays in greater detail is absorption of gamma rays by extragalactic soft-photon fields. This absorption results in a VHE spectrum, measured here on Earth, which is a convolution of the true source spectrum and effects due to extragalactic background light (EBL). By accurately measuring the intrinsic spectrum it should be possible to address many of the outstanding issues of AGN physics, such as the primary particle population responsible for gamma-ray production, whilst also uncovering information regarding the density and nature of the EBL. Determination of the effect of the EBL requires detection and study of a greater number of extragalactic sources of gamma rays at varying redshift. With this in mind a number of new gamma-ray selection techniques have been developed and tested, with emphasis placed on selecting gamma rays in a region of the spectrum not normally targeted by standard Whipple analyses. Details of these developments were provided in the preceding chapter. This chapter presents results following application of the analyses to a sample of 16 BL-Lac objects. A summary of the observations of each source is provided and in the case of a non-detection, flux upper limits are calculated and compared to the predictions of a number of authors. By combining observations from all objects a search is also made to determine if there is any evidence for low-level emis-

sion, below the sensitivity of the current Whipple instrument. The chapter concludes with an in-depth discussion of a possible detection of the object 1ES 0806+524.

6.2 Analysis

Based on flux predictions detailed in Costamante and Ghisellini (2002) and Stecker et al. (1996) a number of BL-Lac objects were identified as being most likely to produce VHE gamma radiation. Before proceeding with the analysis of these objects, quality checks were applied to ensure observations were carried out in stable weather conditions. These quality checks comprised a χ^2 test to determine if the telescope trigger rate was constant over the course of a data run. After eliminating poor-weather observations, a sample of 16 BL-Lac objects remained, a summary of which is provided in Table 2.3. Over the last four seasons, stretching from September 2001 to July 2004, a total of 255 hours of observations were carried out on these objects. A detailed breakdown of the observations, including the amount of data recorded in *ON/OFF* and *TRACKING* mode (Section 4.3.4), is provided in Table 6.1. All data were subject to standard calibration and cleaning processes, followed by selection of gamma rays using the box and *Kernel* methods, as detailed in the previous chapter (Chapter 5).

In the case of box selection, for a given source, all data recorded in *ON/OFF* and *TRACKING* mode, over the course of four seasons, were combined. Gamma rays were selected using *Supercuts*, *Minicuts* and *Modified Supercuts*, and the excess number of events calculated using the matched approach for background estimation. The distribution of the parameter *alpha* is extremely useful for determining if an event excess is really due to gamma rays, and accordingly the *alpha* distribution for each selection is provided for inspection. By their very definition BL-Lac objects are highly variable at all wavelengths, with observations of a number of sources at VHE showing that flux levels in this energy range can increase on the scale of hours or shorter (Gaidos et al., 1996; Catanese et al., 1998). To determine if any of these sources exhibited short episodes of increased flux, a χ^2 test for consistency with zero rate, on a run-by-run basis, was applied. This test was identical to that used in Section 5.2.4. As a complement to the χ^2 test, the distribution of run-by-run significance is provided for examination. The overall significance and χ^2 test results are summarised in Table 6.2.

For *Kernel* selection, all *ON/OFF* data recorded over the four observing seasons were combined and analysed. Data recorded in *TRACKING* mode were not used for two reasons. The first is due to the nature of *Kernel* selec-

tion and the *TRACKING* approach to background estimation. The *Kernel* method selects events based on the convolution of a number of parameters, including *alpha*. When analysing data in *TRACKING* mode the shape of the *alpha* distribution is used to estimate the background number of events. Accordingly, when applying *Kernel* analysis to *TRACKING* data the *alpha* parameter cannot be included in the convolved selection cut as usual, rather it is introduced as a subsequent selection cut. The powerful nature of the *alpha* parameter as a discriminant means that the *Kernel* is not very efficient when utilised in this way (Dunlea, 2001). The second reason for applying *Kernel* analysis to *ON/OFF* data only, is due to the fact that the use of *Kernel* selection combined with matched data has proved unstable (due to differences between the *ON* and control datasets).

As discussed previously, the threshold for the lowest-energy *Kernel* is not constant from season to season. This means that, when using this selection, it is incorrect to combine observations from different seasons. To solve this problem a *size* cut of 250 d.c. was applied to the low-energy *Kernel* selection, producing a constant software threshold throughout the four seasons. The solution resulted in a rise in threshold and since the analysis was originally designed to target gamma-ray events of the lowest possible energy this is particularly undesirable. As a compromise, the *Kernel* with the 250 d.c. *size* cut included was applied to all observations on a given source combined, while the same *Kernel* without the *size* cut was applied to observations of a source within any given season. *Alpha* distributions are not provided since the *alpha* parameter is already folded into the *Kernel* selection. In keeping with the approach used during box selection, a search was also carried out for episodes of increased flux activity and distributions of run-by-run significance are provided for review. When applying the variability test to events selected with the low-energy *Kernel* for a given season, the number of trials is taken into account using the the approach outlined in Section 5.2.4. A summary of the *Kernel* results is provided in Table 6.3 and Table 6.4.

In the case of a non-detection, flux upper limits were calculated using the method of Aharonian et al. (2000), described in Chapter 4. When utilising this approach, the number of *ON* and *OFF* source counts is used to calculate a counts upper limit according to Helene (1983). Using contemporaneous Crab Nebula observations the count upper limit is converted to a flux upper limit in terms of the Crab Nebula, which may then be converted to a true flux upper limit using the known form of the VHE Crab Nebula spectrum. The advantage of using an approach which relies on real observations, compared to the more traditional method based on simulated collection areas, is that systematic errors, caused by Monte-Carlo simulations of air showers and detector response, are minimised. The only possible source of error is the

use of simulations to estimate the energy threshold of the system. Since gamma-ray rate depends on the particular elevation at which observations are carried out, it is important to utilise Crab Nebula data with a similar elevation distribution to that of the source under investigation. In this work Crab Nebula data chosen from an elevation range between two standard deviations above and below the mean source elevation was utilised. In the case of a negative gamma-ray rate, that is where the number of candidate gamma rays in the *OFF* dataset is greater than that in the *ON*, the counts upper limit was calculated using an *ON*-source count equal to the *OFF*-source count. Due to the limited *ON/OFF* observations and the difficulty of combining data from different seasons, upper limits were not calculated for *Kernel* analysis. For each source two upper limit values were calculated, corresponding to events selected using *Minicuts* and *Modified Supercuts*. The more constraining of these was subsequently converted to an integral flux upper limit above 300 GeV, by assuming a Crab Nebula like spectrum, so that comparison with the predictions of Stecker et al. (1996) and Costamante and Ghisellini (2002) could be made. Both *Minicuts* and *Modified Supercuts* flux upper limits were also converted to a differential flux at 236 GeV and 403 GeV respectively, in correspondence with the energy threshold of each selection method. By doing so it was possible to compare these limits to the spectral energy distribution plots of Costamante and Ghisellini (2002).

6.3 Results

In the case of box selection there is no evidence for steady gamma-ray emission from any object, as evidenced by the statistically insignificant excesses obtained (Table 6.2). This null result is illustrated by the *alpha* distributions (Figure 6.1 - 6.16), which show the *ON* and *OFF* counts to be mutually consistent, as expected in the absence of a gamma-ray source. Results of the χ^2 test are consistent with zero rate on a run-by-run basis, indicating a lack of evidence for short periods of flaring activity throughout the observations. The consistency of the results with zero emission is illustrated by the significance distributions (Figure 6.1 - 6.16) which are well described by a Gaussian distribution of zero mean and unit variance.

Application of *Kernel* analysis to combined data on each source, over the course of four seasons, is also consistent with a null result. Furthermore there is no evidence for flaring activity throughout the observing period, a fact demonstrated by the high probability for a rate consistent with zero (Table 6.3) and also by the shape of the significance distributions (Figure 6.1 - 6.16). The lowest-energy *Kernel* selection, applied to data on a given source

	Mean Elevation	Total Hours Observed	Total Hours Used	*ON/OFF* All	*ON/OFF* 2000 /'01	*ON/OFF* 2001 /'02	*ON/OFF* 2002 /'03	*ON/OFF* 2003 /'04	*TRACKING* All	*TRACKING* 2000 /'01	*TRACKING* 2001 /'02	*TRACKING* 2002 /'03	*TRACKING* 2003 /'04
1ES 0033+595	59.9	27.4	16.3	9.2	–	4.2	1.8	3.2	7.1	–	4.1	0.3	2.7
1ES 0120+340	78.1	36.4	29.3	3.7	–	3.2	0.5	–	25.5	13.2	2.3	2.6	7.4
RGB J0214+517	64.9	23.0	16.6	5.5	–	5.5	–	–	11.1	–	–	5.1	6.0
1ES 0229+200	73.4	30.1	26.3	8.5	–	8.0	0.5	–	17.8	3.4	9.0	1.3	4.1
1ES 0323+022	58.1	8.6	5.9	–	–	–	–	–	5.9	–	2.2	2.5	1.2
1ES 0806+524	65.9	36.5	27.7	19.3	–	15.6	3.7	–	8.6	–	2.6	0.9	5.1
1ES 1011+496	70.0	5.8	4.0	–	–	–	–	–	4.0	–	–	–	4.0
RXJ 1136+673	52.2	9.7	8.6	–	–	–	–	–	8.6	2.7	0.3	4.2	1.4
1ES 1553+113	66.2	9.7	8.0	0.5	–	0.5	–	–	7.5	0.9	2.7	3.9	–
1ES 1727+502	65.3	6.9	6.3	1.4	–	–	–	1.4	4.9	0.3	0.5	2.3	1.8
1ES 1741+196	71.8	6.2	5.1	–	–	–	–	–	5.1	–	0.9	2.9	1.3
1ES 0145+138	68.6	7.9	6.8	–	–	–	–	–	6.8	5.1	1.3	0.4	–
1ES 1118+424	67.8	5.0	4.3	–	–	–	–	–	4.3	3.3	1.0	–	–
1ES 2321+419	71.8	10.4	8.8	0.5	–	–	–	0.5	8.3	3.1	3.7	–	1.5
3C 66A	74.0	24.2	20.2	2.3	0.5	–	–	1.8	17.9	3.2	2.8	0.5	11.4
BL Lac	69.9	6.3	4.8	–	–	–	–	–	4.8	1.4	1.0	0.5	1.9

Table 6.1: Summary of observations on BL-Lac objects analysed throughout this work. The total amount of time dedicated to each source is shown, along with the amount of data remaining after exclusion of observations which took place during periods of adverse weather. Also shown is the amount of data recorded in *ON/OFF* and *TRACKING* mode, including a breakdown of the year-by-year observations. A summary of the properties of the objects is provided in Table 2.3.

Selection:	Supercuts			Minicuts			Modified Supercuts		
Source	Excess (σ)	Rate (min^{-1})	P_{χ^2}	Excess (σ)	Rate (min^{-1})	P_{χ^2}	Excess (σ)	Rate (min^{-1})	P_{χ^2}
1ES 0033+595	1.766	0.208 ± 0.118	0.83	1.529	0.359 ± 0.235	0.45	2.046	0.210 ± 0.102	0.92
1ES 0120+340	-0.682	-0.059 ± 0.087	0.40	-0.938	-0.179 ± 0.191	0.12	-1.428	-0.102 ± 0.071	0.67
RGB J0214+517	-0.006	-0.001 ± 0.100	0.66	-0.729	-0.154 ± 0.212	0.91	-0.345	-0.030 ± 0.087	0.50
1ES 0229+200	1.353	0.123 ± 0.091	0.50	-0.546	-0.112 ± 0.206	0.54	1.333	0.101 ± 0.075	0.42
1ES 0323+022	1.549	0.286 ± 0.184	0.73	-0.222	-0.084 ± 0.377	0.25	1.275	0.206 ± 0.161	0.96
1ES 0806+524	1.099	0.090 ± 0.082	0.39	0.542	0.103 ± 0.189	0.98	2.021	0.136 ± 0.067	0.62
1ES 1011+496	0.672	0.147 ± 0.219	0.61	-0.912	-0.416 ± 0.456	0.11	1.315	0.237 ± 0.180	0.52
RXJ 1136+673	0.488	0.073 ± 0.149	0.34	0.750	0.227 ± 0.302	0.02	0.346	0.045 ± 0.128	0.65
1ES 1553+113	0.245	0.032 ± 0.132	0.18	-0.062	-0.018 ± 0.294	0.49	1.137	0.130 ± 0.115	0.08
1ES 1727+502	-0.410	-0.056 ± 0.137	0.58	-1.725	-0.529 ± 0.306	0.05	0.013	0.002 ± 0.119	0.80
1ES 1741+196	1.016	0.150 ± 0.147	0.13	-1.660	-0.577 ± 0.347	0.42	0.335	0.044 ± 0.131	0.54
1ES 0145+138	-0.069	-0.015 ± 0.212	0.05	-1.109	-0.515 ± 0.464	0.90	-0.446	-0.076 ± 0.170	0.03
1ES 1118+424	0.206	0.054 ± 0.262	0.61	-1.581	-0.975 ± 0.617	0.46	0.094	0.019 ± 0.202	0.45
1ES 2321+419	-0.376	-0.053 ± 0.140	0.08	0.791	0.240 ± 0.304	0.58	-0.374	-0.044 ± 0.118	0.13
3C 66A	-0.997	-0.107 ± 0.107	0.44	-0.666	-0.151 ± 0.226	0.09	-0.770	-0.068 ± 0.089	0.83
BL Lac	0.411	0.084 ± 0.203	0.08	0.212	0.086 ± 0.406	0.48	0.233	0.041 ± 0.176	0.09

Table 6.2: Results of application of box selections to BL Lac data. All three box selections were utilised, the traditional *Supercuts*, the newly developed *Minicuts* and *Modified Supercuts*. Results of the χ^2 test for variable emission are shown. Based on these results there is no evidence for the presence of a new source of VHE gamma radiation.

Size Range:	No Limit			250 - 450 d.c			$\geq$ 450 d.c.		
Source	Excess (σ)	Rate (min^{-1})	P_{χ^2}	Excess (σ)	Rate (min^{-1})	P_{χ^2}	Excess (σ)	Rate (min^{-1})	P_{χ^2}
1ES 0033+595	0.287	0.02 ± 0.08	0.58	-0.266	-0.09 ± 0.36	0.29	-0.394	-0.03 ± 0.07	0.62
1ES 0120+340	0.209	0.02 ± 0.09	0.57	-1.333	-0.74 ± 0.55	0.34	0.080	0.00 ± 0.06	0.40
RGBJ0214+517	0.210	0.02 ± 0.09	0.44	-1.213	-0.63 ± 0.52	0.33	0.357	0.02 ± 0.07	0.54
1ES 0229+200	-0.084	-0.01 ± 0.07	0.79	0.964	0.40 ± 0.42	0.14	0.842	0.04 ± 0.05	0.79
1ES 0806+524	2.352	0.11 ± 0.05	0.005	1.349	0.36 ± 0.26	0.04	0.655	0.02 ± 0.03	0.06
1ES 1553+113	0.535	0.14 ± 0.27	0.60	2.358	3.76 ± 1.59	0.02	0.762	0.18 ± 0.23	0.43
1ES 1727+502	0.333	0.05 ± 0.14	0.25	-0.607	-0.39 ± 0.65	0.31	-0.229	-0.02 ± 0.10	0.78
1ES 2321+419	0.788	0.21 ± 0.27	0.44	0.324	0.36 ± 1.10	0.74	0.392	0.07 ± 0.18	0.70
3C 66A	-0.765	-0.09 ± 0.12	0.81	-1.048	-0.70 ± 0.67	0.63	-0.542	-0.05 ± 0.09	0.86

Table 6.3: Results of application of *Kernel* selections to BL-Lac data. The *Kernel*, optimised in three *size* bands, was applied and χ^2 test for variable emission carried out. Results following application of the lowest-energy *Kernel* are given elsewhere (Table 6.4). Based on these results it is concluded that there is no evidence for gamma-ray emission at a statistically significant level.

Source	Year	Excess σ	Rate (min^{-1})	P_{χ^2}	P_{trials}
1ES 0033+595	2001/02	0.625	0.67 ± 1.07	0.30	0.65
	2002/03	0.054	0.06 ± 1.16	5×10^{-4}	0.002
	2003/04	-2.136	-1.98 ± 0.93	0.64	0.955
1ES 0120+340	2001/02	-1.078	-1.15 ± 1.06	0.31	0.52
	2002/03	0	0	1.00	1.00
RGBJ0214+517	2001/02	-0.875	-0.84 ± 0.95	0.08	0.08
1ES 0229+200	2001/02	1.408	1.10 ± 0.78	0.10	0.20
	2002/03	-0.815	-1.86 ± 2.28	0.41	0.66
1ES 0806+524	2001/02	5.282	3.16 ± 0.60	3×10^{-6}	7×10^{-6}
	2002/03	0.478	0.37 ± 0.77	0.022	0.044
1ES 1553+113	2001/02	1.859	5.51 ± 2.97	0.06	0.06
1ES 1727+502	2003/04	-0.798	-1.03 ± 1.29	0.25	0.25
1ES 2321+419	2003/04	-0.727	-1.83 ± 2.51	0.47	0.47
3C 66A	2000/01	-0.417	-1.36 ± 3.26	0.68	0.90
	2003/04	1.048	1.30 ± 1.24	0.79	0.96

Table 6.4: Results of application of lowest-energy *Kernel* selection to BL-Lac data. Due to variable energy thresholds this selection can only be applied to data recorded throughout any given season. For all except one observation there is no evidence for a gamma-ray excess. Rather interestingly, in the case of observations on 1ES 0806+524 throughout the season 2001/2002, a $5.3\,\sigma$ is evident. This result is discussed in more detail in Section 6.7.

Source	Flux$_{>0.3\,TeV}$ (x 10^{-11} cm^{-2} s^{-1})			
	Fossati	Costamante	Stecker	Whipple†
1ES 0033+595	2.04	0.25	–	3.94
1ES 0120+340	0.28	0.30	–	1.32
RGB J0214+517	5.93	0.07	–	1.72
1ES 0229+200	0.96	0.31	0.20	1.95
1ES 0323+022	0.84	0.01	0.50	5.05
1ES 0806+524	1.36	–	–	2.19
1ES 1011+496	0.12	0.14	–	5.35
RXJ 1136+673	0.92	0.10	–	8.46
1ES 1553+113	0.20	0.42	–	3.03
1ES 1727+502	5.19	0.07	0.50	2.34
1ES 1741+196	3.59	0.29	0.40	2.68
1ES 0145+138	–	–	0.55	3.09
1ES 1118+424	–	–	0.38	3.83
1ES 2321+419	–	–	0.13	2.26
3C 66A	0.14	–	–	1.63
BL Lac	3.32	0.17	–	3.57

Table 6.5: Results of upper-limit calculations. Upper limits were calculated in the case of *Minicuts* and *Modified Supercuts*. Using the more constraining of these result an integral flux upper limit above 300 GeV was derived by assuming a Crab Nebula like spectrum. Where available, the equivalent predictions by Stecker et al. (1996) and Costamante and Ghisellini (2002) are provided for comparison. († Flux upper limits calculated during this work)

over the course of an individual observing season, yields one statistically significant result. Application of this *Kernel* selection to data recorded on 1ES 0806+524 during season 2001/2002 produced a $5\,\sigma$ excess in the *ON* dataset which, if real, would represent the first detection of a gamma-ray source in this energy range using the IACT. Detailed discussion of the result is reserved for Section 6.7. For all other objects the observed excess in the low-energy range was consistent with zero, both in terms of overall emission and on a run-by-run basis.

The results of the upper-limit calculations are interesting. In all cases the calculated flux upper limits are consistent with the synchrotron self Compton (SSC) predictions quoted by Costamante and Ghisellini (2002) and Stecker et al. (1996). In contrast, some results prove to be inconsistent with predictions made by the same authors using a modified version of the Fossati parameterisation (Fossati et al., 1998; Donato et al., 2001). A detailed discussion of possible reasons for the inconsistency and its implications is reserved for Section 6.6.

6.4 Individual Object Overviews

In the preceding section a summary of the overall analysis results has been provided. In the case of some objects there were aspects of their results which warrant some discussion. With this in mind a brief overview of results obtained from each object will now be presented.

6.4.1 1ES 0033+595

In the case of 1ES 0033+595, although box selection failed to produce a significant detection, there appears to be a preponderance toward a positive excess in all three *size* bands. This trend is evident in the *alpha* distributions (Figure 6.1) which show a small disparity between the *ON* and *OFF* counts at small *alpha*, and also in the significance distributions which appear slightly shifted toward the positive. Although the shift is not statistically significant it may indicate the presence of a gamma-ray flux in the dataset that is too weak to be detected by the current telescope. The fact that the more sensitive *Kernel* selection fails to show a similar trend (Table 6.3 and Table 6.4) somewhat reduces the likelihood of this being the case; however, more observations are required in order to draw firm conclusions.

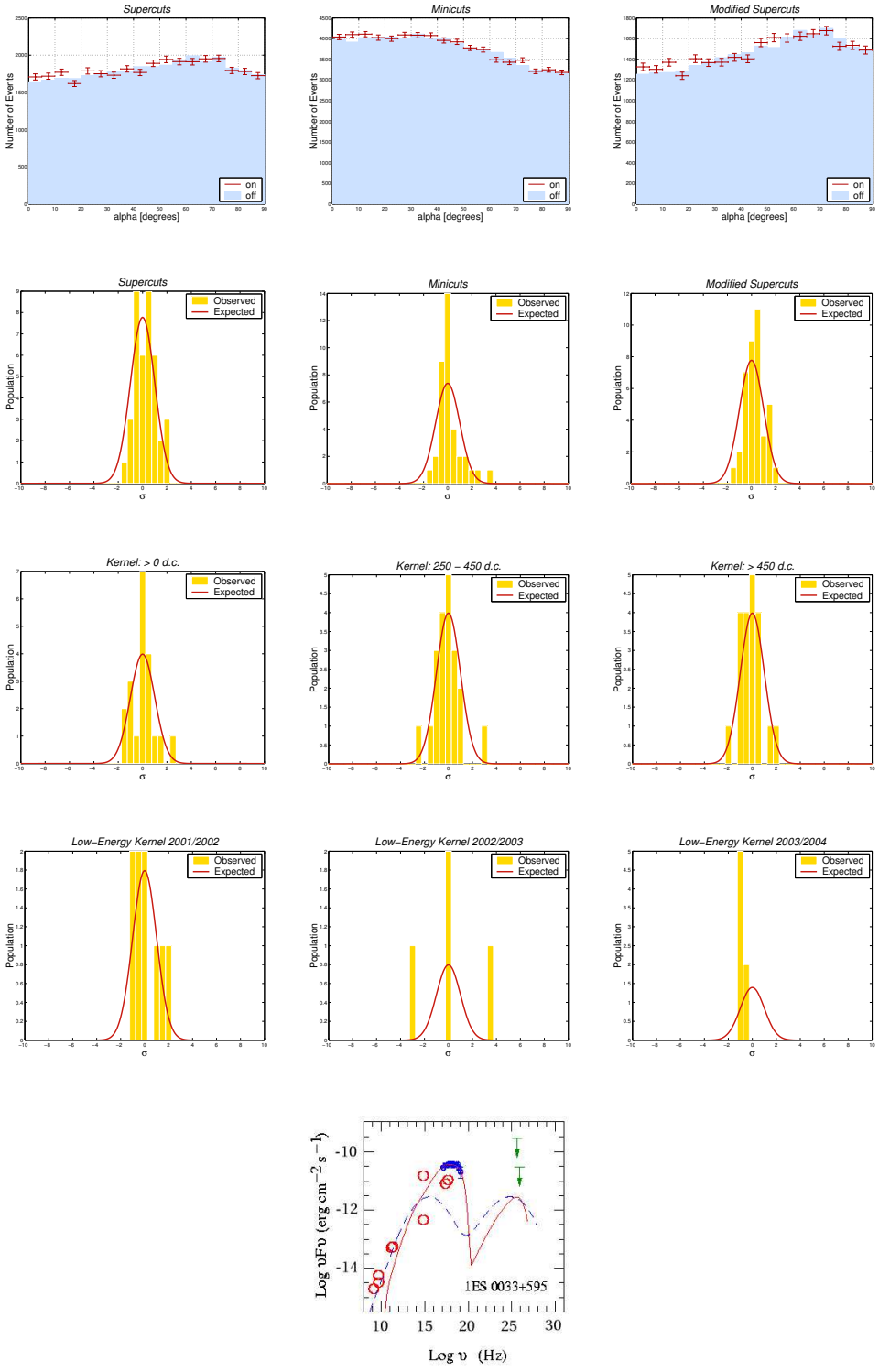

Figure 6.1: Results of analysis of 1ES 0033+595.

6.4.2 1ES 0120+340

All results on this object are consistent with zero, following application of both box selection and *Kernel* selection (Table 6.2, 6.3). The probability for a rate consistent with zero is high, indicating a lack of evidence for flaring activity. The flux upper limits, calculated based on box-selection results are in agreement with the predictions of Costamante and Ghisellini (2002) using the SSC model and the modified Fossati parameterisation (Fossati et al., 1998; Donato et al., 2001).

6.4.3 RGB J0214+517

While all results are consistent with zero, in the case of RGB J0214+517 the flux upper limit calculated using the *Modified Supercuts* selection is inconsistent with the predictions of Costamante and Ghisellini (2002) using a modified version of the Fossati parameterisation (Fossati et al., 1998; Donato et al., 2001). Based on the Fossati model a $5\,\sigma$ level detection should be achievable in as little as 3.5 hours; however, the results presented in this work (Table 6.2), following analysis of 17 hours of data, fail to provide any evidence for a gamma-ray excess. The failure of the model in this case is highlighted by the upper-limit calculations which yield a flux much lower that the predicted value (Table 6.5) and also by the spectral energy distribution which is inconsistent with the predicted flux at 403 GeV (Figure 6.3). The implications of this result are discussed in Section 6.6.

6.4.4 1ES 0229+200

Following application of box selections to data recorded on 1ES 0229+200 results fail to provide a positive detection; however, the *alpha* distributions indicate the presence of a small excess in the case of *Supercuts* and *Modified Supercuts*. For both of these selections there may also be a small shift in the significance distribution toward the positive, possibly indicating the presence of a weak gamma-ray flux. The fact that the *Kernel* selection produces a result that is consistent with zero suggests the lack of any gamma-ray signal in the dataset and further observations are advised. The lowest-energy *Kernel* was applied to data recorded during 2001/2002 and 2002/2003, yielding a null result. The 2002/2003 dataset comprised a single observation only and in such cases the validity of the χ^2 test result is unclear.

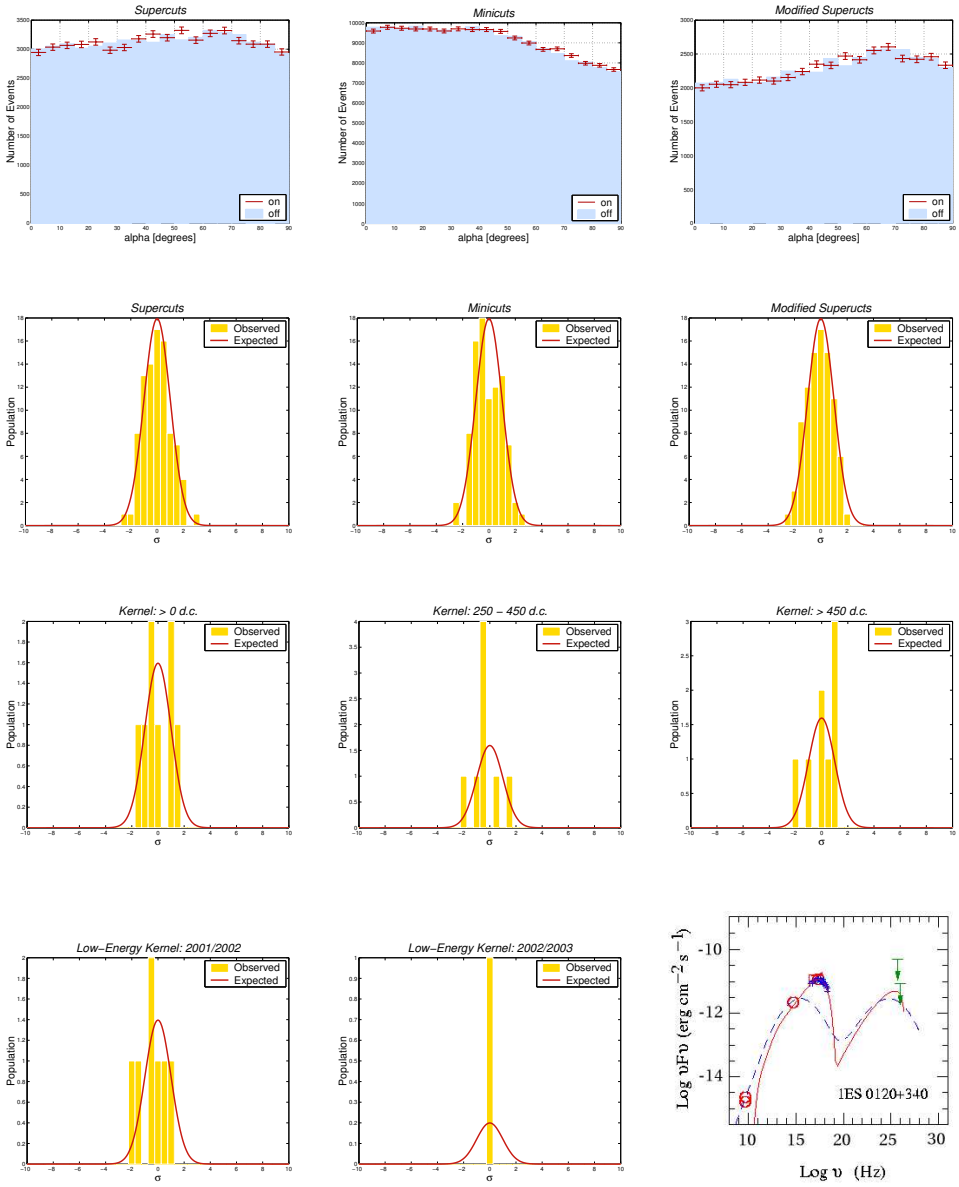

Figure 6.2: Results of analysis of 1ES 0120+340.

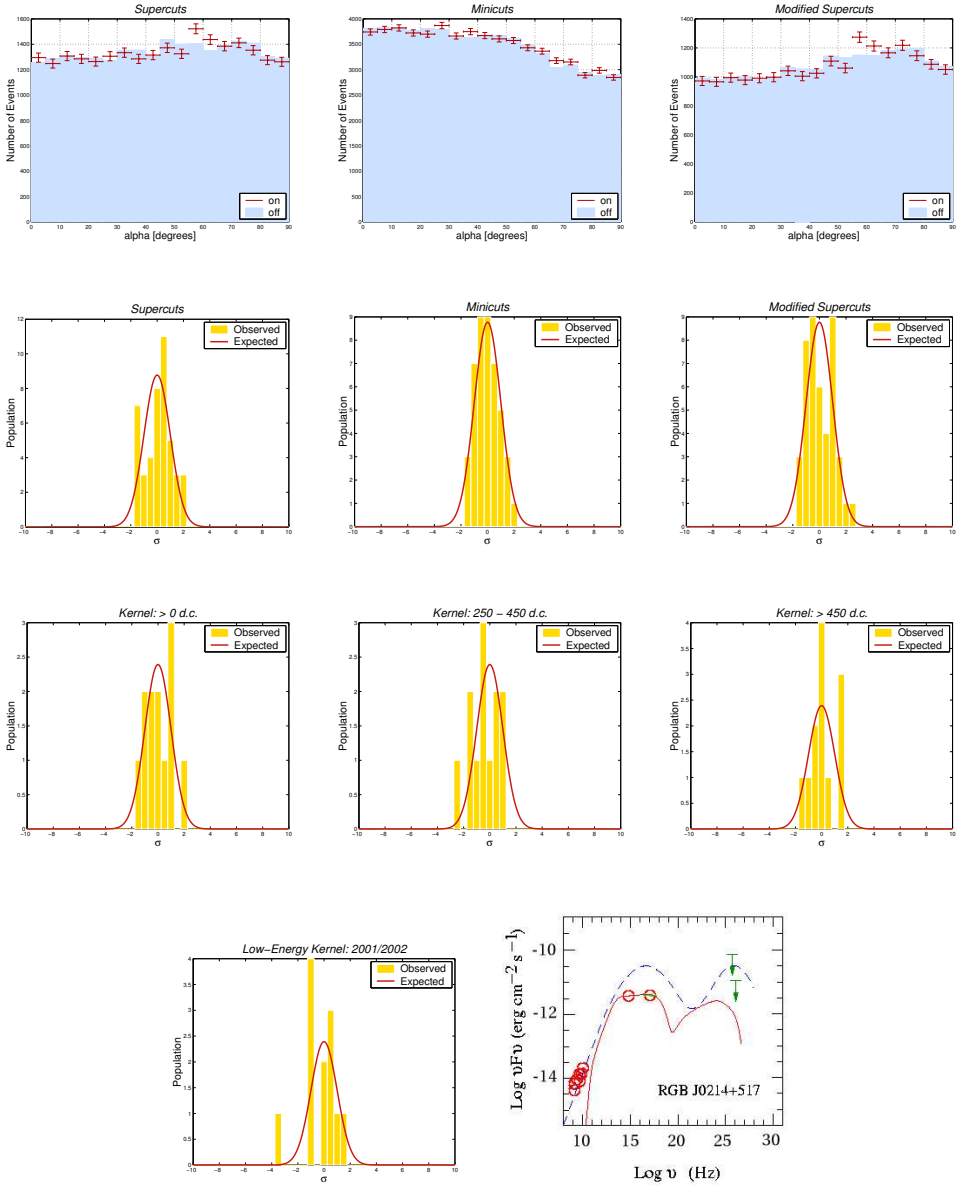

Figure 6.3: Results of analysis of RGB J0214+517.

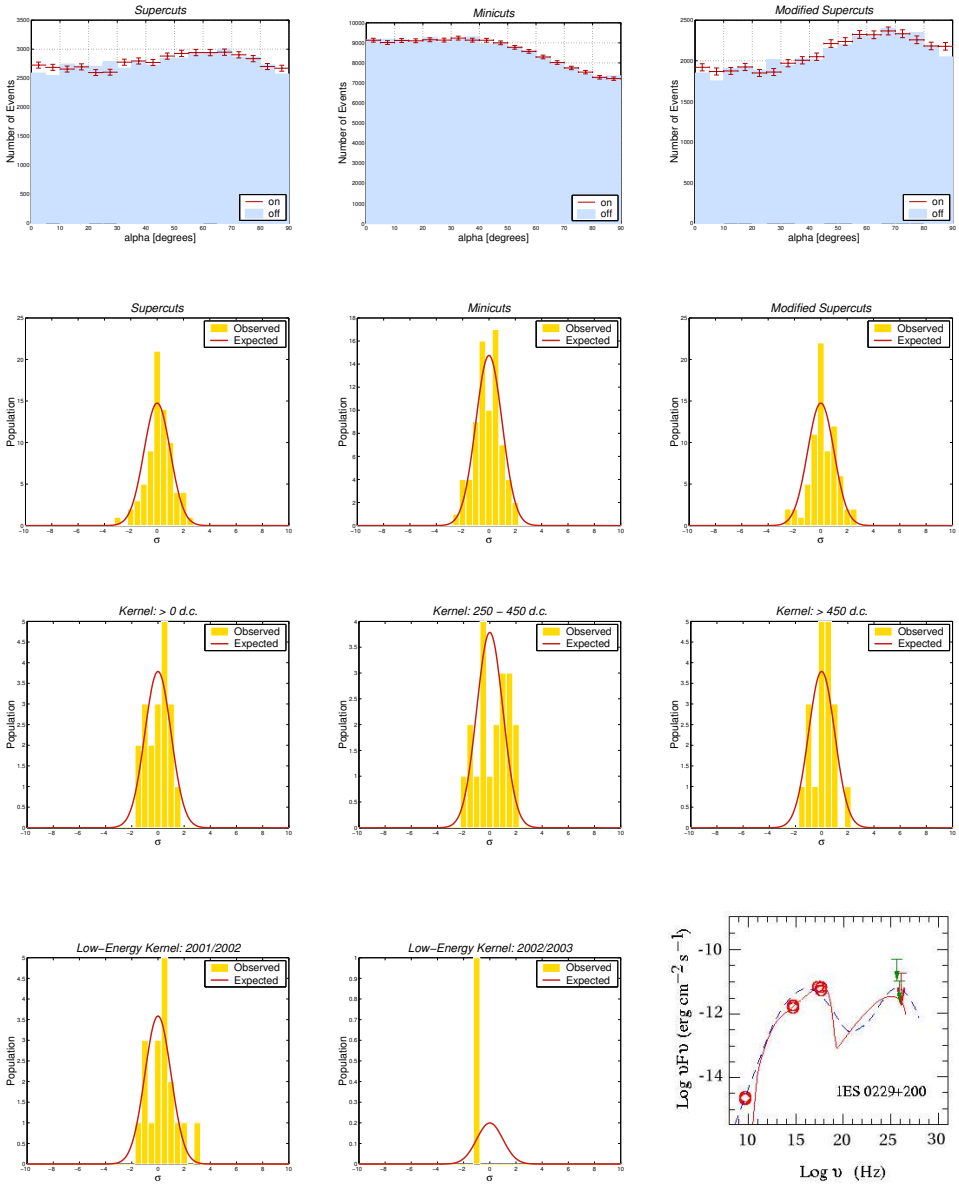

Figure 6.4: Results of analysis of 1ES 0229+200.

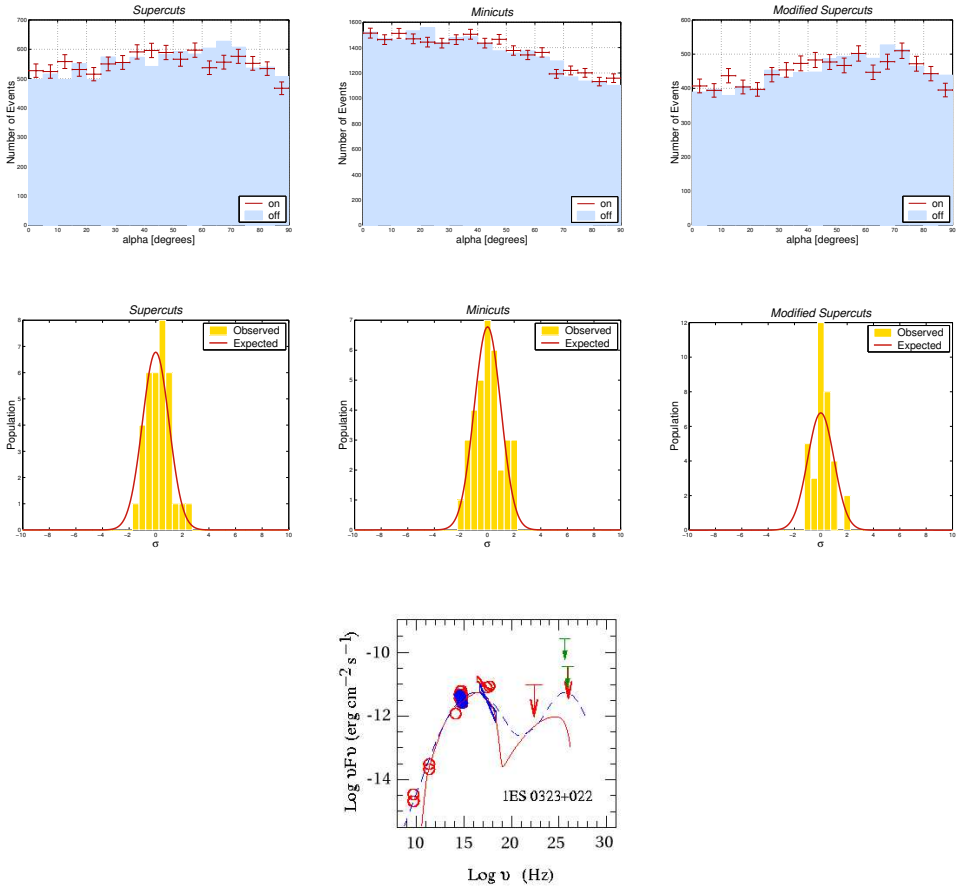

Figure 6.5: Results of analysis of 1ES 0323+022.

6.4.5 1ES 0323+022

Observations of 1ES 0323+022 produced a small positive excess in the *ON* dataset following application of *Supercuts* and *Modified Supercuts*. As already stated, this may be evidence of some low-level emission; however, a study of the *alpha* distribution (Figure 6.5) suggest that this is not so. For a true gamma-ray source one expects the distribution of the *alpha* parameter to peak at zero, and gradually fall off as *alpha* increases. Figure 6.5 shows that the majority of the *ON*-source excess occurs in the 10° to 15° range, and accordingly is unlikely to be genuine. It was not possible to analyse this object using the *Kernel* selection method as all observations comprised *TRACKING* data.

6.4.6 1ES 0806+524

While results obtained following analysis of 1ES 0806+524 with box selection and standard *Kernel* selection failed to produce a statistically significant excess, application of the lowest-energy *Kernel* to 2001/2002 data yielded a $5\,\sigma$ detection. The result of the χ^2 test for a rate consistent with zero is extremely low, even after accounting for the number of trials, proving the presence of non-zero emission. This fact is illustrated beautifully by the significance distribution (Figure 6.6) which shows a clear shift toward positive values. The fact that this excess does not come from a single scan, rather it is evenly distributed over a number of files, is encouraging and suggests that throughout 2001/2002 1ES 0806+524 may have been in a sustained state of high flux. The results following application of the other *Kernel* selections also produce a positive excess, albeit only at the $2\,\sigma$ level. This may be evidence for gamma-ray emission which is peaked at low energy and would explain why a significant detection was obtained only when using the lowest-energy *Kernel*. This unexpected result was subjected to a deeper analysis, a summary of which is presented in Section 6.7.

6.4.7 1ES 1011+496

Observations of this object comprised *TRACKING* data only, thus *Kernel* analysis was not applied. Following application of box selection no statistically significant excess was observed and the χ^2 test for a rate consistent with zero yielded high probability values. Flux upper limits calculated based on these results (Table 6.5, Figure 6.7) are consistent with the levels quoted by Costamante and Ghisellini (2002).

6.4.8 1ES 1136+678

While all results on this object are consistent with a null detection, the application of the χ^2 test to events selected using *Minicuts* yields a rather low probability for zero emission. While not sufficiently low to warrant rejection of the null hypothesis, again this may be evidence for a shift in the significance distribution toward positive excess. Examination of Figure 6.8 shows that the significance distribution is very well approximated by a Gaussian with a mean of zero and standard deviation equal to one, and as a result it is concluded that there is no evidence for a non-zero rate. While the calculated flux upper limits are in agreement with the predictions of Costamante and Ghisellini (2002) the limited *ON*-source exposure, and observations of the Crab Nebula in a similar elevation range, do not allow a true test of the

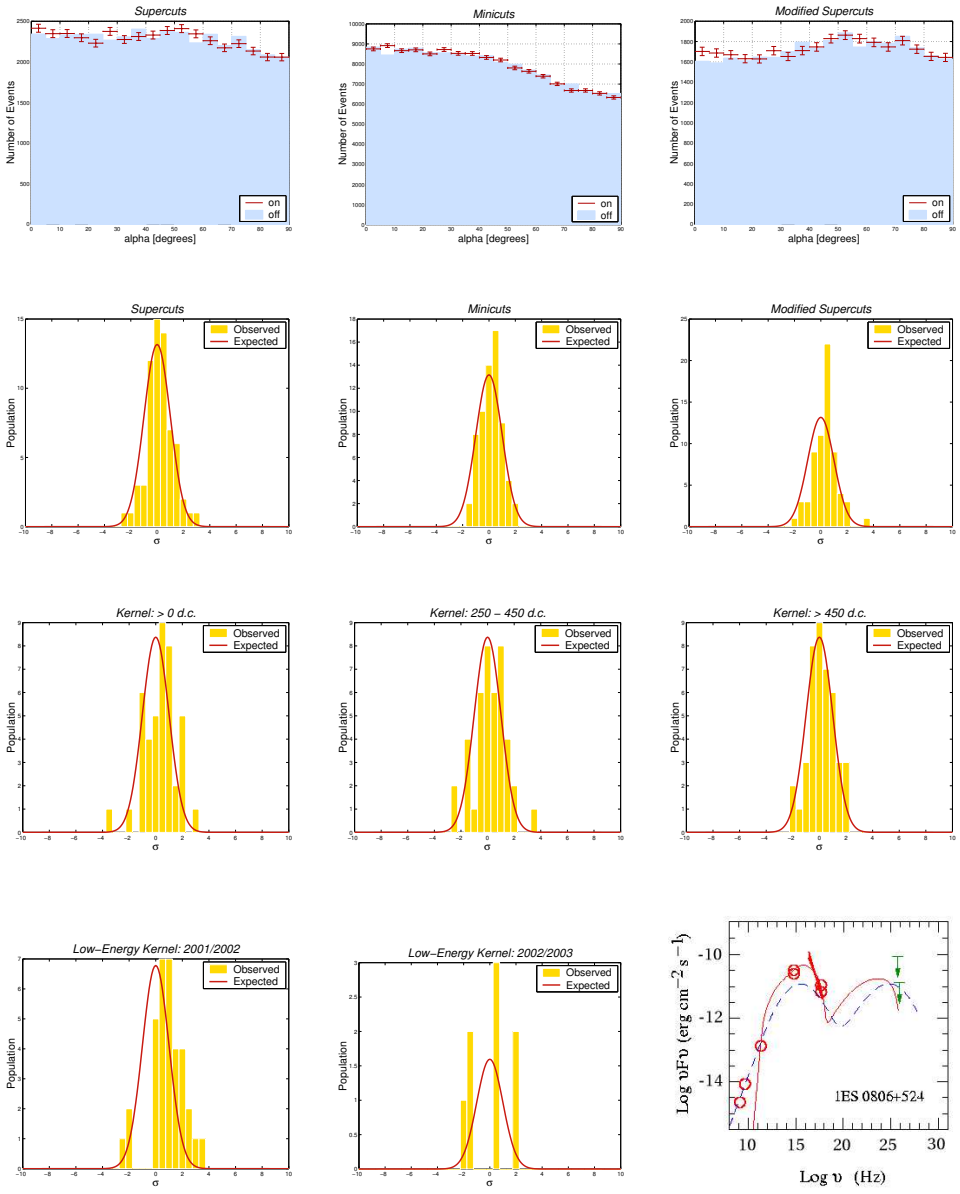

Figure 6.6: Results of analysis of 1ES 0806+524.

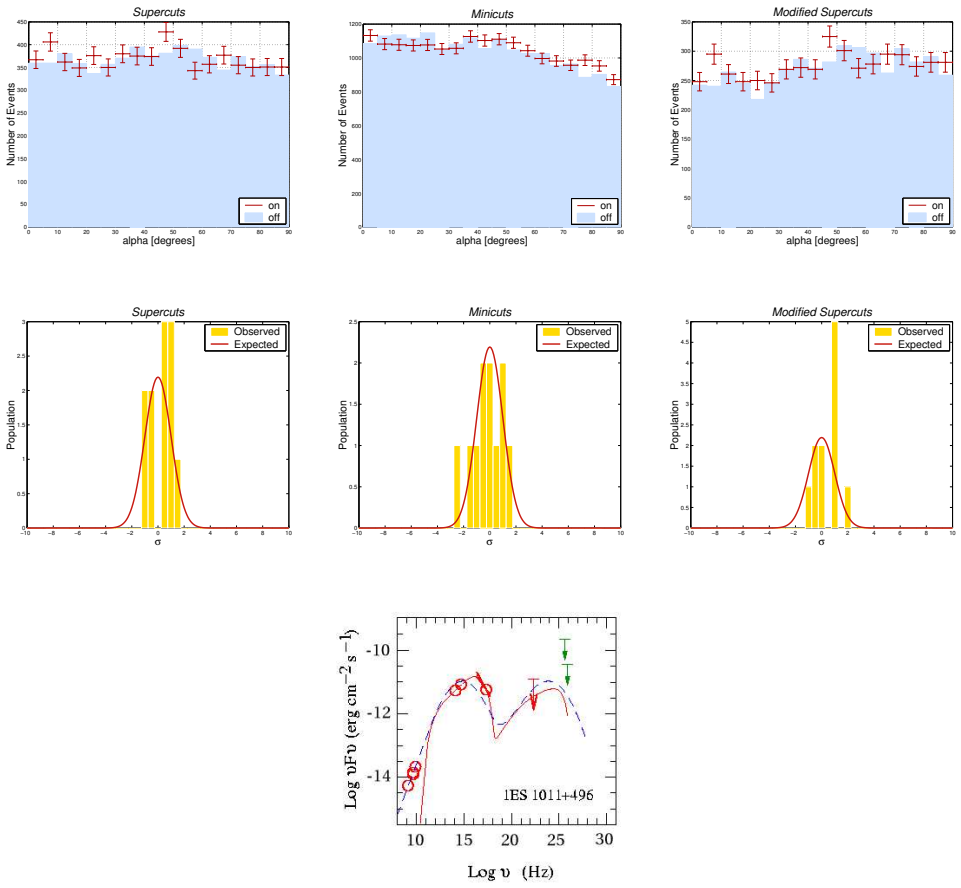

Figure 6.7: Results of analysis of 1ES 1011+496.

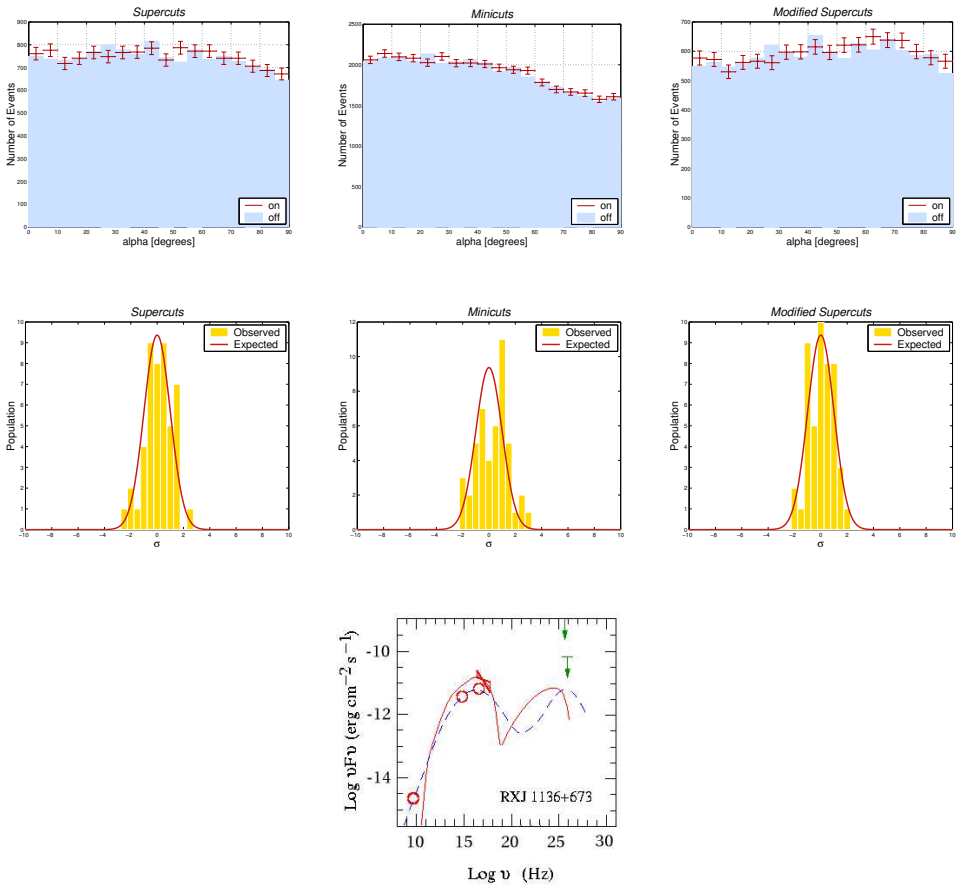

Figure 6.8: Results of analysis of 1ES 1136+673.

models to be carried out.

6.4.9 1ES 1553+113

While analysis of data taken on this object failed to provide a significant detection there is evidence for a possible weak signal when the low-energy *Kernel* selection is applied (with a *size* cut of 250 d.c. included). The fact that this 2.4 σ excess decreases when the lowest-energy *Kernel* selection is applied to the dataset suggests that a genuine gamma-ray signal is not present. It should also be noted that the dataset to which *Kernel* analysis was applied comprised a single 28-minute run.

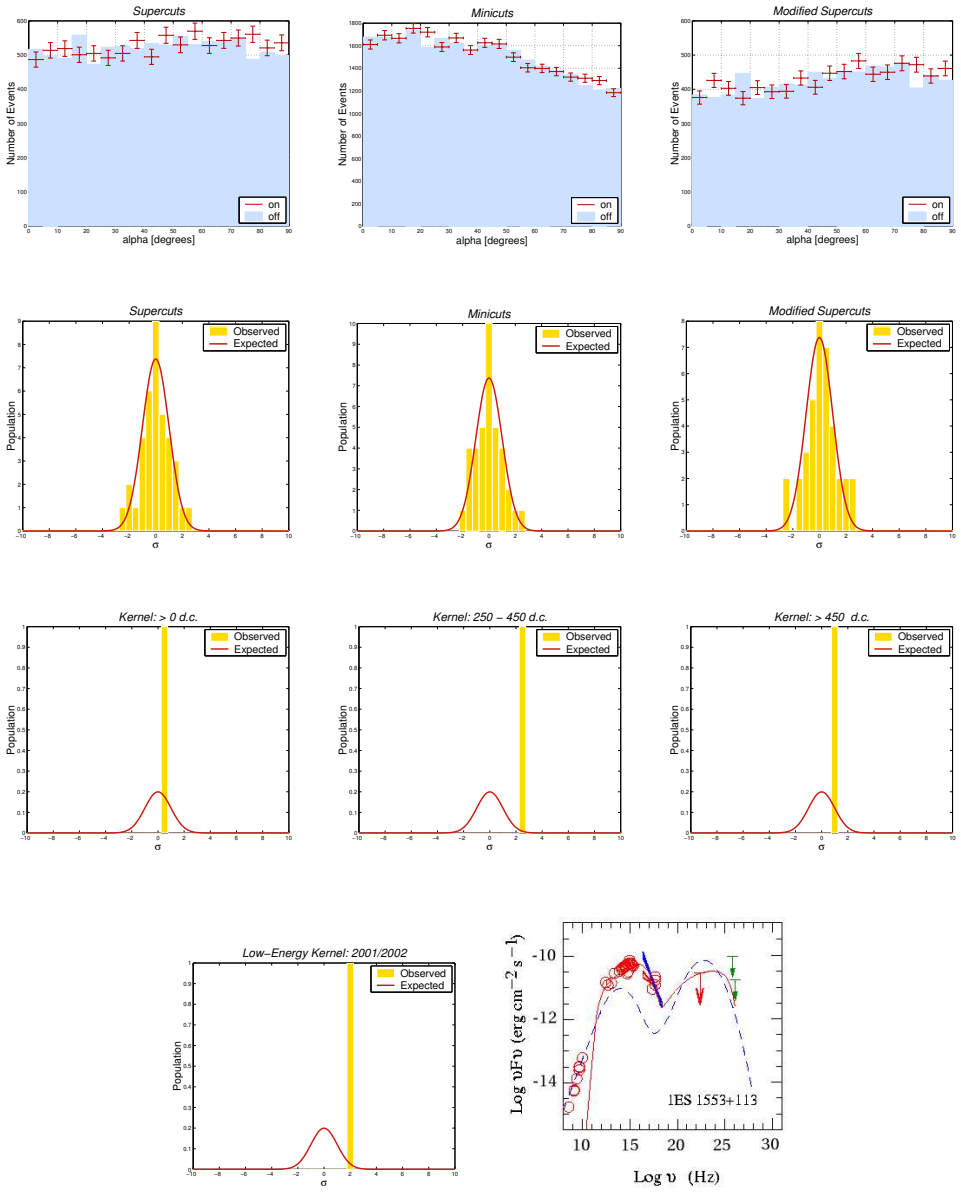

Figure 6.9: Results of analysis of 1ES 1553+113.

6.4.10 1ES 1727+502

The *alpha* distributions produced following application of box selection appear to be quite noisy (Figure 6.10), with both positive and negative differences between the *ON* and *OFF* counts evident. In spite of the obvious disparity a statistically significant excess is not obtained. It is most likely that differences between the distributions are caused by somewhat poorly chosen control data. The integral flux upper limit above 300 GeV is consistent with the SSC-model predictions of Stecker et al. (1996) and Costamante and Ghisellini (2002). The upper limits are, however, inconsistent with the flux quoted by Costamante and Ghisellini (2002) using the modified Fossati parameterisation (Fossati et al., 1998; Donato et al., 2001). Using Fossati's description of blazars, the time required to observe 1ES 1727+502 at the $5\,\sigma$ level was estimated to be 4.4 hours. Observations of this object totaled 6 hours; yet there is no evidence for even a small excess. This inconsistency is further highlighted by the flux upper limit calculated using *Modified Supercuts* which falls below the predicted flux (Table 6.5, Figure 6.10). Reasons for this non-agreement and its possible implications are discussed in Section 6.6.

6.4.11 1ES 1741+196

The *alpha* distributions produced following application of *Supercuts* and *Modified Supercuts* (Figure 6.11) indicate the presence of an *ON*-source excess in the first bin; however, this is not statistically significant (Table 6.2). Based on the predicted flux using the SSC models of Stecker et al. (1996) and Costamante and Ghisellini (2002) the non-detection of 1ES 1741+196 is expected. While the time required for a $5\,\sigma$ detection was estimated to be nine hours using the modified Fossati parameterisation (Costamante and Ghisellini, 2002; Donato et al., 2001; Fossati et al., 1998) and total observations of this object was only six hours, one would still expect the presence of some small excess in the data. The lack of such an excess suggests that the Fossati parameterisation is not suitable for describing this object, a point further illustrated by the flux upper limit results. The integral flux upper limit, calculated using the *Modified Supercuts* result, falls below the flux predicted by the Fossati method (Table 6.5, Figure 6.11). This inconsistency is discussed in detail in Section 6.6.

6.4.12 1ES 0145+138

Although results on this object are consistent with zero, in the case of *Supercuts* and *Modified Supercuts* there are quite low probabilities for a rate

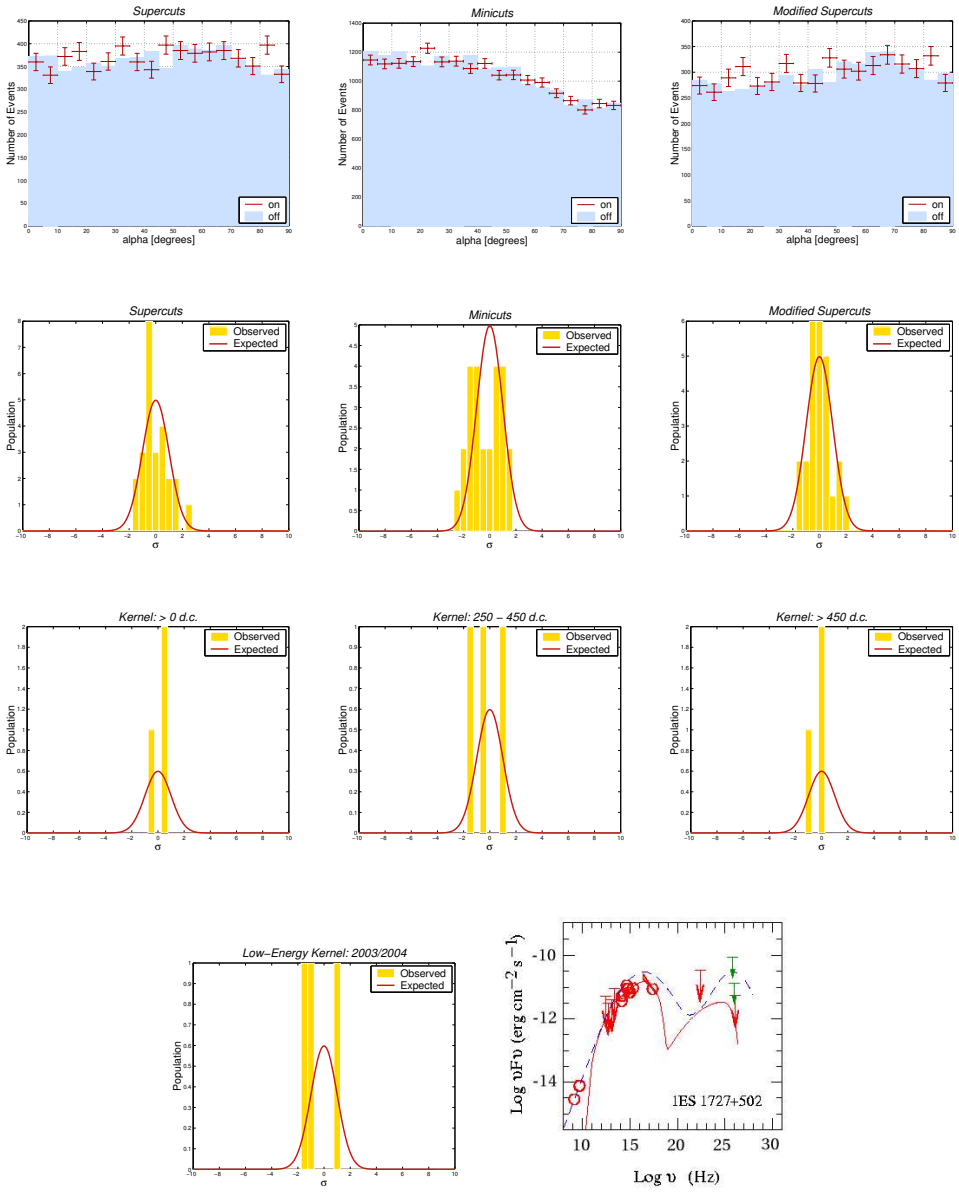

Figure 6.10: Results of analysis of 1ES 1727+502.

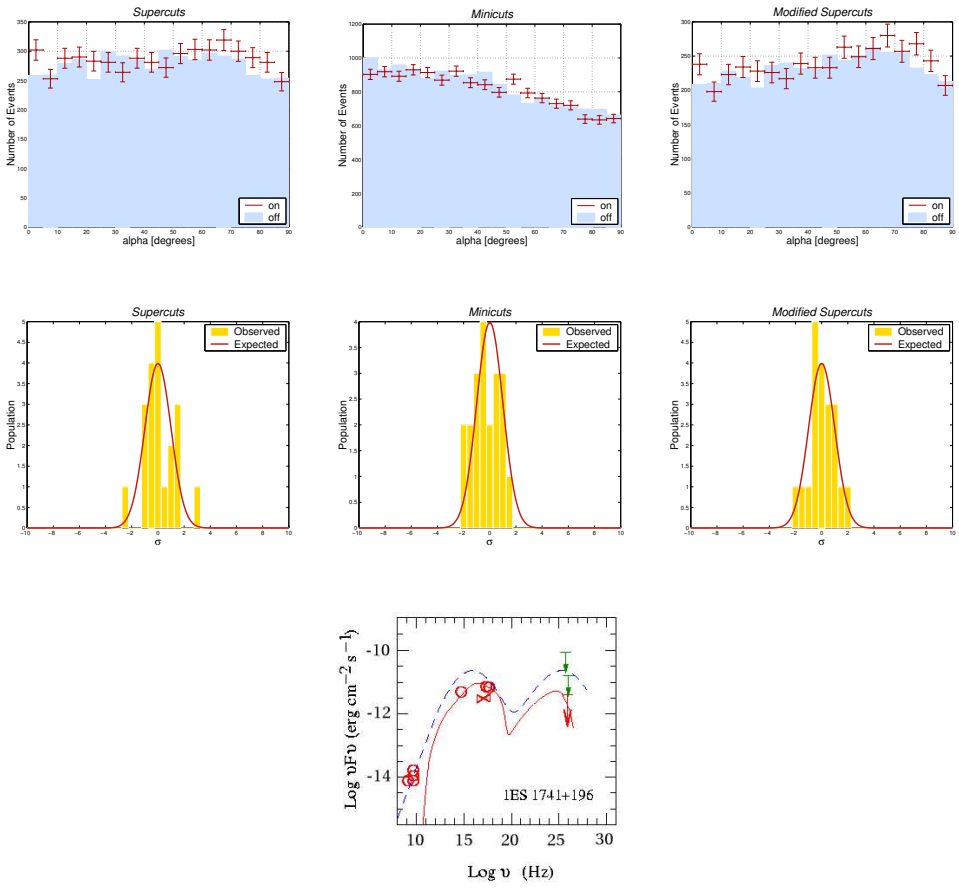

Figure 6.11: Results of analysis of 1ES 1741+196.

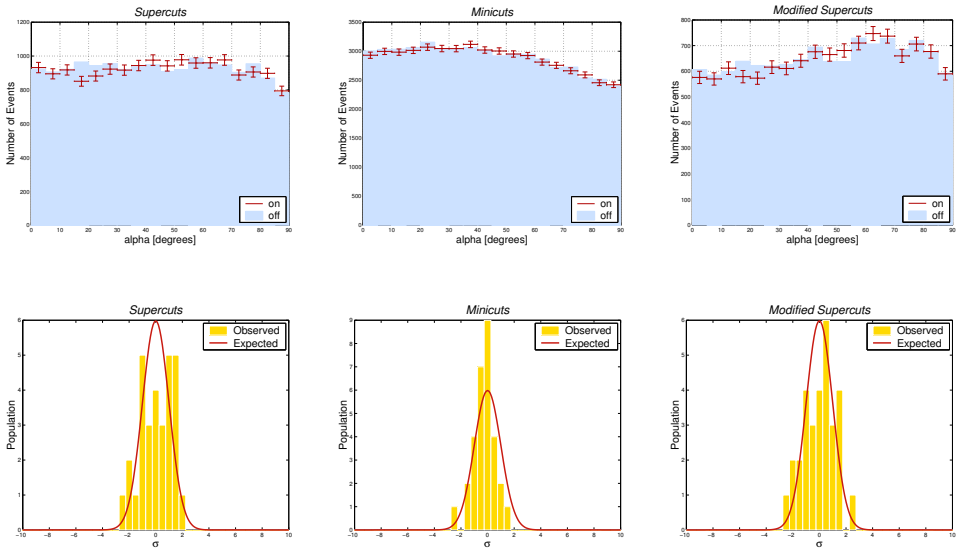

Figure 6.12: Results of analysis of 1ES 0145+38.

consistent with zero (Table 6.2). This may be indicative of a shift in the significance distribution toward the positive, however examination of this distribution (Figure 6.12) shows that this is not the case. It is most likely that the low probabilities are due to some relatively large positive and negative deviations away from zero. It is concluded that there is no evidence for gamma-ray emission in the dataset.

6.4.13 1ES 1118+424

Analysis of this object yielded results which are consistent with zero emission. *Kernel* analysis was not applied as all observations comprised *TRACKING* data only. Although the *alpha* distributions (Figure 6.13) are quite bumpy, there is no evidence for an excess in the *ON* dataset at small *alpha*. It is most likely that differences in the distributions are due to limitations in choosing the most suitable control data (Section 5.7). The flux upper limits are consistent with those presented by Stecker et al. (1996) and Costamante and Ghisellini (2002).

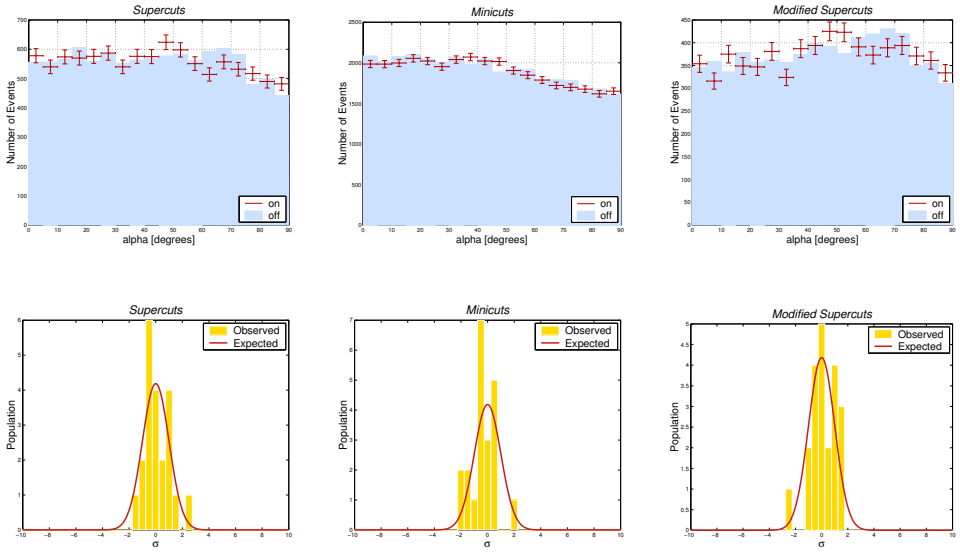

Figure 6.13: Results of analysis of 1ES 1118+424.

6.4.14 1ES 2321+419

In a similar way to 1ES 1118+424 the *alpha* distributions produced following box analysis of this object are somewhat noisy. The results of both box and *Kernel* analysis are consistent with zero emission, both in terms of overall excess and on a run-by-run basis. This object is not included in the catalogue of Costamante and Ghisellini (2002); however, the flux upper limits calculated in this work are entirely consistent with the predictions of Stecker et al. (1996).

6.4.15 3C 66A

Following detection of this source with EGRET (Hartman et al., 1999) and a claimed detection by the Crimean Astrophysical Observatory group in 1998 (Neshpor et al., 1998), 3C 66A was observed by the Whipple telescope for each of the four subsequent seasons. As one of two low-frequency BL Lacs included in this sample, if the VHE detection was confirmed it would be a first for this subclass of object. Even more importantly, given its high redshift, a confirmed detection would necessitate a re-think of current theories of gamma-ray absorption. Results of box and *Kernel* selection do not provide any evidence for the presence of a gamma-ray signal. The integral flux upper limit, calculated using the *Modified Supercuts* result, is consistent

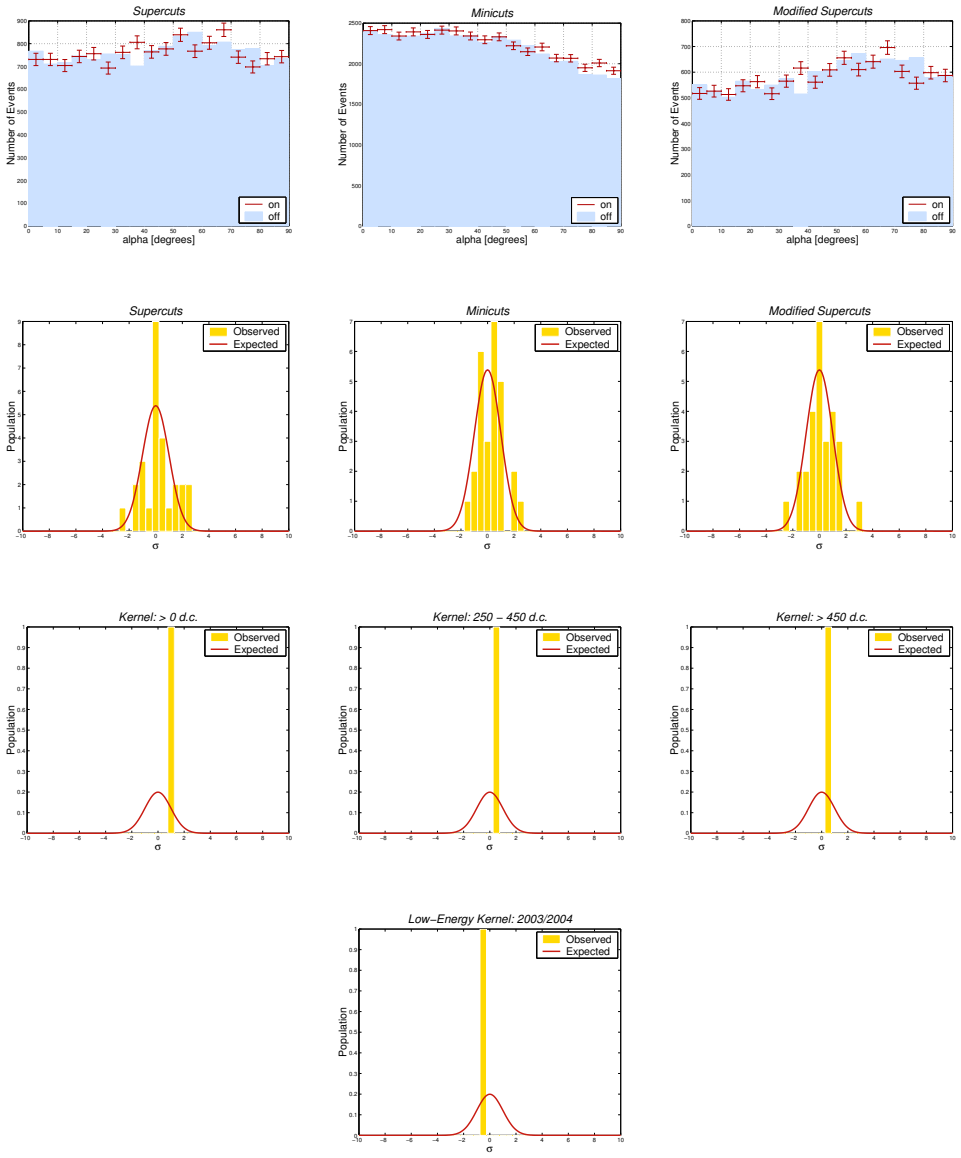

Figure 6.14: Results of analysis of 1ES 2321+419.

with the value quoted by Costamante and Ghisellini (2002) using the Fossati parameterisation (Table 6.5, Figure 6.15). A gamma-ray flux of $(3 \pm 1) \times 10^{-11}$ photons cm^{-2} s^{-1} above 900 GeV is quoted by Neshpor et al. (1998). Assuming a Crab Nebula like spectrum it is possible to convert the flux upper limit of this work to an upper limit above 900 GeV so that a comparison may be made. By doing so, a flux less than 3.2×10^{-12} photons cm^{-2} s^{-1} is obtained which is an order of magnitude less that that quoted by Neshpor et al. (1998). Although these results are inconsistent, it is difficult to draw any firm conclusions due to the non-contemporaneous nature of both sets of observations. Since BL Lacs are defined by their variable nature it is entirely possible that the Crimean detection of this object occurred during a prolonged period of increased flux, before the source returned to its quiescent state. The fact that this object is considered an unlikely TeV emitter is due to its distant location; however, it should be noted that the frequently quoted redshift value (z$\approx$0.444) may not be accurate (Kildea, 2004). Observations of this object, carried out previously by Whipple (Catanese et al., 1997b) and HEGRA (Aharonian et al., 2000), failed to produce a detection and the Crimean result remains unconfirmed.

6.4.16 BL Lac

Detection of this object in the gamma-ray domain was first reported following observations with EGRET (Catanese et al., 1997), whilst flux upper limits in the VHE range were also provided based on Whipple observations. Following a claimed detection of this object by the Crimean Astrophysical observatory group in 2001 (Neshpor et al., 2001), BL Lac was again observed by the Whipple telescope during each of the last four observing seasons. Small positive excesses are evident in the *alpha* distributions (Figure 6.16) following application of box selection; however, the results (Table 6.2) show that these are not statistically significant. The χ^2 probabilities for a rate consistent with zero are high in the case of *Minicuts*, but rather low for *Supercuts* and *Modified Supercuts*. Although still consistent with zero emission, these results may indicate a small shift in the significance distribution toward positive values. Examination of the significance distribution (Figure 6.16) proves that this is not the case; the low probabilities are due to both positive and negative fluctuations. All observations of this object were carried out in *TRACKING* mode, thus it was not possible to apply *Kernel* analysis. The calculated flux upper limit of 3.57×10^{-11} photons cm^{-2} s^{-1} is in agreement with predictions based on the SSC model and modified Fossati parameterisation presented in Costamante and Ghisellini (2002) (Table 6.5, Figure 6.16). In the claimed detection of BL Lac a $7.2\,\sigma$ excess was reported in conjunction

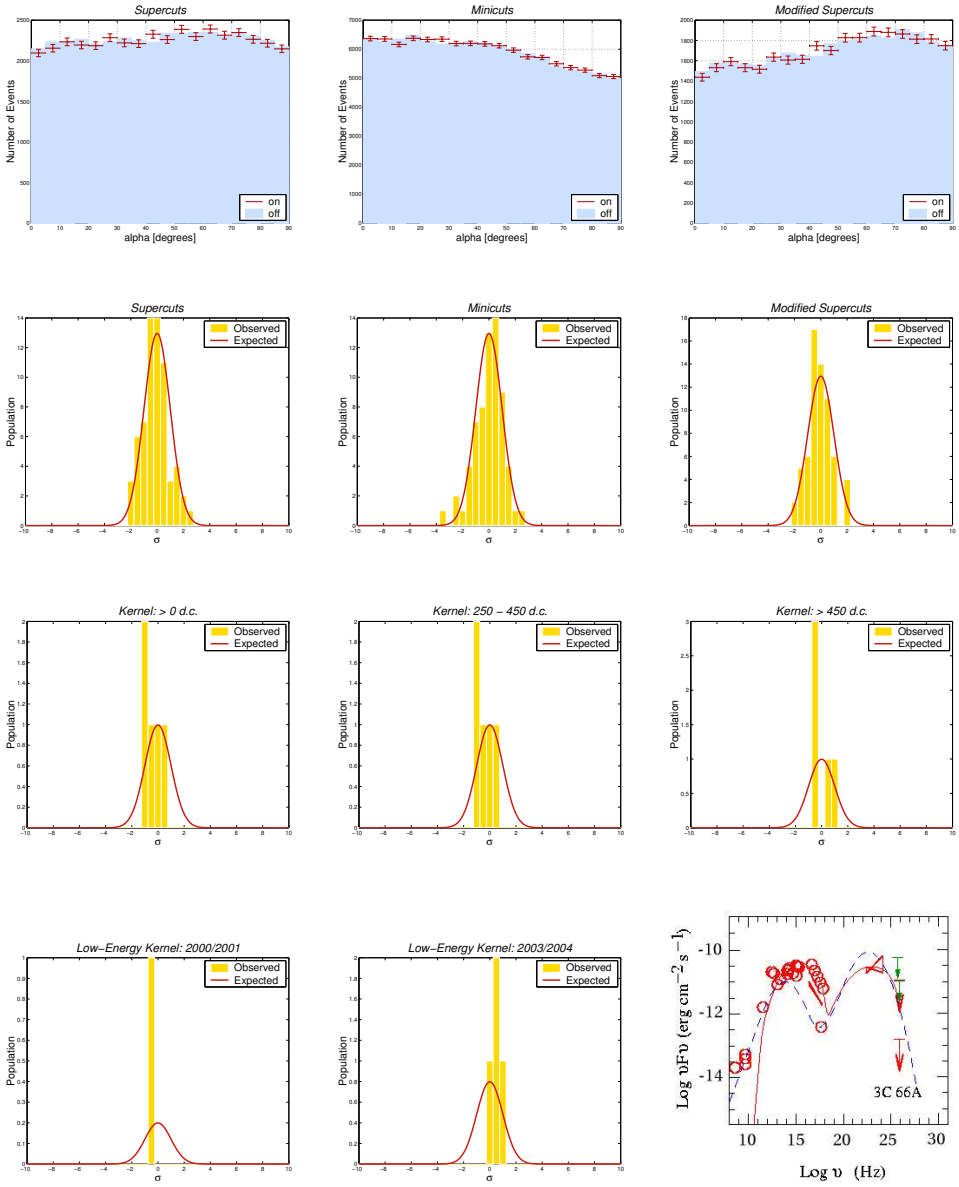

Figure 6.15: Results of analysis of 3C 66A.

with a flux above 1 TeV of $2.1 \pm 0.4 \times 10^{-11}$ cm^{-2} s^{-1} (Neshpor et al., 2001). For comparison the flux upper limit derived in this work was converted to an upper limit above this energy, by assuming a Crab Nebula like spectrum. The result, a flux less than 5.9×10^{-12} photons cm^{-2} s^{-1}, strongly contradicts the Crimean result; however, because of the non-contemporaneous nature of the two sets of observations it is difficult to draw any firm conclusions. It is possible that the Crimean detection occurred while BL Lac was in a high state of flux, while Whipple observed the object in its quiescent state. In support of this view, BL Lac was observed to be optically quite bright throughout the period of Crimean observations while observations with EGRET also provided evidence for flaring in the GeV range (Bloom et al., 1997). The Crimean group offers evidence of variable flux in the TeV range; however, given the large error on their calculations it is difficult to say if this variation is real. Observations of this source by the Whipple (Catanese et al., 1997a) and HEGRA groups (Aharonian et al., 2000) failed to produce a positive detection.

6.5 Source Stacking

In the preceding section, results of analysis of 16 BL-Lac objects have been presented. In all except one case, no significant excess of gamma rays was observed following application of box selection and *Kernel* analysis. For the object 1ES 0806+524 a possible detection, using the low-energy *Kernel* on data recorded in 2001/2002, has been observed and will be discussed in detail later (Section 6.7). The non-detection of the majority of objects is somewhat disappointing but expected, given the flux sensitivity of the current Whipple telescope and the predictions of Stecker et al. (1996) and Costamante and Ghisellini (2002). It may be that these objects are emitting gamma rays but in insufficient quantities for detection with the Whipple telescope. In other parts of the astronomy community, when a group of objects are not clearly detected, it is common to combine their observations in the hope of achieving a statistically significant result. A positive result would then imply that the objects (or at least some of them) are emitting radiation but at an individual level below the flux sensitivity of the detector. To determine if this phenomenon was present in Whipple observations of BL Lacs, all data recorded on these objects over the past four years were combined and treated as a single dataset. In keeping with the method already applied to individual sources, for box selection all *ON/OFF* and *TRACKING* observations were combined and analysed using the matched approach to background estimation. This was a non-trivial task, as the process by which control data for

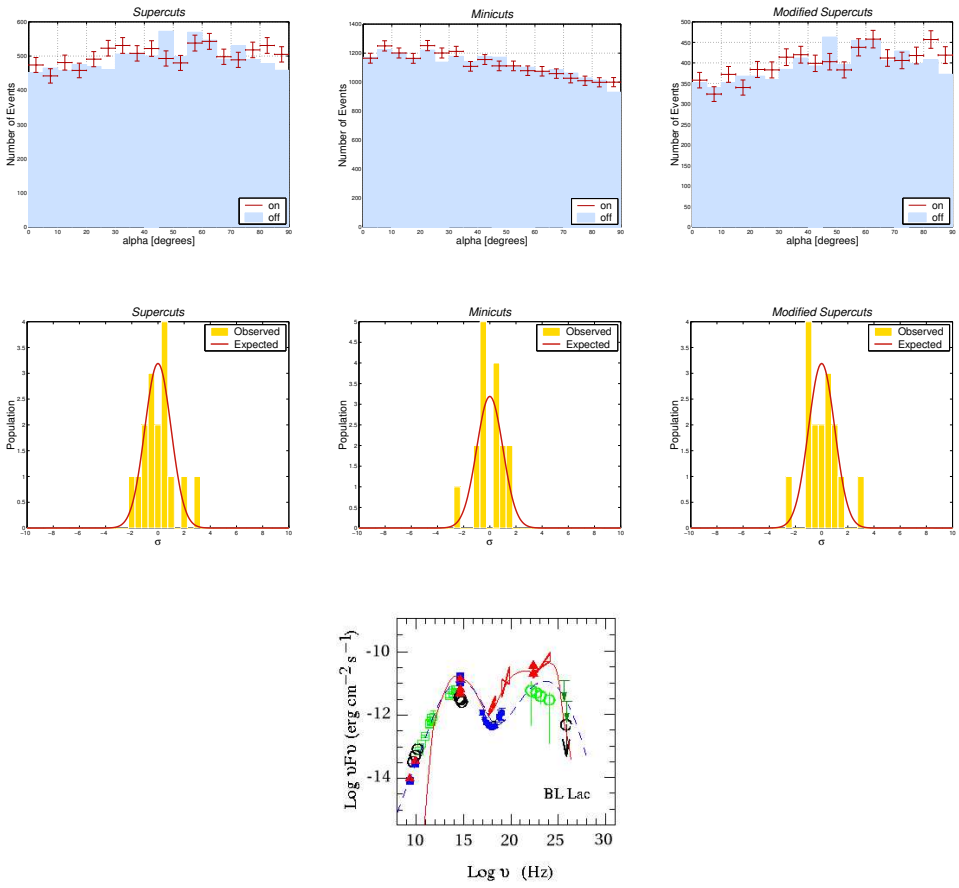

Figure 6.16: Results of analysis of BL Lac.

TRACKING observations is chosen required re-implementation. The reason for this is as follows: when detailing the matched approach to background estimation (Section 5.7) it was stated that, for statistical reasons, no control run should be used more than once. When the original matching process was applied, it was done on a source-by-source basis, thus it is possible and very likely that a given *OFF* run is used as control for a number of sources. To account for this subtlety the matching algorithm was re-applied making sure that all *OFF* runs, including those used in the *ON/OFF* dataset, were utilised only once. Application of *Kernel* analysis was a simpler process; because it can only be applied to *ON/OFF* observations there was no re-analysis required. The lowest-energy *Kernel* was not applied to this data, due to the variable nature of its energy threshold from season to season.

Results of the application of box selection and *Kernel* selection to this stacked dataset are shown Table 6.6 and Figure 6.17. The *ON/OFF alpha* distributions produced by box selection are extremely well matched, with no evidence of an excess at small *alpha* values. The significance values obtained reflect this, showing no meaningful excess of events in the *ON* dataset. To determine if there was any evidence for a short-duration flux increase, the χ^2 test for constant rate was applied. In all three cases the rate is consistent with zero, a fact highlighted by the significance distributions which are very well contained by a Gaussian of zero mean and unit variance. Results following application of the *Kernel* are similar; there is no suggestion of a statistically significant excess or a variable rate. The probability of zero rate is quite small in the case of the low-energy *Kernel*; however, the significance distribution shows that this is most likely due to a small negative deviation away from zero. Based on these results it is concluded that there is no evidence to suggest that any of these objects are VHE gamma-ray emitters.

6.6 Discussion

Analysis of a sample of 16 BL Lacs has been presented. A number of selection techniques, optimised in different *size* bands, have been applied and in all except one case no significant excess has been observed. Discussion of the possible detection of 1ES 0806+524 is reserved for Section 6.7. The choice of these objects as promising TeV gamma-ray sources was based on flux predictions presented in Stecker et al. (1996) and Costamante and Ghisellini (2002), and in an attempt to constrain these predictions flux upper limits have been derived. The results obtained will now be discussed in terms of theoretical model predictions.

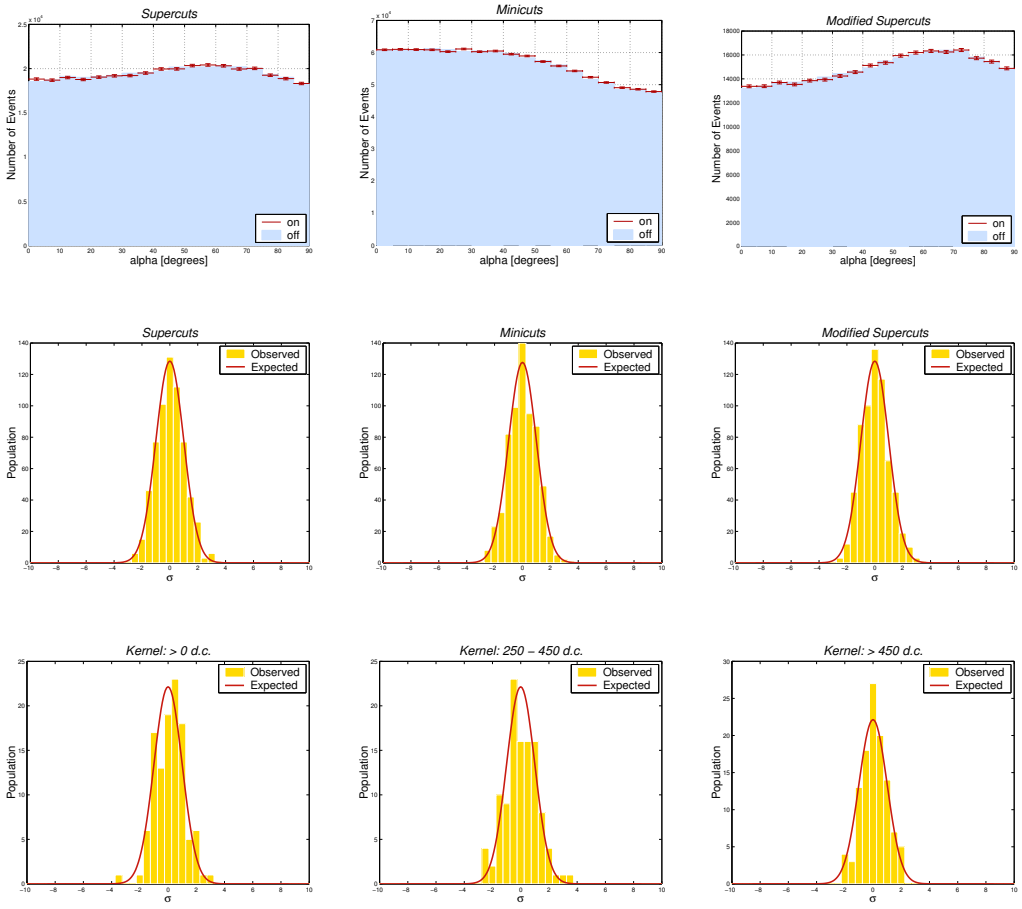

Figure 6.17: *Alpha* distributions and significance distributions produced following application of box selection and *Kernel* analysis to data from 16 BL-Lac objects, combined into a single, stacked dataset. There is no evidence for the presence of low-level emission based on these plots.

Selection / *Size* Range	Excess (σ)	Rate (min^{-1})	P_{χ^2}
Box			
Supercuts	0.397	0.013 ± 0.032	0.08
Minicuts	0.301	0.021 ± 0.071	0.33
Modified Supercuts	0.614	0.016 ± 0.027	0.48
Kernel			
> 0 d.c.	1.688	0.05 ± 0.003	0.19
250 - 450 d.c.	0.353	0.06 ± 0.16	0.02
≥ 450 d.c.	0.585	0.01 ± 0.02	0.87

Table 6.6: Results of analysis of stacked data. Following the non-detection of individual sources it was decided that by combining all observations it might be possible to demonstrate that emission is present but at an individual level too low to be seen with the Whipple telescope.

6.6.1 The Synchrotron Self Compton Model

Both Stecker et al. (1996) and Costamante and Ghisellini (2002) use a synchrotron self Compton model to estimate VHE gamma-ray flux. Based upon the measured spectral energy distribution of Markarian 421, Stecker et al. (1996) derived an approximate scaling law relating the x-ray flux in the 1 - 2 KeV range to the VHE flux in the 200 - 300 GeV range. Details of this process are provided in Chapter 2. Thus the main requirement for an object being a likely TeV emitter is a high x-ray flux. Costamante and Ghisellini (2002) use a slightly more complex method for identifying potential TeV candidates. Again assuming a SSC model, the production of VHE gamma rays requires the presence of highly-energetic electrons and a population of soft photons for up-scattering. Using the time-averaged x-ray flux as a measure of the energetic electron component and the radio emission as a measure of the soft photon density, Costamante and Ghisellini (2002) identify probable TeV sources as having high x-ray and radio flux. The TeV fluxes are then estimated based on a homogeneous synchrotron self Compton fit to the synchrotron peak.

The required observation time for detection of each source was calculated based on these flux predictions and an estimate of the current sensitivity of the Whipple telescope (Section 2.5.3). In the case of the SSC predictions of

Stecker et al. (1996) the minimum time required to observe any of the objects in the BL-Lac sample at the 5σ level is approximately 400 hours. Based on the estimates of Costamante and Ghisellini (2002) detection of any of the sample at a similar level would require approximately 600 hours. Given these results and the fact that the maximum exposure on any one object was 36.5 hours, the non detection of these sources is not surprising. It is not possible to dedicate a large amount of time to a single object with the current telescope, as due to the nature of the technique only approximately 800 hours observations are carried out each year. Realistically the only way of detecting these objects with current instruments is to serendipitously observe them during a period of high flux. The Whipple observing program is organised with this in mind; short snapshots of the most likely candidates are recorded at regular intervals, in the hope of observing an object while in a high state of flux. In such cases observations of other objects are suspended and a continuous exposure on the flaring source is carried out. The x-ray flux of an object is also used as means for identifying possible periods of increased emission. Using this approach the BL Lac 1ES 1959+650 was confirmed as a TeV gamma-ray emitter following observations by Whipple during an extended period of increased flux (Holder et al., 2003).

The upper limits calculated in this work agree with the flux predictions of both Costamante and Ghisellini (2002) and Stecker et al. (1996); however, longer exposure times are required to truly test the models. The potential of the approach to identifying gamma-ray sources is highlighted by the fact that two objects on the original list of gamma-ray candidates (1ES 2344+514 and 1ES 1959+650) have since been confirmed as TeV emitters (Holder et al., 2003; Aharonian et al., 2004), while another two, 3C 66A and BL Lac, have reported detections (Neshpor et al., 1998, 2001). Next generation detectors such as VERITAS, with a flux sensitivity above 300 GeV of 8×10^{-13} photons cm^{-2} s^{-1} for a Crab Nebula like spectrum (a 5σ detection in 50 hours observations) will allow these predictions to be tested in just a few hours of observations. It should be noted that, while the predictions of Stecker et al. (1996) include possible effects due to intergalactic absorption (for details see Section 2.5.1 and Section 2.5.2), the flux levels quoted by Costamante and Ghisellini (2002) do not. As a result it is entirely possible that the flux estimates provided by Costamante and Ghisellini (2002) are overly optimistic and the time necessary for detection is, in reality, much longer.

6.6.2 The Fossati et al. (1998) Parameterisation

The original Fossati parameterisation used radio luminosity to describe the average SED of blazars. Donato et al. (2001) have modified this approach so

that objects with low radio luminosity or higher synchrotron peak are more accurately described. Costamante and Ghisellini (2002) apply this latter method to estimate the VHE gamma-ray flux, with a further refinement for high-peaked BL Lacs included. Based on this approach, the times required for a 5σ detection were calculated and in general are much less than those predicted by the SSC models of Stecker et al. (1996) and Costamante and Ghisellini (2002). For some objects, the exposure time is sufficient for a significant excess to be observed and the non-detection of all objects clearly contradicts the Fossati approach. The inconsistency is further highlighted by upper limit calculations: in the case of three objects, RGB J0214+517, 1ES 1727+502 and 1ES 1741+196, the flux levels determined in this work are less than the values predicted by the Fossati parameterisation. A possible explanation is that the Fossati model may be more suitable to describing the spectral energy distribution of sources that are in a high state of flux. Its derivation was based on a sample of BL-Lac objects including the known TeV emitters, thus the dataset was somewhat biased toward higher states of emission. It should also be noted that the parameterisation was designed to describe the average SED of sources with equal synchrotron and self-Compton power, which is generally the case when a source is flaring but not necessarily true when in quiescence. This explanation is given credence by the fact that the Fossati parameterisation provides an excellent fit to observations of Markarian 421 during periods of flaring.

6.7 The case of 1ES 0806+524

Analysis of 1ES 0806+524 produced no significant excess of *ON*-source events when box selection techniques were applied. Application of the *Kernel* to the combined set of observations on this source also failed to yield a positive result, however analysis of data recorded throughout season 2001/2002, with the lowest-energy *Kernel*, produced a highly significant 5σ detection. This is a very interesting result and, if real would represent the first detection of a VHE source in this energy band, using the imaging atmospheric Cherenkov technique. In addition, a confirmed detection would have a number of exciting scientific implications. Detection in this energy range alone would suggest a source spectrum quite different to any of the established sources (Krennrich et al., 2001), indicating a very sharp cut-off, perhaps occurring at the acceleration site itself or due to interaction with intergalactic soft photon fields. The latter explanation is particularly attractive, as evidence for EBL absorption has already been reported in the case of H 1426+428 (Petry et al., 2002). With a similar redshift, a confirmed detection of 1ES 0806+524 in

such a restricted energy domain could reveal much more information about the EBL.

Before proceeding with a detailed discussion of the physical implications of the result it is necessary to investigate the result in greater detail. There are a number of reasons for doing so: this detection has occurred using a relatively novel analysis method and, although the *Kernel* has been thoroughly tested for possible systematic errors, something may have been overlooked. Even more importantly, in this case we are dealing with very small gamma-ray events, just above the telescope hardware threshold. This region is notorious for its sensitivity to small differences in observing conditions, normally caused by changes to the instrument or sky-brightness variations. Such systematic differences affect the number of pixels passing *picture/boundary* cleaning, which transmits to a difference in the shape and orientation of the Cherenkov images. As a result, a search for gamma rays in this region in particular may be prone to false excesses.

There are a number of ways by which the excess observed in the case of 1ES 0806+524 could arise: it may be caused by anomalous errors in the dataset; it could be due to an unstable selection procedure; a gross sky-brightness difference is a known source of bias; or it may just be that 1ES 0806+524 is a genuine gamma-ray source. In an attempt to determine the nature of the excess observed for 1ES 0806+524 each possible source of bias will now be addressed in sequence.

6.7.1 Corrupt Data

The *ON/OFF* observing approach utilises a method for background estimation which assumes that the *OFF*-source field is an accurate representation of the background level in the *ON*-source field of view. During variable weather conditions this is not necessarily true, as the frequency with which the telescope triggers is highly dependent on atmospheric conditions. To eradicate this source of bias, all data analysed in this work was subject to a preselection process which, based on the raw trigger rate, eliminated poor-weather observations from further analysis. In spite of the careful selection of data, for some objects a number of files were observed to yield spurious results, with wildly fluctuating excesses evident after applying box selections. In some cases these results were accompanied by atypical *alpha* distributions showing a gross shift toward large *alpha* values. Although the source of this effect is unknown, it is possibly due to some fatal software error, either when the data were being recorded or archived.

To determine if this effect was evident in the 1ES 0806+524 result, the run-by-run rate and significance distributions were constructed. If the excess

was due to errors in the dataset one would expect the majority of the significance to emanate from a small number of scans, with the others yielding a null result. The rate and significance distributions are shown in Figure 6.18 and provide proof that the event excess is not due to a small cohort of corrupt data files. Clearly the excess is divided relatively evenly between each of the points, with most of the results centred around a value above zero. This fact is highlighted further by the cumulative excess distributions. The relatively smooth growth in excess as the size of the dataset increases indicates that each file contributes a similar amount to the overall effect. It is possible that a similar error is present in each of the files; however, given the large number of scans and the relatively extended timespan over which the observations were carried out, this is highly improbable. Therefore, based on these results, it is concluded that the 1ES 0806+524 result is not caused by corrupt data.

6.7.2 The *Kernel* Selection Algorithm

During development the *Kernel* was rigorously tested for evidence of instability, that is the introduction of a false signal owing to small differences between the *ON* and *OFF* datasets. Although no such evidence was found in the case of *ON/OFF* observations, it is possible that some sources of error were overlooked. Since the *Kernel* operates at extremely low energy and is reliant on simulated data, it is reasonable to suspect that it may not be as robust as traditional gamma-ray selection procedures such as *Supercuts*. If this were true, the *Kernel* itself could prove to be the source of the 1ES 0806+524 detection.

To determine if there was any evidence for the *Kernel* being over-sensitive to dataset differences, the results of the 1ES 0806+524 analysis were compared to those of the other objects analysed. Although the BL-Lac dataset contained 16 objects, seven of these comprised data recorded in *TRACKING* mode only, and therefore were not included in the *Kernel* analysis. This leaves a rather limited dataset of nine objects and because of variations in energy threshold observations from different seasons may not be combined. As a result our final sample was actually made up of 14 points pertaining to data on a given source for each season it was observed. The results of this comparison are illustrated in Figure 6.19 and for reference the expected Gaussian distribution in the case of a null dataset is included. Clearly the *Kernel* shows no evidence for the presence of wildly fluctuating results. Although the dataset is relatively small, it is entirely consistent with zero emission in all instances except that of 1ES 0806+524 throughout the 2001/2002 observing season. This indicates that instability of the *Kernel* technique is itself an unlikely source of the excess obtained for 1ES 0806+524.

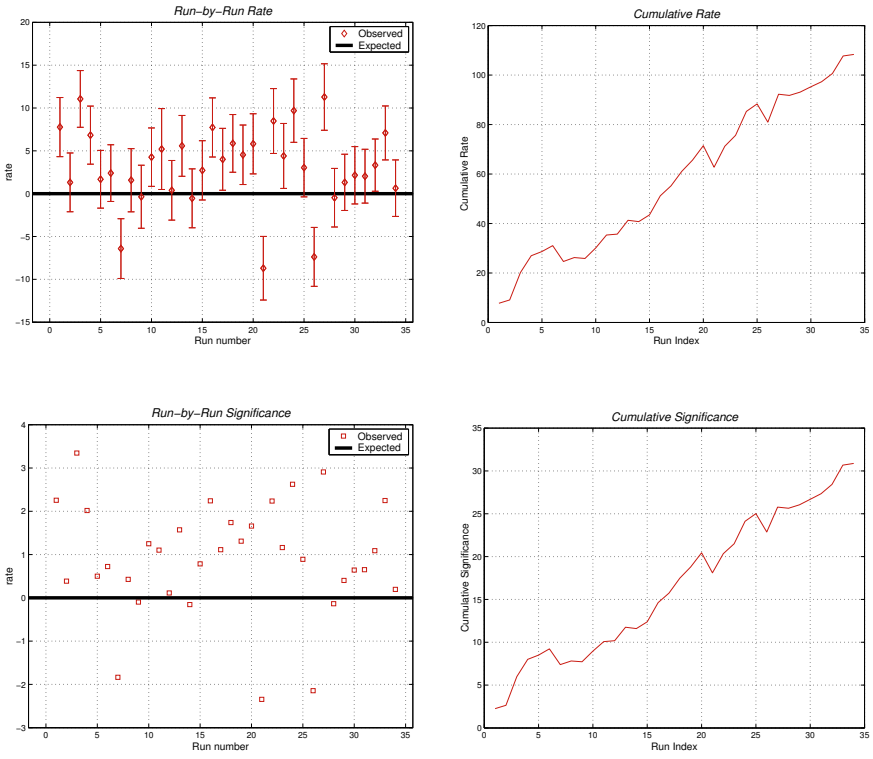

Figure 6.18: Run-by-run rate and significance, and cumulative rate and significance. To rule out the possibility that the 1ES 0806+524 excess was the result of some corrupt data it was decided to investigate the relative contribution of each observation to the overall result. In the figures provided it is clear that the excess is evenly distributed between most files in the dataset, indicating that corrupt data is unlikely to be the source of the observed excess.

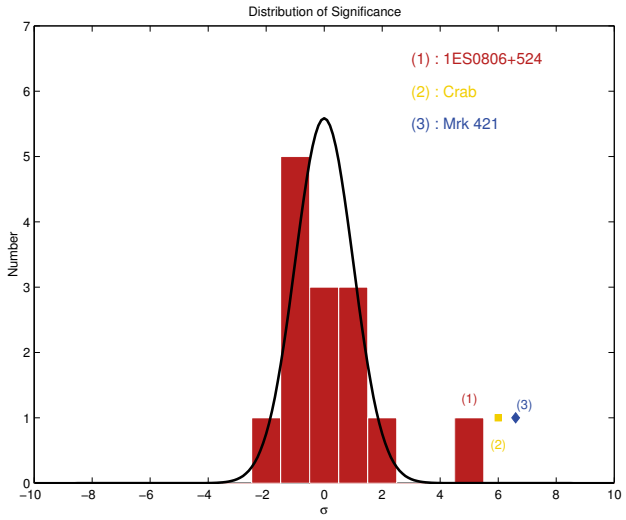

Figure 6.19: Distribution of significance obtained following analysis of all nine BL-Lac candidate objects over the course of four observing seasons, using the lowest-energy *Kernel*. Taking into account that observations on a source for different seasons must be treated on an individual basis the distribution contains 16 elements. For comparison the results following identical analysis of the Crab Nebula and Markarian 421 are also shown.

Application of the *Kernel* to an established gamma-ray source should provide an additional test of the technique. In the case of a known source, one would expect a valid analysis method to reveal a positive excess in an energy range similar to that in which 1ES 0806+524 was detected. A non-detection, although not entirely conclusive, would strongly suggest that the analysis method is not stable. With this in mind, two of the most readily observed VHE gamma-ray sources, the Crab Nebula and Markarian 421, were analyzed using the same *Kernel* method applied in the detection of 1ES 0806+524. The results of these analyses are also shown in Figure 6.19 and are encouraging. Both the Crab Nebula and Markarian 421 are observed at statistically significant levels, proving that the *Kernel* is capable of identifying real gamma-ray events in this energy domain. The fact that these two established sources and 1ES 0806+524 are detected, while all other results are gathered tightly around zero, indicates that the *Kernel* selection technique itself is almost certainly not responsible for generation of the 1ES 0806+524 excess.

Comparison of Image Parameters

The fact that *Kernel* analysis identifies an excess of events when applied to two established sources is encouraging, lending confidence to the validity of the selection process. Although all three results are from an identical energy region this does not necessarily mean that the *ON*-source excess in each case is due to images with similar characteristics. If it could be shown that events with similar properties are responsible for the excess obtained in the case of all three objects, this would lend additional confidence to the validity of the approach and detection of 1ES 0806+524. In an attempt to determine if this were true, parameter distributions were constructed for Markarian 421, the Crab Nebula and 1ES 0806+524. Two parameters were deemed sufficient for comparison, *size* because it provides a measure of the light content and energy of the events, and *alpha* because it is such a powerful discriminant. The results of this process are presented in Figure 6.20 and Figure 6.21, showing the *ON* and *OFF* distributions, the difference distributions and the cumulative difference distributions of events selected by the *Kernel*.

The *size* distributions (Figure 6.20) are very interesting and show that in some respect all three sources differ, with events of different *size* making up the majority of excess for each source. For both Markarian 421 and the Crab Nebula the *ON* and *OFF* distributions are similar below approximately 160 d.c., with little gain in terms of excess. In sharp contrast 1ES 0806+524 draws a lot of its excess from events with *size* less than this value. This trend is even more evident from studying the cumulative significance distribution.

In the case of 1ES 0806+524 the excess begins to increase around 60 d.c., however for the other two objects this growth only begins around 130 d.c.. 1ES 0806+524 gains little excess for events with *size* above 250 d.c. while it is from this region that both Markarian 421 and the Crab Nebula select the majority of their gamma-ray events.

The *alpha* distributions (Figure 6.21) reveal a similar pattern. The distributions for Markarian 421 and the Crab Nebula differ by a small amount; however, the difference between these two objects and 1ES 0806+524 is distinct. For Markarian 421 most of the events that constitute the gamma-ray signal have *alpha* values less than 20°, as evidenced by a flattening of the cumulative distribution beyond this point. In the case of the Crab Nebula dataset very little excess is derived from events with *alpha* values greater than 30°. The extra spread in this distribution, compared to Markarian 421, is probably due to a shift in the *size* distribution toward smaller values (Figure 6.20). Events with a lower light content tend to comprise a smaller number of pixels thereby making it more difficult to accurately reconstruct their arrival direction. The *alpha* distribution for 1ES 0806+524 is notably different; there is an excess of events in the *ON* dataset for all values of *alpha* up to 90°. Again this may be attributed to the observed shift in the *size* distribution toward smaller *size* (Figure 6.20), as the major axis of such tiny images is extremely difficult to define.

The stability of the *Kernel* technique has been further verified by the null results obtained following analysis of a number of objects. It is tempting to conclude that the detection of two established sources using the *Kernel* is further proof of the applicability of the approach and of the veracity of the 1ES 0806+524 detection. However, it has been shown that a large portion of the 1ES 0806+524 excess comes from a population of events that are not present in the Markarian 421 or Crab Nebula datasets. Furthermore the *alpha* distributions indicate that 1ES 0806+524 draws its excess from events with *alpha* values ranging from 0° all the way out to 90°, or in other words detection is effectively based on a *shape* selection only (Section 3.4). It should be noted that such selections have proved particularly sensitive to bias caused by differences in sky brightness (Cawley, 1993).

6.7.3 *ON* - *OFF* Sky Brightness Differences

As already stated, the *Kernel* algorithm selects events of extremely low energy, right down to the hardware threshold of the telescope. In this region bias due to differences between the *ON* and control datasets are likely to be most pronounced. The two main sources of bias are: changes in the response of the instrument and variations in brightness between different regions of

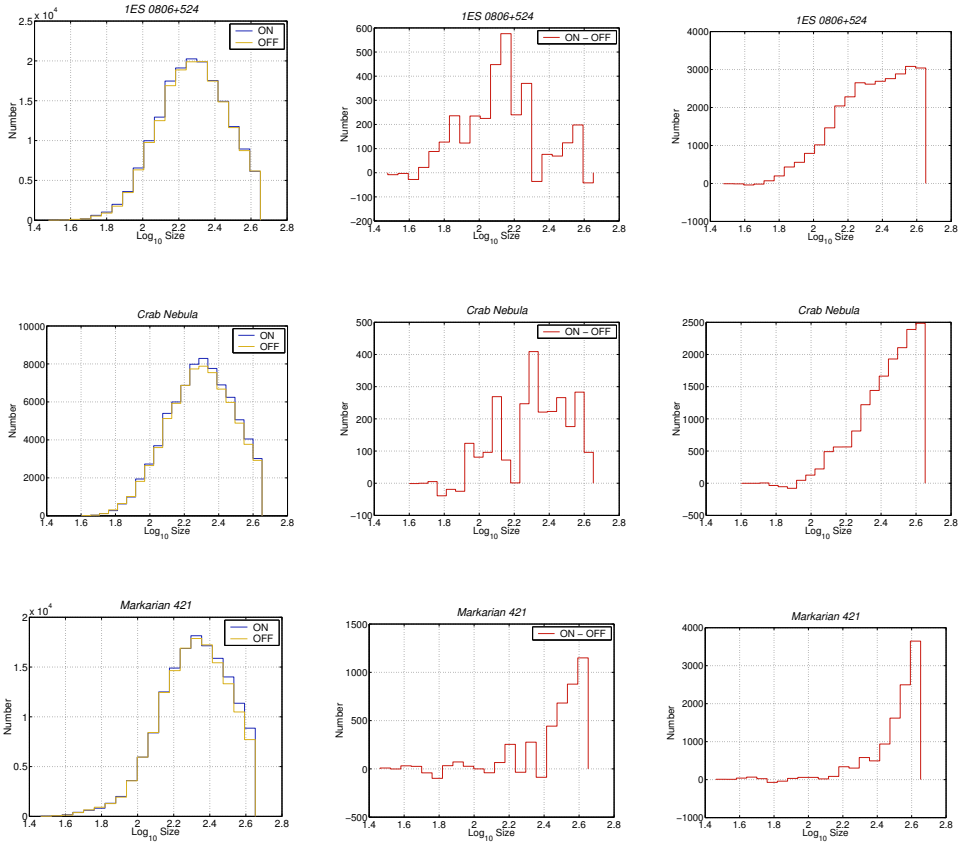

Figure 6.20: *Size* distributions for 1ES 0806+524, Markarian 421 and the Crab Nebula. The left-hand column shows the *ON* and *OFF size* distributions, the middle column shows the *ON* - *OFF* difference distribution, and the right-hand column shows the cumulative difference distribution. It is clear that the 1ES 0806+524 excess contains a population of small-*size* events not present in the other two sources.

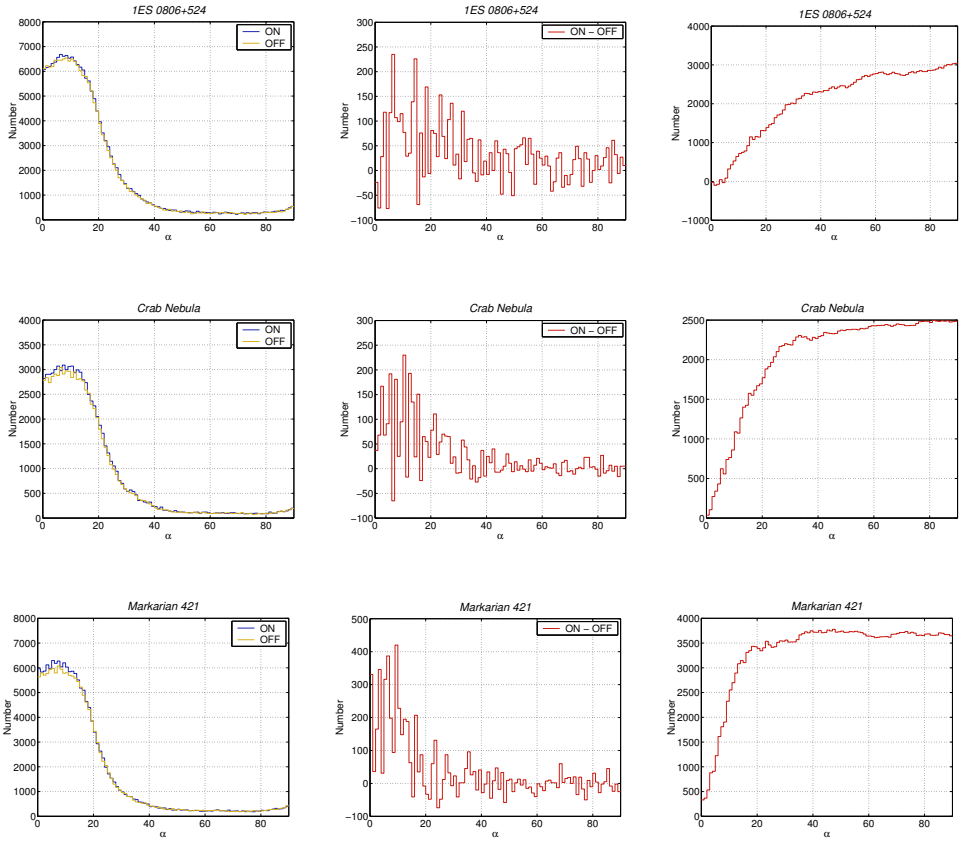

Figure 6.21: *Alpha* distributions for 1ES 0806+524, Markarian 421 and the Crab Nebula. The left-hand column shows the *ON* and *OFF* *alpha* distributions, the middle column shows the *ON* - *OFF* difference distribution, and the right-hand column shows the cumulative difference distribution. It is clear that the 1ES 0806+524 detection comprises a number of events with large values of *alpha*. In other words detection is based on, effectively, a *shape* selection only.

sky. The former is probably less important as instrumental effects should be present in both the *ON* and *OFF* datasets, thereby canceling each other out. Differences between the *ON* and *OFF* fields, caused by the presence of bright stars in the field of view, are known to be capable of introducing, into a set of observations, a false excess or deficit. Although noise padding (Cawley, 1993) has proved successful in counteracting this effect, it has only really been tested in the case of traditional selection methods at higher energy. Noise padding is not expected to work well when dealing with events close to the hardware threshold of the telescope for the following reason: padding works by adding noise to a PMT from the darker region of sky so that its signal amplitude is sufficiently large to pass *picture/boundary* cleaning. In the case of extremely low-energy events there is an absence of pixels to which noise can be added, due to the presence of the hardware trigger. Thus it is unclear if padding is sufficiently robust when dealing with very small images, as in the case of detection of 1ES 0806+524. The success of noise padding in extreme situations has recently been called into question (Kildea, 2002; O'Neill, 2004).

A gross sky-brightness difference should manifest itself as a difference in trigger rate between one set of observations and another, assuming similar instrumental conditions and elevation distribution. For 1ES 0806+524 there is a raw excess at the $11\,\sigma$ level suggesting that a sky-brightness difference may be present. This disparity is reduced following application of noise padding and *picture/boundary* cleaning; however, a $7\,\sigma$ effect still persists. Although this is worrying, it is far from conclusive; the excess of events after cleaning is not necessarily responsible for the excess obtained after selection. The presence of such an excess is not evident when analysing data on the same object during the subsequent season, in fact a large deficit of $14\,\sigma$ is observed in the raw dataset, which is reduced to $4\,\sigma$ following image cleaning. These results suggest that an overall sky-brightness disparity may not be the source of the 1ES 0806+524 detection.

In an attempt to prove if the excess is due to sky brightness, the mean noise level for the *ON* and *OFF* fields was calculated for 1ES 0806+524 and, for reference, all the other objects analysed in this work. As an approximation to the overall sky brightness the mean pedestal variance over the entire camera for a set of observations was used. The results of these measurements are presented in Figure 6.22, and indicate that, overall, the *ON* and *OFF*-source fields for 1ES 0806+524 are very similar. A small positive excess is evident; however, compared to the other objects analysed this is not atypical. The fact that none of these objects are observed at a significant level suggests that the level of background-light difference present in the 1ES 0806+524 dataset is not the source of the event excess. Furthermore both

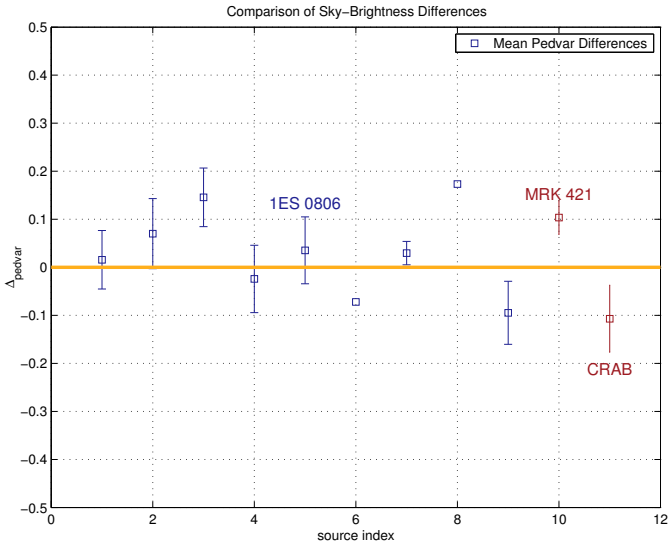

Figure 6.22: Net sky-brightness differences between the *ON* and *OFF* fields for a number of objects analysed in this work. Evidently the *ON* and *OFF* fields of view for 1ES 0806+524 are very similar with regard to total background light level.

Markarian 421 and the Crab Nebula possess *ON/OFF* fields which are quite different in comparison, yet a gamma-ray signal is observed in both cases. The possibility of these detections also being caused by brightness effects is diminished by the fact that, in the case of Markarian 421, the *ON* field is brighter than the *OFF*, while the opposite is true for the Crab Nebula. These results indicate that the *Kernel* is not particularly dependent on background light levels, and that in the case of 1ES 0806+524 there is no significant difference between the source and control fields of view.

In addition to comparing 1ES 0806+524 to other observations a search was also performed for a possible correlation between the magnitude of the significance and mean *pedestal-variance* difference within the 1ES 0806+524 dataset. By comparing the significance and *pedestal-variance* difference for each *ON/OFF* pair it was possible to determine if the excess was dependent on brightness. The results of this analysis are presented in Figure 6.23. The distribution of significance shows no obvious shift to higher values as the *pedestal-variance* difference increases. This non-effect is further highlighted by the cumulative significance plot, which shows that the increase in significance is relatively steady and uncorrelated with brightness difference. Based on these results it is not possible to conclude that a gross sky-brightness difference is the source of the 1ES 0806+524 result.

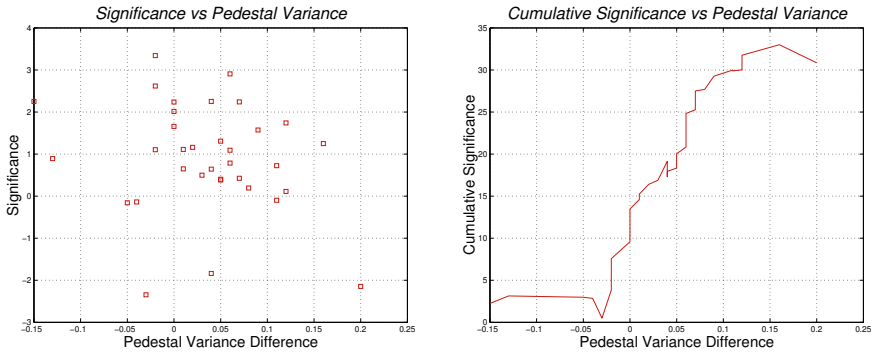

Figure 6.23: Comparison of significance to *pedestal-variance* difference. Based on these plots there is nothing to suggest that the 1ES 0806+524 excess is correlated with differences in sky-brightness.

Although it has been proved that the 1ES 0806+524 *ON* and *OFF* fields of view are similar in terms of overall brightness, it is still possible that significant differences exist between the two regions of sky. This statement is easily explained; two fields of view which vary greatly from region to region may still appear homogeneous provided that, overall, the differences cancel each other out. Such an occurrence would explain all the results obtained so far, including the similarity between the total background light levels of the *ON* and *OFF* fields and the event excess observed in the raw dataset. The probability of dissimilar *ON* and *OFF* fields is increased by reviewing the observing records, which show that during observations of 1ES 0806+524 a number of PMTs were regularly turned off by the observers. This strongly suggests the presence of a star (or many stars) in the field of view, a fact confirmed by examining an optical image of the region around 1ES 0806+524 identical to that observed by the Whipple telescope (Figure 6.24). From this picture it is clear that a bright star (B Magnitude: 4.83, V Magnitude: 4.80) is present in the field of view.

To determine if this star had an adverse effect on the dataset, in terms of regions of camera in which a sky-brightness effect was evident, the *pedestal-variance* difference between *ON* and *OFF* fields was calculated, this time on a tube-by-tube basis. Care was taken to eliminate those PMTs that were turned off during the course of an observing run, and for comparison the number of times each PMT was switched off was also determined. The results of this process are shown, superimposed on a picture of the Whipple camera, in Figure 6.25. From these plots it is clear that there are regions of

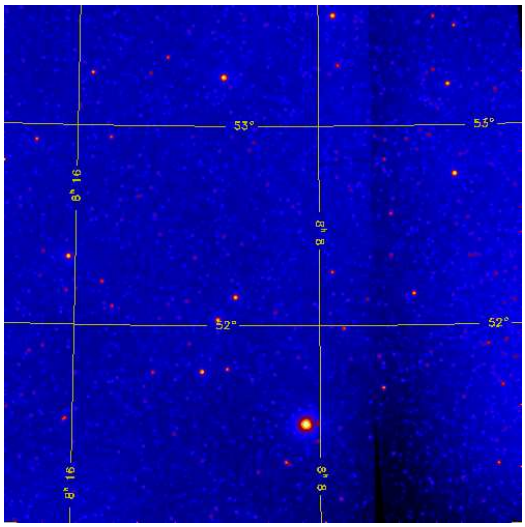

Figure 6.24: Optical image of the region of sky covered by the Whipple 10m telescope when observing 1ES 0806+524, which is at the centre of the field of view. The star *27 Lyn* (B Magnitude: 4.83, V Magnitude: 4.80) is visible in the lower part of the image.

the *ON* and *OFF* fields that differ by a significant amount. In the upper left quadrant of the camera there are a bank of PMTs that are turned off on a regular basis which, taking into account rotation of the sky during a three-month-long observing period, is indicative of a bright star. In spite of the turning off of tubes in this region a high noise level is still evident and is most likely caused by leakage of starlight into surrounding PMTs. Other regions of the camera also show evidence for increased brightness in the *ON* or *OFF* field, however the frequency with which PMTs are turned off is quite low. This difference in sky brightness is probably due to the number of low-luminosity stars present in the field of view (Figure 6.24).

Based on these observations it is concluded that the earlier analysis of the *ON* and *OFF* source fields was not sufficiently robust to highlight differences due to sky brightness, arising from stars in the field of view. As stated earlier the overall result, although suggestive of similar sky regions, only proves that the net amount of background light present in the *ON* and *OFF* datasets is similar. In this case such a result is produced by two vastly different fields, with the same average light intensity. This result provides a possible source of the excess obtained from 1ES 0806+524. To investigate this further, a two-dimensional map of the location of gamma-ray events selected by the

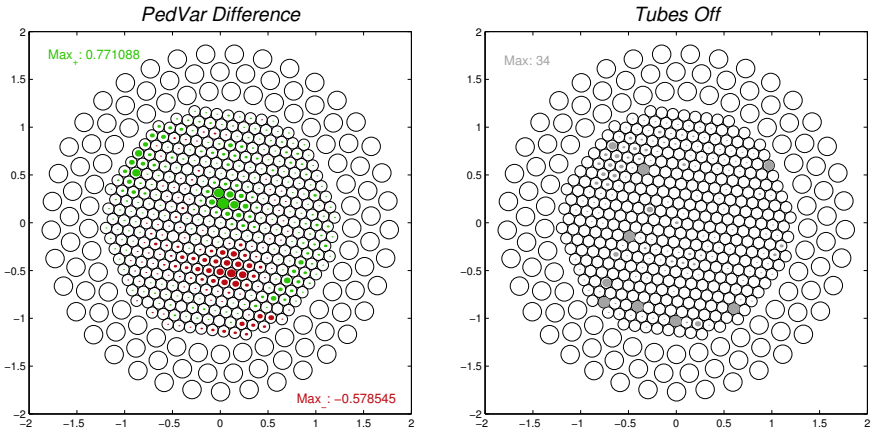

Figure 6.25: Map of the Whipple camera. On the left the *pedestal-variance* difference between the *ON* and *OFF* fields of 1ES 0806+524 is shown. The fraction of each pixel filled with colour is a measure of the magnitude of the difference, with a positive difference shown in green and a negative difference shown in red. On the right the frequency with which each pixel is turned off is shown, where the number of times each pixel is turned off is represented by the size of the coloured pixel. A number of regions of the clearly differ in terms of brightness, while the presence of a bright star, in the top left corner of the camera, is indicated by the large number of PMTs turned off.

Source	$P_{Rayleigh}$
1ES 0806+524	7.5×10^{-11}
Crab Nebula	0.476
Markarian 421	0.178

Table 6.7: Results obtained following application of the Rayleigh test (Mardia, 1987) for a uniform field of view. For a true gamma-ray source one would expect a uniform distribution of image centroids. The low probability of this being true, as obtained in the case of 1ES 0806+524, indicates that the detection of 1ES 0806+524 is almost certainly false.

Kernel was constructed, based on the image centroids. Figure 6.26 shows this image, and for reference similar maps are provided in the case of the Crab Nebula and Markarian 421 detections. This image is particularly conclusive; the majority of the event excess comes from a single quadrant of the camera, which is untypical when compared to the other sources. To further highlight this fact, the significance for each quadrant of the camera was calculated and overlaid in Figure 6.26. In the case of the Crab Nebula detection, the excess is relatively evenly distributed throughout the four quadrants of the camera, with a slight bias toward the left hand side. A similar pattern is evident for Markarian 421; however, here the bias seems to be in the lower half of the camera. For 1ES 0806+524 the results differ vastly, an approximate $6\,\sigma$ excess comes from the upper left quadrant with roughly $1\,\sigma$ provided by each of the other three. As a final analysis the Rayleigh test (Mardia, 1987) was applied to the data, to determine the probability of the image locations being evenly distributed across the field of view. The results of this test (Table 6.7) show that for Markarian 421 and the Crab Nebula the images locations are evenly distributed over the field of view, as one would expect in the case of a true gamma-ray source. In contrast, for 1ES 0806+524 the probability of an isotropic distribution of image centroids is extremely low. As a result of this grossly asymmetric result it is concluded that the signal obtained in the case of 1ES 0806+524 is most likely false.

Although the detection of 1ES 0806+524 has been all but disproved it is still unclear how this false excess was produced. The answer may be provided by determining the type of events responsible for the detection. With this in mind, parameter distributions were constructed for the top left-hand quadrant of the camera and the other three quadrants combined, the results of which are illustrated in Figure 6.27 and Figure 6.28. From the *size*

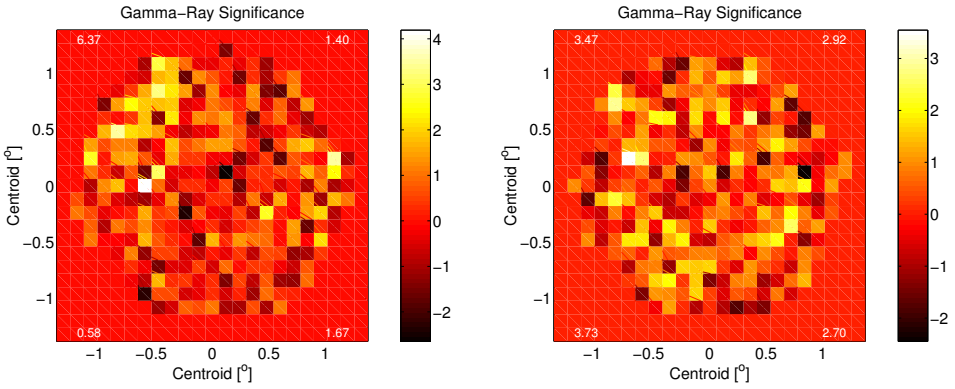

(a) 1ES 0806+524

(b) The Crab Nebula

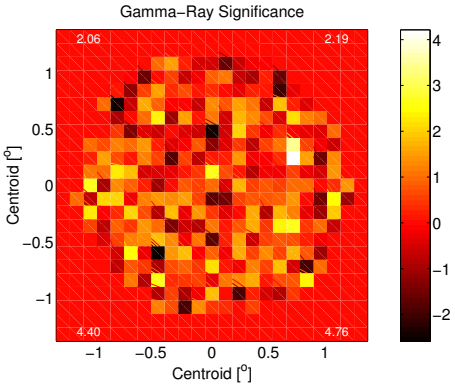

(c) Markarian 421

Figure 6.26: Two-dimensional map showing the location of gamma-rays that make up the *ON*-source excess, for three objects. The colour scale represents the gamma-ray excess, measured in units of standard deviations (or σ). For the two established sources the gamma-ray events are relatively evenly distributed across the camera, however for 1ES 0806+524 the vast majority of events come from a single quadrant. This strongly suggests that the excess is not due to gamma rays and is probably related, in some way, to sky-brightness differences.

distributions it is clear that there is a cohort of events present in the first quadrant of the camera that is absent from the other three. These events are extremely small, a fact highlighted by the difference and cumulative distributions. For the first quadrant of the camera approximately 30 % of the excess comes from events with *size* less than 160 d.c., while in the rest of the camera the *ON* and *OFF* distributions are virtually identical below this point. The *alpha* distributions (Figure 6.28) are even more instructive; for the three quadrants combined most of the excess comes from events with *alpha* values less than 30°. In the first quadrant the picture is very different, with excess evident for all values of *alpha*. As discussed earlier this spread in the *alpha* distributions may be due to the smaller-*sized* events. Interestingly the images from the three quadrants combined appear to have similar properties to the events responsible for the detection of Markarian 421 and the Crab Nebula and further highlights the fact that something untoward is occurring in one quadrant of the camera which is producing an excess of gamma-ray like events.

Although it is tempting to identify sky-brightness as the sole reason for the excess of events observed for 1ES 0806+524, the facts do not fully support this explanation. The sky-brightness map (Figure 6.25), obtained using the *pedestal-variance* distributions prove that positive brightness differences exist in the top left quadrant of the camera. However, an equally sized difference exists in a number of other parts of the camera, yet there is nothing to suggest a gross excess of *ON*-source events in these regions. A possible explanation may be provided by observing the location of the top three PMTs for each event, in terms of the amount of light contributed to the overall *size*, or the *loc1*, *loc2* and *loc3* parameters. A map of the camera showing the sum of these three parameters is provided in Figure 6.29. From the difference distribution it is obvious that a bank of PMTs in the top left corner of the camera triggers more often during observations *ON*-source than *OFF*-source. This difference cannot be attributed solely to the bright star in this region as the *OFF* distribution shows that the same tubes trigger with increased frequency. The appearance of this type of effect, present in both the *ON* and *OFF* field of view, is indicative of an instrumental problem, most likely a higher than average gain or a number of damaged PMTs. Based on all the results presented in the last four sections, the source of the 1ES 0806+524 excess is explained as follows: in the top left-hand quadrant of the camera there are a number of misbehaving PMTs which, on average, trigger more often than most other PMTs. While such an occurrence is also present in other regions of the camera the small increase in background light levels (due to the presence of a bright star) results in these PMTs triggering more frequently in the *ON* dataset than in the *OFF*. Normally such an

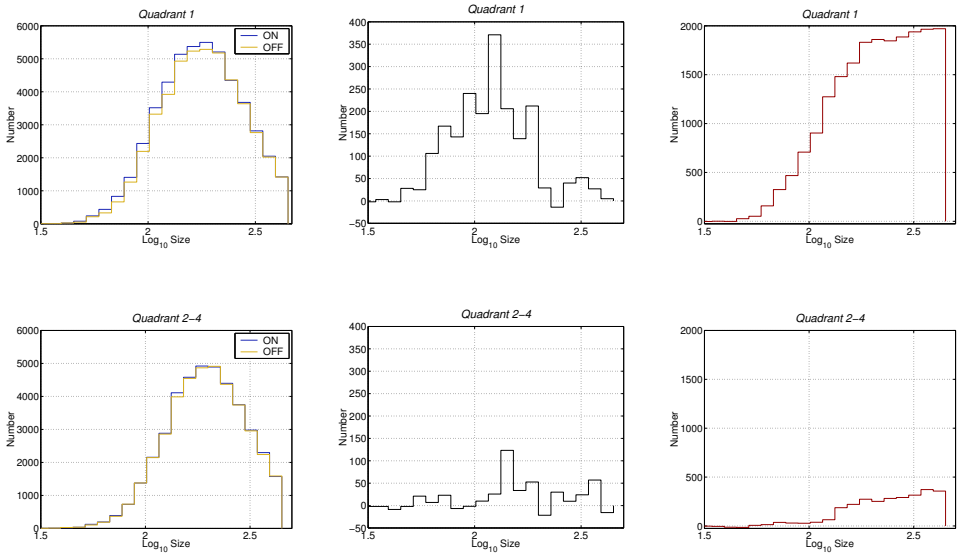

Figure 6.27: *Size* distributions for events from the top left-hand corner of the camera and the other three quadrants combined. The left-hand column shows the *ON* and *OFF size* distributions, the middle column shows the *ON* - *OFF* difference distribution, and the right-hand column shows the cumulative difference distribution. It is clear that the first quadrant contains an excess of extremely small images, which are absent from the other three quadrants. Note that the number of events in the three quadrants combined is normalised to that of the first quadrant.

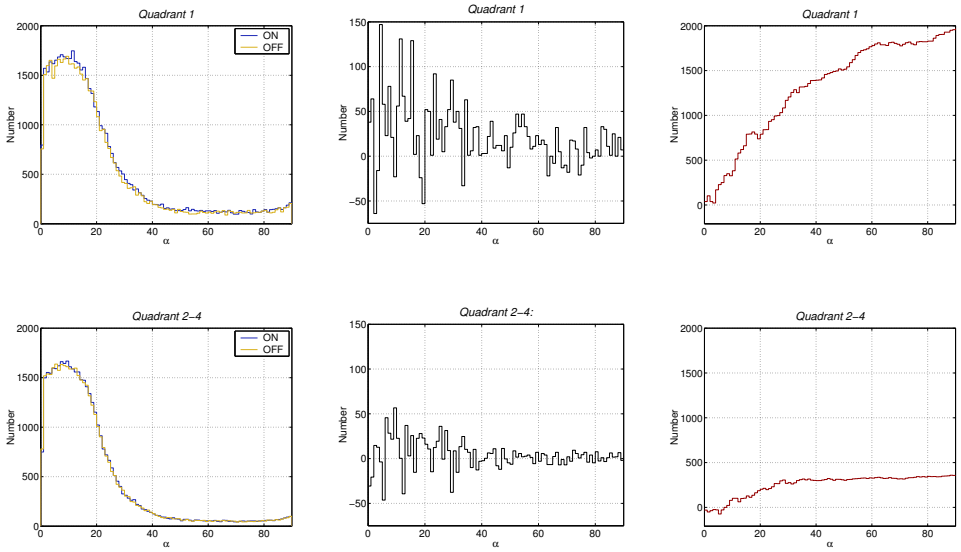

Figure 6.28: *Alpha* distributions for events from the top left-hand corner of the camera and the other three quadrants combined. The left-hand column shows the *ON* and *OFF alpha* distributions, the middle column shows the *ON* - *OFF* difference distribution, and the right-hand column shows the cumulative difference distribution. It is clear that the first quadrant contains an excess of events which are randomly orientated, a pattern not repeated in the other three quadrants. Note that the number of events in the three quadrants combined is normalised to that of the first quadrant.

occurrence would not pose a problem, as these low-amplitude images would be eliminated by software trigger cuts utilised by traditional box selections. The large number of PMTs turned off in this region of the camera result in compact Cherenkov images, that are similar to gamma rays in shape but randomly orientated. This explanation is supported by the *loc* distribution obtained from observations of the same object during the following season (Figure 6.29). The less frequent triggering of the same set of PMTs in the top left-hand corner is probably due to a decrease in gains (Section 4.2.5). Accordingly, the small increase in light from the star, present in this region, is not sufficient to push the amplitude of the PMTs above the triggering threshold and an excess of small events is not produced. As a result observations of 1ES 0806+524 during 2002/2003 fail to register an excess of events similar to that obtained during 2001/2002. It is concluded that in the case of 1ES 0806+524 a series of highly-unlikely events have contrived to produce a population of events which bear a remarkable similarity to low-energy gamma rays, thereby resulting in a false detection of this object.

6.8 Summary

A number of different analysis techniques have been applied to a sample of 16 BL-Lac objects in the search for new sources of VHE gamma radiation. Results of box analyses produced no statistically significant event excess in the *ON* dataset. Results of the *Kernel*, applied to all data for a given source combined, also failed to produce a detection, however application of the lowest-energy *Kernel* to data recorded on BL Lac 1ES 0806+524, throughout season 2001/2002, yielded a $5\,\sigma$ excess. A more detailed study of this result proved the detection to be false, resulting from a combination of inhomogeneity in the camera and sky-brightness differences. Although an unlikely series of events contrived to produce this detection it has illustrated the care required when searching for gamma-ray sources at such low energies. In an attempt to determine if emission from these objects existed, but at a level too low for detection by Whipple, observations on all objects were combined and analysed as a single dataset. No evidence for emission was found. Upper limits were imposed in an attempt to constrain the analytical models used to predict the VHE gamma-ray flux level of these objects. The results obtained are entirely consistent with the synchrotron self Compton models of Costamante and Ghisellini (2002) and Stecker et al. (1996); however, in some cases they are inconsistent with a modified version of the Fossati classification of BL Lacs (Fossati et al., 1998; Donato et al., 2001). It is concluded that the Fossati approach, by its very construction, overestimates the level of

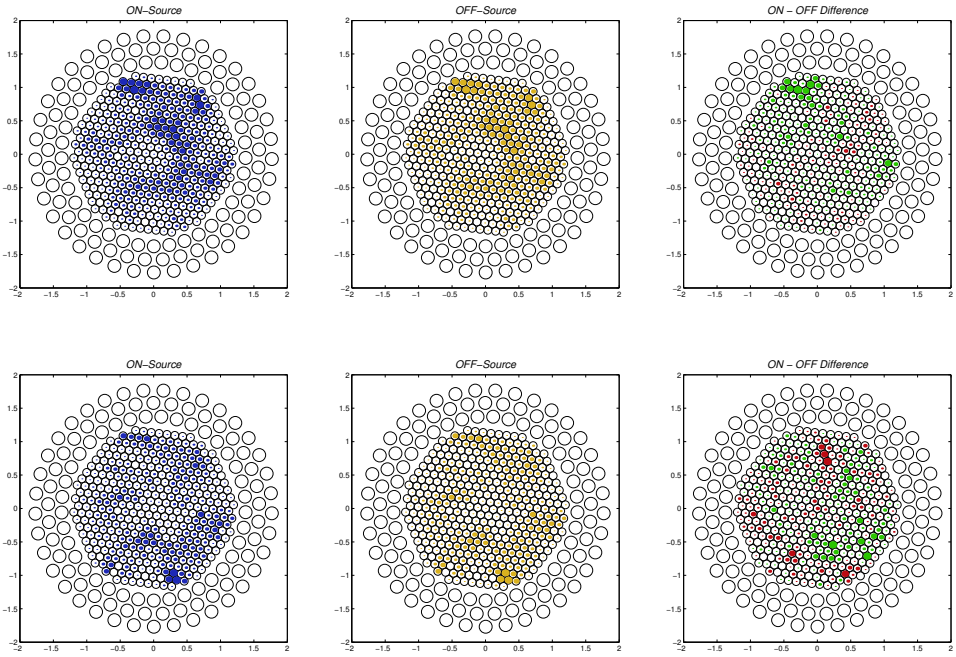

Figure 6.29: The location of the three PMTs which contributed the most light to each Cherenkov event. The top row shows the *loc1 + loc2 + loc3* distribution for observations of 1ES 0806+524 during 2001/2002, while the bottom set of plots the same for observation carried out during 2002/2003. It is clear that the increased frequency with which a group of PMTs in the top left-hand corner of the camera triggers during 2001/2002 is not observed in the 2002/2003 dataset. The fraction of each pixel filled with colour provides a relative measure of the number of times in which it contributed the majority of light to the overall Cherenkov image.

VHE emission from some objects. Finally, based on the SSC predictions, it is predicted that next generation instruments (Section 1.4.4) such as VERITAS, with their greater flux sensitivity, should be capable of detecting these objects in a few hours of observation. However a word of caution is advised here as some predictions quoted in this work do not account for gamma-ray attenuation on the EBL. Thus it is possible and likely that the predicted flux levels are overly optimistic and that a greater amount of observing time will be required for detection of these objects.

Chapter 7

Conclusion

Over the last decade the field of ground-based gamma-ray astronomy has enjoyed a period of unprecedented growth following the establishment of a number of new gamma-ray observatories and detection of several new sources of TeV gamma radiation. In spite of the great advances made during this time there are still many questions regarding gamma-ray astrophysics which remain unanswered. These questions include: the primary population of particles responsible for gamma-ray production, the reason as to why so few of the EGRET-detected AGN are observed in the TeV energy regime and the effect of extragalactic background light on VHE gamma-ray spectra measured here on Earth. The answer to these questions will, at the very least, require detection and study of a greater number of VHE gamma-ray sources. In an attempt to expand the TeV source catalogue, this work has concentrated on searching for new sources of gamma rays using the Imaging Atmospheric Cherenkov Technique. As part of this process a number of issues have been addressed including:

- Development of new gamma-ray selection techniques, in an attempt to detect gamma rays in an energy range not normally targeted by standard analyses.
- A systematic investigation of the stability of various background estimation techniques.
- Prediction of gamma-ray fluxes. Using the analytical models of a number of authors the expected level of gamma-ray emission in the TeV range was calculated. Based on these calculations the most promising candidates for emission at VHE were identified.
- Analysis of a sample of 16 BL-Lac objects in the search for VHE emission from AGN. Using the new analyses developed throughout this work

16 BL Lacs were examined for evidence of an overall gamma-ray flux or periods of flaring activity.

- A detailed investigation of the apparent detection of one BL Lac, 1ES 0806+524. By examining this result the problems of sky-brightness differences between the *ON*- and *OFF*-source fields, when operating close to the hardware threshold of the Whipple telescope, have been highlighted.

The results of each of these topics will now be summarised, and the possibility of further development discussed.

7.1 Gamma-Ray Selection

The standard selection criteria (*Supercuts*) utilised by the Whipple Collaboration have proved very successful, with detection of a number of sources of VHE gamma rays (Weekes et al., 1989; Punch et al., 1992; Quinn et al., 1996; Holder et al., 2003). The traditional methods are not, however, without disadvantage, namely a bias against events of very low and very high energy. In an attempt to lower the energy threshold of the standard analysis, two novel selection methods have been developed in this work. The first, known as *Minicuts*, is based on the box-selection methodology and works by defining a multi-dimensional region of parameter space in which the majority of gamma rays reside. Using a dataset containing a large number of gamma rays, the selection was specifically designed to compliment *Supercuts*, that is to minimise the overlap between events selected by each method. By targeting low-energy events (as low as 236 GeV), not normally selected by standard analysis methodologies, access to a hitherto unexplored region of the gamma-ray spectrum was realised. The method was proved successful with detection of two established sources, the Crab Nebula and Markarian 421, at low energy.

The second gamma-ray selection method, known as *Kernel* multivariate analysis, discriminates between gamma-ray events and background by comparing each Cherenkov image to a reference database of real background and simulated gamma-ray images. The *Kernel* has been successfully applied previously (Dunlea, 2001; Kildea, 2002), however to increase efficiency at lower energy significant development has been carried out during this work. Furthermore, to verify its applicability a number of stability tests have been applied. Using the *Kernel* it has been been proved that extremely low-energy gamma-ray events may be selected (as low as 140 GeV), right down to the hardware threshold of the telescope. Again this new approach has proved

successful, with detection of the Crab Nebula and Markarian 421 in a low-energy domain unexploited by standard analysis. One disadvantage of the *Kernel* selection technique is the amount of time required for the analysis of a medium-sized dataset. Because the *Kernel* technique works by comparing every event in the analysis dataset to those in the reference datasets, it is computationally extremely intensive. Typically the complete analysis of a single *ON/OFF* pair using the *Kernel* approach takes approximately one hour, compared to just a few minutes for traditional box selections. This problem may be relieved by applying the lattice approach outlined in Dunlea (2001) or by using clusters of high-speed processors.

Further development of the *Kernel* may be possible, and a number of issues raised during this work warrant a more detailed investigation. The *Kernel* approach is highly dependent on its twin reference datasets of simulated gamma rays and real background. Therefore, increased selection efficiency may be achieved by using simulations which are more representative of genuine gamma-ray events. For example, during development of the *Kernel* technique, its efficiency was observed to be reliant on the level of injected noise in the gamma-ray simulations. Accordingly the use of one set of simulations when analysing a source with a high background light level may not be suitable for application to a source with low night-sky background. Similarly, the choice of the background database is important when aiming to maximise selection efficiency. Most selection methods are relatively successful at discriminating between high-energy gamma-ray and hadronic events; however, they have decreased sensitivity when distinguishing low-energy events from single local muons and electrons. Although the real background database already contains a large number of these type of events, it may be possible to boost the discriminating ability of the *Kernel* technique by injecting, into the background dataset, simulated muon and electron events.

The *Kernel* approach to gamma-ray selection may be particularly suitable for use with next-generation IACT arrays. The nature of the *Kernel*, that is its convolution of many parameters into a single score, makes it ideal for use with stereoscopic data, where a huge amount of information is available on each shower. By combining this information into a single set and comparing with a database of simulations and background, the complexities of stereoscopic analysis are accounted for in a relatively simple manner. In addition the convolution of several different parameters may allow the *Kernel* to identify more subtle features of gamma-ray showers that traditional linear analyses are not capable of detecting, thereby facilitating more efficient discrimination. It should be noted, however, that such an analysis would require a significantly larger set of simulations than currently necessary for analysing single-telescope data. This should not present a genuine problem

as, given the current rate of development of single computers and computational clusters, generation of the necessary simulations should be possible in a reasonable amount of time.

As part of the development of both *Minicuts* and *Kernel* selection it was shown that selection within a number of limited *size* bands is more efficient than a single selection over an unlimited range. This result is somewhat expected, considering the nature of the IACT. As the energy of the gamma-ray primaries increase, the shape and orientation of the resultant images change. In the case of a higher energy gamma-ray, one would expect a larger atmospheric cascade to yield more Cherenkov light, thus forming an image which is more intense, slightly longer and wider, and with its major axis better defined. Therefore by applying different (and optimised) selection strategies in several restricted *size* bands, more efficient selection may be achieved. This fact should be kept in mind when developing new selection methodologies for next-generation experiments.

7.2 Background Estimation

As part of this thesis an investigation of methods for background estimation was performed. The preferred approach of *ON/OFF* analysis, whereby the background level in the *ON* run is estimated based on a control set of observations, is not always suitable. This is particularly true when observing a rapidly variable source and accordingly an alternative method for estimating background is sought. Traditionally *TRACKING* analysis is used, whereby the background level is calculated from the *ON* data itself in conjunction with the *tracking ratio* (Section 4.3.4). This approach assumes the shape of the *alpha* distribution is consistent in the absence of a gamma-ray source, a measure of which is provided by the *tracking ratio*. Recently the assumption of a constant *tracking ratio* has been called into question and has direct implications for detection of weak gamma-ray sources. To determine the validity of this assumption, two tests were applied; (1) for constant *tracking ratio* over the course of a given observing season and (2) for constant *tracking ratio* over different dark-field regions. Based on these tests it was concluded that in most cases there is no reason to doubt the consistency of the *tracking ratio*. Although for some seasons the *tracking ratio* is unstable, the source of the instability may be attributed to changes in the instrument. Under such circumstances it was concluded that a single value *tracking ratio* should not be used. As an additional test of the *TRACKING* approach to background estimation it was determined how a small change ($\approx 5\,\%$) in *tracking ratio* could affect the observed gamma-ray excess. The results of this process

showed that, in the case of *Supercuts*, a small change is only important when the size of the dataset being analysed becomes quite large ($\approx$ 80 files, each of 28 minute duration). The results of this test when applying a selection in a lower energy range, such as that in which *Minicuts* operates, are more serious. A small change in *tracking ratio* becomes important for a much smaller dataset ($\approx$ 20 files, each of 28 minutes duration). Based on these results it was concluded that, while the *tracking ratio* is relatively stable, small differences between darkfield regions can have an adverse effect on signal estimation when dealing with a weak detection. Under such circumstances, application of *TRACKING* analysis is not advised.

A third method of background estimation, known as matched analysis, has been detailed in this work. As part of the matching process, a number of tests were applied to determine if this approach was unstable, that is if it is capable of introducing a false gamma-ray excess or deficit. Based on the results of these tests it was concluded that matching analysis provides an accurate method for estimating background when used in conjunction with box analyses. In contrast, utilisation of the *Kernel* selection method with matched data was shown to be capable of producing spurious results, and thus its application was deemed unsafe.

The matching process identifies the most suitable control dataset (i.e. an *OFF* run from another source) for a given *ON*-source observation, based on a number of parameters (Section 5.7). Although this process is designed so that the number of background counts in the *ON* and *OFF* datasets are similar, in most cases a difference is evident. To eliminate this disparity, a scaling factor is applied to the *OFF* dataset so that the number of background events in the *ON* and *OFF* are equal. In the case of box selection, the scaler is simply the ratio of events passing *shape* and *trigger* cuts with values of *alpha* between 20° and 60°. For the *Kernel*, the scaler is the ratio of the number of events that fail *Kernel* selection in the *ON* dataset to the number that fail in the *OFF*. The requirement of a scaling factor is indicative of the limitations of the matching algorithm. In an ideal situation, where the *ON* and *OFF* background levels are statistically equivalent, a scaling factor would not be required. A more accurate approach to choosing the most appropriate *OFF* data (at least in the case of box selection) may be as follows: the most suitable *OFF* run is one in which the number of events passing *shape* and *trigger* cuts and with *alpha* values outside a predefined gamma-ray domain, is equal to that in the *ON*. Thus it is possible to choose the best candidate *OFF* run by applying an *ON/OFF*-type analysis to a given *ON* run in conjunction with all *OFF* runs. Using a χ^2 test, the most suitable match would then be identified as that for which the *ON/OFF* distributions are most similar in the predefined *alpha* range. In terms of computation time,

this approach is extremely intensive, requiring a complete analysis of every possible *ON/OFF* combination. The overhead may be somewhat reduced by applying some preselection process which could, in some way, be based on the current matching algorithm, that is only those *ON/OFF* pairs with similar elevation, throughput, night-sky background etc. would be subjected to the more rigorous matching procedure. By doing so it may be possible to eliminate the need for a scaling factor, which would lend additional confidence to the matched approach for background estimation. A more successful matching algorithm may even allow for application of the *Kernel* method in conjunction with matched data.

7.3 A Search for New Sources of Very High Energy Gamma Rays

In the search for new sources of VHE gamma radiation the newly developed analysis methods were applied, in conjunction with *Supercuts*, to a sample of 16 BL-Lac objects. The BL Lacs were chosen as those most likely to emit gamma rays in the TeV energy band, using model predictions based on observations at longer wavelengths (Costamante and Ghisellini, 2002; Stecker et al., 1996; Fossati et al., 1998; Donato et al., 2001). A search was performed for steady gamma-ray emission and short-duration flaring, however no evidence was found for either. In one case, that of 1ES 0806+524, a $5\,\sigma$ excess was observed following application of the lowest-energy *Kernel* selection to data recorded during a single season. A more detailed investigation of the result revealed that the *ON*-source excess was not genuine, rather it was the result of a combination of instrumental and sky-brightness effects. The 1ES 0806+524 result provides a warning in relation to selection of events close to the hardware threshold of the telescope. This region is notorious for being susceptible to small differences between *ON* and *OFF* datasets, which are capable of introducing a false deficit or excess. Based on the results of 1ES 0806+524 it is concluded that when searching for gamma rays at this energy, additional tests should be applied for possible sources of bias.

Following the non-detection of any of the 16 BL-Lac objects, flux upper limits were imposed in an attempt to constrain the theoretical gamma-ray emission models presented by Costamante and Ghisellini (2002) and Stecker et al. (1996). In the case of the synchrotron self Compton (SSC) models of Costamante and Ghisellini (2002) and Stecker et al. (1996) the predicted spectral energy distributions (SEDs) are entirely consistent with observational results. However, for some objects, the upper limits obtained were in

contradiction to SEDs predicted using a modified version of the Fossati phenomenological parameterisation (Costamante and Ghisellini, 2002; Donato et al., 2001; Fossati et al., 1998). Based on these results it is concluded that, while the Fossati model may provide an accurate description of the SEDs of objects in a high state of flux, it overestimates the flux level of objects in their more quiescent state. Although the observations agree with the SSC predictions of Costamante and Ghisellini (2002) and Stecker et al. (1996), the amount of observing time allocated to these objects is not sufficient to genuinely test the models, and deeper exposures are required. Continued observations of these objects is advised, as although the time required for a $5\,\sigma$ detection is large there is always a possibility of observing the objects during a period of increased flux. Such an occurrence has already been seen in the case of the BL Lac 1ES 1959+650 which, although identified as one of the most promising candidates for TeV emission, was only detected by the Whipple telescope during a prolonged period of high flux (Holder et al., 2003). With this in mind it is recommended that observations of these objects continue, using a *target of opportunity* approach. Under such a scheme the objects are observed for a limited amount of time (≈ 10 minutes) at regular intervals, followed by more intensive follow-up observations if evidence for increased activity is seen.

Next-generation IACT arrays, with their greater flux sensitivity (Weekes, 2003a), should be capable of detecting these objects at a significant level in just a few hours observations. It should be noted, however, that most flux predictions reported here do not take into account possible effects of gamma-ray absorption by extragalactic background light and thus the actual time necessary for source detection could be much longer.

7.4 Summary

In conclusion, this thesis details the search for new sources of VHE gamma radiation, motivated by the expansion of the extragalactic TeV source catalogue. Although no new sources have been detected the work has introduced alternative selection techniques which have proved capable of identifying a low-energy gamma-ray excess. Additionally, an alternative method for estimating the background level in IACT data has been investigated. These methods should prove useful when designing new analyses for use with next-generation experiments such as VERITAS.

Appendix A

Datasets

A.1 Crab Nebula

ON ID	OFF ID	N2 ID	UT Date
gt015916	gt015915	gt015908	001005
gt015918	gt015917	gt015908	001005
gt016063	gt016064	gt016045	001101
gt016091	gt016092	gt016090	001105
gt016432	gt016433	gt016419	001130
gt016466	gt016467	gt016457	001204
gt016468	gt016469	gt016457	001204
gt016488	gt016489	gt016487	001206
gt016490	gt016491	gt016487	001206
gt016500	gt016501	gt016498	001207
gt016531	gt016530	gt016522	001217
gt016596	gt016597	gt016580	001222
gt016708	gt016709	gt016702	001227
gt016744	gt016745	gt016728	001228
gt016765	gt016766	gt016753	001229
gt016882	gt016883	gt016877	010119

2000/01 data used to measure performance of box and Kernel selections, and to estimate the energy threshold of the detector for different seasons.

ON ID	OFF ID	N2 ID	UT Date
gt018386	gt018387	gt018371	011018
gt018388	gt018389	gt018371	011018
gt018450	gt018451	gt018433	011021
gt018920	gt018921	gt018908	011218
gt018923	gt018924	gt018908	011218
gt018940	gt018941	gt018934	011219
gt018942	gt018943	gt018934	011219
gt018965	gt018966	gt018958	011220
gt018967	gt018968	gt018958	011220
gt018989	gt018990	gt018986	011222
gt019002	gt019003	gt019001	011223
gt019041	gt019042	gt019033	020107
gt019073	gt019074	gt019067	020109
gt019077	gt019078	gt019067	020109
gt019106	gt019107	gt019105	020112
gt019127	gt019128	gt019119	020113

2001/02 data used to measure performance of box and Kernel selections, and to estimate the energy threshold of the detector for different seasons.

ON ID	OFF ID	N2 ID	UT Date
gt022717	gt022718	gt022708	020915
gt022725	gt022726	gt022719	020916
gt022903	gt022904	gt022896	021104
gt022925	gt022926	gt022907	021105
gt022927	gt022928	gt022907	021105
gt022943	gt022944	gt022938	021106
gt022947	gt022948	gt022946	021106
gt022949	gt022950	gt022946	021106
gt022951	gt022952	gt022946	021106
gt022969	gt022970	gt022954	021107
gt023009	gt023010	gt022996	021109
gt023036	gt023037	gt023035	021111
gt023038	gt023039	gt023035	021111
gt023053	gt023054	gt023047	021112
gt023055	gt023056	gt023047	021112
gt023062	gt023063	gt023058	021113

2002/03 data used to measure performance of box and Kernel selections, and to estimate the energy threshold of the detector for different seasons.

ON ID	OFF ID	N2 ID	UT Date
gt025735	gt025734	gt025724	031120
gt025738	gt025739	gt025724	031120
gt025740	gt025741	gt025724	031120
gt025755	gt025756	gt025743	031121
gt025759	gt025760	gt025743	031121
gt025761	gt025762	gt025743	031121
gt025763	gt025764	gt025743	031121
gt025778	gt025779	gt025765	031122
gt025781	gt025782	gt025765	031122
gt025783	gt025784	gt025765	031122
gt025785	gt025786	gt025765	031122
gt025802	gt025803	gt025790	031123
gt025804	gt025805	gt025790	031123
gt025828	gt025829	gt025812	031124
gt025868	gt025869	gt025858	031127
gt025889	gt025890	gt025884	031129
gt026109	gt026110	gt026100	040113
gt026121	gt026122	gt026111	040116
gt026186	gt026187	gt026185	040127
gt026276	gt026277	gt026268	040213
gt026399	gt026400	gt026394	040219
gt026442	gt026443	gt026437	040222
gt026491	gt026492	gt026488	040311
gt026686	gt026687	gt026684	040323

Data used to optimise the Kernel selection.

ON ID	OFF ID	N2 ID	UT Date
gt025283	gt025284	gt025266	030926
gt025382	gt025383	gt025367	031001
gt025487	gt025488	gt025470	031021
gt025505	gt025506	gt025489	031022
gt025526	gt025527	gt025508	031023
gt025550	gt025551	gt025529	031024
gt025736	gt025737	gt025724	031120
gt025757	gt025758	gt025743	031121
gt025965	gt025967	gt025952	031217
gt026045	gt026046	gt026038	031225
gt026049	gt026050	gt026048	031225
gt026052	gt026053	gt026048	031225
gt026164	gt026165	gt026158	040119
gt026512	gt026513	gt026516	040315

2003/04 data used to measure performance of box and Kernel selections, and to estimate the energy threshold of the detector for different seasons.

A.2 1ES 0033+595

ON ID	OFF ID	N2 ID		UT Date	
		(on)	(off)	(on)	(off)
gt018320	gt018321	gt018313		011015	
gt018441	gt018442	gt018433		011021	
gt018661	gt018662	gt018651		011115	
gt018685	gt018686	gt018677		011116	
gt018850	gt018851	gt018845		011214	
gt018885	gt018886	gt018883		011217	
gt018887	gt018888	gt018883		011217	
gt019035	gt019036	gt019033		020107	
gt019069	gt019070	gt019067		020109	
gt022809	gt022810	gt022811		021012	
gt022914	gt022915	gt022907		021105	
gt023084	gt023085	gt023079		021125	
gt023548	gt023549	gt023546		030105	
gt025437	gt025438	gt025430		031018	
gt025445	gt025446	gt025441		031019	
gt025447	gt025448	gt025441		031019	
gt025464	gt025465	gt025455		031020	
gt025498	gt025499	gt025489		031022	
gt025517	gt025518	gt025508		031023	
gt025538	gt025539	gt025529		031024	
gt018382	gt018347	gt018371	gt018331	011018	011016
gt018319	gt018367	gt018313	gt018352	011015	011017
gt018400	gt018439	gt018393	gt018433	011019	011021
gt018401	gt018436	gt018393	gt018433	011019	011021
gt018381	gt018481	gt018371	gt018475	011018	011023
gt018341	gt018327	gt018331	gt018313	011016	011015
gt018359	gt018369	gt018352	gt018352	011017	011017
gt018340	gt018389	gt018331	gt018371	011016	011018
gt018360	gt018527	gt018352	gt018520	011017	011026
gt018272	gt018489	gt018263	gt018475	011012	011023
gt018660	gt018698	gt018651	gt018677	011115	011116
gt022881	gt022871	gt022879	gt022855	021103	021101
gt022808	gt022793	gt022811	gt022786	021012	021011
gt025366	gt025359	gt025357	gt025357	030930	030930
gt025346	gt025340	gt025337	gt025337	030929	030929
gt025439	gt025533	gt025430	gt025529	031018	031024
gt025462	gt025504	gt025455	gt025489	031020	031022
gt025300	gt025342	gt025286	gt025337	030927	030929
gt025607	gt025579	gt025600	gt025575	031028	031026

Data used in the analysis of *1ES 0033+595*. Note that elements without entries in the off columns correspond to pure *ON/OFF* data, while those with a full set of entries are *MATCHED* data.

A.3 1ES 0120+340

ON ID	OFF ID	N2 ID		UT Date	
		(on)	(off)	(on)	(off)
gt018322	gt018323	gt018313		011015	
gt018324	gt018325	gt018313		011015	
gt018493	gt018494	gt018491		011024	
gt018577	gt018578	gt018569		011111	
gt018595	gt018596	gt018587		011112	
gt018664	gt018665	gt018651		011115	
gt018711	gt018712	gt018699		011117	
gt022850	gt022851	gt022841		021031	
gt016427	gt016402	gt016419	gt016394	001130	001129
gt015865	gt015851	gt015858	gt015837	001002	001001
gt016255	gt016272	gt016245	gt016245	001125	001125
gt016426	gt016431	gt016419	gt016419	001130	001130
gt016873	gt016918	gt016877	gt016915	010119	010121
gt016033	gt016058	gt016023	gt016045	001030	001101
gt016446	gt016414	gt016440	gt016394	001201	001129
gt016538	gt016571	gt016534	gt016560	001218	001220
gt016872	gt016885	gt016877	gt016877	010119	010119
gt016369	gt016263	gt016364	gt016245	001128	001125
gt015843	gt015797	gt015837	gt015794	001001	000929
gt016069	gt016081	gt016065	gt016065	001102	001102
gt015751	gt015845	gt015748	gt015837	000927	001001
gt015986	gt015978	gt015970	gt015970	001025	001025
gt015735	gt015756	gt015734	gt015748	000926	000927
gt015902	gt015872	gt015899	gt015858	001004	001002
gt016644	gt016762	gt016640	gt016753	001225	001229
gt016703	gt016709	gt016702	gt016702	001227	001227
gt016733	gt016738	gt016728	gt016728	001228	001228
gt016316	gt016323	gt016309	gt016309	001127	001127
gt016225	gt016265	gt016215	gt016245	001124	001125
gt016755	gt016781	gt016753	gt016775	001229	001230
gt016123	gt016231	gt016113	gt016215	001118	001124
gt015765	gt015906	gt015759	gt015899	000928	001004
gt016622	gt016760	gt016619	gt016753	001224	001229
gt016400	gt016433	gt016394	gt016419	001129	001130
gt016155	gt016379	gt016147	gt016364	001120	001128
gt016565	gt016750	gt016560	gt016728	001220	001228
gt016050	gt016062	gt016045	gt016045	001101	001101
gt016519	gt016557	gt016515	gt016545	001216	001219
gt015707	gt015917	gt015704	gt015908	000925	001005
gt018421	gt018427	gt018411	gt018411	011020	011020
gt018457	gt018484	gt018452	gt018475	011022	011023
gt018633	gt018667	gt018630	gt018651	011114	011115
gt018285	gt018255	gt018281	gt018248	011013	011011
gt018776	gt018702	gt018772	gt018699	011120	011117
gt018740	gt018688	gt018733	gt018677	011118	011116
gt018283	gt018301	gt018281	gt018294	011013	011014
gt018799	gt018606	gt018796	gt018587	011121	011112
gt018546	gt018598	gt018540	gt018587	011108	011112
gt018276	gt018304	gt018263	gt018294	011012	011014
gt018764	gt018778	gt018760	gt018772	011119	011120
gt022977	gt022937	gt022973	gt022930	021108	021106
gt023423	gt023425	gt023415	gt023415	021231	021231
gt023473	gt023447	gt023469	gt023443	030102	030101

gt023505	gt023508	gt023500	gt023500	030103	030103
gt022916	gt022941	gt022907	gt022938	021105	021106
gt023445	gt023456	gt023443	gt023443	030101	030101
gt023402	gt023386	gt023398	gt023378	021229	021228
gt022882	gt022863	gt022879	gt022855	021103	021101
gt023264	gt023193	gt023261	gt023170	021209	021205
gt023562	gt023518	gt023558	gt023500	030106	030103
gt022866	gt022865	gt022855	gt022855	021101	021101
gt023670	gt023701	gt023667	gt023692	030123	030126
gt023246	gt023239	gt023241	gt023221	021208	021207
gt023204	gt023337	gt023170	gt023330	021206	021214
gt023223	gt023306	gt023221	gt023294	021207	021211
gt023662	gt023746	gt023660	gt023741	030122	030129
gt025303	gt025299	gt025286	gt025286	030927	030927
gt026008	gt026011	gt026005	gt026005	031220	031220
gt025944	gt026000	gt025941	gt025986	031214	031219
gt025991	gt025957	gt025986	gt025952	031219	031217
gt090001	gt025306	gt025367	gt025286	031001	030927
gt025650	gt025531	gt025648	gt025529	031030	031024
gt025651	gt025443	gt025648	gt025441	031030	031019
gt025583	gt025458	gt025575	gt025455	031026	031020
gt026104	gt026198	gt026100	gt026185	040113	040127
gt026114	gt026140	gt026111	gt026135	040116	040118
gt025992	gt025998	gt025986	gt025986	031219	031219
gt026032	gt026050	gt026027	gt026048	031223	031225
gt025281	gt025270	gt025266	gt025266	030926	030926
gt025989	gt025967	gt025986	gt025952	031219	031217
gt025632	gt025491	gt025625	gt025489	031029	031022
gt025974	gt026073	gt025969	gt026066	031218	031226
gt025711	gt025741	gt025704	gt025724	031119	031120
gt025347	gt025396	gt025337	gt025388	030929	031002
gt025451	gt025424	gt025441	gt025422	031019	031017
gt025861	gt025831	gt025858	gt025812	031127	031124
gt026041	gt026002	gt026038	gt025986	031225	031219
gt025973	gt026053	gt025969	gt026048	031218	031225
gt025684	gt025863	gt025682	gt025858	031117	031127
gt025839	gt025369	gt025836	gt025367	031125	031001

Data used in the analysis of *1ES 0120+340*. Note that elements without entries in the off columns correspond to pure *ON/OFF* data, while those with a full set of entries are *MATCHED* data.

A.4 RGB J0214+517

ON ID	OFF ID	N2 ID		UT Date	
		(on)	(off)	(on)	(off)
gt018326	gt018327	gt018313		011015	
gt018443	gt018444	gt018433		011021	
gt018480	gt018481	gt018475		011023	
gt018597	gt018598	gt018587		011112	
gt018741	gt018742	gt018733		011118	
gt018852	gt018853	gt018845		011214	
gt018889	gt018890	gt018883		011217	
gt018909	gt018910	gt018908		011218	
gt018935	gt018936	gt018934		011219	
gt019039	gt019040	gt019033		020107	
gt019145	gt019146	gt019143		020114	
gt019147	gt019148	gt019143		020114	
gt023744	gt023803	gt023741	gt023790	030129	030131
gt023795	gt023777	gt023790	gt023765	030131	030130
gt023794	gt023805	gt023790	gt023790	030131	030131
gt023725	gt023733	gt023722	gt023722	030128	030128
gt022918	gt022952	gt022907	gt022946	021105	021106
gt023506	gt023531	gt023500	gt023527	030103	030104
gt023770	gt023772	gt023765	gt023765	030130	030130
gt022885	gt022860	gt022879	gt022855	021103	021101
gt023724	gt023701	gt023722	gt023692	030128	030126
gt023745	gt023833	gt023741	gt023817	030129	030201
gt023769	gt023800	gt023765	gt023790	030130	030131
gt023880	gt023933	gt023877	gt023925	030203	030206
gt023879	gt023931	gt023877	gt023925	030203	030206
gt023853	gt023952	gt023849	gt023945	030202	030207
gt022867	gt022863	gt022855	gt022855	021101	021101
gt023824	gt023890	gt023817	gt023877	030201	030203
gt025330	gt025306	gt025324	gt025286	030928	030927
gt025390	gt025342	gt025388	gt025337	031002	030929
gt025282	gt025280	gt025266	gt025266	030926	030926
gt025452	gt025458	gt025441	gt025455	031019	031020
gt025302	gt025299	gt025286	gt025286	030927	030927
gt026042	gt026002	gt026038	gt025986	031225	031219
gt025391	gt025369	gt025388	gt025367	031002	031001
gt025990	gt026000	gt025986	gt025986	031219	031219
gt026113	gt026110	gt026111	gt026100	040116	040113
gt025945	gt025967	gt025941	gt025952	031214	031217
gt025331	gt025354	gt025324	gt025337	030928	030929
gt025689	gt025823	gt025682	gt025812	031117	031124
gt025946	gt026073	gt025941	gt026066	031214	031226
gt026037	gt026050	gt026027	gt026048	031223	031225
gt025686	gt025658	gt025682	gt025648	031117	031030
gt025840	gt025371	gt025836	gt025367	031125	031001

Data used in the analysis of *RGB J0214+517*. Note that elements without entries in the off columns correspond to pure *ON/OFF* data, while those with a full set of entries are *MATCHED* data.

A.5 1ES 0229+200

ON ID	OFF ID	N2 ID		UT Date	
		(on)	(off)	(on)	(off)
gt018291	gt018292	gt018281		011013	
gt018308	gt018309	gt018294		011014	
gt018426	gt018427	gt018411		011020	
gt018446	gt018447	gt018433		011021	
gt018497	gt018498	gt018491		011024	
gt018579	gt018580	gt018569		011111	
gt018666	gt018667	gt018651		011115	
gt018687	gt018688	gt018677		011116	
gt018854	gt018855	gt018845		011214	
gt018892	gt018893	gt018883		011217	
gt018912	gt018913	gt018908		011218	
gt018937	gt018938	gt018934		011219	
gt018959	gt018960	gt018958		011220	
gt019037	gt019038	gt019033		020107	
gt019071	gt019072	gt019067		020109	
gt019121	gt019122	gt019119		020113	
gt019123	gt019124	gt019119		020113	
gt019169	gt019170	gt019167		020115	
gt023370	gt023371	gt023362		021227	
gt016054	gt016058	gt016045	gt016045	001101	001101
gt015849	gt015851	gt015837	gt015837	001001	001001
gt016257	gt016263	gt016245	gt016245	001125	001125
gt016896	gt016894	gt016897	gt016897	010120	010120
gt016372	gt016323	gt016364	gt016309	001128	001127
gt016075	gt016081	gt016065	gt016065	001102	001102
gt015867	gt015845	gt015858	gt015837	001002	001001
gt016624	gt016738	gt016619	gt016728	001224	001228
gt016139	gt016272	gt016128	gt016245	001119	001125
gt016036	gt016025	gt016023	gt016023	001030	001030
gt016521	gt016571	gt016515	gt016560	001216	001220
gt016125	gt016265	gt016113	gt016245	001118	001125
gt015989	gt015980	gt015970	gt015970	001025	001025
gt016157	gt016379	gt016147	gt016364	001120	001128
gt015913	gt015917	gt015908	gt015908	001005	001005
gt016006	gt016062	gt015994	gt016045	001026	001101
gt018482	gt018449	gt018475	gt018433	011023	011021
gt018891	gt018890	gt018883	gt018883	011217	011217
gt018278	gt018255	gt018263	gt018248	011012	011011
gt018511	gt018484	gt018506	gt018475	011025	011023
gt018461	gt018469	gt018452	gt018452	011022	011022
gt018560	gt018606	gt018552	gt018587	011109	011112
gt018550	gt018598	gt018540	gt018587	011108	011112
gt018669	gt018662	gt018651	gt018651	011115	011115
gt018802	gt018694	gt018796	gt018677	011121	011116
gt018361	gt018444	gt018352	gt018433	011017	011021
gt018293	gt018301	gt018281	gt018294	011013	011014
gt018829	gt018904	gt018826	gt018883	011207	011217
gt018261	gt018439	gt018248	gt018433	011011	011021
gt018342	gt018323	gt018331	gt018313	011016	011015
gt018549	gt018594	gt018540	gt018587	011108	011112
gt018343	gt018311	gt018331	gt018294	011016	011014

gt018425	gt018325	gt018411	gt018313	011020	011015
gt018424	gt018494	gt018411	gt018491	011020	011024
gt018405	gt018527	gt018393	gt018520	011019	011026
gt018402	gt018321	gt018393	gt018313	011019	011015
gt018362	gt018369	gt018352	gt018352	011017	011017
gt018768	gt018778	gt018760	gt018772	011119	011120
gt022886	gt022860	gt022879	gt022855	021103	021101
gt022888	gt022863	gt022879	gt022855	021103	021101
gt022919	gt023014	gt022907	gt022996	021105	021109
gt022790	gt022775	gt022786	gt022761	021011	021010
gt022868	gt022871	gt022855	gt022855	021101	021101
gt025978	gt025957	gt025969	gt025952	031218	031217
gt026009	gt026011	gt026005	gt026005	031220	031220
gt025670	gt025491	gt025667	gt025489	031101	031022
gt025721	gt025706	gt025704	gt025704	031119	031119
gt025948	gt025967	gt025941	gt025952	031214	031217
gt025483	gt025465	gt025470	gt025455	031021	031020
gt026033	gt026000	gt026027	gt025986	031223	031219
gt026010	gt026002	gt026005	gt025986	031220	031219
gt026044	gt025998	gt026038	gt025986	031225	031219
gt025409	gt025396	gt025401	gt025388	031003	031002
gt025654	gt025531	gt025648	gt025529	031030	031024
gt026070	gt026046	gt026066	gt026038	031226	031225

Data used in the analysis of *1ES 0229+200*. Note that elements without entries in the off columns correspond to pure *ON/OFF* data, while those with a full set of entries are *MATCHED* data.

A.6 1ES 0323+022

ON ID	OFF ID	N2 ID		UT Date	
		(on)	(off)	(on)	(off)
gt018714	gt018662	gt018699	gt018651	011117	011115
gt018466	gt018439	gt018452	gt018433	011022	011021
gt018600	gt018598	gt018587	gt018587	011112	011112
gt018582	gt018704	gt018569	gt018699	011111	011117
gt018639	gt018594	gt018630	gt018587	011114	011112
gt018512	gt018481	gt018506	gt018475	011025	011023
gt018804	gt018742	gt018796	gt018733	011121	011118
gt018640	gt018694	gt018630	gt018677	011114	011116
gt018290	gt018321	gt018281	gt018313	011013	011015
gt018770	gt018778	gt018760	gt018772	011119	011120
gt018404	gt018442	gt018393	gt018433	011019	011021
gt018289	gt018304	gt018281	gt018294	011013	011014
gt018617	gt018698	gt018609	gt018677	011113	011116
gt023475	gt023497	gt023469	gt023469	030102	030102
gt023509	gt023525	gt023500	gt023500	030103	030103
gt023767	gt023810	gt023765	gt023790	030130	030131
gt023743	gt023682	gt023741	gt023678	030129	030125
gt023477	gt023438	gt023469	gt023415	030102	021231
gt023448	gt023461	gt023443	gt023443	030101	030101
gt023534	gt023533	gt023527	gt023527	030104	030104
gt023792	gt023800	gt023790	gt023790	030131	030131
gt023387	gt023384	gt023378	gt023378	021228	021228
gt023564	gt023518	gt023558	gt023500	030106	030103
gt023664	gt023699	gt023660	gt023692	030122	030126
gt023820	gt023890	gt023817	gt023877	030201	030203
gt023408	gt023612	gt023398	gt023606	021229	030110
gt023851	gt023701	gt023849	gt023692	030202	030126
gt023552	gt023511	gt023546	gt023500	030105	030103
gt023585	gt023554	gt023581	gt023546	030107	030105
gt025723	gt025702	gt025704	gt025692	031119	031118
gt025355	gt025352	gt025337	gt025337	030929	030929
gt025846	gt025813	gt025836	gt025812	031125	031124
gt025979	gt026011	gt025969	gt026005	031218	031220
gt025950	gt026002	gt025941	gt025986	031214	031219

Data used in the analysis of *1ES 0323+022*. Note that all data here is *MATCHED*.

A.7 1ES 0806+524

ON ID	OFF ID	N2 ID		UT Date	
		(on)	(off)	(on)	(off)
gt018862	gt018863	gt018845		011214	
gt018864	gt018865	gt018845		011214	
gt018901	gt018902	gt018883		011217	
gt018926	gt018927	gt018908		011218	
gt018945	gt018946	gt018934		011219	
gt018947	gt018948	gt018934		011219	
gt018970	gt018971	gt018958		011220	
gt018993	gt018994	gt018986		011222	
gt018995	gt018996	gt018986		011222	
gt019043	gt019044	gt019033		020107	
gt019062	gt019063	gt019049		020108	
gt019079	gt019080	gt019067		020109	
gt019108	gt019109	gt019105		020112	
gt019132	gt019133	gt019119		020113	
gt019155	gt019156	gt019143		020114	
gt019193	gt019194	gt019191		020119	
gt019207	gt019208	gt019206		020120	
gt019225	gt019226	gt019218		020121	
gt019408	gt019409	gt019384		020212	
gt019428	gt019429	gt019448		020213	
gt019476	gt019477	gt019474		020215	
gt019478	gt019479	gt019474		020215	
gt019480	gt019481	gt019474		020215	
gt019482	gt019483	gt019474		020215	
gt019499	gt019500	gt019496		020216	
gt019501	gt019502	gt019496		020216	
gt019526	gt019527	gt019524		020219	
gt019597	gt019598	gt019591		020306	
gt019611	gt019612	gt019605		020309	
gt019652	gt019653	gt019644		020311	
gt019673	gt019674	gt019667		020312	
gt019694	gt019695	gt019688		020313	
gt019716	gt019717	gt019712		020314	
gt019742	gt019743	gt019730		020315	
gt023959	gt023960	gt023957		030210	
gt024128	gt024129	gt024124		030324	
gt024231	gt024232	gt024229		030331	
gt024234	gt024235	gt024229		030331	
gt024255	gt024256	gt024253		030401	
gt024287	gt024288	gt024285		030403	
gt024414	gt024415	gt024416		030420	
gt024422	gt024423	gt024424		030421	
gt018944	gt018938	gt018934	gt018934	011219	011219
gt018900	gt018913	gt018883	gt018908	011217	011218
gt018809	gt018686	gt018796	gt018677	011121	011116
gt018676	gt018598	gt018651	gt018587	011115	011112
gt018821	gt018758	gt018814	gt018733	011122	011118
gt019868	gt021146	gt019866	gt021139	020402	020420
gt023569	gt023533	gt023558	gt023527	030106	030104
gt023588	gt023504	gt023581	gt023500	030107	030103
gt025574	gt025533	gt025552	gt025529	031025	031024

gt026191	gt026187	gt026185	gt026185	040127	040127
gt026124	gt026150	gt026111	gt026135	040116	040118
gt025932	gt025930	gt025926	gt025926	031202	031202
gt026357	gt026465	gt026341	gt026456	040217	040226
gt026173	gt026110	gt026158	gt026100	040119	040113
gt025834	gt025792	gt025812	gt025790	031124	031123
gt025924	gt025919	gt025914	gt025914	031201	031201
gt025810	gt025739	gt025790	gt025724	031123	031120
gt025925	gt025920	gt025914	gt025914	031201	031201
gt026003	gt026002	gt025986	gt025986	031219	031219
gt025898	gt025865	gt025884	gt025858	031129	031127
gt025852	gt025867	gt025836	gt025858	031125	031127
gt026086	gt026053	gt026084	gt026048	031231	031225
gt026054	gt026011	gt026038	gt026005	031225	031220

Data used in the analysis of *1ES 0806+524*. Note that elements without entries in the off columns correspond to pure *ON/OFF* data, while those with a full set of entries are *MATCHED* data.

A.8 1ES 1011+496

ON ID	OFF ID	N2 ID		UT Date	
		(on)	(off)	(on)	(off)
gt026356	gt026334	gt026341	gt026320	040217	040216
gt026691	gt026662	gt026684	gt026646	040323	040321
gt026216	gt026198	gt026213	gt026185	040129	040127
gt026154	gt026150	gt026135	gt026135	040118	040118
gt026332	gt026387	gt026320	gt026368	040216	040218
gt026192	gt026209	gt026185	gt026200	040127	040128
gt026762	gt026717	gt026760	gt026707	040409	040326
gt026204	gt026194	gt026200	gt026185	040128	040127
gt026153	gt026221	gt026135	gt026213	040118	040129
gt026059	gt026011	gt026038	gt026005	031225	031220
gt026060	gt025957	gt026038	gt025952	031225	031217

Data used in the analysis of *1ES 1011+496*. Note that all data here is *MATCHED*.

A.9 1ES 1136+673

ON ID	OFF ID	N2 ID		UT Date	
		(on)	(off)	(on)	(off)
gt019507	gt019505	gt019496	gt019496	020216	020216
gt023843	gt023808	gt023817	gt023790	030201	030131
gt024051	gt024072	gt024047	gt024063	030309	030310
gt024022	gt024018	gt024015	gt024015	030307	030307
gt024473	gt024454	gt024469	gt024455	030425	030424
gt023844	gt023782	gt023817	gt023765	030201	030130
gt024159	gt024157	gt024154	gt024154	030326	030326
gt023493	gt023518	gt023469	gt023500	030102	030103
gt024437	gt024419	gt024432	gt024416	030422	030420
gt024262	gt024210	gt024253	gt024207	030401	030330
gt024297	gt024312	gt024285	gt024308	030403	030404
gt024217	gt024224	gt024207	gt024207	030330	030330
gt024147	gt024127	gt024138	gt024124	030325	030324
gt023719	gt023735	gt023704	gt023722	030127	030128
gt023895	gt023890	gt023877	gt023877	030203	030203
gt023919	gt023952	gt023903	gt023945	030204	030207
gt023577	gt023627	gt023558	gt023621	030106	030111
gt024176	gt024117	gt024171	gt024114	030327	030323
gt024338	gt024362	gt024330	gt024348	030405	030406
gt024447	gt024618	gt024444	gt024607	030423	030503
gt023464	gt023450	gt023443	gt023443	030101	030101
gt023764	gt023680	gt023741	gt023678	030129	030125
gt023785	gt023810	gt023765	gt023790	030130	030131
gt024199	gt024327	gt024194	gt024308	030328	030404
gt024372	gt024333	gt024367	gt024330	030407	030405
gt024421	gt024595	gt024416	gt024587	030420	030502
gt024317	gt024394	gt024308	gt024381	030404	030408
gt024141	gt024034	gt024138	gt024031	030325	030308
gt024384	gt024443	gt024381	gt024432	030408	030422
gt026206	gt026161	gt026200	gt026158	040128	040119
gt026692	gt026599	gt026684	gt026611	040323	040319
gt026809	gt026580	gt026799	gt026583	040414	040318

Data used in the analysis of *1ES 1136+673*. Note that all data here is *MATCHED*.

A.10 1ES 1553+113

ON ID	OFF ID	N2 ID		UT Date	
		(on)	(off)	(on)	(off)
gt019977	gt019978	gt019964		020409	
gt017777	gt017771	gt017760	gt017760	010421	010421
gt017867	gt017862	gt017858	gt017858	010517	010517
gt017744	gt017705	gt017728	gt017699	010417	010415
gt017798	gt017793	gt017781	gt017781	010423	010423
gt022036	gt022034	gt022023	gt022023	020505	020505
gt021052	gt021019	gt021035	gt021016	020413	020412
gt019960	gt019950	gt019947	gt019947	020408	020408
gt019930	gt019943	gt019916	gt019931	020406	020407
gt022021	gt022045	gt022012	gt022042	020504	020506
gt019519	gt019468	gt019496	gt019449	020216	020214
gt022171	gt022261	gt022155	gt022260	020513	020520
gt022190	gt022142	gt022181	gt022139	020514	020512
gt021073	gt021137	gt021057	gt021130	020414	020419
gt022064	gt022070	gt022055	gt022068	020507	020508
gt024074	gt024069	gt024063	gt024063	030310	030310
gt024358	gt024362	gt024348	gt024348	030406	030406
gt024616	gt024614	gt024607	gt024607	030503	030503
gt024225	gt024220	gt024207	gt024207	030330	030330
gt024389	gt024374	gt024381	gt024367	030408	030407
gt024467	gt024484	gt024455	gt024469	030424	030425
gt024532	gt024525	gt024519	gt024519	030428	030428
gt024322	gt024327	gt024308	gt024308	030404	030404
gt024717	gt024702	gt024712	gt024699	030523	030522
gt024246	gt024264	gt024229	gt024253	030331	030401
gt024046	gt024040	gt024031	gt024031	030308	030308
gt024755	gt024751	gt024748	gt024748	030526	030526
gt024798	gt024826	gt024794	gt024824	030531	030602
gt024401	gt024342	gt024395	gt024330	030409	030405
gt024087	gt024055	gt024080	gt024047	030311	030309
gt024630	gt024578	gt024624	gt024570	030504	030501
gt024302	gt024290	gt024285	gt024285	030403	030403
gt024739	gt024817	gt024734	gt024809	030525	030601
gt024186	gt024162	gt024171	gt024154	030327	030326
gt024706	gt024766	gt024699	gt024763	030522	030527
gt024008	gt024020	gt023999	gt024015	030303	030307
gt024409	gt024394	gt024405	gt024381	030410	030408

Data used in the analysis of *1ES 1553+113*. Note that elements without entries in the off columns correspond to pure *ON/OFF* data, while those with a full set of entries are *MATCHED* data.

A.11 1ES 1727+502

ON ID	OFF ID	N2 ID		UT Date	
		(on)	(off)	(on)	(off)
gt024344	gt024345	gt024330		030405	
gt024361	gt024362	gt024348		030406	
gt024377	gt024378	gt024367		030407	
gt017797	gt017793	gt017781	gt017781	010423	010423
gt017745	gt017785	gt017728	gt017781	010417	010423
gt019961	gt019950	gt019947	gt019947	020408	020408
gt021053	gt021019	gt021035	gt021016	020413	020412
gt022218	gt022204	gt022210	gt022196	020516	020515
gt022172	gt022141	gt022155	gt022139	020513	020512
gt024328	gt024324	gt024308	gt024308	030404	030404
gt024347	gt024374	gt024330	gt024367	030405	030407
gt024249	gt024274	gt024229	gt024253	030331	030401
gt024062	gt024069	gt024047	gt024063	030309	030310
gt024228	gt024220	gt024207	gt024207	030330	030330
gt024189	gt024162	gt024171	gt024154	030327	030326
gt024275	gt024264	gt024253	gt024253	030401	030401
gt024391	gt024394	gt024381	gt024381	030408	030408
gt024329	gt024281	gt024308	gt024279	030404	030402
gt024306	gt024290	gt024285	gt024285	030403	030403
gt024088	gt024055	gt024080	gt024047	030311	030309
gt024412	gt024327	gt024405	gt024308	030410	030404
gt026831	gt026601	gt026818	gt026611	040415	040319
gt026994	gt026771	gt026992	gt026766	040428	040412
gt026777	gt026664	gt026766	gt026646	040412	040321
gt026811	gt026504	gt026799	gt026501	040414	040314

Data used in the analysis of *1ES 1727+502*. Note that elements without entries in the off columns correspond to pure *ON/OFF* data, while those with a full set of entries are *MATCHED* data.

A.12 1ES 1741+196

ON ID	OFF ID	N2 ID		UT Date	
		(on)	(off)	(on)	(off)
gt022219	gt022213	gt022210	gt022210	020516	020516
gt022053	gt022070	gt022042	gt022068	020506	020508
gt021054	gt021019	gt021035	gt021016	020413	020412
gt022137	gt022071	gt022124	gt022068	020511	020508
gt022208	gt022204	gt022196	gt022196	020515	020515
gt022173	gt022142	gt022155	gt022139	020513	020512
gt024365	gt024374	gt024348	gt024367	030406	030407
gt024251	gt024220	gt024229	gt024207	030331	030330
gt024732	gt024702	gt024722	gt024699	030524	030522
gt024364	gt024342	gt024348	gt024330	030406	030405
gt024747	gt024744	gt024734	gt024734	030525	030525
gt024392	gt024324	gt024381	gt024308	030408	030404
gt024307	gt024294	gt024285	gt024285	030403	030403
gt024379	gt024335	gt024367	gt024330	030407	030405
gt024346	gt024345	gt024330	gt024330	030405	030405
gt024276	gt024264	gt024253	gt024253	030401	030401
gt025015	gt024973	gt025007	gt024968	030629	030626
gt026865	gt026771	gt026856	gt026766	040418	040412
gt026814	gt026717	gt026799	gt026707	040414	040326
gt026886	gt026580	gt026872	gt026583	040419	040318

Data used in the analysis of *1ES 1741+196*. Note that all data here is *MATCHED*.

A.13 1ES 0145+138

ON ID	OFF ID	N2 ID		UT Date	
		(on)	(off)	(on)	(off)
gt015866	gt015851	gt015858	gt015837	001002	001001
gt016037	gt016072	gt016023	gt016065	001030	001102
gt016074	gt016081	gt016065	gt016065	001102	001102
gt016256	gt016272	gt016245	gt016245	001125	001125
gt015929	gt015915	gt015921	gt015908	001006	001005
gt015928	gt015862	gt015921	gt015858	001006	001002
gt016053	gt016058	gt016045	gt016045	001101	001101
gt016647	gt016738	gt016640	gt016728	001225	001228
gt015912	gt015917	gt015908	gt015908	001005	001005
gt016370	gt016406	gt016364	gt016394	001128	001129
gt015987	gt015982	gt015970	gt015970	001025	001025
gt016623	gt016571	gt016619	gt016560	001224	001220
gt016611	gt016557	gt016605	gt016545	001223	001219
gt016512	gt016462	gt016507	gt016457	001215	001204
gt015903	gt015845	gt015899	gt015837	001004	001001
gt016645	gt016762	gt016640	gt016753	001225	001229
gt016004	gt015980	gt015994	gt015970	001026	001025
gt016140	gt016323	gt016128	gt016309	001119	001127
gt016520	gt016750	gt016515	gt016728	001216	001228
gt018459	gt018469	gt018452	gt018452	011022	011022
gt018713	gt018704	gt018699	gt018699	011117	011117
gt018496	gt018498	gt018491	gt018491	011024	011024
gt018547	gt018594	gt018540	gt018587	011108	011112
gt018286	gt018255	gt018281	gt018248	011013	011011
gt018800	gt018694	gt018796	gt018677	011121	011116
gt018422	gt018427	gt018411	gt018411	011020	011020
gt018611	gt018742	gt018609	gt018733	011113	011118
gt018767	gt018778	gt018760	gt018772	011119	011120
gt022963	gt022960	gt022954	gt022954	021107	021107
gt022978	gt022838	gt022973	gt022830	021108	021030

Data used in the analysis of *1ES 0145+138*. Note that all data here is *MATCHED*.

A.14 1ES 1118+424

ON ID	OFF ID	N2 ID		UT Date	
		(on)	(off)	(on)	(off)
gt016751	gt016750	gt016728	gt016728	001228	001228
gt016717	gt016738	gt016702	gt016728	001227	001228
gt016886	gt016921	gt016877	gt016915	010119	010121
gt016417	gt016272	gt016394	gt016245	001129	001125
gt016339	gt016406	gt016309	gt016394	001127	001129
gt016603	gt016571	gt016580	gt016560	001222	001220
gt016599	gt016584	gt016580	gt016580	001222	001222
gt016483	gt016476	gt016472	gt016472	001205	001205
gt016661	gt016762	gt016640	gt016753	001225	001229
gt016602	gt016557	gt016580	gt016545	001222	001219
gt016503	gt016465	gt016498	gt016457	001207	001204
gt016493	gt016462	gt016487	gt016457	001206	001204
gt016689	gt016931	gt016671	gt016915	001226	010121
gt016846	gt016732	gt016844	gt016728	010104	001228
gt019437	gt019419	gt019448	gt019384	020213	020212
gt019461	gt019472	gt019449	gt019449	020214	020214
gt019100	gt019112	gt019088	gt019105	020111	020112
gt019331	gt019409	gt019320	gt019384	020209	020212
gt019506	gt019505	gt019496	gt019496	020216	020216
gt018983	gt018994	gt018976	gt018986	011221	011222
gt019048	gt019044	gt019033	gt019033	020107	020107

Data used in the analysis of *1ES 1118+424*. Note that all data here is *MATCHED*.

A.15 1ES 2321+419

ON ID	OFF ID	N2 ID		UT Date	
		(on)	(off)	(on)	(off)
gt025298	gt025299	gt025286		030927	
gt015864	gt015872	gt015858	gt015858	001002	001002
gt015900	gt015904	gt015899	gt015899	001004	001004
gt015764	gt015845	gt015759	gt015837	000928	001001
gt015750	gt015756	gt015748	gt015748	000927	000927
gt015733	gt015738	gt015729	gt015734	000926	000926
gt015703	gt015906	gt015704	gt015899	000925	001004
gt015682	gt015917	gt015678	gt015908	000924	001005
gt018657	gt018667	gt018651	gt018651	011115	011115
gt018774	gt018795	gt018772	gt018772	011120	011120
gt018337	gt018311	gt018331	gt018294	011016	011014
gt018632	gt018696	gt018630	gt018677	011114	011116
gt018477	gt018481	gt018475	gt018475	011023	011023
gt018708	gt018598	gt018699	gt018587	011117	011112
gt018846	gt018897	gt018845	gt018883	011214	011217
gt018739	gt018737	gt018733	gt018733	011118	011118
gt018418	gt018444	gt018411	gt018433	011020	011021
gt018545	gt018594	gt018540	gt018587	011108	011112
gt018840	gt018851	gt018835	gt018845	011210	011214
gt018842	gt018888	gt018835	gt018883	011210	011217
gt018839	gt018886	gt018835	gt018883	011210	011217
gt018454	gt018489	gt018452	gt018475	011022	011023
gt018841	gt018834	gt018835	gt018826	011210	011207
gt025326	gt025306	gt025324	gt025286	030928	030927
gt025295	gt025270	gt025286	gt025266	030927	030926
gt025296	gt025280	gt025286	gt025266	030927	030926
gt025325	gt025383	gt025324	gt025367	030928	031001

Data used in the analysis of *1ES 2321+419*. Note that elements without entries in the off columns correspond to pure *ON/OFF* data, while those with a full set of entries are *MATCHED* data.

A.16 3C 66A

ON ID	OFF ID	N2 ID		UT Date	
		(on)	(off)	(on)	(off)
gt015850	gt015851	gt015837		001001	
gt025305	gt025306	gt025286		030927	
gt025395	gt025396	gt025388		031002	
gt025956	gt025957	gt025952		031217	
gt026012	gt026011	gt026005		031220	
gt016258	gt016263	gt016245	gt016245	001125	001125
gt016038	gt016056	gt016023	gt016045	001030	001101
gt016073	gt016058	gt016065	gt016045	001102	001101
gt015988	gt016081	gt015970	gt016065	001025	001102
gt015846	gt015845	gt015837	gt015837	001001	001001
gt016371	gt016323	gt016364	gt016309	001128	001127
gt016035	gt016025	gt016023	gt016023	001030	001030
gt016895	gt016894	gt016897	gt016897	010120	010120
gt016138	gt016284	gt016128	gt016280	001119	001126
gt015768	gt015872	gt015759	gt015858	000928	001002
gt016124	gt016379	gt016113	gt016364	001118	001128
gt016052	gt016062	gt016045	gt016045	001101	001101
gt015848	gt015917	gt015837	gt015908	001001	001005
gt016005	gt015980	gt015994	gt015970	001026	001025
gt018710	gt018667	gt018699	gt018651	011117	011115
gt018423	gt018427	gt018411	gt018411	011020	011020
gt018445	gt018447	gt018433	gt018433	011021	011021
gt018495	gt018498	gt018491	gt018491	011024	011024
gt018743	gt018704	gt018733	gt018699	011118	011117
gt018460	gt018489	gt018452	gt018475	011022	011023
gt018599	gt018580	gt018587	gt018569	011112	011111
gt018485	gt018442	gt018475	gt018433	011023	011021
gt018581	gt018598	gt018569	gt018587	011111	011112
gt018636	gt018688	gt018630	gt018677	011114	011116
gt018801	gt018694	gt018796	gt018677	011121	011116
gt018779	gt018778	gt018772	gt018772	011120	011120
gt018383	gt018309	gt018371	gt018294	011018	011014
gt018288	gt018255	gt018281	gt018248	011013	011011
gt018548	gt018594	gt018540	gt018587	011108	011112
gt018287	gt018311	gt018281	gt018294	011013	011014
gt018765	gt018742	gt018760	gt018733	011119	011118
gt022769	gt022797	gt022761	gt022786	021010	021011
gt025520	gt025491	gt025508	gt025489	031023	031022
gt025962	gt025967	gt025952	gt025952	031217	031217
gt025394	gt025338	gt025388	gt025337	031002	030929
gt025961	gt026000	gt025952	gt025986	031217	031219
gt025963	gt026002	gt025952	gt025986	031217	031219
gt025328	gt025299	gt025324	gt025286	030928	030927
gt025888	gt025930	gt025884	gt025926	031129	031202
gt025453	gt025458	gt025441	gt025455	031019	031020
gt025397	gt025354	gt025388	gt025337	031002	030929
gt025842	gt025831	gt025836	gt025812	031125	031124
gt025669	gt025443	gt025667	gt025441	031101	031019
gt025960	gt025998	gt025952	gt025986	031217	031219
gt026043	gt026073	gt026038	gt026066	031225	031226
gt025348	gt025270	gt025337	gt025266	030929	030926

gt025611	gt025432	gt025600	gt025430	031028	031018
gt025636	gt025531	gt025625	gt025529	031029	031024
gt025947	gt025920	gt025941	gt025914	031214	031201
gt026102	gt026194	gt026100	gt026185	040113	040127
gt025540	gt025424	gt025529	gt025422	031024	031017
gt026030	gt026046	gt026027	gt026038	031223	031225
gt026034	gt026050	gt026027	gt026048	031223	031225
gt025610	gt025549	gt025600	gt025529	031028	031024
gt025633	gt025527	gt025625	gt025508	031029	031023
gt026036	gt026053	gt026027	gt026048	031223	031225
gt025878	gt025919	gt025876	gt025914	031128	031201
gt026029	gt026110	gt026027	gt026100	031223	040113
gt026018	gt025994	gt026005	gt025986	031220	031219
gt026016	gt025917	gt026005	gt025914	031220	031201

Data used in the analysis of *3C 66A*. Note that elements without entries in the off columns correspond to pure *ON/OFF* data, while those with a full set of entries are *MATCHED* data.

A.17 BL Lac

ON ID	OFF ID	N2 ID		UT Date	
		(on)	(off)	(on)	(off)
gt015749	gt015747	gt015748	gt015748	000927	000927
gt015863	gt015870	gt015858	gt015858	001002	001002
gt015696	gt015738	gt015704	gt015734	000925	000926
gt018735	gt018742	gt018733	gt018733	011118	011118
gt018437	gt018442	gt018433	gt018433	011021	011021
gt018299	gt018449	gt018294	gt018433	011014	011021
gt018413	gt018489	gt018411	gt018475	011020	011023
gt018395	gt018436	gt018393	gt018433	011019	011021
gt025077	gt025075	gt025068	gt025068	030702	030702
gt025118	gt025167	gt025106	gt025161	030705	030707
gt023001	gt022860	gt022996	gt022855	021109	021101
gt025364	gt025354	gt025357	gt025337	030930	030929
gt025421	gt025432	gt025418	gt025430	031016	031018
gt025463	gt025465	gt025455	gt025455	031020	031020
gt025261	gt025233	gt025251	gt025220	030922	030920
gt025450	gt025424	gt025441	gt025422	031019	031017

Data used in the analysis of *BL Lac*. Note that all data here is *MATCHED*.

Appendix B

Hillas Parameters

Suppose the i^{th} PMT is given coordinates x_i, y_i (in degrees) and registers a signal s_i. The origin of the coordinate system is in the centre of the array of PMTs. An ellipse is fitted to the image and the Hillas parameters are calculated relative to the centre. For a graphical description of the parameters see Figure 4.12.

The fitting of the ellipse employs the following simple moments:

$$
\begin{aligned}
\langle x \rangle &= \frac{\Sigma s_i x_i}{\Sigma s_i}, \\
\langle y \rangle &= \frac{\Sigma s_i y_i}{\Sigma s_i}, \\
\langle x^2 \rangle &= \frac{\Sigma s_i {x_i}^2}{\Sigma s_i}, \\
\langle y^2 \rangle &= \frac{\Sigma s_i {y_i}^2}{\Sigma s_i}, \\
\langle xy \rangle &= \frac{\Sigma s_i x_i y_i}{\Sigma s_i}, \\
\langle x^3 \rangle &= \frac{\Sigma s_i {x_i}^3}{\Sigma s_i}, \\
\langle y^3 \rangle &= \frac{\Sigma s_i {y_i}^3}{\Sigma s_i}, \\
\langle x^2 y \rangle &= \frac{\Sigma s_i {x_i}^2 y_i}{\Sigma s_i}, \\
\langle x y^2 \rangle &= \frac{\Sigma s_i x_i {y_i}^2}{\Sigma s_i},
\end{aligned}
$$

and

$$\begin{aligned}
\sigma_{x^2} &= \langle x^2 \rangle - \langle x \rangle^2, \\
\sigma_{y^2} &= \langle y^2 \rangle - \langle y \rangle^2, \\
\sigma_{xy} &= \langle xy \rangle - \langle x \rangle \langle y \rangle, \\
\sigma_{x^3} &= \langle x^3 \rangle - 3\langle x \rangle \langle x^2 \rangle + 2\langle x \rangle^3, \\
\sigma_{y^3} &= \langle y^3 \rangle - 3\langle y \rangle^2 \langle y \rangle + 2\langle y \rangle^3, \\
\sigma_{x^2y} &= \langle x^2 y \rangle - 2\langle xy \rangle \langle x \rangle + 2\langle x \rangle^2 \langle y \rangle - \langle x^2 \rangle \langle y \rangle, \\
\sigma_{xy^2} &= \langle xy^2 \rangle - 2\langle xy \rangle \langle y \rangle + 2\langle x \rangle \langle y \rangle^2 - \langle x \rangle \langle y^2 \rangle.
\end{aligned}$$

Given the following definitions:

$$\begin{aligned}
k &= \sigma_{y^2} - \sigma_{x^2}, \\
l &= \sqrt{k^2 + 4\sigma_{xy}^2}, \\
m &= \langle y^2 \rangle - \langle x^2 \rangle, \\
n &= \sqrt{m^2 + 4\langle xy \rangle^2}, \\
u &= 1 + \frac{k}{l}, \\
v &= 2 - u,
\end{aligned}$$

the Hillas parameters are calculated from:

$$\begin{aligned}
\langle Size \rangle &= \sum s_i, \\
\langle Length \rangle^2 &= \frac{\sigma_{x^2} + \sigma_{y^2} + l}{2}, \\
\langle Width \rangle^2 &= \frac{\sigma_{x^2} + \sigma_{y^2} - l}{2}, \\
\langle Miss \rangle^2 &= \frac{u\langle x \rangle^2 + v\langle y \rangle^2}{2} - \frac{2\langle xy \rangle \sigma_{xy}}{l}, \\
\langle Distance \rangle^2 &= \langle x \rangle^2 + \langle y \rangle^2, \\
\langle Alpha \rangle &= \sin^{-1}\left(\frac{\langle Miss \rangle}{\langle Distance \rangle}\right), \\
\langle Azwidth \rangle^2 &= \frac{\langle x^2 \rangle + \langle y^2 \rangle - n}{2}.
\end{aligned}$$

The calculation of the parameter *Asymmetry* requires the angle, ψ, between

the x-axis and the major axis of the ellipse. It is convenient to define p:

$$\begin{aligned}
\psi &= \tan^{-1}\left(\frac{(k+l)\langle y\rangle + 2\sigma_{xy}\langle x\rangle}{2\sigma_{xy}\langle y\rangle - (k-l)\langle x\rangle}\right), \\
p &= \sigma_{x^3}\cos^3\psi + 3\sigma_{x^2y}\sin\psi\cos^2\psi + 3\sigma_{xy^2}\cos\psi\sin^2\psi \\
&+ \sigma_{y^3}\sin^3\psi, \\
\langle Asymmetry\rangle^3 &= \frac{p}{\langle Length\rangle}.
\end{aligned}$$

Appendix C

The VERITAS Collaboration

United States
Smithsonian Astrophysical Observatory
Purdue University
Iowa State University
Washington University, St. Louis
University of Chicago
University of Utah
University of California, Los Angeles
Associate Members, USA

Canada
McGill University, Montreal

Ireland
National University of Ireland, Dublin
Galway-Mayo Institute of Technology
Cork Institute of Technology
Associate Members, Ireland

United Kingdom
University of Leeds
Associate Members, UK

Bibliography

Aharonian, F., Akhperjanian, A., Barrio, J., Beilicke, M., Bernlöhr, K., Börst, H., Bojahr, H., Bolz, O., Contreras, J., Cornils, R., Cortina, J., Denninghoff, S., Fonseca, V., Girma, M., Gonzalez, J., Götting, N., Heinzelmann, G., Hermann, G., Heusler, A., Hofmann, W., Horns, D., Jung, I., Kankanyan, R., Kestel, M., Kettler, J., Kohnle, A., Konopelko, A., Kornmeyer, H., Kranich, D., Krawczynski, H., Lampeitl, H., Lopez, M., Lorenz, E., Lucarelli, F., Magnussen, N., Mang, O., Meyer, H., Mirzoyan, R., Moralejo, A., Ona, E., Padilla, L., Panter, M., Plaga, R., Plyasheshnikov, A., Pühlhofer, G., Rauterberg, G., Röhring, A., Rhode, W., Robrade, J., Rowell, G., Sahakian, V., Samorski, M., Schilling, M., Schröder, F., Sevilla, I., Siems, M., Stamm, W., Tluczykont, M., Völk, H. J., Wiedner, C. A., and Wittek, W.: 2002a, A&A **384**, L23

Aharonian, F., Akhperjanian, A., Barrio, J., Bernlöhr, K., Börst, H., Bojahr, H., Bolz, O., Contreras, J., Cortina, J., Denninghoff, S., Fonseca, V., Gonzalez, J., Götting, N., Heinzelmann, G., Hermann, G., Heusler, A., Hofmann, W., Horns, D., Ibarra, A., Iserlohe, C., Jung, I., Kankanyan, R., Kestel, M., Kettler, J., Kohnle, A., Konopelko, A., Kornmeyer, H., Kranich, D., Krawczynski, H., Lampeitl, H., Lopez, M., Lorenz, E., Lucarelli, F., Magnussen, N., Mang, O., Meyer, H., Mirzoyan, R., Moralejo, A., Ona, E., Padilla, L., Panter, M., Plaga, R., Plyasheshnikov, A., Prahl, J., Pühlhofer, G., Rauterberg, G., Röhring, A., Rhode, W., Rowell, G. P., Sahakian, V., Samorski, M., Schilling, M., Schröder, F., Siems, M., Stamm, W., Tluczykont, M., Völk, H. J., Wiedner, C. A., and Wittek, W.: 2001, A&A **370**, 112

Aharonian, F., Akhperjanian, A., Beilicke, M., Bernlöhr, K., Börst, H., Bojahr, H., Bolz, O., Coarasa, T., Contreras, J., Cortina, J., Denninghoff, S., Fonseca, V., Girma, M., Götting, N., Heinzelmann, G., Hermann, G., Heusler, A., Hofmann, W., Horns, D., Jung, I., Kankanyan, R., Kestel, M., Kettler, J., Kohnle, A., Konopelko, A., Kornmeyer, H., Kranich, D., Krawczynski, H., Lampeitl, H., Lopez, M., Lorenz, E., Lucarelli, F., Mag-

nussen, N., Mang, O., Meyer, H., Milite, M., Mirzoyan, R., Moralejo, A., Ona, E., Panter, M., Plyasheshnikov, A., Prahl, J., Pühlhofer, G., Rauterberg, G., Reyes, R., Rhode, W., Ripken, J., Röhring, A., Rowell, G. P., Sahakian, V., Samorski, M., Schilling, M., Schröder, F., Siems, M., Sobzynska, D., Stamm, W., Tluczykont, M., Völk, H. J., Wiedner, C. A., Wittek, W., Uchiyama, Y., Takahashi, T., and HEGRA Collaboration: 2002b, A&A **393**, L37

Aharonian, F., Akhperjanian, A., Beilicke, M., Bernlöhr, K., Börst, H.-G., Bojahr, H., Bolz, O., Coarasa, T., Contreras, J. L., Cortina, J., Costamante, L., Denninghoff, S., Fonseca, M. V., Girma, M., Götting, N., Heinzelmann, G., Hermann, G., Heusler, A., Hofmann, W., Horns, D., Jung, I., Kankanyan, R., Kestel, M., Kohnle, A., Konopelko, A., Kornmeyer, H., Kranich, D., Lampeitl, H., Lopez, M., Lorenz, E., Lucarelli, F., Mang, O., Mazine, D., Meyer, H., Mirzoyan, R., Moralejo, A., Ona-Wilhelmi, E., Panter, M., Plyasheshnikov, A., Prahl, J., Pühlhofer, G., de los Reyes, R., Rhode, W., Ripken, J., Rowell, G., Sahakian, V., Samorski, M., Schilling, M., Siems, M., Sobzynska, D., Stamm, W., Tluczykont, M., Vitale, V., Völk, H. J., Wiedner, C. A., and Wittek, W.: 2003a, A&A **403**, 523

Aharonian, F., Akhperjanian, A., Beilicke, M., Bernlöhr, K., Börst, H.-G., Bojahr, H., Bolz, O., Coarasa, T., Contreras, J. L., Cortina, J., Denninghoff, S., Fonseca, M. V., Girma, M., Götting, N., Heinzelmann, G., Hermann, G., Heusler, A., Hofmann, W., Horns, D., Jung, I., Kankanyan, R., Kestel, M., Kohnle, A., Konopelko, A., Kornmeyer, H., Kranich, D., Lampeitl, H., Lopez, M., Lorenz, E., Lucarelli, F., Mang, O., Meyer, H., Mirzoyan, R., Moralejo, A., Ona-Wilhelmi, E., Panter, M., Plyasheshnikov, A., Pühlhofer, G., de los Reyes, R., Rhode, W., Ripken, J., Robrade, J., Rowell, G., Sahakian, V., Samorski, M., Schilling, M., Siems, M., Sobzynska, D., Stamm, W., Tluczykont, M., Vitale, V., Völk, H. J., Wiedner, C. A., and Wittek, W.: 2003b, A&A **406**, L9

Aharonian, F., Akhperjanian, A., Beilicke, M., Bernlöhr, K., Börst, H.-G., Bojahr, H., Bolz, O., Coarasa, T., Contreras, J. L., Cortina, J., Denninghoff, S., Fonseca, V., Girma, M., Götting, N., Heinzelmann, G., Hermann, G., Heusler, A., Hofmann, W., Horns, D., Jung, I., Kankanyan, R., Kestel, M., Konopelko, A., Kornmeyer, H., Kranich, D., Lampeitl, H., Lopez, M., Lorenz, E., Lucarelli, F., Mang, O., Mazin, D., Meyer, H., Mirzoyan, R., Moralejo, A., Ona-Wilhelmi, E., Panter, M., Plyasheshnikov, A., Pühlhofer, G., de los Reyes, R., Rhode, W., Ripken, J., Rowell, G., Sahakian, V., Samorski, M., Schilling, M., Siems, M., Sobzynska, D., Stamm,

W., Tluczykont, M., Vitale, V., Völk, H. J., Wiedner, C. A., and Wittek, W.: 2004, A&A **421**, 529

Aharonian, F. A., Akhperjanian, A. G., Barrio, J. A., Bernlöhr, K., Bojahr, H., Calle, I., Contreras, J. L., Cortina, J., Daum, A., Deckers, T., Denninghoff, S., Fonseca, V., Gonzalez, J. C., Heinzelmann, G., Hemberger, M., Hermann, G., Heß, M., Heusler, A., Hofmann, W., Hohl, H., Horns, D., Ibarra, A., Kankanyan, R., Kettler, J., Köhler, C., Konopelko, A., Kornmeyer, H., Kestel, M., Kranich, D., Krawczynski, H., Lampeitl, H., Lindner, A., Lorenz, E., Magnussen, N., Meyer, H., Mirzoyan, R., Moralejo, A., Padilla, L., Panter, M., Petry, D., Plaga, R., Plyasheshnikov, A., Prahl, J., Pühlhofer, G., Rauterberg, G., Renault, C., Rhode, W., Röhring, A., Sahakian, V., Samorski, M., Schmele, D., Schröder, F., Stamm, W., Völk, H. J., Wiebel-Sooth, B., Wiedner, C., Willmer, M., and Wittek, W.: 1999, A&A **349**, 11

Aharonian, F. A., Akhperjanian, A. G., Barrio, J. A., Bernlöhr, K., Bojahr, H., Calle, I., Contreras, J. L., Cortina, J., Daum, A., Deckers, T., Denninghoff, S., Fonseca, V., Gonzalez, J. C., Heinzelmann, G., Hemberger, M., Hermann, G., Heß, M., Heusler, A., Hofmann, W., Hohl, H., Horns, D., Ibarra, A., Kankanyan, R., Kestel, M., Kettler, J., Köhler, C., Konopelko, A., Kornmeyer, H., Kranich, D., Krawczynski, H., Lampeitl, H., Lindner, A., Lorenz, E., Magnussen, N., Mang, O., Meyer, H., Mirzoyan, R., Moralejo, A., Padilla, L., Panter, M., Petry, D., Plaga, R., Plyasheshnikov, A., Prahl, J., Pühlhofer, G., Rauterberg, G., Renault, C., Rhode, W., Röhring, A., Sahakian, V., Samorski, M., Schmele, D., Schilling, M., Schröder, F., Stamm, W., Völk, H. J., Wiebel-Sooth, B., Wiedner, C., Willmer, M., and Wittek, W.: 2000, A&A **353**, 847

Amenomori, M., Ayabe, S., Cao, P. Y., Danzengluobu, Ding, L. K., Feng, Z. Y., Fu, Y., Guo, H. W., He, M., Hibino, K., Hotta, N., Huang, Q., Huo, A. X., Izu, K., Jia, H. Y., Kajino, F., Kasahara, K., Katayose, Y., Labaciren, Li, J. Y., Lu, H., Lu, S. L., Luo, G. X., Meng, X. R., Mizutani, K., Mu, J., Nanjo, H., Nishizawa, M., Ohnishi, M., Ohta, I., Ouchi, T., Ren, J. R., Saito, T., Sakata, M., Sasaki, T., Shi, Z. Z., Shibata, M., Shiomi, A., Shirai, T., Sugimoto, H., Taira, K., Tan, Y. H., Tateyama, N., Torii, S., Utsugi, T., Wang, C. R., Wang, H., Xu, X. W., Yamamoto, Y., Yu, G. C., Yuan, A. F., Yuda, T., Zhang, C. S., Zhang, H. M., Zhang, J. L., Zhang, N. J., Zhang, X. Y., Zhaxisangzhu, Zhaxiciren, Zhou, W. D., and The Tibet As Γ Collaboration: 1999, ApJ **525**, L93

Amenomori, M., Ayabe, S., Cui, S. W., Danzengluobu, Ding, L. K., Ding, X. H., Feng, C. F., Feng, Z. Y., Gao, X. Y., Geng, Q. X., Guo, H. W., He, H. H., He, M., Hibino, K., Hotta, N., Hu, H., Hu, H. B., Huang, J., Huang, Q., Jia, H. Y., Kajino, F., Kasahara, K., Katayose, Y., Kawata, K., Labaciren, Le, G. M., Li, J. Y., Lu, H., Lu, S. L., Meng, X. R., Mizutani, K., Mu, J., Nanjo, H., Nishizawa, M., Ohnishi, M., Ohta, I., Ouchi, T., Ozawa, S., Ren, J. R., Saito, T., Sakata, M., Sasaki, T., Shibata, M., Shiomi, A., Shirai, T., Sugimoto, H., Taira, K., Takita, M., Tan, Y. H., Tateyama, N., Torii, S., Tsuchiya, H., Udo, S., Utsugi, T., Wang, B. S., Wang, H., Wang, X., Wang, Y. G., Xue, L., Yamamoto, Y., Yang, X. C., Ye, Z. H., Yu, G. C., Yuan, A. F., Yuda, T., Zhang, H. M., Zhang, J. L., Zhang, N. J., Zhang, X. Y., Zhang, Y., Zhaxisangzhu, and Zhou, X. X.: 2003, ApJ **598**, 242

Amenomori, M. and The Tibet As Γ Collaboration: 2001, in *American Institute of Physics Conference Series*, pp 557–+

Antonucci, R. R. J. and Miller, J. S.: 1985, ApJ **297**, 621

Arqueros, F., Ballestrin, J., Berenguel, M., Borque, D. M., Camacho, E. F., Diaz, M., Gebauer, H.-J., Enriquez, R., and Plaga, R.: 2002, *Astroparticle Physics* **17**, 293

Atkins, R., Benbow, W., Berley, D., Blaufuss, E., Bussons, J., Coyne, D. G., Delay, R. S., DeYoung, T., Dingus, B. L., Dorfan, D. E., Ellsworth, R. W., Falcone, A., Fleysher, L., Fleysher, R., Gisler, G., Gonzalez, M. M., Goodman, J. A., Haines, T. J., Hays, E., Hoffman, C. M., Kelley, L. A., Laird, R. W., McCullough, J., McEnery, J. E., Miller, R. S., Mincer, A. I., Morales, M. F., Nemethy, P., Noyes, D., Ryan, J. M., Samuelson, F. W., Schneider, M., Shen, B., Shoup, A., Sinnis, G., Smith, A. J., Sullivan, G. W., Tumer, O. T., Wang, K., Wascko, M., Williams, D. A., Westerhoff, S., Wilson, M. E., Xu, X., and Yodh, G. B.: 2003, ApJ **595**, 803

Badran, H.: 2001a, *Optimization of Supercuts 2001.*, VERITAS Collaboration Internal memo

Badran, H. M.: 2001b, in *AIP Conf. Proc. 587: Gamma 2001: Gamma-Ray Astrophysics*, pp 281–+

Baixeras, C. et al.: 2004

Bednarek, W.: 1998, A&A **336**, 123

Biller, S. D., Buckley, J., Burdett, A., Bussons Gordo, J., Carter-Lewis, D. A., Fegan, D. J., Finley, J., Gaidos, J. A., Hillas, A. M., Krennrich, F., Lamb, R. C., Lessard, R., McEnery, J. E., Mohanty, G., Quinn, J., Rodgers, A. J., Rose, H. J., Samuelson, F., Sembroski, G., Skelton, P., Weekes, T. C., and Zweerink, J.: 1998, *Physical Review Letters* **80**, 2992

Blackett, P.: 1948, *Physical Society Gassiot Committee Report* 34

Blandford, R. D. and Levinson, A.: 1995, ApJ **441**, 79

Bloom, S. D., Bertsch, D. L., Hartman, R. C., Sreekumar, P., Thompson, D. J., Balonek, T. J., Beckerman, E., Davis, S. M., Whitman, K., Miller, H. R., Nair, D., Roberts, L. C., Tosti, G., Massaro, E., Nesci, R., Maesano, M., Montagni, F., Jang, M., Bock, H. A., Dietrich, M., Herter, M., Otterbein, K., Pfeiffer, M., Seitz, T., and Wagner, S.: 1997, ApJ **490**, L145+

Bloom, S. D. and Marscher, A. P.: 1996, ApJ **461**, 657

Bond, J. R., Carr, B. J., and Hogan, C. J.: 1986, ApJ **306**, 428

Boone, L. M., Hinton, J. A., Bramel, D., Chae, E., Covault, C. E., Fortin, P., Gingrich, D. M., Hanna, D. S., Mukherjee, R., Mueller, C., Ong, R. A., Ragan, K., Scalzo, R. A., Schuette, D. R., Théoret, C. G., and Williams, D. A.: 2002, ApJ **579**, L5

Bottcher, M. and Dermer, C. D.: 1998, in *Abstracts of the 19th Texas Symposium on Relativistic Astrophysics and Cosmology, held in Paris, France, Dec. 14-18, 1998. Eds.: J. Paul, T. Montmerle, and E. Aubourg (CEA Saclay).*

Bradbury, S. M., Deckers, T., Petry, D., Konopelko, A., Aharonian, F., Akhperjanian, A. G., Barrio, J. A., Beglarian, A. S., Beteta, J. J. G., Contreras, J. L., Cortina, J., Daum, A., Feigl, E., Fernandez, J., Fonseca, V., Frass, A., Funk, B., Gonzalez, J. C., Haustein, V., Heinzelmann, G., Hemberger, M., Hermann, G., Hess, M., Heusler, A., Holl, I., Hofmann, W., Horns, D., Kankanian, R., Kirstein, O., Koehler, C., Kranich, D., Krawczynski, H., Kornmayer, H., Lampeitl, H., Lindner, A., Lorenz, E., Magnussen, N., Meyer, H., Mirzoyan, R., Moeller, H., Moralejo, A., Padilla, L., Panter, M., Plaga, R., Prahl, J., Prosch, C., Puehlhofer, G., Rauterberg, G., Rhode, W., Sahakian, V., Samorski, M., Sanchez, J. A., Schmele, D., Stamm, W., Ulrich, M., Voelk, H. J., Westerhoff, S., Wiebel-Sooth, B., Wiedner, C. A., Willmer, M., and Wirth, H.: 1997, A&A **320**, L5

Buckley, J. H., Akerlof, C. W., Carter-Lewis, D. A., Catanese, M., Cawley, M. F., Connaughton, V., Fegan, D. J., Finley, J. P., Gaidos, J. A., Hillas, A. M., Krennrich, F., Lamb, R. C., Lessard, R. W., McEnery, J. E., Mohanty, G., Quinn, J., Rodgers, A. J., Rose, H. J., Rovero, A. C., Schubnell, M. S., Sembroski, G., Srinivasan, R., Weekes, T. C., and Zweerink, J.: 1998, A&A **329**, 639

Carter-Lewis, D.: 1992, Whipple Collaboration Internal memo

Catanese, M., Akerlof, C. W., Badran, H. M., Biller, S. D., Bond, I. H., Boyle, P. J., Bradbury, S. M., Buckley, J. H., Burdett, A. M., Bussons Gordo, J., Carter-Lewis, D. A., Cawley, M. F., Connaughton, V., Fegan, D. J., Finley, J. P., Gaidos, J. A., Hall, T., Hillas, A. M., Krennrich, F., Lamb, R. C., Lessard, R. W., Masterson, C., McEnery, J. E., Mohanty, G., Quinn, J., Rodgers, A. J., Rose, H. J., Samuelson, F. W., Schubnell, M. S., Sembroski, G. H., Srinivasan, R., Weekes, T. C., Wilson, C. W., and Zweerink, J.: 1998, ApJ **501**, 616

Catanese, M., Akerlof, C. W., Biller, S. D., Boyle, P., Buckley, J. H., Carter-Lewis, D. A., Cawley, M. F., Connaughton, V., Dingus, B. L., Fegan, D. J., Fichtel, C. E., Finley, J. P., Gaidos, J. A., Gear, W. K., Hartman, R. C., Hillas, A. M., Krennrich, F., Lamb, R. C., Lessard, R. W., Lin, Y. C., McEnery, J. E., Marscher, A. P., Mohanty, G., Mukherjee, R., Quinn, J., Robson, E. I., Rodgers, A. J., Rose, H. J., Samuelson, F. W., Sembroski, G., Schubnell, M. S., Stevens, J. A., Teraesranta, H., Thompson, D. J., Weekes, T. C., Wilson, C., and Zweerink, J.: 1997a, ApJ **480**, 562

Catanese, M., Boyle, P. J., Buckley, J. H., Burdett, A. M., Gordo, J. B., Carter-Lewis, D. A., Cawley, M. F., Fegan, D. J., Finley, J. P., Gaidos, J. A., Hillas, A. M., Krennrich, F., Lamb, R. C., Lessard, R. W., Masterson, C., McEnery, J. E., Mohanty, G., Quinn, J., Rodgers, A. J., Rose, H. J., Samuelson, F. W., Sembroski, G. H., Srinivasan, R., Weekes, T. C., and Zweerink, J.: 1997b, in *AIP Conf. Proc. 410: Proceedings of the Fourth Compton Symposium*, pp 1376–+

Catanese, M. et al.: 1995, in M. Cresti (ed.), *Workshop Towards a Major Cherenkov Detector (Padova)*, p. 335

Catanese, M. et al.: 1997

Cawley, M.: 1993, in R. Lamb (ed.), *Workshop Towards a Major Cherenkov Detector (Calgary)*, p. 176

Cawley, M. F.: 1993, in *Towards a Major Atmospheric Cherenkov Detector – II for TeV Astro/Particle Physics*, pp 176–+

Cawley, M. F., Clear, J., Fegan, D. J., Gibbs, K., Gorham, P., Lamb, R. C., MacRae, I., MacKeown, P. K., Porter, N. A., Stenger, V. S., Turver, K. E., and Weekes, T. C.: 1983, in N. Durgaprasad (ed.), *Proceedings of the 18th International Cosmic Ray Conference (Bangalore)*, p. 118

Cawley, M. F., Fegan, D. J., Harris, K., Kwok, P. W., Hillas, A. M., Lamb, R. C., Lang, M. J., Lewis, D. A., Macomb, D., Reynolds, P. T., Schmid, D. J., Vacanti, G., and Weekes, T. C.: 1990, *Experimental Astronomy* **1**, 173

Chadwick, P. M., Daniel, M. K., Lyons, K., McComb, T. J. L., McKenny, J. M., Nolan, S. J., Orford, K. J., Osborne, J. L., Rayner, S. M., and Turver, K. E.: 2000a, A&A **364**, 165

Chadwick, P. M., Dickinson, M. R., Dipper, N. A., Holder, J., Kendall, T. R., McComb, T. J. L., Orford, K. J., Osborne, J. L., Rayner, S. M., Roberts, I. D., Shaw, S. E., and Turver, K. E.: 1998, *Astroparticle Physics* **9**, 131

Chadwick, P. M., Lyons, K., McComb, T. J. L., Orford, K. J., Osborne, J. L., Rayner, S. M., Shaw, S. E., and Turver, K. E.: 2000b, in *American Institute of Physics Conference Series*, pp 210–+

Chadwick, P. M., Lyons, K., McComb, T. J. L., Orford, K. J., Osborne, J. L., Rayner, S. M., Shaw, S. E., Turver, K. E., and Wieczorek, G. J.: 1999, *Astroparticle Physics* **11**, 145

Chadwick, P. M., McComb, T. J. L., and Turver, K. E.: 1990, *Journal of Physics G Nuclear Physics* **16**, 1773

Chincarini, G., Angelini, L., Barbier, L., Barthelmy, S., Burrows, D., Caraveo, P., Chester, M., Chincarini, G., Citterio, O., Cline, T., Cominsky, L., Corbet, R., Cordova, F., Cropper, M., Feigelson, E., Fenimore, E., Frail, D., Gehrels, N., Garmire, G., Giommi, P., Horner, S., Hurley, K., Jahoda, K., Lebrun, F., Marshall, F., Mason, K., Meszaros, P., Mushotzky, R., Norris, J., Nousek, J., Paczynski, B., Palmer, D., Parsons, A., Paul, J., Roming, P., Sasseen, T., Smale, A., Stella, L., Tagliaferri, G., Townsley, L., Tueller, J., Turner, M., Vietri, M., Ward, M., Wells, A., White, N., Whitlock, L., Willingale, R., Zhang, W., and Zerbi, F. M.: 2003, in *Astronomy, Cosmology and Fundamental Physics*, pp 432–+

Clark, G. W., Garmire, G. P., and Kraushaar, W. L.: 1968, ApJ **153**, L203+

Cocconi, G.: 1959, *Proceedings of the 6th International Cosmic Ray Conference (Moscow, USSR)* **2**, 309

Coppi, P.: 1999, *Workshop Summary for Cracow 1997*

Costamante, L. and Ghisellini, G.: 2002, A&A **384**, 56

Danaher, S., Fegan, D. J., Porter, N. A., Weekes, T. C., and Cole, T.: 1982, *Solar Energy* **28**, 335

Dar, A. and Laor, A.: 1997, ApJ **478**, L5+

Davies, J. and Cotton, E.: 1957, *Journal of Solar Energy* **1**, 16

de la Calle Perez, I.: 2003, *Ph.D. thesis*, University of Leeds

de la Calle Perez, I. and Holder, J.: 2001, *Tracking Ratio Stability*, VERITAS Collaboration Internam memo

de Naurois, M., Holder, J., Bazer-Bachi, R., Bergeret, H., Bruel, P., Cordier, A., Debiais, G., Dezalay, J.-P., Dumora, D., Durand, E., Eschstruth, P., Espigat, P., Fabre, B., Fleury, P., Hérault, N., Hrabovsky, M., Incerti, S., Le Gallou, R., Münz, F., Musquère, A., Olive, J.-F., Paré, E., Québert, J., Rannot, R. C., Reposeur, T., Rob, L., Roy, P., Sako, T., Schovanek, P., Smith, D. A., Snabre, P., and Volte, A.: 2002, ApJ **566**, 343

Dermer, C. D. and Schlickeiser, R.: 1993, ApJ **416**, 458

Dermer, C. D., Schlickeiser, R., and Mastichiadis, A.: 1992, A&A **256**, L27

Dermer, C. D., Sturner, S. J., and Schlickeiser, R.: 1997, ApJS **109**, 103

Derome, L. and The AMS Collaboration: 2003, in *SF2A-2003: Semaine de l'Astrophysique Francaise*, pp 399–+

Djannati-Ataı, A. and The CAT Collaboration: 2003, in *ASP Conf. Ser. 290: Active Galactic Nuclei: From Central Engine to Host Galaxy*, pp 291–+

Donato, D., Ghisellini, G., Tagliaferri, G., and Fossati, G.: 2001, A&A **375**, 739

Dowdall, C.: 2003, *Instrumentation and Software for the VERITAS Project and the Detection of TeV Gamma-Ray Emission from the BL Lacertae Object 1ES1959+650*

Dunlea, S.: 2001, *Ph.D. thesis*, National University of Ireland

Dunlea, S., Moriarty, P., and Fegan, D. J.: 2001, in *Proceedings of the 27th International Cosmic Ray Conference (Hamburg, Germany)*, Vol. 7, p. 2939

Enomoto, R., Tanimori, T., Naito, T., Yoshida, T., Yanagita, S., Mori, M., Edwards, P. G., Asahara, A., Bicknell, G. V., Gunji, S., Hara, S., Hara, T., Hayashi, S., Itoh, C., Kabuki, S., Kajino, F., Katagiri, H., Kataoka, J., Kawachi, A., Kifune, T., Kubo, H., Kushida, J., Maeda, S., Maeshiro, A., Matsubara, Y., Mizumoto, Y., Moriya, M., Muraishi, H., Muraki, Y., Nakase, T., Nishijima, K., Ohishi, M., Okumura, K., Patterson, J. R., Sakurazawa, K., Suzuki, R., Swaby, D. L., Takano, K., Takano, T., Tokanai, F., Tsuchiya, K., Tsunoo, H., Uruma, K., Watanabe, A., and Yoshikoshi, T.: 2002, Nature **416**, 823

Fegan, D.: 1992, in *Towards a Major Atmospheric Cerenkov Detector for TeV Astro/particle Physics*, pp 3–+

Fegan, D.: 2002, *The Outer Limits*, VERITAS Collaboration Internal memo

Fegan, D., Akerlof, C., Breslin, A., Buckley, J., Cawley, M., Chantell, M., Connaughton, V., Fennell, S., Gaidos, J., Hagan, J., Hillas, A., Kerrick, A., Lamb, R., Lessard, R., Lewis, D., McEnery, J., Meyer, D., Mohanty, G., Punch, M., Quinn, J., Reynolds, P., Rovero, A., Rose, H., Schubnell, M., Sembroski, G., Urban, M., Weekes, T., West, M., Wilson, C., and Zweerink, J.: 1994, in T. Kifune (ed.), *Proceedings of the 3rd International Workshop 'Towards a Major Cherenkov Detector' (Tokyo)*, p. 149, Universal Academy Press, Inc.

Fichtel, C. E., Hartman, R. C., Kniffen, D. A., Thompson, D. J., Ogelman, H., Ozel, M. E., Tumer, T., and Bignami, G. F.: 1975, ApJ **198**, 163

Finley, J. P., Bond, J. H., Bradbury, S. M., Breslin, A. C., Buckley, J. H., Burdett, A. M., Carson, M., Carter-Lewis, D. A., Catanese, M., Cawley, M. F., Dunlea, S., D'Vali, M., Fegan, D. J., Fegan, S. J., Gaidos, J. A., Hall, T. A., Hillas, A. M., Horan, D., Knapp, J., Krennrich, F., Lebohec, S., Lessard, R. W., Masterson, C., McKerman, B., Quinn, J., Rose, H. J., Samuelson, F. W., Sembroski, G. H., Vassiliev, V. V., and Weekes, T. C.: 2000, in *American Institute of Physics Conference Series*, pp 301–+

Fossati, G., Maraschi, L., Celotti, A., Comastri, A., and Ghisellini, G.: 1998, MNRAS **299**, 433

Frank, I. and Tamm, I.: 1937, *Dokl. Akad. Nauk.* **14**, 109

Fruin, J. H. and Jelley, J. V.: 1968, *Canadian J. Phys* **44**, S1118

Gaidos, J. A., Akerlof, C. W., Biller, S. D., Boyle, P. J., Breslin, A. C., Buckley, J. H., Carter-Lewis, D. A., Catanese, M., Cawley, M. F., Fegan, D. J., Finley, J. P., Hillas, A. M., Krennrich, F., Lamb, R. C., Lessard, R., McEnery, J., Mohanty, G., Moriarty, P., Quinn, J., Rodgers, A., Rose, H. J., Samuelson, F., Schubnell, M. S., Sembroski, G., Srinivasan, R., Weekes, T. C., Wilson, C. L., and Zweerink, J.: 1996, Nature **383**, 319

Galbraith, W. and Jelley, J. V.: 1953, *Nature* **171**, 349

Garrington, S. T. and Conway, R. G.: 1991, MNRAS **250**, 198

Ghisellini, G., Celotti, A., Fossati, G., Maraschi, L., and Comastri, A.: 1998, MNRAS **301**, 451

Ghisellini, G. and Madau, P.: 1996, MNRAS **280**, 67

Ghisellini, G., Padovani, P., Celotti, A., and Maraschi, L.: 1993, ApJ **407**, 65

Gillanders, G. G., Boyle, P. J., Buckley, J. H., Burdett, A. M., Bussons Gordo, J., Carter-Lewis, D. A., Catanese, M., Cawley, M. F., Fegan, D. J., Finley, J. P., Gaidos, J. A., Hillas, A. M., Krennrich, F., Lamb, R. C., Lang, M. J., Lessard, R., Masterson, C., McEnery, J. E., Mohanty, G., Moriarty, P., Quinn, J., Rodgers, A. J., Rose, H. J., Samuelson, F. W., Sembroski, G. H., Srinivasan, R., Weekes, T. C., and Zweerink, J.: 1997, *Proceedings of the 25th International Cosmic Ray Conference (Durban, South Africa), vol. 3, eds. M. S. Potgieter, C. Raubenheimer, and D. J. van der Walt, p. 185. Transvaal, South Africa: Potchefstroom University, 1997.* **3**, 185

Gotting, N. et al.: 2003

Greisen, K.: 1956, *Prog. Cosmic Ray Phys.* 3

Hanbury-Brown, R.: 1966, *Philips Tech Rev* **27**, 141

Hand, D.: 1982, *Kernel Discriminant Analysis*, John Wiley & Sons, Inc., Chichester

Hartman, R. C., Bertsch, D. L., Bloom, S. D., Chen, A. W., Deines-Jones, P., Esposito, J. A., Fichtel, C. E., Friedlander, D. P., Hunter, S. D., McDonald, L. M., Sreekumar, P., Thompson, D. J., Jones, B. B., Lin, Y. C., Michelson, P. F., Nolan, P. L., Tompkins, W. F., Kanbach, G., Mayer-Hasselwander, H. A., Mücke, A., Pohl, M., Reimer, O., Kniffen, D. A., Schneid, E. J., von Montigny, C., Mukherjee, R., and Dingus, B. L.: 1999, ApJS **123**, 79

Hartman, R. C. and Boettcher, M.: 1999, *Bulletin of the American Astronomical Society* **31**, 1395

HEGRA Collaboration, Konopelko, A., Hemberger, M., Aharonian, F., Daum, A., Hofmann, W., Köhler, C., Krawczynski, H., Völk, H. J., Akhperjanian, A., Barrio, J., Bernlöhr, K., Bojahr, H., Contreras, J., Cortina, J., Deckers, T., Denninghoff, S., Fernandez, J., Fonseca, V., Gonzalez, J., Haustein, V., Heinzelmann, G., Hermann, G., Hess, M., Heusler, A., Hohl, H., Holl, I., Horns, D., Kankanian, R., Kestel, M., Kettler, J., Kirstein, O., Kornmayer, H., Kranich, D., Lampeitl, H., Lindner, A., Lorenz, E., Magnussen, N., Meyer, H., Mirzoyan, R., Möller, H., Moralejo, A., Padilla, L., Panter, M., Petry, D., Plaga, R., Plyasheshnikov, A., Prahl, J., Prosch, C., Pühlhofer, G., Rauterberg, G., Rhode, W., Röhring, A., Sahakian, V., Samorski, M., Sanchez, J., Schmele, D., Schroeder, F., Stamm, W., Wiebel-Sooth, B., Wiedner, C. A., Willmer, M., and Wirth, H.: 1999, *Astroparticle Physics* **10**, 275

Heitler, W.: 1954, in *International Series of Monographs on Physics, Oxford: Clarendon, 1954, 3rd ed.*

Helene, O.: 1983, *Nuclear Instruments and Methods* **212**, 319

Hill, D. and Porter, N.: 1961, *Nature* **191**, 690

Hillas, A.: 1985, in *Proc. 19th I.C.R.C. (La Jolla)*, Vol. 3, p. 445

Hillas, A. M.: 1996, *Space Science Reviews* **75**, 17

Hillas, A. M., Akerlof, C. W., Biller, S. D., Buckley, J. H., Carter-Lewis, D. A., Catanese, M., Cawley, M. F., Fegan, D. J., Finley, J. P., Gaidos, J. A., Krennrich, F., Lamb, R. C., Lang, M. J., Mohanty, G., Punch, M., Reynolds, P. T., Rodgers, A. J., Rose, H. J., Rovero, A. C., Schubnell, M. S., Sembroski, G. H., Vacanti, G., Weekes, T. C., West, M., and Zweerink, J.: 1998, ApJ **503**, 744

Hinton, J. A.: 2004, *New Astronomy Review* **48**, 331

Hoffman, C. M., Sinnis, C., Fleury, P., and Punch, M.: 1999, *Reviews of Modern Physics* **71**, 897

Holder, J.: 2004, Private Communication

Holder, J., Bond, I. H., Boyle, P. J., Bradbury, S. M., Buckley, J. H., Carter-Lewis, D. A., Cui, W., Dowdall, C., Duke, C., de la Calle Perez, I., Falcone, A., Fegan, D. J., Fegan, S. J., Finley, J. P., Fortson, L., Gaidos, J. A., Gibbs, K., Gammell, S., Hall, J., Hall, T. A., Hillas, A. M., Horan, D., Jordan, M., Kertzman, M., Kieda, D., Kildea, J., Knapp, J., Kosack, K., Krawczynski, H., Krennrich, F., LeBohec, S., Linton, E. T., Lloyd-Evans, J., Moriarty, P., Müller, D., Nagai, T. N., Ong, R., Page, M., Pallassini, R., Petry, D., Power-Mooney, B., Quinn, J., Rebillot, P., Reynolds, P. T., Rose, H. J., Schroedter, M., Sembroski, G. H., Swordy, S. P., Vassiliev, V. V., Wakely, S. P., Walker, G., and Weekes, T. C.: 2003, ApJ **583**, L9

Holder, J. and The Celeste Collaboration: 2001, in *American Institute of Physics Conference Series*, pp 635–+

Horan, D.: 2001, *Ph.D. thesis*, National University of Ireland

Horan, D., Badran, H. M., Bond, I. H., Bradbury, S. M., Buckley, J. H., Carson, M. J., Carter-Lewis, D. A., Catanese, M., Cui, W., Dunlea, S., Das, D., de la Calle Perez, I., D'Vali, M., Fegan, D. J., Fegan, S. J., Finley, J. P., Gaidos, J. A., Gibbs, K., Gillanders, G. H., Hall, T. A., Hillas, A. M., Holder, J., Jordan, M., Kertzman, M., Kieda, D., Kildea, J., Knapp, J., Kosack, K., Krennrich, F., Lang, M. J., LeBohec, S., Lessard, R., Lloyd-Evans, J., McKernan, B., Moriarty, P., Muller, D., Ong, R., Pallassini, R., Petry, D., Quinn, J., Reay, N. W., Reynolds, P. T., Rose, H. J., Sembroski, G. H., Sidwell, R., Stanton, N., Swordy, S. P., Vassiliev, V. V., Wakely, S. P., and Weekes, T. C.: 2002, ApJ **571**, 753

Horan, D. and Weekes, T. C.: 2004, *New Astron. Rev.* **48**, 527

Horns, D., Kohnle, A., and The HEGRA Collaboration: 2001, in *Astronomische Gesellschaft Meeting Abstracts*, pp 201–+

Itoh, C., Enomoto, R., Yanagita, S., Yoshida, T., Tanimori, T., Okumura, K., Asahara, A., Bicknell, G. V., Clay, R. W., Edwards, P. G., Gunji, S., Hara, S., Hara, T., Hattori, T., Hayashi, S., Hayashi, S., Kabuki, S., Kajino, F., Katagiri, H., Kawachi, A., Kifune, T., Kubo, H., Kushida, J., Matsubara, Y., Mizumoto, Y., Mori, M., Moro, H., Muraishi, H., Muraki, Y., Naito, T., Nakase, T., Nishida, D., Nishijima, K., Ohishi, M., Patterson, J. R.,

Protheroe, R. J., Sakurazawa, K., Swaby, D. L., Tokanai, F., Tsuchiya, K., Tsunoo, H., Uchida, T., Watanabe, A., Watanabe, S., and Yoshikoshi, T.: 2003, A&A **402**, 443

Jelley, J.: 1958, *Cerenkov Radiation and its Applications*, Pergamon Press, Oxford

Jelley, J.: 1967, *Progress in Elementary Particles and Cosmic Ray Physics*, Vol. 9, p. 41, North Holland

Kazanas, D. and Mastichiadis, A.: 1999, ApJ **518**, L17

Kifune, T., Tanimori, T., Ogio, S., Tamura, T., Fujii, H., Fujimoto, M., Hara, T., Hayashida, N., Kabe, S., Kakimoto, F., Matsubara, Y., Mizumoto, Y., Muraki, Y., Suda, T., Teshima, M., Tsukagoshi, T., Watase, Y., Yoshikoshi, T., Edwards, P. G., Patterson, J. R., Roberts, M. D., Rowell, G. P., and Thornton, G. J.: 1995, ApJ **438**, L91

Kildea, J.: 2002, *Ph.D. thesis*, National University of Ireland

Kildea, J.: 2003, *Proceedings of the 28th International Cosmic Ray Conference (Tsukuba, Japan), 2003.*

Kildea, J.: 2004, Private Communication

Kniffen, D. A., Bertsch, D. L., Fichtel, C. E., Hartman, R. C., Hunter, S. D., Kanbach, G., Kwok, P. W., Lin, Y. C., Mattox, J. R., Mayer-Hasselwander, H. A., Michelson, P. F., von Montigny, C., Nolan, P. L., Pinkau, K., Schneid, E., Sreekumar, P., and Thompson, D. J.: 1993, ApJ **411**, 133

Krawczynski, H., Hughes, S. B., Horan, D., Aharonian, F., Aller, M. F., Aller, H., Boltwood, P., Buckley, J., Coppi, P., Fossati, G., Götting, N., Holder, J., Horns, D., Kurtanidze, O. M., Marscher, A. P., Nikolashvili, M., Remillard, R. A., Sadun, A., and Schröder, M.: 2004, ApJ **601**, 151

Krennrich, F., Badran, H. M., Bond, I. H., Bradbury, S. M., Buckley, J. H., Carter-Lewis, D. A., Catanese, M., Cui, W., Dunlea, S., Das, D., de la Calle Perez, I., Fegan, D. J., Fegan, S. J., Finley, J. P., Gaidos, J. A., Gibbs, K., Gillanders, G. H., Hall, T. A., Hillas, A. M., Holder, J., Horan, D., Jordan, M., Kertzman, M., Kieda, D., Kildea, J., Knapp, J., Kosack, K., Lang, M. J., LeBohec, S., McKernan, B., Moriarty, P., Müller, D., Ong, R., Pallassini, R., Petry, D., Quinn, J., Reay, N. W., Reynolds, P. T., Rose, H. J., Sembroski, G. H., Sidwell, R., Stanton, N., Swordy,

S. P., Vassiliev, V. V., Wakely, S. P., and Weekes, T. C.: 2001, ApJ **560**, L45

Krennrich, F., Biller, S. D., Bond, I. H., Boyle, P. J., Bradbury, S. M., Breslin, A. C., Buckley, J. H., Burdett, A. M., Gordo, J. B., Carter-Lewis, D. A., Catanese, M., Cawley, M. F., Fegan, D. J., Finley, J. P., Gaidos, J. A., Hall, T., Hillas, A. M., Lamb, R. C., Lessard, R. W., Masterson, C., McEnery, J. E., Mohanty, G., Moriarty, P., Quinn, J., Rodgers, A. J., Rose, H. J., Samuelson, F. W., Sembroski, G. H., Srinivasan, R., Vassiliev, V. V., and Weekes, T. C.: 1999, ApJ **511**, 149

Krennrich, F., Bond, I. H., Bradbury, S. M., Buckley, J. H., Carter-Lewis, D. A., Cui, W., de la Calle Perez, I., Fegan, D. J., Fegan, S. J., Finley, J. P., Gaidos, J. A., Gibbs, K., Gillanders, G. H., Hall, T. A., Hillas, A. M., Holder, J., Horan, D., Jordan, M., Kertzman, M., Kieda, D., Kildea, J., Knapp, J., Kosack, K., Lang, M. J., LeBohec, S., Moriarty, P., Müller, D., Ong, R. A., Pallassini, R., Petry, D., Quinn, J., Reay, N. W., Reynolds, P. T., Rose, H. J., Sembroski, G. H., Sidwell, R., Stanton, N., Swordy, S. P., Vassiliev, V. V., Wakely, S. P., and Weekes, T. C.: 2002, ApJ **575**, L9

Lang, M. J., Carter-Lewis, D. A., Fegan, D. J., Fegan, S. J., Hillas, A. M., Lamb, R. C., Punch, M., Reynolds, P. T., and Weekes, T. C.: 2004, A&A **423**, 415

Lebohec, S. and Holder, J.: 2003, *Astroparticle Physics* **19**, 221

Lessard, R.: 1996, *Ph.D. thesis*, University College Dublin

Lessard, R. W., Bond, I. H., Boyle, P. J., Bradbury, S. M., Buckley, J. H., Burdett, A. C., Carter-Lewis, D. A., Catanese, M., Cawley, M. F., Dunlea, S., D'Vali, M., Fegan, D. J., Fegan, S. J., Finley, J. P., Gaidos, J. A., Hall, T. A., Hillas, A. M., Horan, D., Knapp, J., Krennrich, F., Le Bohec, S., Masterson, C., Quinn, J., Rose, H. J., Samuelson, F. W., sembroski, G. h., and Vassiliev, V. V.: 1999, in *Proceedings of the 26th International Cosmic Ray Conference (Salt Lake City)*, Vol. 3, p. 488

Lewis, D.: 1990, *Experimental Astronomy* **1**, 213

Lloyd-Evans, J., Coy, R. N., Lambert, A., Lapikens, J., Patel, M., Reid, R. J. O., and Watson, A. A.: 1983, Nature **305**, 784

Mücke, A., Protheroe, R. J., Engel, R., Rachen, J. P., and Stanev, T.: 2003, *Astroparticle Physics* **18**, 593

Macomb, D. J., Akerlof, C. W., Aller, H. D., Aller, M. F., Bertsch, D. L., Bruhweiler, F., Buckley, J. H., Carter-Lewis, D. A., Cawley, M. F., Cheng, K.-P., Dermer, C., Fegan, D. J., Gaidos, J. A., Gear, W. K., Hall, C. R., Hartman, R. C., Hillas, A. M., Kafatos, M., Kerrick, A. D., Kniffen, D. A., Kondo, Y., Kubo, H., Lamb, R. C., Makino, F., Makishima, K., Marscher, A., McEnery, J., McHardy, I. M., Meyer, D. I., Moore, E. M., Ramos, E., Robson, E. I., Rose, H. J., Schubnell, M. S., Sembroski, G., Stevens, J. A., Takahashi, T., Tashiro, M., Weekes, T. C., Wilson, C., and Zweerink, J.: 1995, ApJ **449**, L99+

Mallet, L.: 1926, *Acad. Sci. (Paris)* **183**, 274

Mannheim, K.: 1996, *Space Science Reviews* **75**, 331

Maraschi, L., Ghisellini, G., and Celotti, A.: 1992, ApJ **397**, L5

Mardia, K.: 1987, *STATISTICS OF DIRECTIONAL DATA*, ACADEMIC PRESS, London and New York

Marscher, A. P. and Gear, W. K.: 1985, ApJ **298**, 114

Masterson, C.: 2004, *First Physics with H.E.S.S.*, Presentation at H.E.S.S. Inauguration (Namibia)

Mastichiadis, A. and Kirk, J. G.: 1997, A&A **320**, 19

Mohanty, G., Biller, S., Carter-Lewis, D. A., Fegan, D. J., Hillas, A. M., Lamb, R. C., Weekes, T. C., West, M., and Zweerink, J.: 1998, *Astroparticle Physics* **9**, 15

Moriarty, P. and Samuelson, F. W.: 2000, in *GeV-TeV Gamma Ray Astrophysics Workshop : towards a major atmospheric Cherenkov detector*, pp 338+

Morrison, P.: 1958, *Nuovo Cimento* **7**, 858

Muraishi, H., Tanimori, T., Yanagita, S., Yoshida, T., Moriya, M., Kifune, T., Dazeley, S. A., Edwards, P. G., Gunji, S., Hara, S., Hara, T., Kawachi, A., Kubo, H., Matsubara, Y., Mizumoto, Y., Mori, M., Muraki, Y., Naito, T., Nishijima, K., Patterson, J. R., Rowell, G. P., Sako, T., Sakurazawa, K., Susukita, R., Tamura, T., and Yoshikoshi, T.: 2000, A&A **354**, L57

Neshpor, Y. I., Chalenko, N. N., Stepanian, A. A., Kalekin, O. R., Jogolev, N. A., Fomin, V. P., and Shitov, V. G.: 2001, *Astronomy Reports* **45**, 249

Neshpor, Y. I., Stepanyan, A. A., Kalekin, O. P., Fomin, V. P., Chalenko, N. N., and Shitov, V. G.: 1998, *Astronomy Letters* **24**, 134

Nishiyama, T.: 1999, in *Proceedings of the 26th International Cosmic Ray Conference (Salt Lake City)*, Vol. 3, p. 370

O'Neill, R.: 2004, *Investigation and application of noise padding techniques to Atmospheric Cherenkov Observations*

Ong, R. A.: 2003

Oser, S., Bhattacharya, D., Boone, L. M., Chantell, M. C., Conner, Z., Covault, C. E., Dragovan, M., Fortin, P., Gregorich, D. T., Hanna, D. S., Mukherjee, R., Ong, R. A., Ragan, K., Scalzo, R. A., Schuette, D. R., Théoret, C. G., Tümer, T. O., Williams, D. A., and Zweerink, J. A.: 2001, ApJ **547**, 949

Paciesas, W. S., Meegan, C. A., Pendleton, G. N., Briggs, M. S., Kouveliotou, C., Koshut, T. M., Lestrade, J. P., McCollough, M. L., Brainerd, J. J., Hakkila, J., Henze, W., Preece, R. D., Connaughton, V., Kippen, R. M., Mallozzi, R. S., Fishman, G. J., Richardson, G. A., and Sahi, M.: 1999, ApJS **122**, 465

Padovani, P. and Giommi, P.: 1995, ApJ **444**, 567

Perlman, E. S., Stocke, J. T., Schachter, J. F., Elvis, M., Ellingson, E., Urry, C. M., Potter, M., Impey, C. D., and Kolchinsky, P.: 1996, ApJS **104**, 251

Petry, D., Bond, I. H., Bradbury, S. M., Buckley, J. H., Carter-Lewis, D. A., Cui, W., Duke, C., de la Calle Perez, I., Falcone, A., Fegan, D. J., Fegan, S. J., Finley, J. P., Gaidos, J. A., Gibbs, K., Gammell, S., Hall, J., Hall, T. A., Hillas, A. M., Holder, J., Horan, D., Jordan, M., Kertzman, M., Kieda, D., Kildea, J., Knapp, J., Kosack, K., Krennrich, F., LeBohec, S., Moriarty, P., Müller, D., Nagai, T. N., Ong, R., Page, M., Pallassini, R., Power-Mooney, B., Quinn, J., Reay, N. W., Reynolds, P. T., Rose, H. J., Schroedter, M., Sembroski, G. H., Sidwell, R., Stanton, N., Swordy, S. P., Vassiliev, V. V., Wakely, S. P., Walker, G., and Weekes, T. C.: 2002, ApJ **580**, 104

Pian, E., Vacanti, G., Tagliaferri, G., Ghisellini, G., Maraschi, L., Treves, A., Urry, M., Fiore, F., Giommi, P., Palazzi, E., Chiappetti, L., and Sambruna, R. M.: 1998, ApJ **492**, L17+

Power-Mooney, B.: 2004, *Ph.D. thesis*, National University of Ireland

Protheroe, R. J., Donea, A.-C., and Reimer, A.: 2003, *Astroparticle Physics* **19**, 559

Punch, M.: 1991, in *Proc. 22nd I.C.R.C. (Dublin)*, Vol. 1, p. 464

Punch, M.: 2005

Punch, M., Akerlof, C. W., Cawley, M. F., Chantell, M., Fegan, D. J., Fennell, S., Gaidos, J. A., Hagan, J., Hillas, A. M., Jiang, Y., Kerrick, A. D., Lamb, R. C., Lawrence, M. A., Lewis, D. A., Meyer, D. I., Mohanty, G., O'Flaherty, K. S., Reynolds, P. T., Rovero, A. C., Schubnell, M. S., Sembroski, G., Weekes, T. C., and Wilson, C.: 1992, Nature **358**, 477

Quinn, J., Akerlof, C. W., Biller, S., Buckley, J., Carter-Lewis, D. A., Cawley, M. F., Catanese, M., Connaughton, V., Fegan, D. J., Finley, J. P., Gaidos, J., Hillas, A. M., Lamb, R. C., Krennrich, F., Lessard, R., McEnery, J. E., Meyer, D. I., Mohanty, G., Rodgers, A. J., Rose, H. J., Sembroski, G., Schubnell, M. S., Weekes, T. C., Wilson, C., and Zweerink, J.: 1996, ApJ **456**, L83+

Quinn, J., Hughes, P., and Gammell, S.: 2001, *Analysis of 2000/2001 Cassiopeia A Data*, VERITAS Collaboration Internal memo

Quinn, M. and Moriarty, P.: 2003, *Optimization of Cuts 2002/3.*, VERITAS Collaboration Internal memo

Reimer, O. and Pohl, M.: 2002, A&A **390**, L43

Rieke, G. H. and Weekes, T. C.: 1969, Technical Report 301, Smithsonian Astrophysical Observatory

Ritz, S. and GLAST Team: 2003, *American Astronomical Society Meeting* **203**,

Roberts, M. D., McGee, P., Dazeley, S. A., Edwards, P. G., Hara, T., Holder, J., Kawachi, A., Kifune, T., Matsubara, Y., Mizumoto, Y., Mori, M., Muraishi, H., Muraki, Y., Naito, T., Nishijima, K., Ogio, S., Osaki, T., Patterson, J. R., Rowell, G. P., Sako, T., Sakurazawa, K., Susukita, R., Tamura, T., Tanimori, T., Thornton, G. J., Yanagita, S., Yoshida, T., and Yoshikoshi, T.: 1999, A&A **343**, 691

Rose, H., Bird, D., Buckley, J., Cawley, M. F., Chantell, M., Harris, K., Lessard, R., Schubnell, M. S., Sembroski, G., and Wilson, C.: 1995, in *Proceeedings of 24th I.C.R.C., (Rome)*, Vol. 3, p. 766

Sambruna, R. M., Urry, C. M., Maraschi, L., Ghisellini, G., Mukherjee, R., Pesce, J. E., Wagner, S. J., Wehrle, A. E., Hartman, R. C., Lin, Y. C., and von Montigny, C.: 1997, ApJ **474**, 639

Samorski, M. and Stamm, W.: 1983, ApJ **268**, L17

Samuelson, F. W.: 1999, *Ph.D. thesis*, Iowa State University

Samuelson, F. W., Biller, S. D., Bond, I. H., Boyle, P. J., Bradbury, S. M., Breslin, A., Buckley, J. H., Burdett, A. M., Buss'ons Gordo, J., Carter-Lewis, D. A., Cantanese, M., Cawley, M. F., Fegan, D. J., Finley, J. P., Gaidos, J. A., Hall, T., Hillas, A. M., Krennrich, F., Lamb, R. C., Lessard, R. W., McEnery, J. E., Masterson, C., Quinn, J., Rodgers, A. J., Rose, H. J., Sembroski, G. H., Srinivasan, R., Vassiliev, V. V., Weekes, T. C., and Zweerink, J.: 1998, ApJ **501**, L17+

Scarsi, L., Bennett, K., Bignami, G. F., Boella, G., Buccheri, R., Hermsen, W., Koch, L., Mayer-Hasselwander, H. A., Paul, J. A., and Pfeffermann, E.: 1977, in *ESA SP-124: Recent Advances in Gamma-Ray Astronomy*, pp 3–11

Scott, D.: 1992, *Multivariate Density Estimation*, p. 125, John Wiley & Sons, Inc., New York

Sikora, M., Begelman, M. C., and Rees, M. J.: 1994, ApJ **421**, 153

Sinnis, C.: 2003, in *Particle Astrophysics Instrumentation. Edited by Peter W. Gorham. Proceedings of the SPIE, Volume 4858, pp. 358-366 (2003).*, pp 358–366

Stamm, W. and Samorski, M.: 1983, *International Cosmic Ray Conference, 18th, Bangalore, India, August 22-September 3, 1983, Conference Papers. Volume 1 (A85-22801 09-93). Bombay, Tata Institute of Fundamental Research, 1983, p. 131-134. Sponsorship: Deutsche Forschungsgemeinschaft.* **1**, 131

Stecker, F. W. and de Jager, O. C.: 1997, ApJ **476**, 712

Stecker, F. W., de Jager, O. C., and Salamon, M. H.: 1992, ApJ **390**, L49

Stecker, F. W., de Jager, O. C., and Salamon, M. H.: 1996, ApJ **473**, L75+

Swanenburg, B. N., Bennett, K., Bignami, G. F., Buccheri, R., Caraveo, P., Hermsen, W., Kanbach, G., Lichti, G. G., Masnou, J. L., Mayer-Hasselwander, H. A., Paul, J. A., Sacco, B., Scarsi, L., and Wills, R. D.: 1981, ApJ **243**, L69

Tanimori, T., Hayami, Y., Kamei, S., Dazeley, S. A., Edwards, P. G., Gunji, S., Hara, S., Hara, T., Holder, J., Kawachi, A., Kifune, T., Kita, R., Konishi, T., Masaike, A., Matsubara, Y., Matsuoka, T., Mizumoto, Y., Mori, M., Moriya, M., Muraishi, H., Muraki, Y., Naito, T., Nishijima, K., Oda, S., Ogio, S., Patterson, J. R., Roberts, M. D., Rowell, G. P., Sakurazawa, K., Sako, T., Sato, Y., Susukita, R., Suzuki, A., Suzuki, R., Tamura, T., Thornton, G. J., Yanagita, S., Yoshida, T., and Yoshikoshi, T.: 1998, ApJ **497**, L25+

Tanimori, T., Naito, T., and Yoshida, T.: 2001

Tavani, M.: 2003, in *Science with the New Generation of High Energy Gamma-Ray Experiments : Between Astrophysics and Astroparticle Physics*, pp 87–+

Teegarden, B. J. and INTEGRAL Science Working Team: 1999, *Bulletin of the American Astronomical Society* **31**, 740

Thompson, D. J., Bertsch, D. L., Dingus, B. L., Esposito, J. A., Etienne, A., Fichtel, C. E., Friedlander, D. P., Hartman, R. C., Hunter, S. D., Kendig, D. J., Mattox, J. R., McDonald, L. M., von Montigny, C., Mukherjee, R., Ramanamurthy, P. V., Sreekumar, P., Fierro, J. M., Lin, Y. C., Michelson, P. F., Nolan, P. L., Shriver, S. K., Willis, T. D., Kanbach, G., Mayer-Hasselwander, H. A., Merck, M., Radecke, H.-D., Kniffen, D. A., and Schneid, E. J.: 1995, ApJS **101**, 259

Ueno, S., Koyama, K., Nishida, M., Yamauchi, S., and Ward, M. J.: 1994, ApJ **431**, L1

Urry, C. M. and Padovani, P.: 1995, PASP **107**, 803

Völk, H. J., Aharonian, F. A., and Breitschwerdt, D.: 1996, in *TeV Gamma-ray Astrophysics. Theory and Observations*, pp 279–297

Vermeulen, R. C. and Cohen, M. H.: 1994, ApJ **430**, 467

Weekes, T. and Turver, K.: 1977, in *Proceedings of the 12th Eslab Symposium (Frascati)*, Vol. ESA SP-124, p. 279

Weekes, T. C.: 1981, *Mercury* **10**, 78

Weekes, T. C.: 2003a, *American Astronomical Society Meeting* **203**,

Weekes, T. C.: 2003b, *Very high energy gamma-ray astronomy*, Very high energy gamma-ray astronomy, by Trevor C. Weekes. IoP Series in astronomy and astrophysics, ISBN 0750306580. Bristol, UK: The Institute of Physics Publishing, 2003

Weekes, T. C., Cawley, M. F., Fegan, D. J., Gibbs, K. G., Hillas, A. M., Kowk, P. W., Lamb, R. C., Lewis, D. A., Macomb, D., Porter, N. A., Reynolds, P. T., and Vacanti, G.: 1989, ApJ **342**, 379

Weekes, T. C., Fazio, G. G., Helmken, H. F., O'Mongain, E., and Ricke, G. H.: 1972, ApJ **174**, 165

Wilson, A. S., Braatz, J. A., Heckman, T. M., Krolik, J. H., and Miley, G. K.: 1993, ApJ **419**, L61+

Yoshikoshi, T., Kifune, T., Dazeley, S. A., Edwards, P. G., Hara, T., Hayami, Y., Kakimoto, F., Konishi, T., Masaike, A., Matsubara, Y., Matsuoka, T., Mizumoto, Y., Mori, M., Muraishi, H., Muraki, Y., Naito, T., Nishijima, K., Oda, S., Ogio, S., Ohsaki, T., Patterson, J. R., Roberts, M. D., Rowell, G. P., Sako, T., Sakurazawa, K., Susukita, R., Suzuki, A., Tamura, T., Tanimori, T., Thornton, G. J., Yanagita, S., and Yoshida, T.: 1997, ApJ **487**, L65+

Zweerink, J. A., Akerlof, C. W., Biller, S. D., Boyle, P., Buckley, J. H., Burdett, A., Bussons Gordo, J., Carter-Lewis, D. A., Catanese, M., Cawley, M. F., Fegan, D. J., Finley, J. P., Gaidos, J. A., Hillas, A. M., Krennrich, F., Lamb, R. C., Lessard, R. W., McEnery, J. E., Mohanty, G., Quinn, J., Rodgers, A. J., Rose, H. J., Samuelson, F. W., Schubnell, M. S., Sembroski, G., Srinivasan, R., Weekes, T. C., and Wilson, C.: 1997, ApJ **490**, L141+